Numéro d'ordre : 2022LYSEC022

THÈSE de DOCTORAT DE L'UNIVERSITÉ DE LYON
opérée au sein de
l'École Centrale de Lyon

École Doctorale 162 : Mécanique, Énergétique, Génie Civil et Acoustique

Spécialité : Mécanique des fluides et Énergétique

Soutenue publiquement le 8 Juin 2022, par :

Cédric BABIN

Impact of Shrouded Stator Cavity Flow on Axial Compressor Performance and Stability

---

Devant le jury composé de :

Antoine DAZIN	Professeur, École Nationale Supérieure d'Arts et Métiers	*Président*
Laurent GICQUEL	Ingénieur de Recherche Senior - HDR, CERFACS	*Rapporteur*
Carl SANGAN	Dr., Reader, Turbomachinery Research Centre, University of Bath	*Rapporteur*
Emma CRONER	Dr., Ingénieur Méthodes, Safran Helicopter Engines	*Examinateur*
Nicolas BINDER	Professeur, ISAE-Supaero	*Examinateur*
Xavier OTTAVY	Directeur de Recherche CNRS, MFAE/LMFA, Ecole Centrale Lyon	*Directeur de Thèse*
Fabrizio FONTANETO	Associate Professor, Von Karman Institute for Fluid Dynamics	*Directeur de Thèse*
Michel DUMAS	Dr., Expert Aerodynamique Compresseur, Safran Aircraft Engines	*Encadrant industriel*

Remerciements

Dans un premier temps je souhaiterais remercier Monsieur Dumas Michel, Monsieur Ottavy Xavier, ainsi que Monsieur Fontaneto Fabrizio de m'avoir choisi et soutenu pour la réalisation de ce travail de thèse. Je remercie également la société Safran Aircraft Engines ainsi que l'Association Nationale Recherche Technologie (ANRT) pour le financement de mes travaux. Pour finir, je remercie the von Karman Institute for Fluid Dynamics de m'avoir accueilli et laissé la possibilité de mener mes activités expérimentales.

Je tiens encore une fois à te remercier Fabrizio pour la place importante que tu as eu afin que ce projet aboutisse. Notre contact au quotidien à l'Institut aura été primordial aussi bien sur le plan scientifique que personnel. Dès le départ, une relation de confiance s'est établie. L'autonomie que tu m'as laissée m'a beaucoup aidé, au fil des années, à structurer mon travail. Petit mot d'affection pour les anciens collègues et collègues de bureau Matteo, Stefano, Riccardo, et Gonçalo. Je vous souhaite de la réussite dans vos projets.

Papi et Mamie je suis tellement heureux que cette opportunité m'a autorisé à m'approcher à une heure et demi de chez vous. Les heures de selle et les discussions cyclo du dimanche matin vont continuer à l'infini dans « Les Weppes ». Grany et Daddy malgré la distance, je pense beaucoup à vous. Votre dernière visite à Bruxelles m'a rappelé à quel point vous me manquiez. Je vous embrasse. Papa et Maman, un « thésard » de plus dans la famille, un peu inattendu. Je vous remercie de m'avoir toujours soutenu dans mes choix. Encore merci Papa pour ta relecture, tes questions, tes conseils, ainsi que tes corrections sur le fond et la forme de ce manuscrit. De gros bisous aussi aux frère/sœur/acolytes/famous Alice La Biche et Cyril Kiki.

Pour finir, une pensée d'amour à Ludivine. Dix ans déjà que l'on partage tout, merci d'être à mes côtés, je t'aime de tout mon cœur.

Résumé

Dans les compresseurs axiaux, des aubes de stator à pied "shrouded" sont utilisées comme solution pour garantir le jeu de fonctionnement axial et radial avec l'assemblage rotor. L'augmentation de pression statique de l'amont vers l'aval du compresseur induit un écoulement de recirculation dans les cavités sous veine ainsi créées. Cet écoulement de fuite est ensuite réinjecté dans la veine principale, au détriment de la performance de l'étage.

L'objectif principal de ce travail a été d'évaluer l'impact des écoulements de fuite cavité sur la performance et la stabilité des compresseurs axiaux. Pour ce faire, des activités de recherche expérimentales et numériques ont été conduites sur l'étage de compresseur H25 et sa cavité sous stator (nombre de Reynolds $Re_r = 2.2 * 10^6$ et rapport d'aspect G = 0.06, en moyenne) disponibles au von Karman Institute for Fluid Dynamics. La sensibilité de la performance de l'étage H25 et de l'écoulement cavité ont été évalués en fonction des conditions d'injection, du vannage du compresseur, et de sa vitesse de rotation, fournissant une base de données sans précédent.

Les résultats obtenus indiquent qu'il existe une dépendance de la performance de l'étage en fonction du débit d'injection dans la cavité. Par exemple, une chute de rendement isentropique de 0,97% pour un débit cavité de 0,56% du débit machine est mesurée au point de dessin du compresseur. Cette chute de la performance est attribuée à une augmentation du blocage de l'écoulement, une augmentation de l'asymétrie de la couche limite, et une augmentation de la température totale en amont de l'aube stator. Il a également été mesuré que les effets des écoulements de fuite cavité sont contenus proche paroi moyeu, et ce, jusqu'à 20% de la hauteur de veine. Par ailleurs, la stabilité de l'étage du compresseur, i.e. marge au pompage, n'est pas affectée par le débit d'injection dans la cavité. Les données obtenues montrent que dans le volume cavité, l'organisation du champ moyen est induite par une interaction réciproque entre la géométrie et l'écoulement. Il est également démontré que l'injection tend à homogénéiser le champ de pression dans la cavité. La comparaison de l'instationnarité de l'écoulement cavité et veine principale indique que la connexion cavité/veine agit comme un filtre pour les instabilités les plus énergétiques issues de la cavité. Parmi ces instabilités, les mesures indiquent une forte présence de l'effet de l'assemblage rotor, qui génère une paroi cavité non lisse. Une analyse de la dynamique de l'écoulement révèle une forte dépendance spatiale des modes cavité, ce qui indique la présence de sources ponctuelles d'instabilité. L'ajout d'injection provoque une augmentation de l'amplitude des modes à basses fréquences, i.e. inférieur à 15% de la fréquence de passage des aubes, pour les points situés dans le passage de l'écoulement d'injection. Pour finir, une évaluation des modes non synchrones de la cavité indique que la fréquence et l'amplitude de ces derniers sont faiblement impactées par le débit de recirculation. Cependant, la fréquence de certaines instabilités varie en fonction des conditions opératives du compresseur. Il est également montré que la vitesse de rotation des modes non synchrones cavité, qui se situe à une vitesse de groupe inférieure à la moitié de la vitesse de rotation du disque, est fortement dépendante de la vitesse de rotation du compresseur.

En conclusion, il a été possible de quantifier la chute de performance du compresseur étudié causée par l'écoulement de fuite cavité. En parallèle, la base de données expérimentale collectée a permis de caractériser les instabilités présentes dans la cavité sous stator. A partir de ces résultats, les recherches futures auront pour objectif de prouver l'origine précise des instabilités cavité. Cela permettra de mieux cerner l'importance de cet écoulement de fuite dans le fonctionnement des compresseurs axiaux tout en autorisant des avancées pour les approches de modélisation basse fidélité des cavités sous stator.

Mots-clés: Compresseur axial, Cavité, Ecoulement de cavité, Ecoulement de fuite, Turbomachine

Abstract

In axial compressors, shrouded stator blades are used to clear the rotor assembly axially and radially. As a consequence, the cavity volumes that are created under the stator platform experience a downstream-to-upstream flow recirculation triggered by the static pressure increase in the main channel. The leakage flow is then re-injected in the power stream, altering the stage performance.

This work objective was to evaluate the impact of cavity leakage flow on the performance and stability of axial compressors. This research used experimental and numerical activities conducted on the von Karman Institute for Fluid Dynamics H25 stage and associated cavity, with average Reynolds number $Re_r = 2.2 * 10^6$ and average aspect ratio G = 0.06. Unprecedented experimental investigation of the cavity flow and its interaction with the power stream was performed. The sensitivity of H25 stage performance and stability as well as the cavity flow were evaluated against injection conditions, compressor throttling and compressor speed. Parametric steady RANS simulations of the stage under injection and full annulus unsteady simulation of the cavity were used to support the findings and state on the relevance of such approach in the preliminary design phase of axial compressors components.

Stage performance is highly affected by the cavity leakage flow. As an example, a stage efficiency reduction of 0.97% is measured for a leakage fraction of 0.56% at machine design point. This performance drop is attributed to the effect of cavity flow on: the blockage ratio, the boundary layer skewness, and total temperature increase at stator row inlet. It is also demonstrated that these effects are contained in the main channel low span region, up to 20% span. The stability, i.e. stall margin, of the machine is found not to be affected by the level of injection. In the cavity, it is showed that there is a mutual interaction between geometry and the cavity flow field organization. The injection homogenizes the cavity flow field and the associated pressure gradient. The comparison between the cavity and main flow unsteadiness indicates that the cavity trench acts as a filter on the most energetic instabilities from the cavity. Among these instabilities, flow measurement present clear traces of the periodic geometrical effect that are induced by the rotor disk mechanical assembly, which causes the cavity walls to be non smooth. A deeper analysis of the cavity dynamics reveals that there is a strong spatial sensitivity for cavity modes amplitude which indicates the presence of local sources of unsteadiness. The leakage injection also triggers an amplitude increase of the low frequencies, typically below 15% of the blade passing frequency, for the points in the leakage flow path. To finish, an evaluation of the disc non-synchronous modes in the cavity indicates that the frequency and amplitude of cavity modes are few sensitive to the leakage fraction. However, the frequency of some of these instabilities is affected by the compressor operating condition. It is also shown that the azimuthal travelling speed of the cavity modes, measured at a group velocity inferior to half of the disc rotation speed, is highly sensitive to rotor disk rotation speed variations.

As a conclusion, it has been possible to quantify the compressor performance degradation induced by the cavity leakage flow. In the same time, the large experimental database collected allowed to characterize the instabilities in the stator shroud cavity. Based on the obtained results, future research aims to prove the origin of the measured cavity instabilities. This will allow to better describe the implication of the cavity flow in the axial compressor flow field and also create new progress for cavity flow low order modelling.

Keywords : Axial Compressor, Cavity, Cavity Flows, Leakage Flow, Turbomachine

Table of Contents

List of Figures

List of Tables

Nomenclature

Greek letters

α	Flow angle[°]
δ	Boundary layer thickness [m]
$\Delta\gamma$	Skewness induced additional turning [°]
η	Efficiency
γ	Heat capacity ratio
γ_e	External streamline flow angle with reference in 3DTBL [°]
γ_w	Flow angle at the wall [°]
ι	Thermal expansion coefficient [1/K]
κ	Thermal diffusivity [m^2/s]
λ	Throttle parameter
λ_t	Cavity through flow parameter
ν	Fluid kinematic viscosity [m^2/s]
μ	Fluid dynamic viscosity [Pa.s]
Ω	Rotor rotational speed [rad/s]
ω_d	Disk rotational speed [rad/s]
ω_s	Flow structure rotational speed [rad/s]
ϕ	Stage flow coefficient
Φ	Meridional flow angle
Π	Pressure ratio
ψ	Stage loading coeffcient
ρ	Fluid density [kg/m^3]
σ	Standard deviation
ξ	Energy (spectra)
ζ_s	Entropy loss coefficient

Variables

BF	Blockage factor
c_p	Specific heat capacity [J/kg.K]
C_w	Reduced flow parameter [$kg/(s^2.Pa.m)$]
f_{EO}	Time resolution. Number of sampled points per rotation
G	Cavity local aspect ratio
g	Acceleration of gravity [m/s^2]
GCI	Grid convergence index
Δh	Enthalpy variation [J]
Δr_X	Labyrinth seal tooth X closing [mm]
h	Cavity width [m]
L_f	Leakage fraction
$\dot{m}$	Mass flow [kg/s]

N	Rotation speed [rpm]
Nn	Compressor rotational speed in percentage of the nominal speed
p	Pressure [mbar]
Q_e	Edge velocity component in 3D boundary layer [m/s]
R	Molar gas constant [J/(K.mol)]
R_i	Inner disc radius [m]
R_o	Outer disc radius [m]
r	Cavity local radius [m]
Re	Reynolds number
Re_i	Cylindrical Reynolds number (Taylor-Couette type flow)
Re_r	Local Reynolds number
S_f	Swirl ratio
Δs	Entropy variation [J/K]
T	Temperature [K]
Ta	Taylor number
U_n	Cross stream velocity component in 3D boundary layer [m/s]
U_s	Stream wise velocity component in 3D boundary layer [m/s]
V_t	Tangential velocity [m/s]
V_z	Axial velocity [m/s]
W	Work [J]
W_r	Stage corrected mass flow [kg/s]

Abbreviations

3HV	Three hole virtual
3DTBL	Three dimensional turbulent boundary layer
CFD	Computational fluid dynamics
DL	Design loading operating point
EO	Engine order. 1 EO = 1 event per rotor wheel revolution
EA	Ensemble average
NAC	Natural cavity
NOC	No cavity
NS	Near stall loading operating point
NL	No leakage
RPM	Rotations per minute
SE	Stall exploration
SM	Stall margin
TC	Taylor Couette
T_f	Temporal fluctuations (around signal ensemble average)
TPG	Transverse pressure gradient
TV	Trench vortex
VKI	von Karman Institute for Fluid Dynamics

Subscripts

$1,2,3,4,2',3',4'$	Thermodynamic stations (Chapter 1)
$0,1,2,4$	Measurement plane
avg	Average
Comp	Compressor
exp	Experimental
i	Internal
in	Inlet
is	Isentropic

j	Flow component
$leak$	Leakage
$local$	Local - Radius dependent
ref	Reference
rot	Rotor
s	Static
sp	Specific
st	Static to total
$stat$	Stator
Turb	Turbine
t	Total
th	Thermodynamic
tt	Total to total
o	Outer
out	Out

Motivation and objectives

Engine manufacturers competitiveness is linked to their ability to produce the most performant products within the current air transport sector regulations. Since the regulations are evolving, engine manufacturers must adapt. The current regulation trend requires an adaptation through performance increase. It means: fuel consumption reduction, low maintenance costs, low noise levels, and limited emissions.

A way to fit the regulations is to improve aircraft engine cycle efficiency. A possibility to obtain an improvement in cycle efficiency is to increase the pressure ratio at the exit of the compressor. In order to reach a higher compressor pressure ratio while ensuring a fixed Mach number at the inlet of the combustion chamber smaller main channel section (and blades) are used. At fixed pressure ratio, compressor blade height is also defined as a function of the final operating window of the whole engine.

With small blades, the main flow cross section is reduced which gives more relative importance to secondary flow located in the blade row end wall regions. The relative importance of technological effects caused by manufacturing and mechanical assembly constraints is also increased. Some of these constraints are fixed and others evolving slower than the need in performance improvement. Among the technological effects mentioned, blade fillets, steps, non smooth contouring of end walls, and clearances cause flow disruption and so efficiency losses.

At the interface between rotor and stator rows, an operational clearance is mandatory for the compressor operation. The presence of such clearance induces flow leakage and flow re injection regions in the main stream. One of the approach used consists in having the seal radius below the hub line of the main channel. To achieve good sealing properties, stator blades are shrouded. Shrouded configuration creates: (1) Cavity volumes below the hub line, (2) an axial clearance at the hub radius between the rotor platform and the stator shroud platform. Caused by negative pressure gradient in the stream wise direction, main flow is ingested in the downstream cavity volume and ejected upstream of the stator row.

The main objective of this work was to evaluate the impact of cavity leakage flows on the performance and stability of axial compressors.

The first step was to evaluate the performance degradation caused by the cavity flow leakage injection into the main channel.

The second step of the work was to understand what components of the main flow field are affected by the cavity flow, hence generates a performance degradation.

Finally, the third and last step was to propose an overview of the cavity flow field in realistic engine conditions. The purpose was to highlight the loss generating mechanism from the cavity and their interaction with the main stream.

At the same time, the feasibility to perform controlled leakage measurement in a closed loop facility equipped with a one stage axial compressor has been evaluated.

In parallel of the experimental work, the relevance of the cavity flow prediction and its impact on compressor performance given by Reynolds averaged simulation (RANS) has been also detailed with respect to the experimental data.

Thesis outline

This manuscript is organized in five chapters. Chapter 1 is an introduction to axial compressor flow. The working principle and the key parameters for performance evaluation of an axial compressor are detailed. Selected flow features are introduced in order to define the role of shroud cavities and associated leakage flow in the main flow path. At the end of Chapter 1, the characteristics of the H25 axial compressor stage studied in this work are presented.

In Chapter 2, a review of the flow in rotor stator cavities is done. This part describes the flow topology encountered in rotor stator cavities composed of parallel disks, coaxial cylinders, and annular cavities. Non dimensional numbers that define the rotor stator cavity geometry and, as a consequence, the induced flow regimes are collected. This chapter then closes on the presentation of the C2 stator shroud cavity geometry used in combination with the H25 stage. The cavity geometry non dimensional numbers are computed to predict the expected flow features. The use of non dimensional numbers also allow to locate the geometry in the literature.

Chapter 3 is a detailed presentation of the experimental and numerical methods used to achieve this work objectives.

Chapter 4 includes first the performance impact of the C2 cavity leakage flow, with forced leakage, on the H25 stage performance and stability. The time averaged and time resolved cavity flow interactions with the main stream are then highlighted. To finish, a time averaged and time resolved description of the cavity flow features is performed.

Finally, Chapter 5 closes the manuscript with a presentation of possible axis of research concerning the cavity flows and their impact on axial compressor performance and stability.

Chapter 1

Axial compressor flow

THis chapter frames the phenomenology and nomenclature to describe and understand axial compressor flow. The first section presents the role of the axial compressor in a turbomachinery assembly. The second section introduces the parameters for axial compressor performance evaluation. Section three summarizes the secondary flow system generated in a blade row. The stability of axial compressor as well as the technological effects impact on the flow field are discussed in sections four and five. To finish, design characteristics of the research stage used in this study are listed.

Contents

1.1 Turbomachines for aircraft propulsion

1.1.1 Operating principle

Turbomachines are rotating assemblies designed to operate a thermodynamic transformation. A turbomachine consists of a single or multi-row rotor that, under the action of aerodynamic forces, ensures the transfer of energy from/to the working fluid meaning that, through the machine, its enthalpy is changed. In aircraft propulsion applications, turbomachines are employed within the gas turbine engine to operate an open thermodynamic cycle with a net power output. The latter is employed to increase the momentum of the working fluid, therefore generating the required propulsive thrust. The Whittle W1 and Von Ohain He.S3B were, in 1939, the first applications of turbomachines as turbopropulsion units. These engines allow thrust in the order of 5kN. As a comparison, last generation turbofan for civil application are capable of continuous thrust value of around 140kN (CFM LEAP 1-A).

1.1.2 Modular construction

Gas turbine engines operate a Joule-Brayton cycle which relies over a compression, an isobaric release of heat, and an expansion. These three phases coincide with three different components: the compressor the burner and the turbine respectively. The modules and stations are represented in Figure 1.1a. The thermodynamic transformations are showed in Figure 1.1b. The design philosophy of such assembly starts from cycle specifications in order to define the thermodynamic requirements for each component. In the design process the correct thermodynamic matching of the modules must be ensured.

The architecture of the turbomachinery assembly lies in the type and positioning of the different elements previously introduced. Most of the existing component architectures are representative of three families. The axial assemblies from which outlet flow is parallel to the machine axis. These machines are defined by limited compression ratios per stage but high mass flow rates. The second family are the centrifugal assemblies. Here the inlet or outlet plane are not aligned with the machine axis. Mass flow is limited but compression capabilities for a single stage are improved with respect to axial assemblies. The third type of turbomachine combine axial and centrifugal assemblies and is called mixed (ex: Turbofan Williams F107). For civil aircraft applications, axial components are used for the most part. The engine display multi flux configuration as shown in Figure 1.1c. In the case of a bi-flux configuration (typical for civil applications), the primary flux brings air to the combustion chamber and follows the Brayton cycle of Figure 1.1b. The work retrieved on the shaft through the primary flux also drives the secondary flux which only performs a compression but accounts for eighty percent of the engine total thrust. Multiple concentric shafts and gearbox can be added to adapt the compressor and turbine wheel speed to the thermodynamic requirements of the target cycle.

For the ideal Brayton cycle, the equation 1.2 and equation 1.3 give the non dimensional useful specific work and the cycle thermodynamic efficiency η_{th}.

$$\Pi = \frac{p_2}{p_1} \tag{1.1}$$

$$\frac{W_{sp}}{c_p T_1} = \frac{W_{Turb} - W_{Comp}}{c_p T_1} = \frac{T_3}{T_1}\left(1 - \frac{1}{\Pi^{\frac{\gamma-1}{\gamma}}}\right) - \left(\Pi^{\frac{\gamma-1}{\gamma}} - 1\right) \tag{1.2}$$

$$\eta_{th} = 1 - \frac{1}{\Pi^{\frac{\gamma-1}{\gamma}}} \tag{1.3}$$

In these equations the specific work output and thermodynamic efficiency depend on the compressor pressure ratio and the temperature ratio T_3/T_1 between turbine inlet and compressor inlet. For a fixed compressor pressure ratio, the specific work output increases with T_3/T_1. For a fixed value of temperature ratio, the compressor pressure ratio needed to maximize the specific work is lower than the one that maximize the cycle efficiency. Here is the difference between military and civil aircraft engines. The first one requires a higher specific work output, hence works at lower compression ratio. The second one favours higher cycle efficiency so operates at higher pressure ratio.

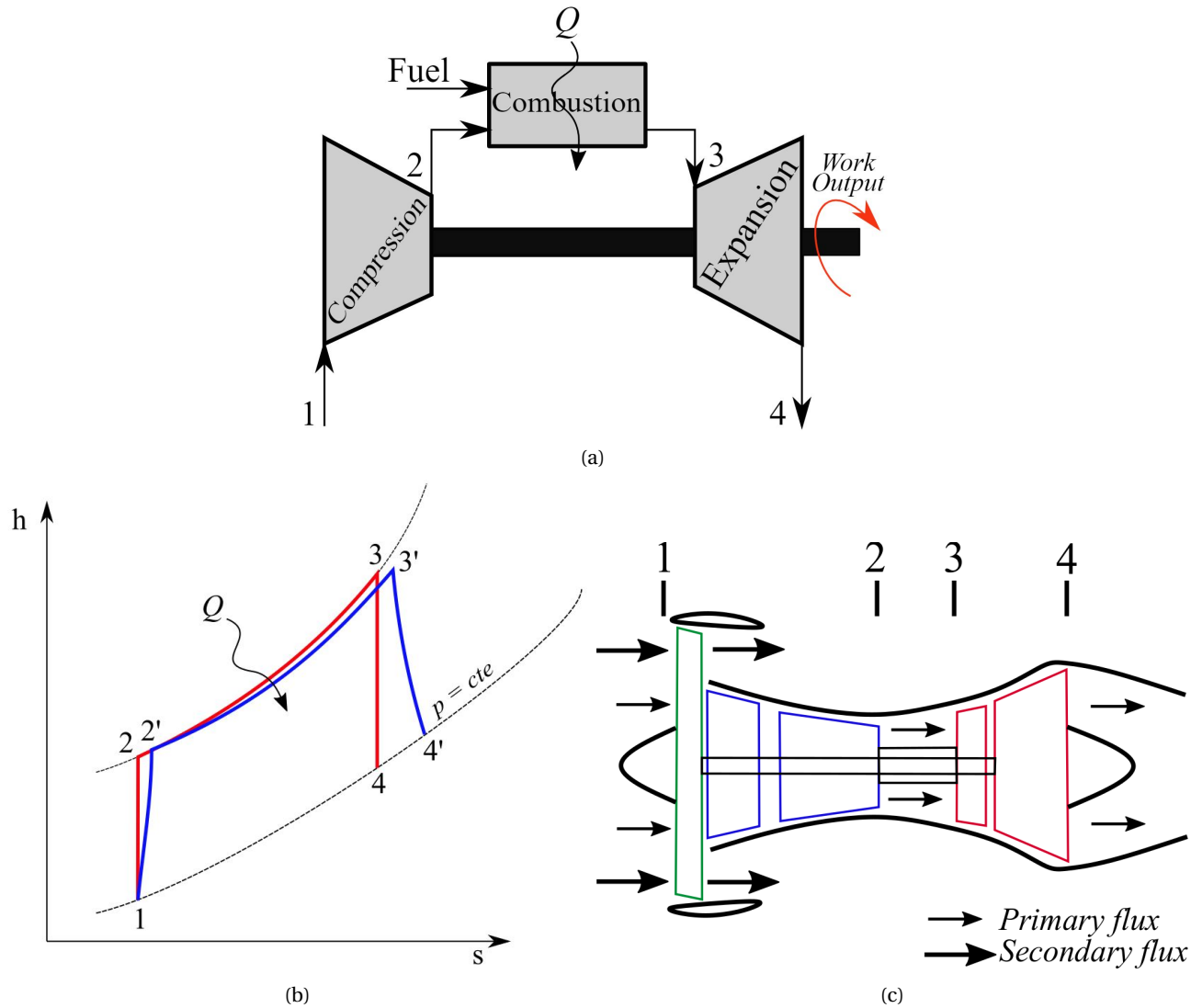

Figure 1.1: (a) - Turbomachine modular construction - (b) Enthalpy - Entropy diagram of ideal (in red) and real (in blue) Brayton cycle for aircraft engine thermodynamic transforms. 1–>2: Compression; 2–>3: Combustion; 3–>4: Expansion - (c) Bi-flux aircraft engine construction.

1.2 Performance of axial compressor

1.2.1 Parameters for performance evaluation

The compression of the air is staged so that the adverse pressure gradient in the flow direction does not lead to boundary layer separation over the blades. Each stage is composed by a succession of two blade rows. The rotor row is responsible for pressure, kinetic, and calorific energy transfer to the fluid. The stator row redirects the flow without energy exchange. The isentropic efficiency η_{is} of an axial compressor compares the specific work transferred to the fluid by an ideal adiabatic process (1–>2 on Figure 1.1b) with the real transformation (1–>2') that includes losses by means of entropy generation. Equation 1.4 highlights the dependency of the isentropic efficiency to the inlet to outlet pressure and temperature ratios. High compression ratios and low temperature increase through the stages maximizes the compressor efficiency.

$$\eta_{is} = \frac{\Delta h_{tis}}{\Delta h_t} = \frac{(\frac{p_{t2'}}{p_{t1}})^{\frac{\gamma-1}{\gamma}} - 1}{\frac{T_{t2'}}{T_{t1}} - 1} \tag{1.4}$$

A Pi-theorem analysis expresses isentropic efficiency (η_{is}) and total to total pressure ratio ($\Pi = \frac{p_{t2'}}{p_{t1}}$) as a function f of aerodynamic and machine geometrical parameters (cf. equation 1.5 where N = rotation speed, D = machine diameter, $\dot{m}$ = absolute mass flow, Re = Reynolds number).

$$\Pi, \eta_{is} = f(\frac{\dot{m}\sqrt{RT_{t1}}}{p_{t1}D^2}, \frac{ND}{\sqrt{RT_{t1}}}, Re, \gamma) \tag{1.5}$$

If the gas properties and the geometry of the compressor are kept constant (i.e. $\gamma = cte, D = cte, Re = cte$) and after the definition of reference conditions (p_{ref}, T_{ref}) the following simplification arises :

$$\Pi, \eta_{is}, \frac{T_{t2'}}{T_{t1}} = f(\frac{\dot{m}\sqrt{\theta}}{\delta}, \frac{N}{\sqrt{\theta}}) \tag{1.6}$$

Where $\theta = \frac{T_{t1}}{T_{ref}}$ and $\delta = \frac{p_{t1}}{p_{ref}}$.

It results that, at fixed Reynolds number, the performance evaluation of a turbomachine in terms of efficiency, pressure ratio and temperature ratio can be done with variation of the corrected mass flow $Wr = \frac{\dot{m}\sqrt{\theta}}{\delta}$ and the corrected rotational speed $Nr = \frac{N}{\theta}$. The rotational speed is further indicated as a percentage of the machine design speed Nn (nominal speed being $Nr = 100Nn$).

The performance of the machine is affected by the losses generated in the blade rows, and their propagation. Loss is attributed to entropy generation. Loss sources are multiple but they are attributed to viscous effects (boundary layers, mixing), the presence of shocks and heat transfer. For isolated compressor rows, stagnation pressure loss coefficient is used with the equation 1.7 between row inlet (*in*) and row outlet(*out*). Loss can also be expressed through an entropy loss coefficient introduced in equation 1.8 (cf. Denton (1993)) where Δs represents the stream wise entropy variation with respect to a reference state (see equation 1.9).

$$\omega = \frac{P_{tout} - P_{tin}}{P_{tin} - P_{in}} \tag{1.7}$$

$$\zeta_s = \frac{T_{out} - \Delta s}{h_{tin} - h_{in}} \tag{1.8}$$

$$\Delta s = C_p ln(\frac{T}{T_{ref}}) - R ln(\frac{P}{P_{ref}}) \tag{1.9}$$

1.2.2 Performance characteristics

In the previous section, the representation of axial compressor performance is based on non-dimensional parameters. From the isentropic total enthalpy change through the compressor, the pressure ratio, efficiency, and total temperature ratio are, at fixed Reynolds number, a function of the corrected mass flow and corrected speed. The characteristic curve of a compressor is presented in Figure 1.2 as a function of pressure ratio (Π) and corrected mass flow (Wr).

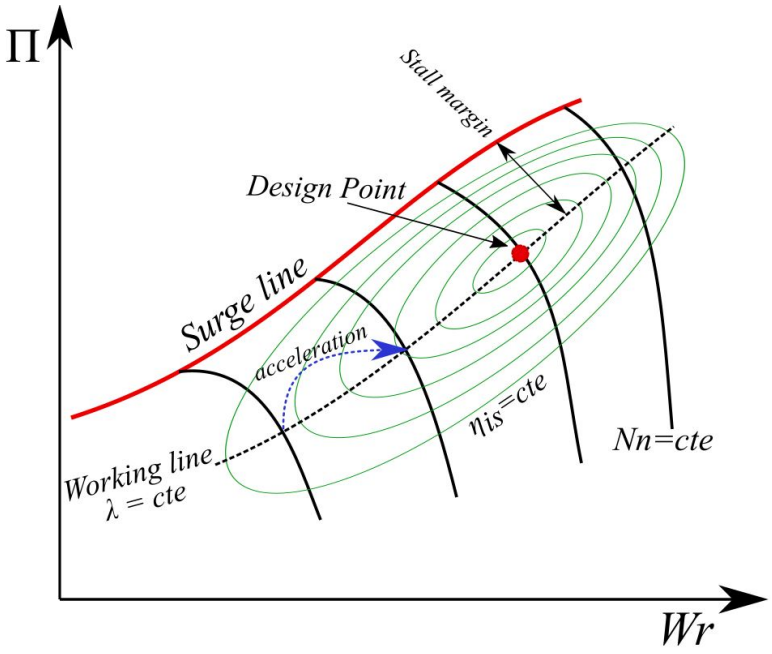

Figure 1.2: Performance curve of an axial compressor in the corrected mass flow/pressure ratio plane.

The design of the machine is centered around the operating point that maximizes the efficiency at nominal speed. At fixed rotational speed, the compressor behaves between two extrema: (1) Chocking; (2) Stall. Chocking condition limits the mass flow at low pressure ratio. At high pressure ratio aerodynamic failure defines for all the rotational speed a stability limit represented by a stall line (or surge line) on the compressor map. The ideal operating line of the compressor is then the line that maximizes the efficiency for each iso-rotating speed line while keeping enough margin with respect to the surge line. Each operating point is identified thanks to its vane (or throttling) parameter λ. It is defined as a function of pressure ratio and corrected mass flow. An example of curve at constant vane parameter is given in Figure 1.2 with the working line (dashed black line).

When subjected to a quick acceleration transient, the machine adapts firstly the rotational speed and only in second time to the mass flow. This leads to a virtual increase of the vane parameter, caused by an increase of rotational speed at fixed mass flow, therefore approaching the stability limit (see quick acceleration - in blue in 1.2). In slow acceleration, the operating point of the machine follows the throttling parameter curves at $\lambda = cte$.

1.3 Axial compressor secondary flow system

1.3.1 Secondary flows

In turbomachinery components, secondary flows are any flow whose direction differs from the main stream direction. Secondary flows are traduced by small and large scale vorticity fluctuations.

The vorticity convection is balanced by sum of viscous diffusion and two types of secondary flows (see Bordji (2015)): (1) First type secondary flows, induced by mean flow deviation; (2) Second type secondary flows generated by turbulent fluctuations. The physical understanding of secondary flow system is critical

for turbomachine design as secondary flow losses by means of entropy generation account for at least one third the total loss.

1.3.2 Junction flow

The first type secondary flow mentionned is found when the main flow encounter an obstacle. The resulting junction flow is typically found at the junction between compressor blades and endwall.

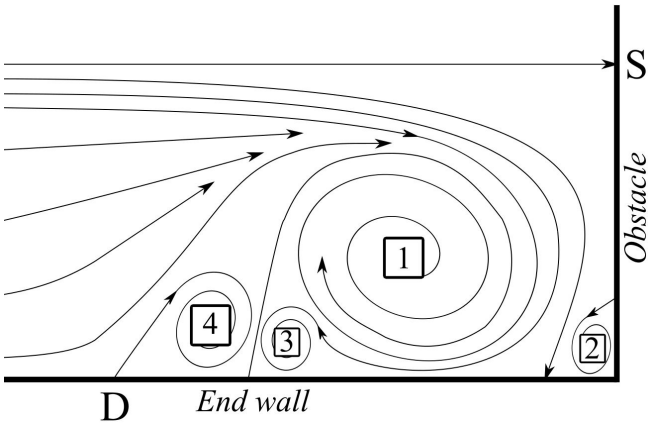

Figure 1.3: Junction flow pattern for a turbulent flow encountering an obstacle. D: Detachment point - S: Stagnation Point - 1: Horseshoe vortex - 2: Corner vortex - 3: Counter vortex - 4: Separation vortex.

The junction flow structure is well described in Simpson (2001) as well as in Ishii and Honami (1986). Junction flow representation is sketched in 1.3. The adverse pressure gradient caused by the presence of the obstacle forces the incoming endwall boundary layer to detach (D). Downstream of the detachment point, the horseshoe vortex (1) is the most identifiable flow feature. However, this region is also characterized by multiple secondary flows. Among those, the corner vortex (2) is the stress induced secondary vortex that links the end wall and obstacle boundary layer. The stability of the boundary layer in that region is dependent from the corner vortex state. The dynamics of the juction flow presented is bimodal in the detachment point area as highlighted in Ishii and Honami (1986) and Bordji (2015). It means that, in a turbulent flow, a zeroflow and a backflow mode alternate non periodically on a frequency range (defined by the Strouhal number St_δ) typically $0.005<St_\delta<0.13$. The flow mixing and resulting heat transfer is affected by the bimodal dynamics of the junction flow. As a consequence, it is presented in Praisner and Smith (2006) that vortices are released from the counter vortex (3) region into the main flow.

1.3.3 Blade row secondary flow system

As shown in Figure 1.4, the horseshoe vortex splits in two legs downstream of the blade leading edge stagnation point. In the case of an isolated airfoil, the junction flow structure generated at the leading edge (cf. Figure 1.3) would remain along the blade pressure and suction side. For axial compressor rows, Figure 1.4 illustrates how the blade polarity (pitch wise pressure gradient) carries the horseshoe vortex legs in the blade row. That is why the description of the flow topology at the blade leading edge is also crucial to explain downstream flow structures interactions in the case of a blade passage. The unbalanced pressure field generates a cross flow (Lakshminarayana and Ravindranath (1982)) from the blade pressure side to the adjacent blade suction side. The flow in the boundary layer region enters the blade passage at lower velocity than in free stream conditions but faces the same azimuthal transverse pressure gradient. To guarantee flow radial equilibrium, the streamlines on the pressure side of the blade that cannot follow the local high radius of curvature of the blade shift to lower radius of curvature. On the other side of the blade channel, the suction side leg of the horseshoe vortex stays attached to the blade.

The pressure side leg of the horseshoe vortex is driven towards the adjacent blade suction side, defining the passage vortex (Kang and Hirsch (1991)). As a consequence, Figure 1.4 shows how the counter-rotating

horseshoe vortex adjacent pressure side leg and suction side leg interact on the blade suction side. Due to this cross flow effect, low momentum fluid accumulates in the hub corner region (Gao et al. (2013)). It increases the turbulent intensity in that area, and also leads to the transport of the corner low energy fluid to higher span along the blade separation line visible in Figure 1.4.

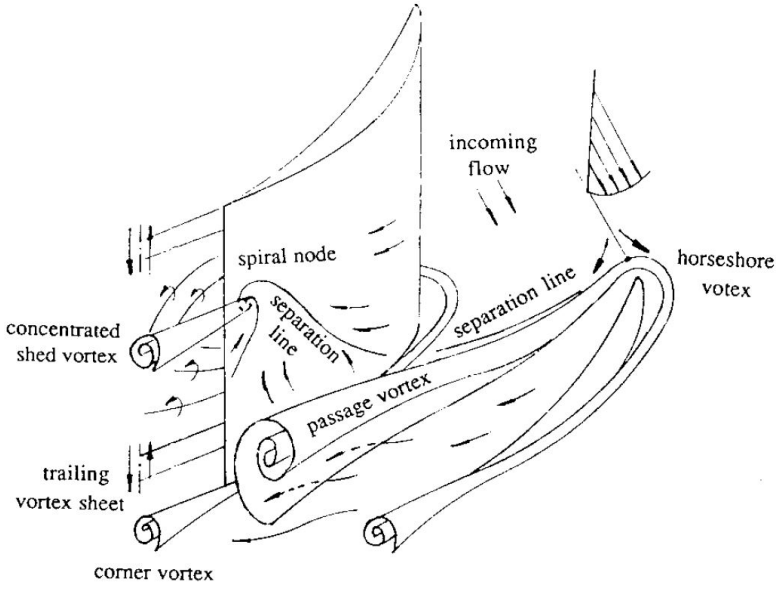

Figure 1.4: Axial compressor blade row secondary flow system - Kang and Hirsch (1991).

The contribution of secondary flow system to compressor stage losses is mainly included into the endwall losses as introduced in Denton (1993) loss decomposition approach. The mutual interaction of blade suction side and endwall boundary layer through the corner vortex affects the loss level. The corner vortex stability influences the total pressure drop and flow section blockage in the blade row. A consequence of corner vortex instability is that flow separation can occur on the blade and on the end wall.

In the blade row, the axial pressure gradient imposes a diffusion on the suction side, while the corner flow is also affected by the radial transverse pressure gradient (TPG) on the blade suction side and by the azimuthal transverse pressure gradient in the blade channel. For three dimensional boundary layers such as the one present on the blade and on the end wall, the TPG affects the momentum balance in the stream wise and cross stream direction.

The state of the blade suction side boundary layer is discussed first and independently from hub boundary layer considerations. To evaluate the state of the blade boundary layer, suction side flow structure identification is possible thanks to singular point analysis (Dallmann (1983))on end wall shear lines. Gbadebo et al. (2005) assess that blade suction side corner separation is an expected behaviour for any blade configuration, independently from variations in geometric parameters, aerodynamic parameters, and inlet boundary layer conditions. However, the intensity of the blade TPG drives the separation radial extension on the blade. In Taylor and Miller (2017), the authors identify blade lean angle and incoming incidence as two drivers of the transverse pressure gradient intensity on the blade. As a result, Figure 1.5 shows that an increase in the blade lean angle generates a stronger transverse pressure gradient. On the suction side of the blade, streamline contraction is enhanced with the TPG. The blade failure at high operating incidence is also dependent upon the TPG magnitude. Change in operating incidence brings more low momentum fluid in the passage vortex, and so in the corner region, due to an increase in the cross flow intensity. For high lean design, failure results in trailing edge separation at high incidence levels. The authors justify this results by showing that high lean cases present higher boundary layer shape factor at the trailing edge, induced by higher stream wise adverse pressure gradient. In Figure 1.5 weak TPG configurations present an overturn in the wall shear lines under the separation line. Prior to blade failure, the radial extent of the loss region in the blade suction side corner, is confined to low span region.

On the end wall, the loss level is also dependent upon the state of the end wall boundary layer. When

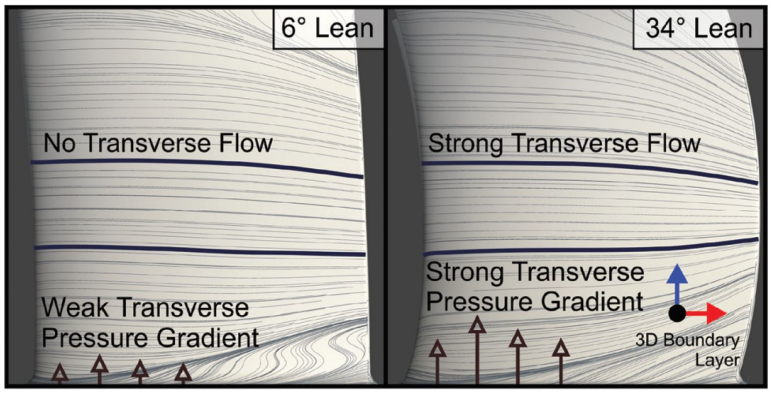

Figure 1.5: Blade lean effect on radial transverse pressure gradient - Taylor and Miller (2017).

corner vortex separation occurs on the blade suction side, it is called closed corner separation. However, some blade design present open corner separation where both blade and end wall boundary layer separate. The loss and blockage generated in the case of open separation is highly detrimental for the blade row performance. The study of Lei et al. (2006) proposes two parameters, based on two dimensional considerations, to evaluate blade design sensitivity to open corner separation. The diffusion parameter (D) (extension of Lieblein (1959) diffusion factor) and the stall indicator(S). D is an image of blade design parameters and inflow conditions. S compares the loading outside the separation region (typically at mid span) and the one close to the end wall. The results of a parametric study on blade design and inlet flow conditions are summarized in Figure 1.6. Two distinct branches among the (S, D) values indicate the close and open nature of the corner separation. The onset of the hub separation comes for the diffusion parameter $D = 0.4 \pm 0.05$. The switch to hub corner stall is also visible with a step in the stall indicator value that coincides with the opening of the separation region.

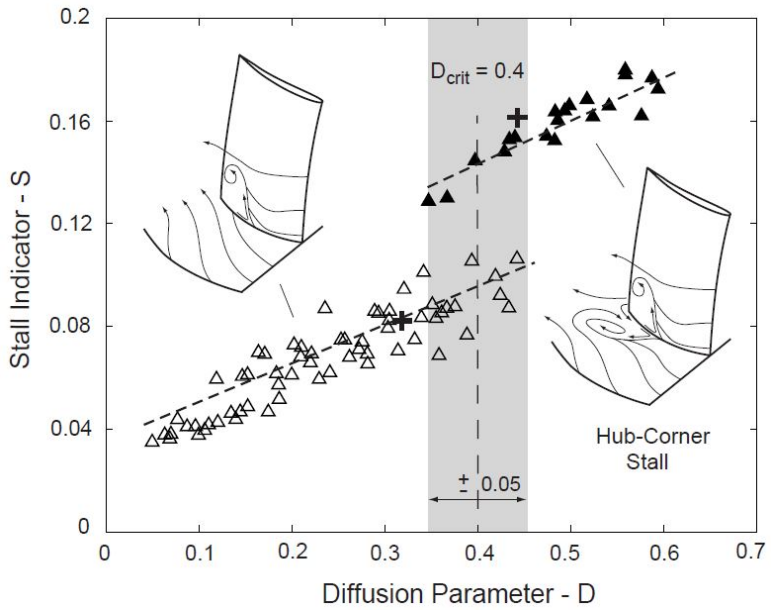

Figure 1.6: Hub corner type flow as a function of Stall indicator and Diffusion parameter - Lei et al. (2006).

The end wall boundary layer in the blade passage is also highly affected by the inlet boundary layer skewness. The inlet boundary layer become skewed due to the change of reference frame between the rotating disk platform and the stator hub (shear driven 3D boundary layer)(see Ahmed and Rajaratnam (1997)). The lag between stress and strain on the hub platform generates turbulence anisotropy (see Johnston and Fiack (1996)). On the stator row inlet hub, the 3D boundary layer created is defined by a velocity component in the

stream wise direction and normal to the stream, the cross stream velocity component, in the rotor rotating direction. Hence, at the row inlet, the end wall flow is overturned. At fixed operating point, the skewness of the inlet boundary layer opposes the cross flow by adding momentum in the cross stream direction. As a consequence a loss reduction is visible in blade suction side corner (Bode et al. (2015) Praisner and Smith (2006)). The end wall skewness also defines, local incidence variations at stator row inlet. The competing effects between reduction in cross flow intensity and increase of operational incidence must be taken into account in the blade design.

The dynamics of the flow in the end wall region is highly unsteady. The first source of unsteadiness comes in the bimodal nature of the junction flow between the blade and end wall. This behaviour is introduced in Zambonini (2016) for the corner flow in an axial compressor cascade. In the configuration investigated, low frequency switch from close to open separation whose amplitude increases with operational incidence are highlighted. The unsteady features of the flow in the end wall region are driven by: (1) The junction flow topology, (2) Blade row inlet flow conditions.

1.4 Stability of axial compressors

The operating range of a gas turbine aero engine is limited by the stable operation of the compressor module. The stability of axial compressor at low mass flow is defined by the range in which the machine is able to impose work without presenting blade stall. As illustrated in Figure 1.2, the surge line defines the stability range of the compressor. Above the stability limit, the compressor flow present disruptive flow features and enters stall inception. Based on a known surge line, the stability margin identifies the stable operation range of the machine. At an operating point (OP) in the compressor map, a definition of the stability margin SM is given in equation 1.10 which uses the pressure ratio Π. The limit point lim is indicated for the same corrected mass flow.

$$\mathrm{SM}_{\mathrm{W}r} = \frac{\Pi_{\mathrm{OP}} - \Pi_{lim}}{\Pi_{lim}} \tag{1.10}$$

The first definition is useful in the case of quick wheel speed acceleration where transient trajectory moves towards the surge line. In the case of an analysis at fixed rotational speed, another definition can be used where the throttling parameter λ of the studied operating point is compared with the limit throttling parameter (see equation 1.11 and Figure 1.2).

$$\mathrm{SM}_{\mathrm{N}n} = \frac{\lambda_{\mathrm{OP}} - \lambda_{lim}}{\lambda_{lim}} \tag{1.11}$$

1.5 Technological effects

Under the name "technological effects" there are a number of features related to the mechanical design which have a direct impact on the aerodynamic performance of the turbomachine. Effects such as operational clearances (both radial and axial), and blade fillets are discussed here after.

1.5.1 Blade tip clearance

Tip clearance is the operating clearance between the rotor blade tip and the casing. The value of the mechanical clearance is computed taking into account the blade geometry change while in rotation, due to thermal and centrifugal effects. In that sense, the cold clearance (rotor not rotating) is always larger than the hot clearance value for a fixed casing radius. Due to the reduction of machine cross section to reach higher pressure ratios, the relative importance of tip gap flow is increased. In the tip gap region, flow physics sees the interaction between : (1) tip leakage flow from blade pressure side to suction side, (2) Boundary layer interaction between the casing end wall and the rotating blade (scraping). The effect of a large tip gap is visible with a reduction of the stall margin (Freeman (1985)). The increased tip leakage flow generates blockage

so that the flow coefficient is affected. Change in local operating incidence due to increased blockage generates off design conditions and affects blade loading span wise distribution. Challenges for tip gap effects prediction on axial compressor flow lies in the ability to properly model the boundary layer behaviour in that region. The prediction of the running mechanical gap in itself is also complex and requires for example a good prediction of the rotor disk expansion due to thermal effects below the hub line.

1.5.2 Blade fillets

The use of blade fillets in axial compressor is in the first place to ensure structural integrity of the rotating assembly at high tip speed. Then, the manufacturing process can also create a fillet due to the tool head size (if for example milling is used). The presence of fillets is beneficial at off design conditions in both rotor and stator rows. The fillet changes the shape of the mechanical junction between the blade and the end wall. The resulting junction flow system is altered with respect to a case without contouring by pushing it away from the blade surface (Bordji (2015)). Concerning the blade suction side corner flow, this reduces the interactions between blade and end wall boundary layer and associated losses. However, blade fillets change blade design parameters such as solidity distribution. This must be anticipated in the preliminary design phase.

1.5.3 Shroud cavities

This section reviews the available information in the literature concerning stator hub shroud cavities. It has been decided to only refer to studies in the frame of axial compressor flow. However, cavity flow and leakage flow/main flow interaction is also a highly covered topic in axial turbine fluid mechanics. It presents a large literature from which physical understanding but also good practices and methodologies for cavity flow analysis in the frame of axial compressor can be derived. A good starting point to explore this part of the literature are the following studies : Chew et al. (2019), Savov et al. (2016).

1.5.3.1 Leakage flow

With the use of shrouded stators, the rotating assembly radially clears the stationary parts below the hub level (cf. Figure 1.7). Axial clearance is maintained between rotor and stator platform. The static pressure increase in the main channel generates an under platform flow recirculation from stator trailing edge to leading edge. The end of the leakage path is associated with the injection of the recirculated flow in the main channel.

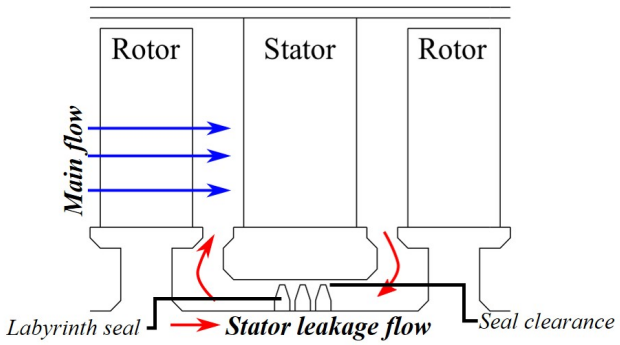

Figure 1.7: Axial compressor shrouded stator configuration.

The flow properties for the cavity flow are simplified in three main parameters. The first one is the leakage fraction (cf. equation 1.12) which is the ratio between the recirculated mass flow and the main channel mass flow. Due to viscous effects, the cavity flow is entrained in the rotor direction. The second parameter is the swirl ratio (cf. equation 1.13) that is the ratio of cavity flow tangential velocity to the one of the rotor assembly. The shear work produced by the disk spinning increases cavity flow temperature

(windage heating). The third parameter is then the total temperature increase from leakage path inlet to leakage path exit at fixed leakage fraction.

$$L_f = \frac{\dot{m}_{cavity}}{W_r} \tag{1.12}$$

$$S_f = \frac{V_t}{\omega * r} \tag{1.13}$$

The cavity volume is decomposed in three areas. The deep cavity is the region containing the seal technology responsible for the radial clearance management between rotor and stator assemblies. The main cavity volumes (upstream and downstream) are located on each side of the seal and are connected to the main channel thanks to a trench. The trench region is the region that manages the axial clearance at the cavity / main channel interface.

Cavity geometry and operating conditions have an impact on the leakage flow properties evolution. The parametric study of Heidegger et al. (1996) highlights that the seal clearance and the wheel speed are the most affecting parameters for cavity flow. Along the leakage flow path, momentum balance is kept with a cavity flow rotating in the direction of the rotor disk. As cavity section changes in the radial and axial direction, it alters the local flow angle.

The seal gap is the restriction where the leakage flow makes is transferred from the downstream part to the upstream part of the shroud cavity. Sohn et al. (2006) illustrate that the flow in the cavity covers multiple pitches in the rotation direction before being re-injected in the main channel. However, at the rim seal, abrupt change in flow angle is identified. There static pressure and shear work induced by the rotor disk changes the enthalpy of the leakage flow. The added kinetic energy is dissipated in the form of vortical flow. The seal gap induced jet contraction reduces the tangential velocity component by a factor of 1.2 (Wellborn and Okiishi (1996)) while increasing the axial velocity by a factor of 2 (Sohn et al. (2006)).

1.5.3.2 Impact on performance and stability

The trench region, as the interaction area between cavity and main flow defines the impact of stator shroud cavity on blade passage flow features. The cavity flow exits the cavity with meridional flow angle and tangential flow angle. Different enthalpy induced by windage heating also triggers flow mixing and local entropy generation. Results obtained by Heidegger et al. (1996) assess the “weight” of the upstream and downstream trench (of the stator blade). In the configuration studied, quantities such as cavity flow tangential velocity and total temperature reach 75% of their upstream trench exit value in the first 15% of span of the downstream trench. The presence of blades upstream and downstream the cavity trench plays a role in the azimuthal distribution of the flow. Focus is set on the cavity trench where flow is re-injected in the main channel.

Downstream blade potential effect

The potential effect of the downstream blade is the first blade effect to impose pitch wise non uniformities in the trench region. The proximity between the blade rows is defined by mechanical limitations and often result in a short trench to downstream leading edge distance. Pitch wise alternate regions of main flow ingress in the cavity and cavity flow egress in the main channel are generated (Heidegger et al. (1996), Demargne and Longley (2000)). Figure 1.8 presents that at low leakage fraction, due to the potential effect of the stator blade, mid-pitch ingestion of the main flow into the cavity is expected. This region pitch wise extent is dependent on the incoming incidence and the leading edge shape. The main flow ingestion is confirmed by a minimum in cavity flow concentration. At higher leakage fraction, the concentration of cavity fluid at -1% span evolves to a more homogeneous pitch wise profile where only cavity flow is present.

Figure 1.9 illustrates the impact of leakage fraction and swirl ratio on the flow radial velocity distribution in the trench. Pitch wise non uniformities remain in the velocity field as leakage fraction is increased (at fixed cavity flow tangential velocity), even in the case where main flow ingress is not present. At fixed leakage fraction, higher swirl ratio induces a pitch wise more homogeneous radial velocity distribution.

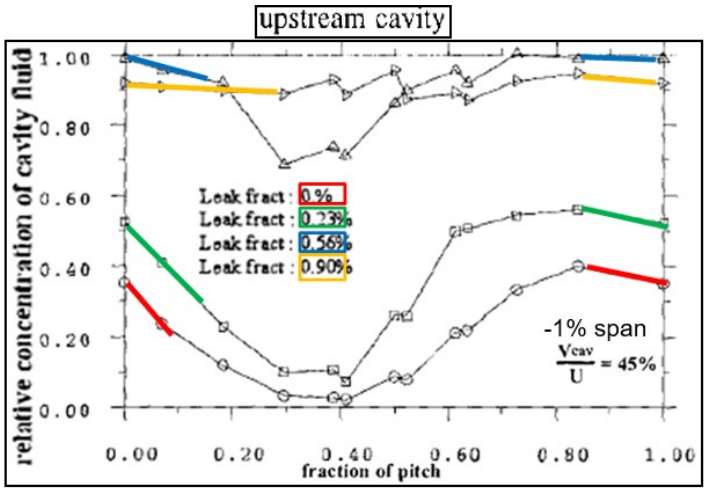

Figure 1.8: Main flow ingestion in the upstream trench at fixed cavity flow tangential velocity and variable leakage fraction - Cavity flow concentration taken a -1% span – If only cavity fluid: Concentration = 1.00 - adapted from Demargne and Longley (2000).

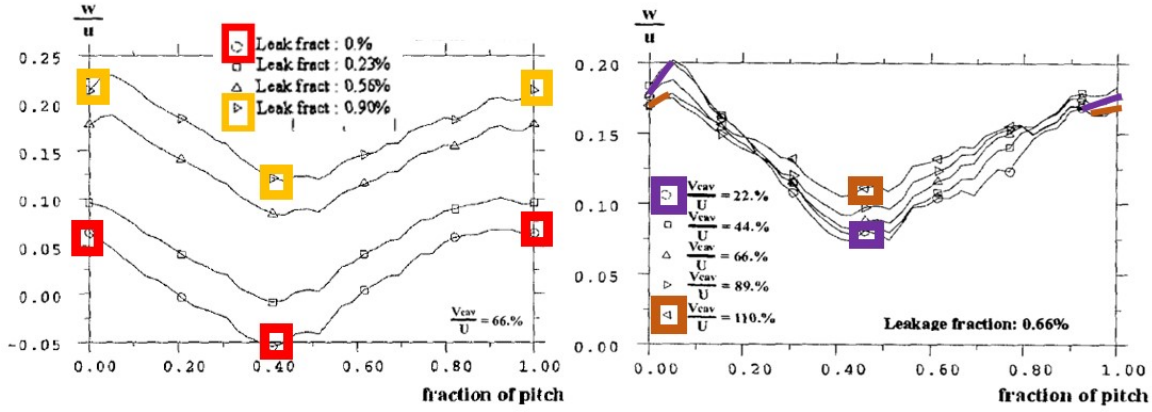

Figure 1.9: Axially average span wise velocity at -1% span in cavity upstream trench - Left: fixed cavity tangential velocity, variable leakage fraction – Right side: fixed leakage fraction, variable cavity tangential velocity - adapted from Demargne and Longley (2000).

As a component of the interactions between cavity and main flow, a trench vortex is created in the last part of the cavity. Visible for low leakage fraction rates, the trench vortex is generated by the rotating disk pumping effect (see Chapter 2) which samples mass flow from the adjacent stationary stator surface at a radius where the disk pumping flow rate exceeds the leakage flow rate. As illustrated by Figure 1.10, the trench vortex position is also affected by the downstream blade potential effect. This flow feature is part of the main flow ingress and the induced mixing process in the cavity trench. When leakage fraction is increased, the trench vortex is pushed out from the cavity (see Mahmood and Turner (2017)).

Wake effect of upstream blade

The effect of the upstream blade on the cavity trench is described in Flores Galindo (2018). The interaction between cavity egress regions and upstream blade wake (with low momentum / high static pressure) generates a wake-leakage vortex, close to the end wall, downstream of the cavity trench. This wake leakage vortex rotates with the main flow and is transported in the following blade row.

Boundary layer skewness

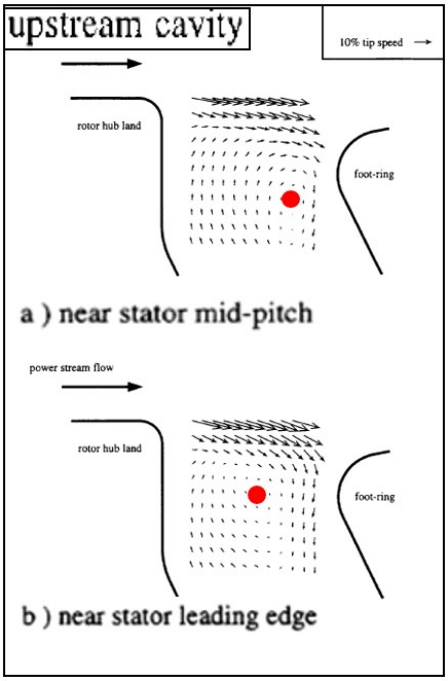

Figure 1.10: Trench vortex position dependence to downstream blade potential effect - Vortex core in red - adapted from Wellborn and Okiishi (1996).

To understand the impact of cavity flow on stage performance, a link is made between the leakage flow and flow structures responsible for losses. The direct impact of leakage flow is limited to the end wall region (see Wellborn and Okiishi (1996)). As a consequence, the end wall secondary flow system is disrupted by the presence of the leakage flow. From an aerodynamic point of view, cavity flow leakage fraction and swirl ratio both affects blade row inlet main flow momentum in axial and azimuthal direction. The injected radial component induces blockage for the upcoming main flow. In a turbomachinery assembly, the swirl ratio can not exceed 1 at cavity outlet. Hence, leakage flow always produces momentum deficit in the azimuthal direction.

The change in reference frame for rotor to stator produces a new boundary layer on the stator platform. The structure of it is three dimensional and illustrated by Figure 1.11. The boundary layer passes form pure shear skewness on the rotor disk, to pressure driven skewness on the stator platform. Below the boundary layer limiting streamline, the velocity vector is composed of a stream wise component (U_s) and a cross stream component (U_n). The edge velocity direction is defined by the angle γ_e with respect to a reference direction, which is typically the mean flow direction. Skewness region is identified as the span wise range where stream wise and cross stream growth rate differ. The boundary collateral region represents part of the boundary layer where stream wise component and cross stream components growth is identical. In the collateral region, the flow is orientated of an angle $\gamma_{\tau w}$ with respect to the reference direction. An indication of the boundary layer skewness additional turning is identified thanks to the angle difference $\Delta\gamma = \gamma_{\tau w} - \gamma_e$.

Variations of the leakage flow properties alter the transition of the flow between rotating and static frame. As a result, the boundary layer skewness downstream of the trench is changed with the leakage. As an example, by increasing cavity outlet swirl ratio, stator hub inlet boundary layer skewness is increased. A possible representation of the three dimensional turbulent boundary layer (3DTBL) components is given in Figure 1.12. The stream wise and cross stream velocity components normalised with the free stream velocity are combined into an hodographic representation. It takes the shape of a triangle with two legs. To obtain such representation, the definition of the edge velocity is fundamental. The methodology presented in De Ruyck et al. (1979) and De Ruyck and Hirsch (1981) is one of the methods available. It has been successfully applied in Manfredi et al. (2020). The inner leg of the hodograph is a projection of the collateral region where the flow orientation is $\gamma_{\tau w}$. The position of the intersection of the triangle legs separates the collateral and skewed regions. The radial position at which $\frac{U_n}{Q_e}$ is maximized, indicates the proportion of

the boundary layer that is skewed. In the skewed region, the outer leg slope is proportional to $-2\gamma_e$ as it has been modelled in Johnston (1960). This result is eventually used in work such as the one of Lei et al. (2006), to include the skewness effect in blade row loss modelling.

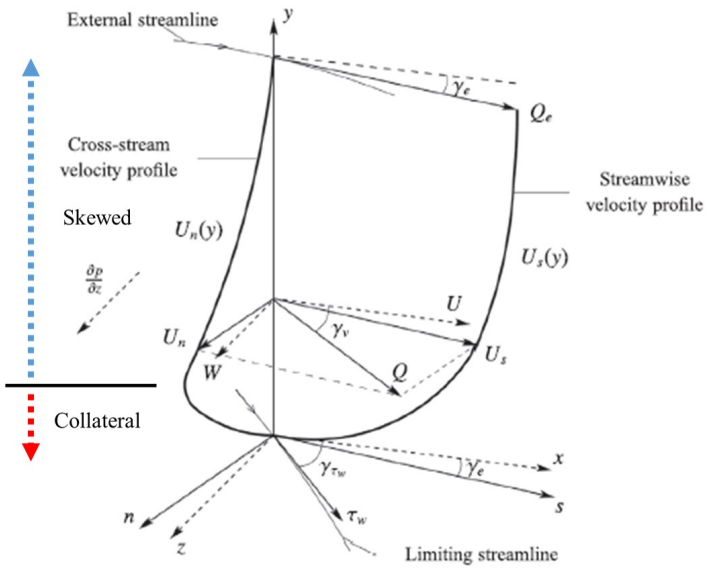

Figure 1.11: Three dimensional boundary layer structure. Collateral and skewed region - External velocity vector Q_e - Stream wise (U_s) and cross stream (U_n) velocity components - adapted from Bentaleb and Leschziner (2013).

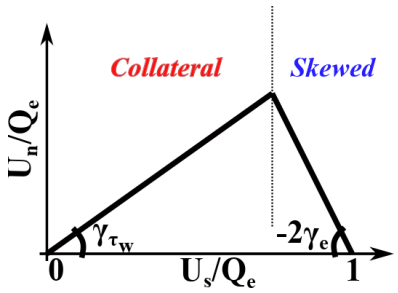

Figure 1.12: Hodographic representation of stream wise (U_s) and cross stream (U_n) velocity components in a three dimensional boundary layer of edge velocity Q_e.

Leakage fraction effect

For a fixed cavity outlet swirl ratio, the amount of low momentum fluid injected in the low span region increases with the leakage fraction. It results in an increase of the cross flow in the blade row. In Figure 1.13, the hub and blade suction side wall shear lines are plotted for cases with low and high leakage. In the case of high leakage (large gap - dashed lines in Figure 1.13), more low momentum fluid is subjected to the same azimuthal pressure gradient than in the nominal case. Consequently, cross flow intensity and blade suction side separation region increase. The size of the suction side separation region drives the main flow blockage at blade row exit. Cavity flow leakage fraction affects blade row end wall loss generative structure. For the same operating point, end wall flow blockage also results in an increase of the flow momentum outside of the blocked region, typically at mid span. That is why, cavity flow indirectly affects the level of profile losses generated by the blade row. In Wellborn and Okiishi (1996) every 1% increase in seal tooth clearance induces 3% pressure rise penalty and a 1-point drop in stage efficiency. These values, similar to the rotor tip clearance effect on stage performance (Yoon et al. (2014)), justify the need to consider cavity flows in the performance evaluation for axial compressors.

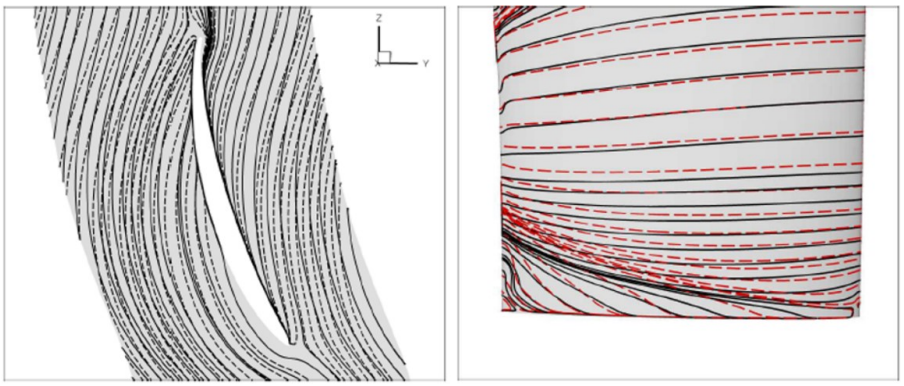

Figure 1.13: Effect of cavity flow on stream traces of wall shear stress: On the hub (Left) – On blade suction side (Right) – nominal gap (continuous line) vs large gap (dashed line) - from Farkas et al. (2013).

Swirl ratio effect

The impact of leakage flow tangential velocity (swirl ratio) on the stage losses is well described in Sohn et al. (2006) and in Demargne and Longley (2000). With increased swirl ratio, inlet flow distribution is more homogeneous and cross flow intensity is reduced. Hub boundary layer skewness also increase downstream of the cavity trench. As a consequence, the size of the corner separation region is reduced in the row downstream of the injection. Figure 1.14 informs on blade row exit loss reduction with cavity swirl ratio increase, at fixed leakage fraction. Stator outlet flow angle also becomes more uniform. Cascade test sections such as the one of Demargne and Longley (2000) allow to evaluate cavity exit tangential velocity close and above the wheel speed. At tangential velocities of the leakage flow close to the wheel speed, it appears that losses become insensitive to the amount of cavity leakage flow. For leakage tangential velocities above the wheel speed, the added tangential momentum compensates the axial momentum deficit and show a reduction in secondary flow losses. This is also visible in Lei et al. (2006) where cases with cavity flow tangential velocity above the wheel speed do present a reduction of the diffusion parameters below the critical value of 0.4.

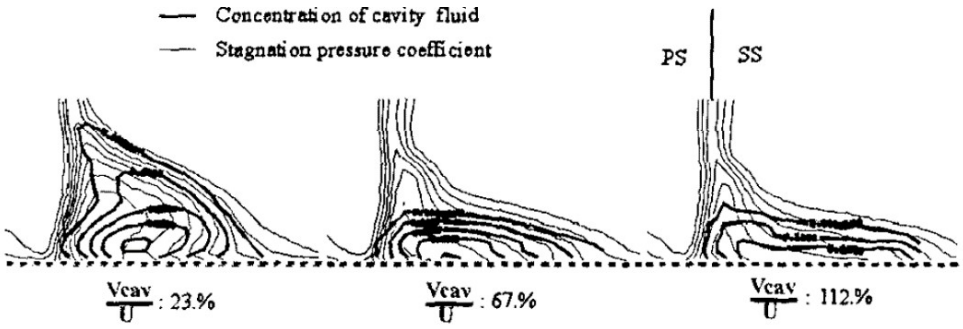

Figure 1.14: Contour of cavity fluid concentration in the downstream blade exit hub region at fixed leakage fraction - Effect of leakage tangential velocity V_{cav} - Rotor wheel speed is noted as U - from Demargne and Longley (2000).

Downstream cavity effect

The downstream cavity is defined between the injection of main channel flow, downstream of the stator row, and the labyrinth seal. It acts on the level of stage losses. Low momentum fluid from the hub corner separation region is sucked into the downstream cavity which reduces the stage total pressure loss. The downstream cavity has no effects on the loss generation mechanisms but modulate the average loss level. However, the presence of the downstream cavity is enhancing windage heating. Already heated cavity flow present in the blade suction side corner can be ingressed in the stage downstream trench and perform multiple loops in the shroud cavity (Ozturk et al. (1998)). As a result, the total windage effect can account for

one third of total stage losses (Kato et al. (2011)). Consequently, the loss level predictions are more accurate with the entire cavity taken into account. Nevertheless, the investigation of the loss generation mechanisms remains compatible with upstream cavity only configurations.

Multistage configuration

The loss mechanisms associated with the local interaction of leakage and main flow contribute to loss propagation through the machine. Off design conditions due to technological effects are generated. Each blade row produces losses due to their own cavity system and due to the non matching conditions generated in the upstream rows. The loss repartition analysis between stages informs on loss propagation for multi-stage assemblies. As an example, the total pressure loss caused by the leakage is higher in the downstream compressor stages. Loss propagation is also amplified for higher loading operating points (Wellborn and Okiishi (1996), Wellborn and Okiishi (1998), Naylor et al. (2009)). Loss repartition and propagation in a six stage axial compressor is presented in Figure 1.15 where pressure loss and windage heating proportions are compared with efficiency drop in the rotating assembly.

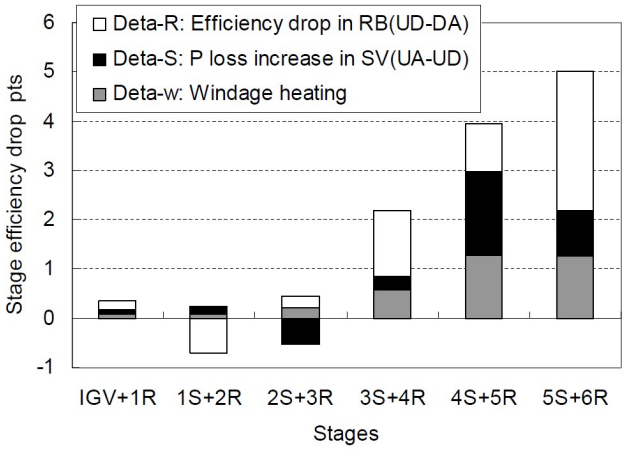

Figure 1.15: Loss propagation in a multistage axial compressor with shrouded stator cavities – Stage efficiency drop with respect to no cavity included CFD simulations - RB : Rotor Blade - SV: Stator Vane - UD, DA, UA, UD indicates measurement sections in the original paper - Kato et al. (2011).

The effect of the cavity flow on compressor stability is evaluated in Wellborn and Okiishi (1996). The authors noticed that in a low speed three stage axial compressor, the labyrinth seal clearance, and so the leakage fraction, is not affecting the stability limit flow coefficient.

1.6 H25 stage design characteristics

This section defines the characteristics of the stage studied in this work. The H25 stage, presented in Figure 1.16 is a research stage developed in the frame of the LEMCOTEC European project (Low Emission Core Engine Technologies) to assess core size effects on high speed axial compressor performance and flow field. The highly three-dimensional blade design presents a low aspect ratio. Design conditions are chosen to be representative of the last stage of conventional, i.e. moderated overall pressure ratio, multi-stage axial compressor for aircraft engines applications. The selection of the H25 stage is then relevant to study cavity flow effects on axial compressor as it has been presented that axial compressor last stages are the most subjected to face cavity flow induced loss propagation in multi-stages assemblies. In Figure 1.16 are introduced the cavity volumes C1 and C2. The C2 cavity is the focal point of this work and more details related to the geometry are given in Chapter 2. The Table 1.1 presents H25 stage design parameters. Measurement of rotor tip gap value at nominal speed is obtained thanks to wear gages measurement at two axial positions and 5 azimuthal positions around the annulus.

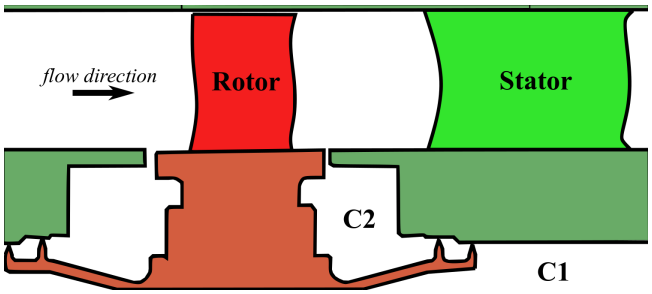

Figure 1.16: Cross section sketch of the H25 axial compressor stage - Rotor row and rotating assembly (in red), Stator row and fixed surfaces (in green) - C1 an C2 cavity volumes.

Parameter	Value
Blade height - H [mm]	25
Hub to tip ratio	0.9
Rotor blade count - N_r	65
Stator blade count - N_s	80
Average tip gap in rotation	<2% span
Pressure ratio - Π	1.25
Nominal speed [rpm]	9650

Table 1.1: H25 stage design parameters.

1.7 Conclusion

Chapter 1 introduced notions on the fluid mechanics of axial compressors. The compressor module is framed in turbomachinery assemblies for aircraft propulsion. The parameters used to evaluate axial compressor performance and stability are outlined, introducing corrected mass flow, pressure ratio, efficiency, and stall margin.

The flow phenomenology and the loss generative structures have been presented in a third part. This allowed to locate and understand the implication of stator shroud cavities in the loss generation process from single blade row to multi-stage assemblies. The first understanding of cavity flow impact on axial compressor performance and stability defines the flow regions and quantities to investigate in the study of the H25 research stage. Interaction regions of cavity and main flow must be investigated through the analysis of the boundary layer adjacent to cavity trenches. It allows the identification of the effect of leakage fraction, swirl ratio, and windage heating. At blade row exit, the end wall region up to 40% span, contains informations about the loss generative mechanisms from which cavity flow contributes. Blade effects should also be included in the analysis as they are modulating the pitch-wise mixing of cavity and main channel flow.

Chapter 2

Rotor Stator cavity flow

The purpose of this chapter is to introduce the flow in rotor stator cavities. In the first place, the flow features and regimes that are generated by two parallel disk are presented. In a second section, the flow between two coaxial cylinders is reviewed. Finally, thanks to the use of non-dimensional numbers, the C2 cavity geometry is put into perspective with respect to the literature detailed in the first two sections.

Contents

2.1 Parallel disk flows

2.1.1 Parallel disk flow features

2.1.1.1 Flow over a rotating disk

In early studies on geostrophic flows, Ekman (1905) identified the impact of an object solid boundary in rotation on the surrounding flow. The resulting flow structure in the viscous layer around the object comes from an equilibrium between the pressure gradient, the Coriolis forces in the fluid and the fluid viscosity. Pressure gradient and variations in the solid rotation speed (Coriolis) induce either cyclonic (low pressure) or anticyclonic (high pressure) large scale circulation parallel to the solid surface. The viscous layer on a rotating solid is often called Ekman layer. The flow outside of the Ekman layer is detailed in the work of Kármán (1921). There, the flow induced by an infinite diameter rotating disk in a fluid at rest, e.g. free disk, is studied. The velocity field gives symmetric solutions along the normal direction to the disk surface.

For the the same case, Cochran (1934) illustrates the disk pumping effect for a disk rotating at angular velocity Ω. The no slip condition on the disk surface imposes that the tangential velocity of the flow scales with the radius. The centrifugal forces imposed by the disc on fluid particles in the boundary layer generates radial outflow. As a result of flux conservation, flow impingement normal to the disc is created to compensate for the outward flow generated in the Ekman layers. The flow topology of a flow initially at rest, over a rotating disk is presented in Figure 2.1. Three dimensional boundary layer is present on the disk surface with its skewness induced by the rotating wall motion. In such rotating flow the boundary layer reaches finite thickness δ that is proportional to $\sqrt{\nu}/\Omega$ where ν is the fluid kinematic viscosity.

The mass flow pumped by the disk is dependent upon the state of the boundary layer on its surface. Similar to a flat plate, free disk boundary layer can be laminar or turbulent. The local Reynolds number given in equation 2.1, where r is the local radius, defines the disk boundary layer state. Above a value of 3.10^5, the disk boundary layer is considered as turbulent. Nevertheless, the laminar to turbulent transition is affected by parameters such as disc roughness. If r indicates the radius, in the case of a laminar boundary layer, the pumped massflow is proportional to r^2, so to the disk area. The entrainment velocity of the flow in the boundary layer is in that case uniform over the disk. For a turbulent boundary layer, the disk pumping flow rate is proportional to $r^{2.6}$. As a consequence, in the case of a turbulent boundary layer, the entrainment velocity increases with the radius.

$$Re_{local} = \frac{\rho \Omega r^2}{\mu} \tag{2.1}$$

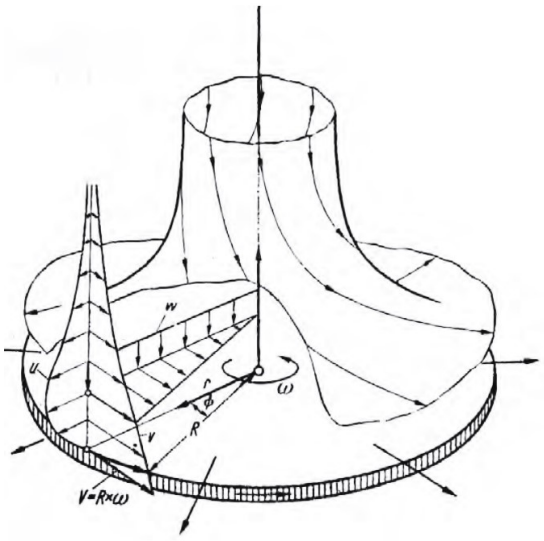

Figure 2.1: Static flow over a rotating disk - Crespo del Arco et al. (2005).

2.1.1.2 Flow over a stationary disk

The Karman flow generates different types of solution dependent on the fluid state far from the disc. In the case where a rotating fluid is travelling on an infinite stationary disk (disk pumping beneath a forced vortex), Bödewadt (1940) gives the auto-similar solutions of the Navier Stokes equations. This flow is characterized by an equilibrium between the centrifugal forces and the pressure gradient. In opposition to the Ekman layer, the viscous layer on the disc in the configuration studied by Bödewadt, now called Bödewadt layer, sees flow travelling inward, towards the disc revolution axis. As presented in Figure 2.2 a circulation is generated close to the disc axis where the accumulated flow is driven out from the disc surface as a consequence of flux conservation.

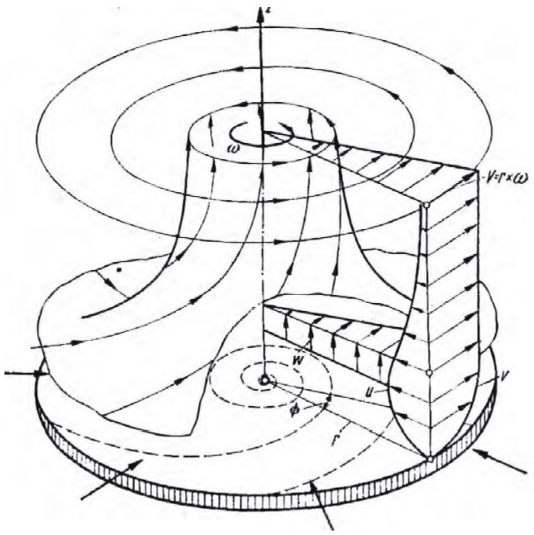

Figure 2.2: Rotating flow over a static disk - Crespo del Arco et al. (2005).

2.1.1.3 Batchelor type flow

For rotor stator cavities with parallel disk flows, non-dimensional numbers are used to define a configuration. The Reynolds number based on disc radius (Re_r) and the aspect ratio G (cavity width h over radius r : $G = \frac{h}{r}$) define the mutual interaction of the Ekman and Bödewadt layer.

As those layers scale with the boundary layer thickness on the disks, Batchelor (1951) gives a solution for high Reynolds number infinite parallel disk flows. Here, the Ekman and Bödewadt layers are separated and can be treated independently. It appears three distinct flow zone in Batchelor type flows as sketched by Figure 2.3 : (1) a centripetal boundary layer on the stator (Bödewadt layer); (2) a central rotating core with zero radial velocity rotating at a tangential velocity V_θ characterized by an entrainment coefficient or swirl ratio (cf. equation 2.2); (3) a centrifugal boundary layer (Ekman layer).

$$S_f = \frac{V_t}{\Omega * r} \tag{2.2}$$

The system described here is the combination of two isolated disks adjacent to a rotating flow. The rotating disk pumped flow is fed, radially inward, from the stator boundary layer, to match the massflow demand. In the case of an enclosed cavity such as the one on Figure 2.3, the stator wetted surface being larger than the rotor one, the stator torque is higher than the rotor torque. As a consequence, the core velocity is expected to rotate with a swirl factor inferior to 0.5.

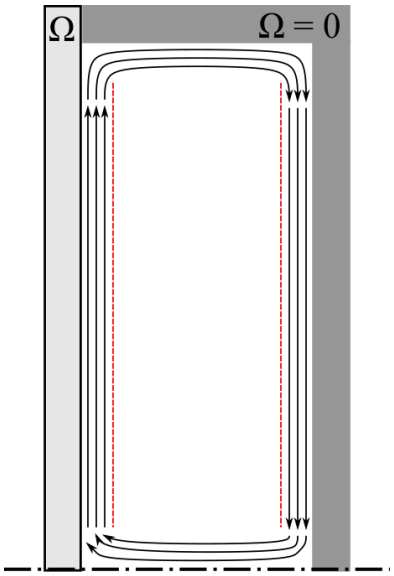

Figure 2.3: Batchelor type flow schematic representation - Rotor and Stator boundary layer

2.1.1.4 Rotor-stator cavity with through-flow

Added flow ventilation in enclosed rotor stator cavity has an effect on the flow topology. In an enclosed cavity, the torque produced by the rotor continuously heat up the flow. In industrial applications, clearances also allow rotor-stator cavity ventilation. The Figure 2.4 presents the effect of added through flow to the rotor stator cavity system.

In the example given, the swirl factor of the added through flow is kept below 0.5 to ensure pumping from the rotating disk. As presented in Figure 2.4a the injected flow is pumped in the rotor disk boundary layer. If the injected mass flow is small, some flow is peeled from the stator boundary layer. This phenomena happens at the radius where the pumping mass flow requested by the disk exceed the injected mass flow. If the injected mass flow increases, the radius at which peeling is created increases. Eventually, for high injected mass flow that exceeds the disk maximal pumping mass flow, flow peeling from the boundary layer is not present in the rotor stator cavity.

The case of a radial inflow is sketched in Figure 2.4b. In that configuration, a point of radial stagnation is present on the rotor disc. The position of the radial stagnation point is dependent of the injected mass flow rate. Below the point of radial stagnation, the swirl ratio of the core flow exceeds one. That is why flow collects inward on the rotor surface. The sensitivity of such configuration to inflow swirl ratio and mass flow is the following one. Inlet swirl ratio has a strong effect at rotor tip but diminishes towards the hub. The trend for the injected mass flow is the opposite. If the rotor stagnation point is at the rotor tip, the flow is inflow / massflow dominated. If the stagnation point is at the rotor hub, the flow is rotationally/swirl dominated. In the given example, Figure 2.4b shows an intermediate regime where flow combines mass flow and swirl effects.

2.1.2 Parallel disk flow regimes

2.1.2.1 Classification

The parallel disk configuration is subjected to flow regimes as a function of system's operating conditions and geometry. Chronologically, literature on the topic ends up in a classification of the different flow regimes for rotor-stator cavities. The publication of Batchelor (1951), identifies that all of the solution for Batchelor type flow present a central rotating core. This is even the case when the parallel disk system is studied at low Reynolds numbers and for disk rotating in opposite direction. The Stewartson solution (see Stewartson (1953)) to the aforementioned case goes towards the "free disc solution", where the rotating disks have no mutual effects and the core flow shows no tangential component. From that point research focused

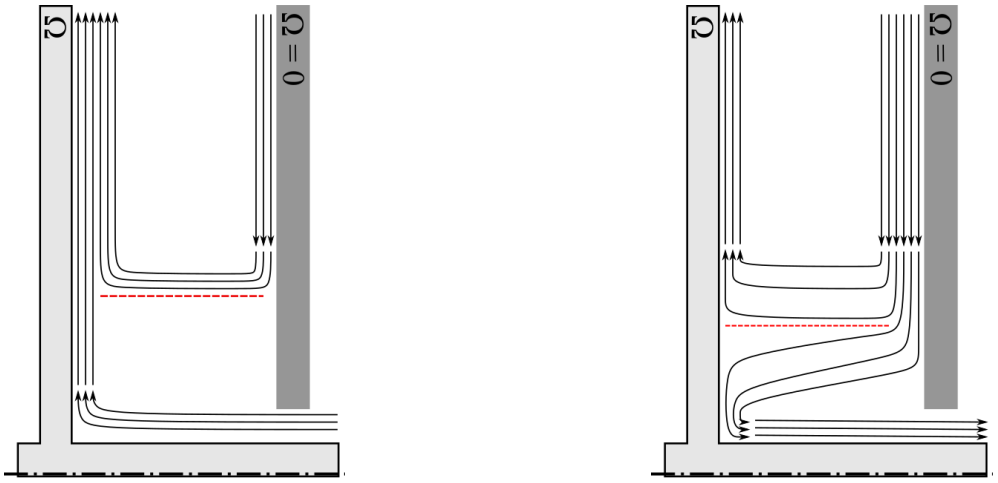

(a) (b)

Figure 2.4: (a) Rotor-Stator cavity with moderate radial outflow - Peeled flow from stator boundary layer to match disk pumping flow needs(radius indicated in red) - (b) Rotor-Stator cavity with radial inflow - intermediate regime of mass flow and swirl dominated regions - Rotor stagnation radius indicated in red.

on assessing the existence and uniqueness of the solutions to such flow. This led to work such as the one of Mellor et al. (1968). For a given rotating Reynolds based on disk spacing h ($Re_h = \rho * \Omega h^2/\mu$),the authors identify three solution branches for the core flow. One, two or three flow cells in the meridional plane. The paper mainly focuses on one cell branch and its two sub-branches the first one being the Batchelor type flow. Hot wire measurements confirm the latter behaviour for the Reynolds number range investigated (0-100). The main outcome of such study is that the free disk solution of Von Karman is not a general limiting case but a limiting case of a certain branch of solution as Reynolds increases. As new flow regimes were discovered, classification based on non-dimensional numbers became necessary. As an example, in the previously cited study, the inter-disc Reynolds number. To dissociate the different flow regimes related to parallel disks flows, one can organize the analysis in two steps:

1- The first step is to evaluate if the Bödewadt and Ekman boundary layers are merged or not. The main driving parameter to differentiate those flow regime is the disk spacing and associated cavity aspect ratio. 2- The Reynolds number based on the radius informs on the laminar or turbulent state of the boundary layers

The work from Daily and Nece (1960) results in the classification flow regimes that are presented in Figure 2.5. Four regimes are introduced as a function of the cavity aspect ratio and of the disk Reynolds number. In turbomachinery applications, with high disk Reynolds numbers, the expected regime is regime four where the boundary layers on the disks are turbulent and separated. Nevertheless, with the complex shapes of axial compressor shroud cavities with highly varying aspect ratio, local behaviour may appear. The dependence to geometry must be handled with care when correlating flow physics and classification for non-academic cases.

2.1.2.2 Instability of Batchelor type flows

In Batchelor type flow, the Ekman and Bödewadt boundary layers can be treated separately. They can present instabilities or modes that are of two types. The first one (called Type I or class B or cross flow instability), consists in spiral waves as presented in Figure 2.6a. The second mode (Type II or class A) is shaped as annular wave patterns as visible in Figure 2.6b.

Instabilities in the disk boundary layer are identified thanks to axial velocity fluctuations (i.e. along revolution axis). Due to their presence, the flow is no more locally parallel to the disks. Parallel disk flows instabilities can be characterized in terms of: (see sketch on Figure 2.7)

(1) The angle between the flow instability pattern and the normal to the geostrophic flow (ϵ); (2) The radial wave number of the instability $k_r = \frac{n_r}{\Delta_r}$, where Δ_r is the radial length occupied by n_r rolls. Its value is usually compared with the disc boundary layer thickness δ; (3) The azimuthal wave number of the instability

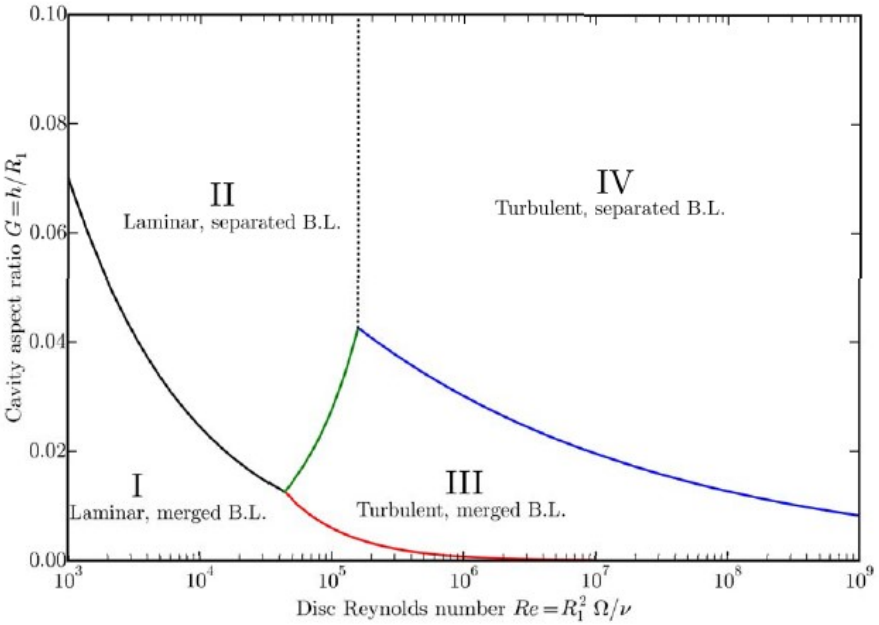

Figure 2.5: Parallel disc flow regimes as a function of cavity aspect ratio and disc Reynolds number - R_1 stands for disk radius - Owen and Rogers (1989).

k_θ; (4) The phase speed; (5) The frequency of the instability, often normalized by the disc rotating frequency so expressed in Engine Order (The disk rotation = 1 Engine Order = 1 EO);

The propagation of the instabilities in the cavity flow field is also referenced to evaluate the cavity system dynamics. Absolute and convective instabilities coexist in the disks boundary layers (Huerre and Monkewitz (1990)). As showed in Figure 2.8b, when an initial impulse grows with time in the whole space domain, the system is considered as absolutely unstable. On the other hand, if the impulse response decays in time at the source location (Figure 2.8a), the system is convectively unstable. The behaviour is the result of a competition between the instability energy growth in time, and the superimposed advection of the main flow (space). The spectral content of an absolute or convectively stable system are different when probing is performed in the fluid domain. A convectively unstable system is acting as an amplifier which induces a wideband type spectra that contains the convected instabilities frequencies. An absolutely unstable system is acting as an oscillator and present sharp peaks if the frequencies associated to the eigen modes of the system are present in the imposed instability.

2.1.2.3 Instability in the Bödewadt layer

Spatial flow organisation in the Bödewadt layer can be either of Type I or Type II. The existence of the instability is conditioned by the rotating Reynolds number of the system. Hence to separate the regimes, a critical local Reynolds number is defined $Re_{\delta c}$ (where $Re_\delta = \Omega\delta r/\nu$ and δ is the disc boundary layer thickness) . Circular waves (type II) are present at low Reynolds number and spiral waves (type I) present at high Reynolds numbers. As an example, the DNS computations from Serre et al. (2001) and the associated linear stability analysis give, for a large aspect ratio cavity (G = 0.2), a critical Reynolds number of $Re_{\delta cII} \sim 20$ for the Type II instability while $Re_{\delta cI} \sim 50$ in the Bödewadt layer. In others studies such as the one of Tuliska-Sznitko et al. (2002) critical Reynolds number are in agreement with the aforementioned values.

The Type I instability is also known as cross flow instability. It can be identified as the velocity profile orthogonal to the wall departs from the classical 2D boundary layer shape and presents an inflexion point in the cross-flow component (example in Lingwood and Alfredsson (2000)). The orientation of the spiral arms is then given by ϵ. Type I instability is characterized by higher radial wavelength than Type II. As the Reynolds number increases, transition to turbulence is expected on the disk (see Savas (1987)). The turbulent transition finally affects the whole domain. A bifurcation from steady state to periodic flow is also

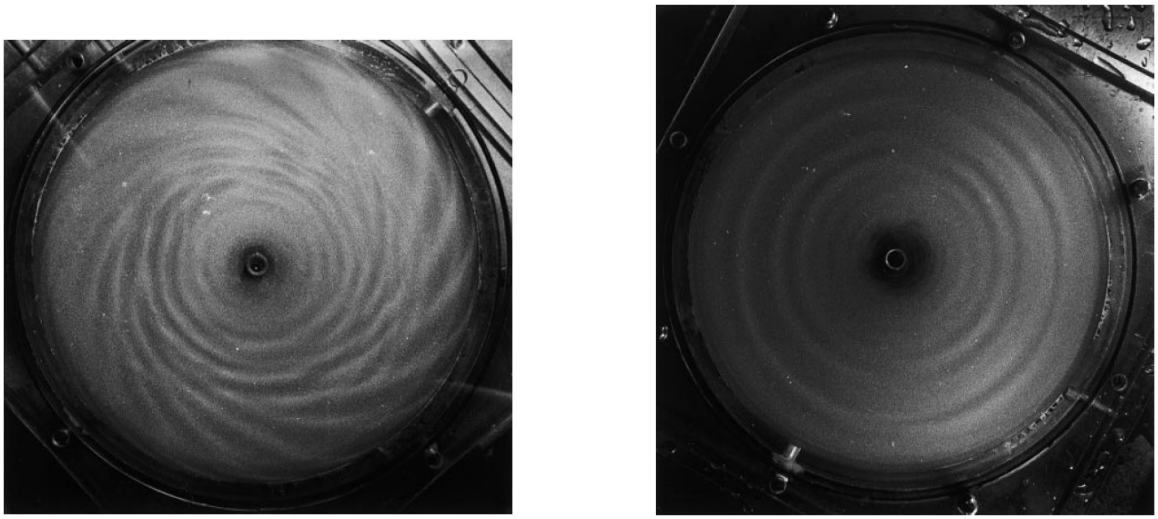

(a) (b)

Figure 2.6: Instability in Batchelor type flow - Flow visualisation - (a) Spiral vortices, Type I instability - (b) Circular waves, Type II instability - Schouveiler et al. (1999).

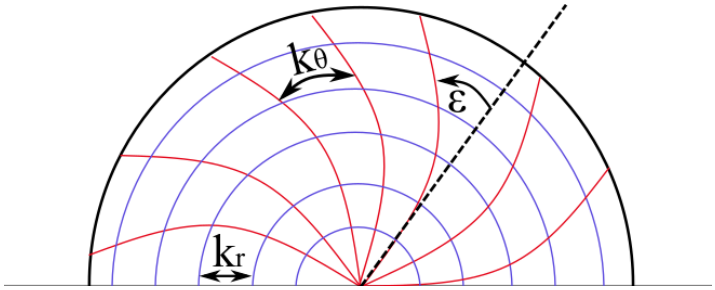

Figure 2.7: Schematic representation of disk boundary layer instabilities - Instability angle ϵ - Radial and azimuthal wave numbers k_r and k_θ.

expected at high Reynolds number (Hopf bifurcation). In Serre et al. (2004), for large aspect ratio cavity, this regime switch happens at Reynolds numbers (Re_r) of around 12000.

The boundary layer response to a perturbation for the time dependent solutions is determined by the largest characteristic time in rotating flows: the viscous diffusion time $t_\nu = h^2/\nu$, where h indicates the cavity width. This time scale is important in numerical studies as it allows, for example, to estimate the convergence time required to stabilize a solution. The viscous diffusion time is also used to determine a time limit in which the absolute/convective instability behaviour can be assessed since all transient behaviours resulting from a local flow perturbation at time t_0 must be damped at time $t_0 + t_\nu$. When instabilities are present in the Bödewadt layer, their amplitude is dependent upon the radius. In an enclosed environment such as rotor-stator cavity, The most probable high energetic fluctuations are generated in the tip to the mid-radius section of the disc. As presented in the study of Serre et al. (2001), the instability magnitude (axial velocity fluctuation) is more important at mid-span in the Bödewadt layer, where the base flow is the largest. Experimental identification of instabilities in the Bödewadt layer are eased by probing the tip to midspan region of the stator disk.

2.1.2.4 Instability in the Ekman layer

The description of the instabilities present in the Ekman layer is analogue to the description provided for the stator disc boundary layer. The same type of instabilities are found (i.e. Type I & II). Nevertheless, higher values of critical/threshold Reynolds numbers for the existence of type I and type II instabilities are observed. To give an example, the study of Serre et al. (2001) provides the following threshold values:

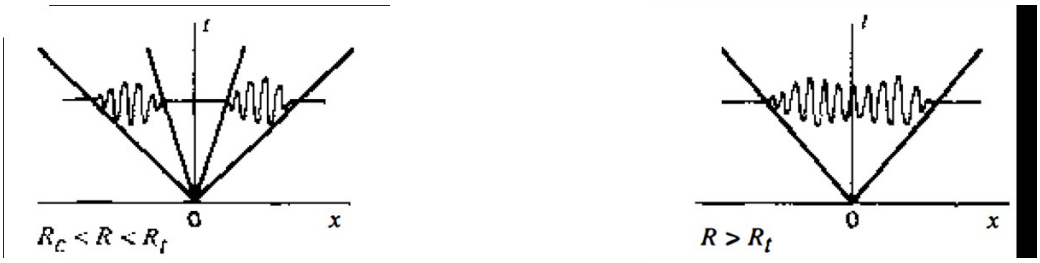

(a) (b)

Figure 2.8: Impulse response to contra propagating travelling waves in (x: space, t: time) plane of parallel flows - (a) Convectively unstable - (b) Absolutely unstable - Huerre and Monkewitz (1990).

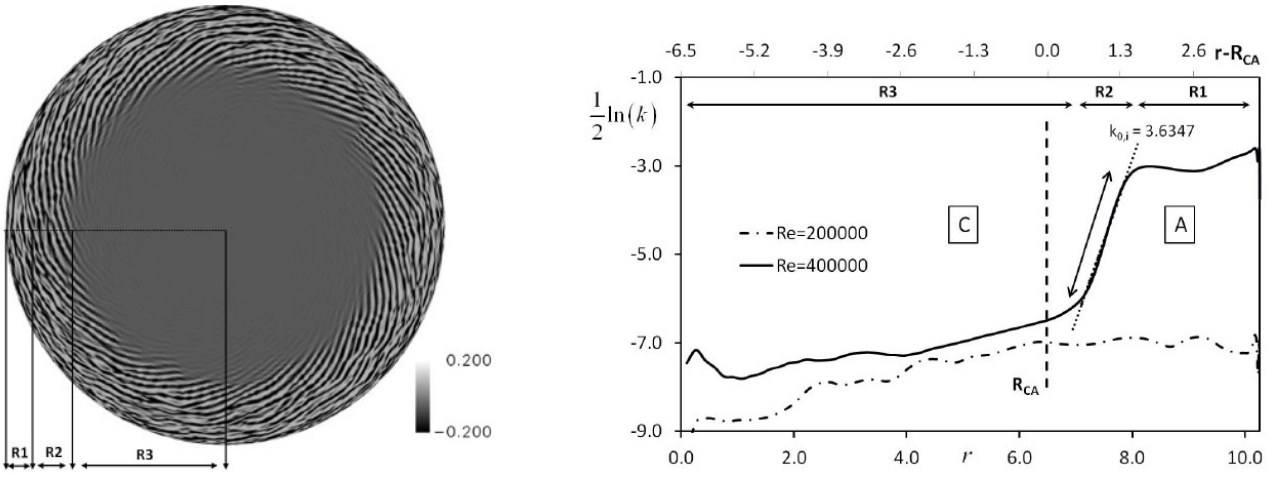

(a) (b)

Figure 2.9: (a) Turbulent rotor disk flow patterns – Iso lines of Q criterion at Re = 400000 – (R1) incipient turbulence; (R2) multi armed spiral front with 68 branches of the absolute mode of crossflow instability; (R3) stable flow region – (b) Turbulent kinetic energy in rotor disc boundary layer at Re = 2.010^5 and Re = 4.010^5 - Convective (C) to absolute (A) instability transition RC-A – Peres et al. (2012).

$Re_{\delta cII}$ 90, $Re_{\delta cI}$ 270.

In the Ekman layer, the convective/absolute instability transition is also associated to the transition to turbulent regime at high Reynolds number (see Peres et al. (2012)). In Figure 2.9a, transitional flow in rotor disk turbulent boundary layer is presented. Following the flow path from the disc center to the outer radius, the iso-lines of Q-criterion illustrates a successive switch from stable flow region (R3), to multi arm spiral vortices cross flow instability (R2), to finally incipient turbulence (R1). The Figure 2.9b underline the brutal growth in turbulent kinetic energy after the convective/absolute instability transition line (RCA) that appears just before the R1 to R2 region transition.

The outtake of the previous two sections is that for rotor stator cavities, boundary layers on discs may present multiple regimes at the same time. As such, the challenge in apparent simple configuration is to understand how one affects the other and what effect this has on the whole cavity dynamics. As an example, the angle of spiral wave front ϵ are of opposite sign between the boundary layer on the rotor disk and the one on the stator disc. Wave numbers also differs and the stability regimes in both layers may be different for the same operating condition. As a result, the flow transfer between the two layers has an effect on Batchelor flow features of, typically on the core flow.

2.1.2.5 Core region - Three dimensionality

In a Batchelor type flow, the core flow between the rotating and stationary discs is a main flow feature characterized by solid body rotation motion. The core region being at the interface of each disc boundary layer, it links the two with three dimensional instability propagation (see Serre et al. (2001)). Core region analysis is interesting to extract the behaviour of macro structures associated with the cavity system. Close to the end walls, the core flow region shows an helicoidal behaviour that allows to transfer the instabilities generated in the Bödewadt layer towards the rotating disc. As already mentioned, the flow transfer is induced by the disc pumping effect in this confined environment. That is why, as discussed in Serre et al. (2001), frequencies that develop either in the Ekman or in the Bödewadt layer can be found dominant elsewhere in the fluid domain. The instability transport is limited when no shaft is present (i.e. not an annular cavity) mainly because instabilities vanished while flow is collecting along the rotation axis. Nevertheless, as mentioned in Bridel-Bertomeu (2016), these configurations highlight instability transfer from the Bödewadt layer through the rotating core. From that perspective, one can conclude that instabilities develop firstly in the disc boundary layers, to be then transmitted to the remaining part of the domain by the core flow.

However, as mentioned in Lingwood and Alfredsson (2000) and Greenspan (1968), external perturbations can also be the cause of core flow instability. As an example, variations of the rotation rate of the rotor-stator system can cause linear and non-linear inertial oscillations in the core. In this case, the core flow instability can then excite boundary layer modes on both discs, meaning that the main driver for the cavity boundary layers modal behaviour is therefore the core flow itself. As a general conclusion, literature shows no general consensus about the dominant impact of the boundary layers on the core flow or vice versa.

2.1.2.6 Temperature effects – Non isothermal flow

The temperature effect in a rotor stator system has been investigated by Serre et al. (2004) with linear stability analysis. The study shows that both Type I and Type II instabilities characteristics are altered by change for different values of the thermal Rossby numbers. The variation of the instabilities characteristics (wave numbers, ϵ, entrainment coefficient) is stronger in the stationary disk boundary layer, mostly due to the proportionality dominant rotor work input in the rotor boundary layer.

2.2 Coaxial cylinder flows

2.2.1 Coaxial cylinder flow features

In this section, a synthetic review is given of the flow developing between two coaxial cylinders (Taylor Couette flows). The idea is to get familiar with flow features that are not linked to the one developed in a Batchelor type flow (see section 2.1) and may contribute to the three dimensionality of the flow in axial compressor rotor-stator cavities.

The flow between two coaxial cylinders is described in terms of flow features. It consists of a system of two boundary layers on each coaxial cylinder and of a bulk flow that separates them. The critical parameters for this system are the relative rotation speed of each cylinder as well as their radius. As such, the non-dimensional numbers describing defining the flow regimes taking place in a Taylor Couette problem are: (1) Inner or outer disk Reynolds number (c.f. equation 2.3 and equation 2.4 respectively); (2) Taylor number (see equation 2.5 where $\eta = \frac{R_i}{R_o}$ is the radius ratio);

$$Re_i = \frac{\Omega_i R_o (R_o - R_i)}{\nu} \tag{2.3}$$

$$Re_o = \frac{\Omega_o R_o (R_o - R_i)}{\nu} \tag{2.4}$$

$$Ta = \frac{(1+\eta)^4(R_o - R_i)^2(R_i + R_o)^2(\Omega i - \Omega_o)^2}{64\eta^2\nu^2} \tag{2.5}$$

2.2.2 Coaxial cylinder flow regimes

In Taylor Couette flow, the Taylor number weight the effect of inertial forces over the effect of viscous forces. It is a stability indicator. Above a value of ~ 1700, Taylor cells (or Taylor vortices) in the bulk flow between two coaxial cylinders are generated. The investigation of Taylor Couette flow regimes was at first done at low Reynolds numbers (see Andereck et al. (1986) for a full review). The classification of flow regimes as a function of inner and outer cylinder Reynolds number is illustrated by Figure 2.10. For applications such as shroud stator cavities, flow regimes frequently belong to the line $Re_o = 0$ since the "outer cylinder" is the stator platform. One can comment on the variety of flow regimes present at low Reynolds number (Re_i <2000) which occupy a specific region of the couple [Re_i ; Re_o]. However, the H25-C2 configuration, characterized by Re_i values as high as $2 * 10^5$ (see Section 2.4), is off the chart, in an unexplored region. A detailed analysis of the low Re_i regimes is not relevant in the present work.

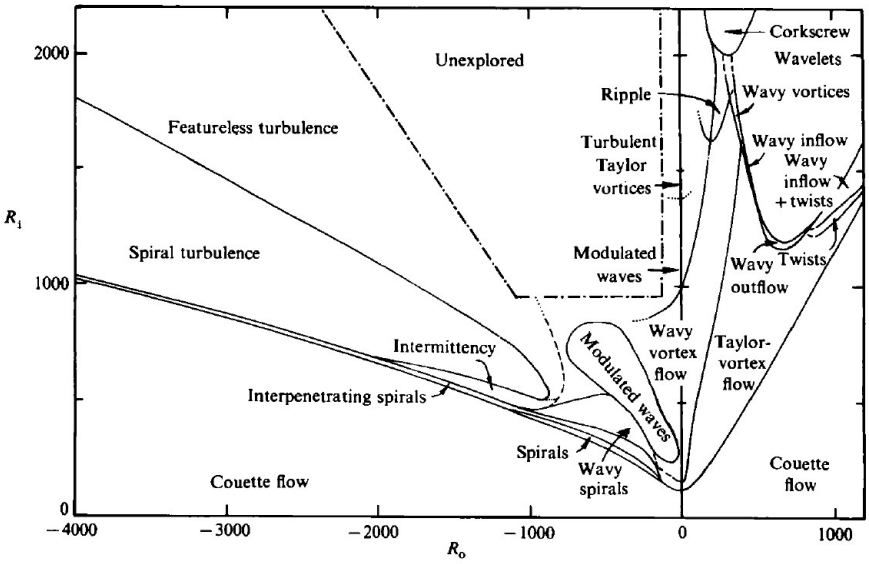

Figure 2.10: Flow regimes in Taylor Couette flow as a function of inner and outer cylinder Reynolds numbers $Re_{i,o}$- Andereck et al. (1986).

Grossmann et al. (2016) reviews the studies of the last two decades where a global interest for coaxial cylinder flows at high Reynolds numbers (over the chaotic limit) has been showed. Typically, the range of studies mentioned lay in the intervals: $10^3 < Re_i < 2 * 10^6$; $10^6 < Ta < 10^{13}$.

Using the analogy that exists between Taylor Couette flow and Rayleigh Bénard flow, the work of Grossmann et al. (2016) implies that in the operating conditions of the C2 cavity, ultimate regime of Taylor Couette flow is expected. In this regime, at around $Re_i \sim 2 * 10^3$), the boundary layers and the bulk flow are fully turbulent, but flow features such as Taylor vortices can still exist. Residuals instabilities from Taylor rolls remain at high Re_i, even over $Re_i = 10^5$. For Taylor Couette flow, different opinions on the threshold value are present in the literature concerning the existence of vortex-like coherent structures. Based on the value of Re_i for the C2 cavity geometry and according to the study of Ostilla-Mónico et al. (2014), the expected regime is a "featureless" ultimate Taylor Couette flow. In that sense, no clear instability pattern can be identified above $Re_i = 3.0 * 10^4$. Studies such as the one of Lathrop et al. (1992) also indicates that above $Re_i = 1.2 * 10^5$ Taylor vortices are no longer identifiable and the flow is in a featureless ultimate regime behaviour. On the contrary, in Lewis and Swinney (1999), the Figure 2.11 shows azimuthal modal activity at low frequency resulting from Taylor vortices that is visible up to $Re_i = 2.7 * 10^5$. The peaks present at high and medium frequency happen to be harmonics of the fundamental modes at low frequencies. This last

study confirms the possibility to detect experimentally azimuthal waves from TC instability.

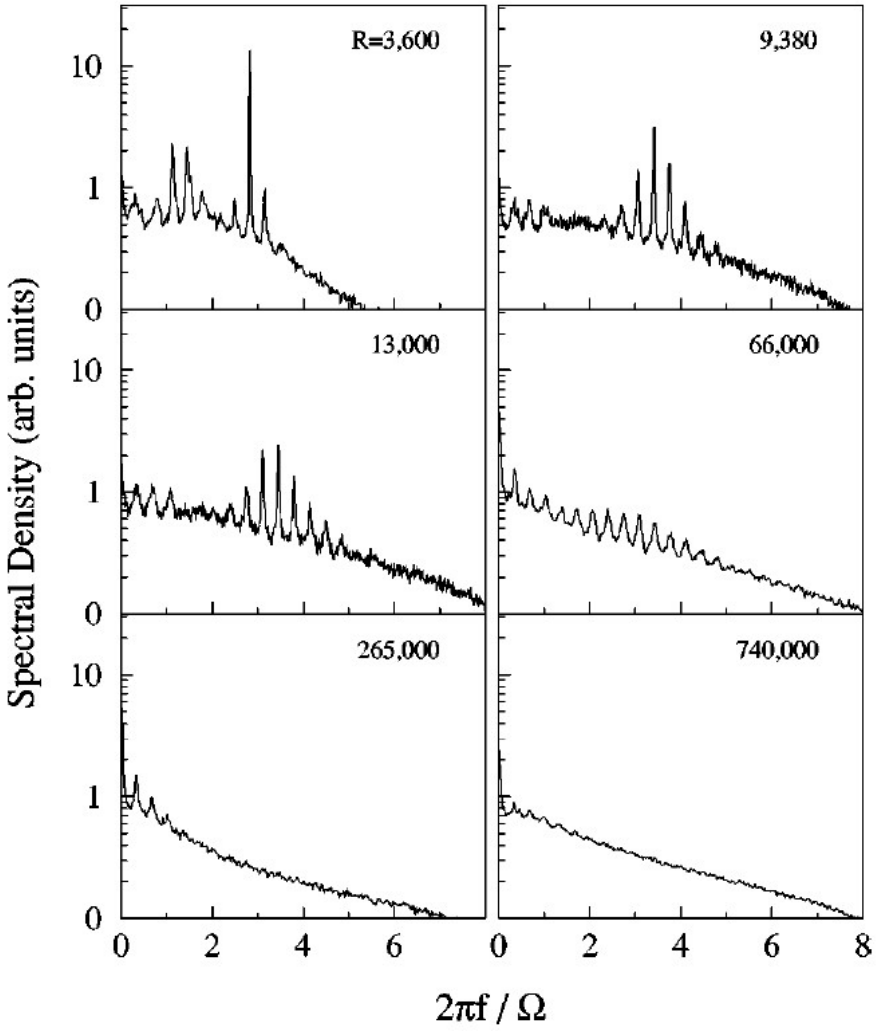

Figure 2.11: Velocity spectral density illustrating the presence of azimuthal travelling waves at varying Reynolds number (noted R here) – Cross correlation of velocity measurement with spacing of 5.5° Lewis and Swinney (1999).

2.3 Extension to annular cavity flows

2.3.1 Confinement and curvature

Confinement in rotor stator systems has an effect on instability thresholds and on the type of instabilities. The notions developed previously ease the understanding of the flow behaviour in the case of an annular cavity. Nevertheless, the added rotating shaft increases the radial confinement of the rotor/stator system. Curvature effects are also amplified with respect to classical rotor/stator system. To get a good description of the flow in turbomachinery-like applications, it is important to introduce the notions of complex regimes, coexistence, and dislocation.

2.3.2 Complex regimes

In high Reynolds number applications with large aspect ratio cavities, complex regime emerges. They are typically regimes where the three dimensionality of the flow and turbulence levels are high (see Serre et al. (2001)). These regimes are easily reached in turbomachinery assemblies. The geometrical constraints imposed in such configuration influence the generation of complex regimes in the boundary layers of each

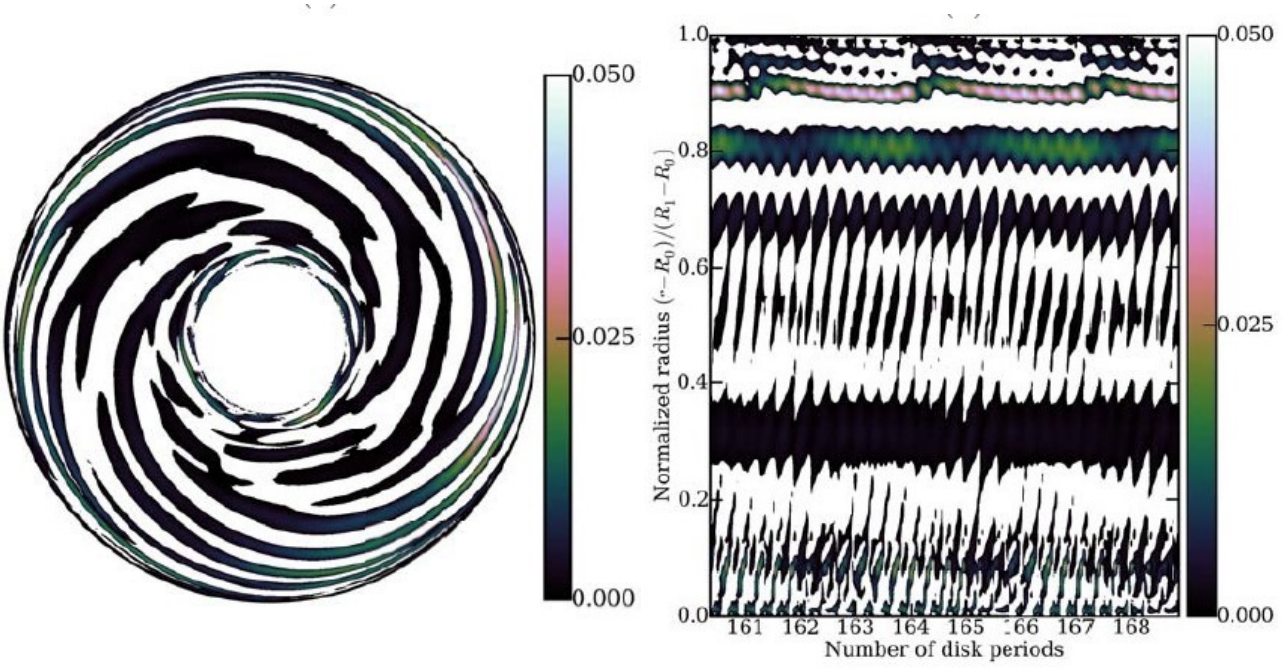

(a) (b)

Figure 2.12: (a) Contour of fluctuations of axial velocity in Ekman layer of annular cavity - (b) Space time diagram of axial velocity fluctuations - Bridel-Bertomeu (2016).

disk. As an example, confinement tends to reduce the appearance of complex regimes where an increased curvature has the opposite effect.

In complex regimes, the flow displays important three-dimensionality. With such behaviour, instabilities propagate in the whole domain. From an experimental point of view, it is easier to get the whole dynamics of the cavity regime scoping in one location. However, it is also more difficult to dissociate and identify the source of the instabilities.

2.3.3 Coexistence

Coexistence appears in complex regimes where both Type I and Type II instabilities are present in the disk boundary layers. This phenomenon was first noticed experimentally in Savas (1987) at high Reynolds number within the Bödewadt layer. Coexistence happens in either Ekman and Bödewadt layers, where spiral and axisymmetric waves exist simultaneously. As an example, on Figure 2.12a taken from Bridel-Bertomeu (2016), Type II (close to the shaft) and Type I (at higher radius / Reynolds numbers) coexist in the Ekman layer of an annular cavity. The three dimensionality of the cavity flow sets the large scale dynamics, but it is clear that in the presence of coexistence, the flow is locally defined with varying source of instability at each radius. As it can be understood, from an experimental point of view, the probing location is critical to characterize the instabilities in the example presented. Measurement location affect instability characteristics identification and the signal content is also influenced by the instability transport history.

2.3.4 Dislocation

Dislocation or “structural defect” is present in complex regimes of disk layer flows. Dislocation takes place when there is coexistence and the flow transition is made from axisymmetric (Type II) to spiral vortices regime (Type I). Another dislocation can also be seen when the number of Type I instability vortices arms increases with the radius (change in azimuthal wavelength). In both cases, phase velocity shifts are observed. These effects are illustrated by Figure 2.12a where dislocation is clearly visible at 30% span and

80% span. Thanks to the Figure 2.12b it is also illustrated that the dislocation phenomena is stationary in time (horizontal line in the space-time diagram). The dislocation is also associated in change in azimuthal and radial wavenumbers. In both Ekman and Bödewadt layers, dislocation is expected when the curvature is increased.

2.3.5 Instability transport

As already mentioned, in the case of no shaft cavity, the instability emerging from the Bödewadt layer vanishes when the flow collects along the machine revolution axis (Savas (1987), Serre et al. (2001), Lingwood and Alfredsson (2000)). The specificity of annular cavities is that the instabilities transport from the Bödewadt layer is done through the shaft boundary layer. Therefore, main instabilities or modes from the Bödewadt layer can be found at other locations (Serre et al. (2001)). If one takes the instabilities frequencies for the rotating ($\sigma 1$) and the stationary ($\sigma 2$) discs, the study indicates that $\sigma 1$ dominates the rotor shroud corner while an equal magnitude of $\sigma 1$ and $\sigma 2$ is found in the rotor-shaft and the stator-shroud corners. In the previous sections, has been presented that the Bödewadt layer is the first unstable component in Batchelor type flow. Due to the transport of instability, the shaft presence can also trigger a transitional behaviour in the Ekman layer. One of the main conclusion of the work of Serre et al. (2001) is that the geometrical confinement, in terms of aspect ratio, plays a role in the definition of the type of instabilities in the disc layers. In annular cavities, the radial confinement caused by the presence of a shaft plays a role in the amplification of the generated boundary layer modes. Bridel-Bertomeu (2016) shows that for different cavity geometries of varying aspect ratio and curvature, only a few modes either axisymmetric or 3D are associated with the cavity dynamic behaviour. By their 3D behaviour, the mode frequencies can be tracked even away from their source region. These few modes appear to be possibly identified by modal decomposition of the signals to extract cavity most energetic pressure bands.

The previous analysis allows to further highlight the link existing between the geometry of the rotor /stator system and the development and propagation of instabilities in the fluid domain. Another key point to put into perspective in this review is that, for turbomachinery applications, local geometries can be the source of modes due to local changes in flow regimes which can then be amplified or damped down by the transport in the Ekman and Bödewadt layers. It has been shown that even at high Reynolds numbers, the number of characteristic modes of a geometry resulting from typical Batchelor flow instabilities is finite and limited. Modal activity can be retrieved even with pin-point measurements and /or modal decomposition. That is why, in the analysis of cavity flow dynamics, it is key to: (1) Have a deep understanding of the base phenomenology in the case of parallel disk and coaxial cylinders, to ease turbomachinery test case results interpretation; (2) For complex arrangement such as the one in turbomachinery applications, perform a non dimensional analysis of the geometry and operating conditions, to predict the global and local flow region that could lead to the most probable instabilities.

2.4 H25-C2 cavity characteristics

The test case of the H25-C2 cavity is presented in this section. The non-dimensional numbers associated with the geometry and the testing environment are introduced. A first interpretation of the geometry is given in order to raise questions to be answered by the experimental and numerical data obtained in this work.

To ease the reading, the span value in the used figures refers to the percentage of main channel height. As a result, the cavity bottom is not at $Span = -1$ since the cavity is shallower than the main channel. The normalized width of the cavity ranges from 0 to 1. Figure 2.13a displays the C2 cavity geometry as well as the rotating (red) and fixed (black) surfaces. The H25 stage labyrinth seal (see Figure 1.16) is located at $Z_{norm} = 1$ while the cavity trench exit is located at $Span = 0$. As it is the case for Batchelor type flow, the cavity fluid motion is expected to be: flow travelling radially upward in the rotor disk boundary layer; flow travelling radially inward in the stator boundary layer.

Non dimensional numbers are computed at the design operating conditions of the machine to describe

the C2 geometry. The cavity aspect ratio (Figure 2.13b) and Reynolds number based on the disc radius (Figure 2.13c) informs that two main region exist according to the classification given in Figure 2.5. Most of the C2 cavity is under the regime of separated turbulent boundary layers. In the trench region, the aspect ratio is as small as turbulent boundary layers are expected to merge (G = 0.0046). The local regimes, in different parts of the cavity, are responsible for the generation of flow instabilities but also define their transport. The cavity trench region is managing the cavity / main channel interaction. The following question is raised concerning the presence of merged boundary layer at that location. Can this affect the instability transport between the cavity flow and the main channel?

The distribution of radius ratio η is given in Figure 2.13d to put the C2 cavity into perspective with respect to Taylor Couette type configurations. To complete the analysis, key non dimensional numbers are presented in Table 2.1 where number ranges are given. When a precise range cannot be defined, indicative values associated with design operating conditions are mentioned.

Non dimensional numbers also give information concerning the analysis of the current geometry. As an example, the viscous diffusion time is an important information to have if CFD modelling is planned. It is the largest characteristic time in rotating flows. Relevant to the generation of time dependent solutions (order of magnitude of transient phenomena lifetime), the CPU time needed to reach a stable solution is directly linked to it and indicates the high numerical effort required to analyse such system.

Another information for the C2 configuration is the indicative Rayleigh number of $2.7e^3 > 1.7e^3$ which indicates the presence of Rayleigh Bénard instabilities in the cavity, i.e. array of contra-rotating vortices induced by the convection mechanisms between heated rotating disk and cooled stator platform.

In the C2 configuration the cavity walls are not smooth due to the mechanical assembly of the H25 stage. Imperfections along the static and rotating surfaces corresponding to realistic turbomachine technological features have a direct impact on the flow field generated in the cavity volume. To ease result analysis in Chapter 4, potential sources of disturbances linked to the machine environment are presented in Figure 2.14. No assembly bolts or bolt head is present in the C2 cavity. The rotor mechanical assembly is composed of individual blades and platforms. Each platform is maintained thanks to a locking pin. As a consequence, the rotor cavity surface is composed of 65 platform junctions and 65 pins.

The stator is composed of 8 sectors of 10 blades that are sealed together which causes the presence of 8 junctions in the path of the cavity flow. In the test section, the C2 volume is also used to route instrumentation. In Figure 2.14, a pipe for pneumatic instrumentation routing is presented. These pipes are in the number of 10 and are equally spaced azimuthally in the cavity. Specific care is taken to monitor the possible consequences of such details. Table 2.2 informs on cavity details and respective frequency markers given in Engine Order. Another characteristic frequency of the cavity system is the Helmholtz frequency. In the case of the C2 cavity it has been estimated at 10.2 [EO] at rotor nominal speed and design operating conditions. This estimation takes into account the cavity trench as the line attached to the cavity volume. In the same way, but taking the last labyrinth seal tooth ad the line, the cavity Helmoltz frequency at nominal speed becomes 16.9 [EO].

Inspired from the definition of Tyler and Sofrin spatial modes in axial compressors (cf.Tyler and Sofrin (1962) and equation 2.6) the frequency markers of the interactions between the rotating and static disk are listed in Table 2.3 for a and b in the interval [0:5] and [-5:5] respectively. The number of rotating elements is taken as 65 on the rotating surface and 8 for the stator disk (Stator sectors). The frequency content from these interactions is expected to be most visible in the cavity trench region where platforms are closer.

$$\mathrm{M}(a,b) = a * \mathrm{N}_r + b * \mathrm{N}_s \tag{2.6}$$

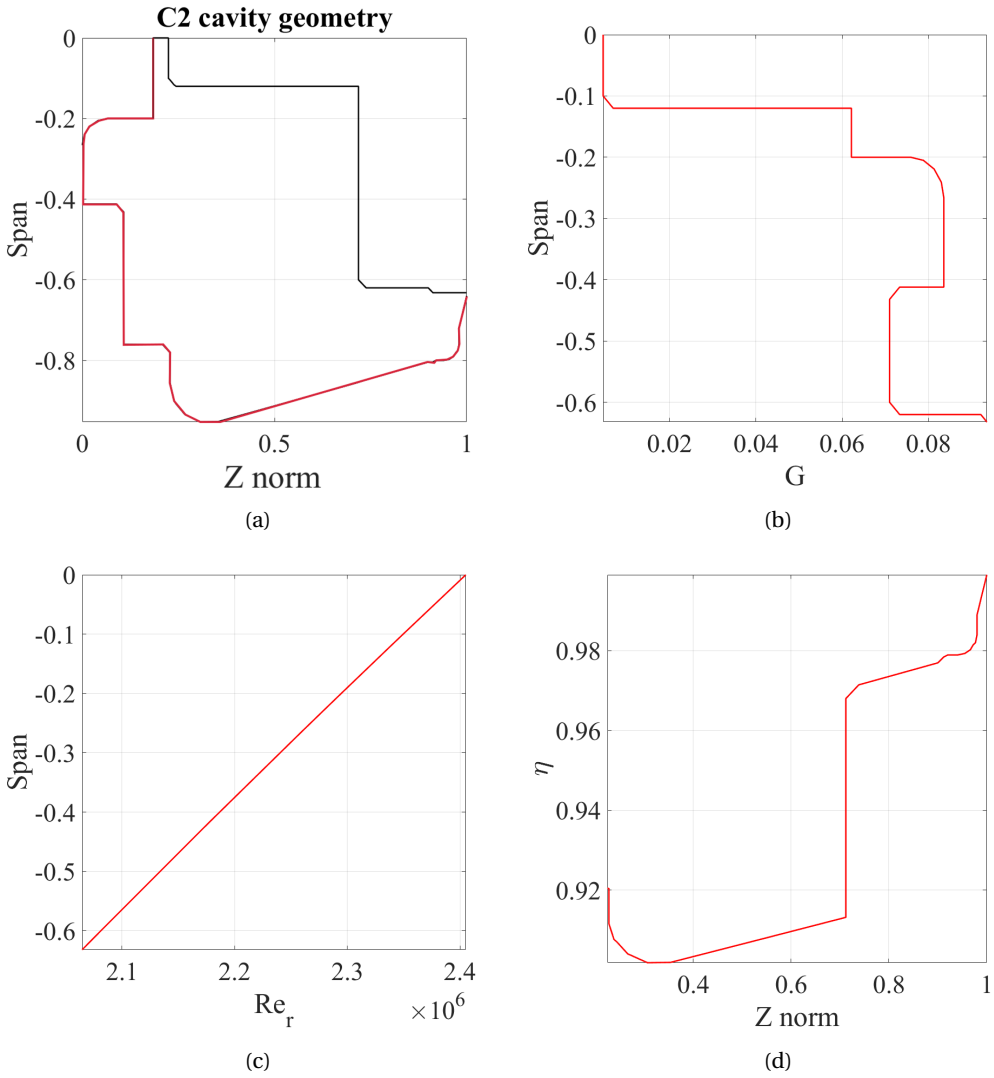

Figure 2.13: (a) H25-C2 cavity geometry, Rotating surface in red - (b) C2 cavity aspect ratio -(c) C2 cavity Reynolds number based on the radius - (d) C2 cavity radius ratio $\eta = \frac{R_i}{R_o}$.

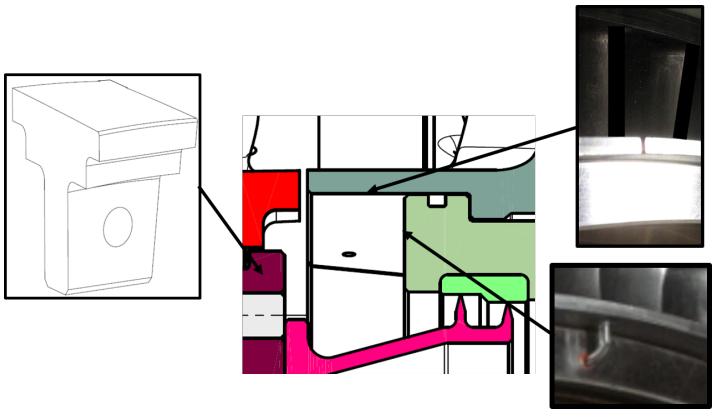

Figure 2.14: Cavity flow disturbance sources in the C2 cavity - Rotor mechanical assembly (left) - Stator sector connection seal (top right) - Instrumentation routing pipe (bottom right).

Table 2.1: Non-dimensional numbers definition and key values for the H25-C2 configuration.

Non-dimensional number	Definition	Value/Range	Notes
Rotating Reynolds number	$\mathrm{R}e_r = \frac{\Omega * r^2}{\nu}$	$1.9e^6 - 2.34e^6$	*see Figure 2.13c*
Inter disc Reynolds number	$\mathrm{R}e_h = \frac{\Omega * h^2}{\nu}$	$52 - 35518$	-
Local Reynolds number (based on δ)	$\mathrm{R}e_\delta = \frac{\Omega * \delta * \mathrm{R}_i}{\nu}$	$1378 - 1529$	-
Cylinder Reynolds number (TC flows)	$\mathrm{R}e_i = \frac{\Omega * \mathrm{R}_i * (\mathrm{R}_o - \mathrm{R}_i)}{\nu}$	$2071 - 2.1e^5$	-
Cavity aspect ratio	$\mathrm{G} = \frac{h}{r}$	$4.6e^{-3} - 0.1$	-
Curvature parameter	$\mathrm{R}_m = \frac{\mathrm{R}_i + \mathrm{R}_o}{\mathrm{R}_o - \mathrm{R}_i}$	19.3	-
Rossby number	$\mathrm{R}o = \frac{\mathrm{V}_t}{\Omega h}$	6.48	*Indicative value in the core flow*
Ekman number	$\mathrm{E}k = \frac{\nu}{\Omega h^2}$	$4.0e^{-5} - 1.9e^{-2}$	-
Rayleigh number	$\mathrm{R}a = \frac{g * \iota * (\mathrm{T}_{rot} - \mathrm{T}_{stat}) * h^3}{\nu * \kappa}$	$2.7e^3$	*Indicative*
Prandtl number	$\mathrm{P}r = \frac{\nu}{\kappa}$	0.708	-
Grashof number	$\mathrm{G}r = \frac{\mathrm{R}a}{\mathrm{P}r}$	$3.9e^3$	*Indicative*
BL thickness scale (Batchelor type flow)	$\delta = \sqrt{\frac{\nu}{\Omega}}$	$1.39e^{-4}[m]$	-
Viscous diffusion time	$t_v = \frac{h^2}{\nu}$	$11.98[s]$	*Based on maximum cavity width*
Radius ratio	$\eta = \frac{\mathrm{R}_i}{\mathrm{R}_o}$	$0.9 - 1$	-
Taylor number	$\mathrm{T}a = \frac{(1+\eta)^4 (\mathrm{R}_o - \mathrm{R}_i)^2 (\mathrm{R}_i + \mathrm{R}_o)^2 (\Omega i - \Omega_o)^2}{64 \eta^2 \nu^2}$	$4.2e^6 - 4.8e^{10}$	-
Helmholtz frequency	$f_h = \frac{c}{2 * \Pi} * \sqrt{\frac{\mathrm{A}_{trench}}{\mathrm{V}_{cav} * \mathrm{L}_{trench}}}$	10.2[EO]	*At 100Nn - Using trench as a line*
Helmholtz frequency	$f_h = \frac{c}{2 * \Pi} * \sqrt{\frac{\mathrm{A}_{laby}}{\mathrm{V}_{cav} * \mathrm{L}_{laby}}}$	16.9[EO]	*At 100Nn - Using labyrinth as a line*

Table 2.2: Geometrical imperfection of the C2 cavity environment - Respective frequency marker.

Element	Number	Characteristic Dimension	Frequency associated (in Engine Orders)
Rotor Platform	65	-	65
Rotor Pins	65	-	65
Platform + Pins	130	-	130
Stator Sector	8	-	-
Stator Support Sector	8	-	-
Pressure tubes routing	10	9% Span	60 (Pipe Wake at 100Nn)
Eccentricity	-	<0.2% Span	-

Table 2.3: Tyler and Sofrin spatial modes M for $N_r = 65$ and $N_s = 8$.

-40	-32	-24	-16	-8	0	8	16	24	32	40
25	33	41	49	57	65	73	81	89	97	105
90	98	106	114	122	130	138	146	154	162	170
155	163	171	179	187	195	203	211	219	227	235
220	228	236	244	252	260	268	276	284	292	300
285	293	301	309	317	325	333	341	349	357	365

2.5 Conclusion

Chapter 2 introduces basic notions regarding rotor stator cavities. Cavity aspect ratio and rotating Reynolds number are key to define the flow field in such configuration. The presence of through flow affects the flow organization in the stator and rotor boundary layer. Type I and Type II instabilities has been presented in the Ekman and Bödewadt layers. Type I or cross flow instability is characteristic for high local Reynolds number before a transition to fully turbulent flow. Since the local Reynolds number evolve with the radius, it is shown that both type of instabilities can coexist on a same disk surface. The evolution of a fully three-dimensional flow is affected by the cavity geometry which, as a consequence, is driving the instability transport.

In a rotor/stator cavity, the stability thresholds are governed by the stator boundary layer, being the least stable element of the system. It is possible to find configurations where Bödewadt layer is fully turbulent while Ekman layer remains in a transitional behaviour. In a second part, the overview of Taylor Couette flow allowed to introduce the different flow regimes between two coaxial cylinders at high Reynolds numbers. In Bridel-Bertomeu (2016), as an example, due to local geometry of a turbomachine cavity assembly, Taylor like vortices appear. Even without being able to clearly demonstrate that the Taylor Couette flow is at the origin of the behaviour observed, it clearly highlights the impact of the local geometry on the rotor stator assembly system. Generated modes can be dominant in the whole cavity and coexist with Type I and Type II instabilities of the Batchelor flow. As a result, high Reynolds number cavity instabilities/modes are the main components of the generated turbulent flow. Beside the complexity of the flow regime generated at high Reynolds number, only few modes are characteristic of the investigated cavity system.

The H25-C2 cavity configuration non dimensional numbers analysis frame this work in the existing literature on rotor stator cavity and coaxial cylinder cavity systems. For the most part, Batchelor type flow with turbulent separated boundary layer is expected from span -0.12 down to span -0.61. Above -0.12 span is the trench region where the turbulent boundary layers are expected to merge if no blade effects are involved. The normalized axial position Z_{norm} = 0.65, splits the cavity geometry in two regions of coaxial cylinders at different radius ratio. The C2 operating conditions are in a featureless regime for Taylor Couette type. A list geometrical features that belong to the cavity environment were presented (platform and pins interaction with the stator sectors, instrumentation routing wake,....). The associated frequencies were estimated in order to highlight, in the flow analysis, the instabilities attributable to the C2 geometry only.

Chapter 3

Experimental and numerical methodologies

THis chapter presents the experimental and numerical methods used to assess the effect of cavity flow on axial compressor performance and stability. In the first part, experimental means are addressed. The existing facility layout is introduced. The modifications made to fulfil this work objectives by means of performing measurements with controlled leakage flow are summarized. The instrumentation used in the test campaign and the calibration process are also detailed, for main flow and cavity flow characterization. The use of the instrumentation as well as the approach for data analysis are presented.

In a second part, the numerical tools that helped support the experimental observations are detailed. The validation of the numerical setup with respect to preliminary experimental dataset is also included in this chapter.

Contents

3.1 Experimental means

3.1.1 Introduction

A literature review on cavity flow experimental investigation and their effect on axial compressor reveals the two type of test section used: blade cascades or rotating machine assemblies. Studies in cascades (Sohn et al. (2006), Demargne and Longley (2000), Taylor, D. J., Longley, J. P. (2019)) allow to have an independent control on flow leakage parameters. Usually performed without "representative" cavity geometries but rather with injection slots, they show flexibility in generating multiple leakage conditions without any mechanical modification of the test section. Furthermore, the cascade configuration eases the use of visualization techniques such as ink-dye, oil-dye, PIV, and concentration measurements of gas mixtures (ethylene, carbon dioxide). At the other end of the spectrum, results obtained in rotating assemblies (Wellborn and Okiishi (1996), Auchoybur and Miller (2018)) use engine-like configurations in which leakage conditions are fixed for a given compressor operating point and shroud cavity geometry.

The analysis of the cavity flow effect on axial compressors relies on the measurement of flow quantities in the main channel. In all the aforementioned studies, probe traversing is at least performed downstream of the stage under investigation. Eventually, probe traversing is done in both radial and azimuthal direction. The type of instrumentation used is either steady, with 3-hole pneumatic probe, 5-hole pneumatic probe, or unsteady using, as an example, Hot Wire Anemometry. The objectives of the main channel measurements are: (1) To highlight the impact of leakage flow on the end wall secondary flow system; (2) To evaluate the span range of leakage flow contribution to local and propagated loss. Aside from main channel flow characterisation, some configurations also present cavity trench measurement (Demargne and Longley (2000), Wellborn and Okiishi (1996)) . To perform such measurements, especially probe traversing, bespoke trench configurations are used in which the axial clearances are larger than the one found in typical out of production turbomachinery modules. The setup scale is mainly limited by probe intrusiveness. Nevertheless, such measurements are able to inform on rotationally induced cavity/main channel interactions. It is also a way to capture in the cavity trench, externally induced ingress and egress regions attributable to blade effects, i.e. pressure driven interactions.

In axial turbine literature, the author found more bespoke test sections for cavity flow analysis. If the objectives of cavity flow characterization differ from compression to expansion module, the experimental setup often uses the same means and philosophy. Two really interesting experimental setup are found in Savov et al. (2016) and Beard et al. (2017). Experimental means used are such as: wall pressure taps (steady), wall pressure transducers (unsteady) in both cavity and main channel, concentration measurements, leakage injection control. Findings of these studies are eventually summarized in Chew et al. (2019) that reviews the rotating flow induced perturbations generated in turbine rotor-stator cavities.

3.1.2 Von Karman Institute R4 facility

The R4 facility is von Karman Institute for Fluid Dynamics test rig for axial compressor studies. The facility layout presented in Figure 3.1 is closed looped and equipped with a speed-controlled DC motor delivering a maximum power of 650 [kW] at a rotational speed of 1000 [RPM]. The drive train consists of a 12:1 gearbox and of a precision torque meter that measures the test section's rotational speed by means of a phonic wheel. Only one notch is present on the phonic wheel to identify rotor position and compute rotational speed. The test section discharges the flow into a large collector (B) connected to the inlet plenum (D) by means of the return duct (C). The inlet plenum hosts the precision throttle valve (E) and the heat exchanger (F). The throttle valve is actuated by a variable DC engine coupled to a 1:236 ratio gear box. This allows an accurate control of the valve position and closing speed down to one micron per second either manually or in automatic mode. For safety purposes, it is also equipped with a fast-opening anti-surge valve. The exchanger block consists in two multi passage tube heat exchangers connected in series in a counter current arrangement and delivering controlled temperature conditions at the test section inlet, with an accuracy of $\pm$ 1[K]. The heat exchanger presents a honeycomb structure to provide the test section with homogeneous flow conditions. To finish, a smooth convergent bell-mouth (A) guides the flow from the

plenum to the test section.

The main interest of the closed loop assembly is that a complete flight envelope can be simulated in one rotation of the machine to address effects such as: Reynolds number effect; Rotational speed effect; Throttling transients; Thermal transient. In this work all the tests were made at atmospheric conditions.

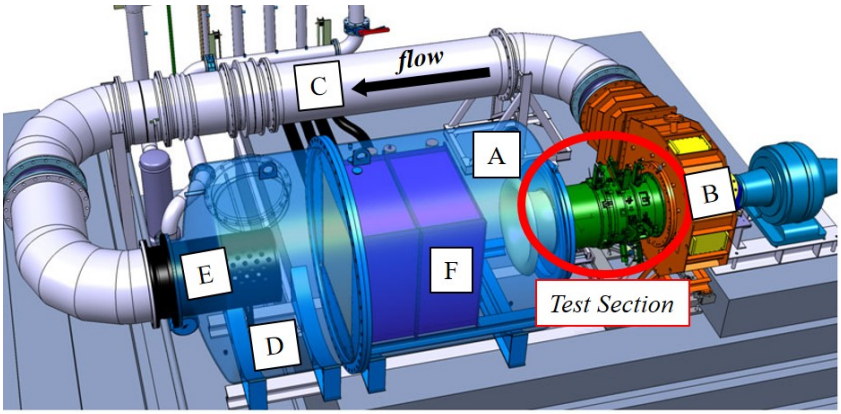

Figure 3.1: von Karman Institute for Fluid Dynamics R4 facility layout.

3.1.3 H25 test section

3.1.3.1 Instrumentation layout

The H25 test section is the configuration under investigation in this study. The meridional view of the test section is presented in Figure 3.2 where rotor and stator rows are respectively identified in red and green. Details about the stage characteristics were presented in Section 1.6. The instrumentation is distributed in four axial planes. Plane 0 is located upstream on the section convergent (seven rotor chord upstream of the rotor). Plane 1 is the stage inlet, located at one rotor chord upstream of the rotor. Plane 2 is the inter row plane. Finally, Plane 4 is the stage exit plane, located 1 rotor chord downstream of the stator blade. The H25 stage is equipped with a shrouded stator configuration. Unlike multistage assemblies, the H25 stage do not present an under platform recirculation. The R4 loop being closed, the cavities adjacent to the rotor disk are closed to the atmosphere. As a consequence, at a given operating point, the hub cavities behave as closed cavities. This argument has eventually been verified through pressurization cycles of the machine under rotation. An example is given in Figure 3.3a which plots the static pressure in Plane 2 in a pressurization cycle test. There the R4 loop was pressurized with a pressure step of 160 [mbar] when the machine was rotating at design operating conditions. The Figure 3.3b plots the pressure step response difference between the static pressure in Plane 2 and static pressure in the disk cavity C1. The reader should be informed that the absolute value for the pressure difference is affected by the probe position with respect to the local flow organisation in the C1 cavity. The increase in R4 loop pressure affects the flow in the C1 cavity which explains the change in pressure difference of 3.5[mbar] prior the pressure step or at maximal pressure. Nevertheless, at fixed loop pressure, typically between 200[s] and 300[s], the pressure difference remains constant which confirms the closed cavity behaviour.

3.1.3.2 Stage performance evaluation

3.1.3.2.1 Rakes

All the steady instrumentation was synchronized with a 2[Hz] time base. The performance of the stage was live monitored during testing and sampled at the same rate using rakes measurements at test section inlet (Plane 0) and stage outlet (Plane 4). In Plane 0, five spanwise rakes as the one illustrated by Figure 3.4 were equipped with both total pressure and total temperature kiel heads. In Plane 4, ten spanwise rakes were used for total pressure (five) and total temperature measurements (five). These elements were distributed

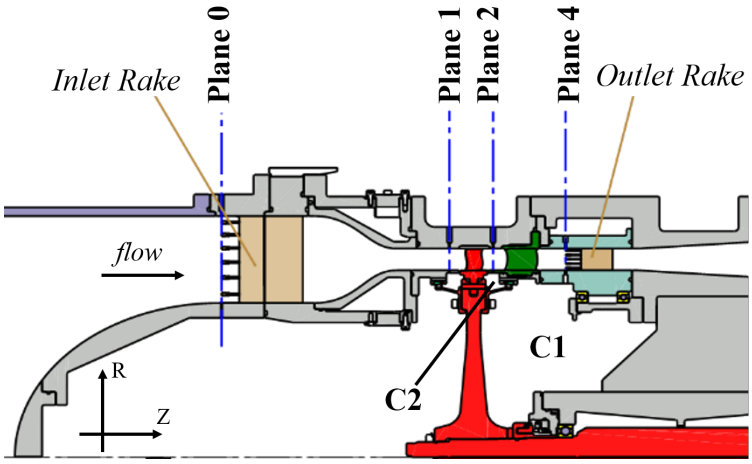

Figure 3.2: H25 test section meridional view - Rotor assembly in red - Stator assembly in green - Measurement planes (0,1,2,4) -Disk cavity C1 and shroud cavity C2 are identified.

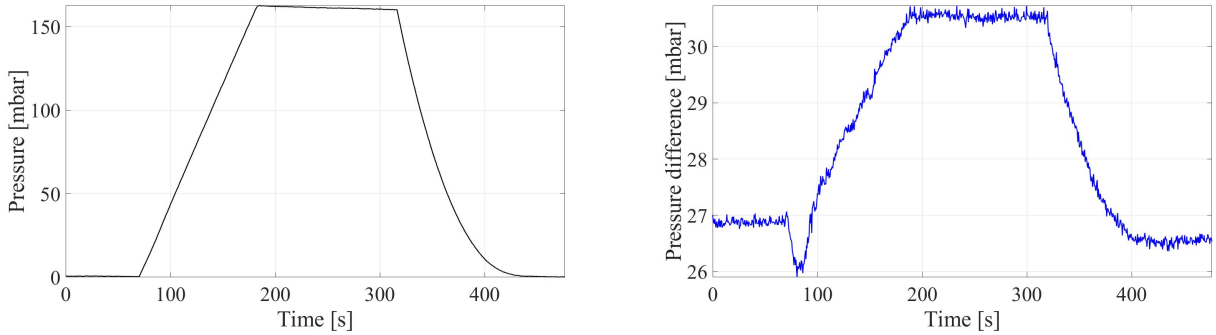

Figure 3.3: R4 loop pressurisation cycle. Pressure step response of the facility at design operating conditions (a) Pressure step in the R4 loop - Differential Static pressure in Plane 2 with respect to design operating conditions - (b) Static pressure difference between Plane 2 and disk chamber C1.

along the machine annulus to limit local flow blockage. The azimuthal positioning of the rakes in the stage outlet plane, relative to the stator row, is such that one stator pitch is covered as, presented in Figure 3.5.

Details about the acquisition system are given here. In Plane 0, a 2.5 [Psi] pressure transducer was used whereas, in Plane 4, measurements were directed to a scanner with a full scale of 15 [Psi]. These scanners were selected to compromise between sensitivity, range and therefore uncertainty. The systematic uncertainty is ±0.08% of the full span, corresponding to 14 [Pa] and 82 [Pa] for the 2.5 [Psi] and 15 [Psi] transducers respectively. To reduce uncertainty, all pressure measurements were differential. The inlet total pressure reference port was measured at the stagnation point of the test section inlet bell mouth by a high precision absolute pressure transducer, whose uncertainty is equal to 0,05% for a full span of 3[bar].

For the temperature measurements, Scanivalve DT3250 temperature scanners were used. The absolute temperature was reconstructed by means of four internal PT100 sensors. K-type thermocouples were used, leading to a systematic uncertainty value of ±0.25 [K]. The dependency of the recovery factor to the yaw angle was evaluated following the calibration procedure in Fontaneto and Lahalle (2016). The typical fully propagated uncertainty level for the temperature recovery factor is in the order ±0.02[K] for the corrected temperature.

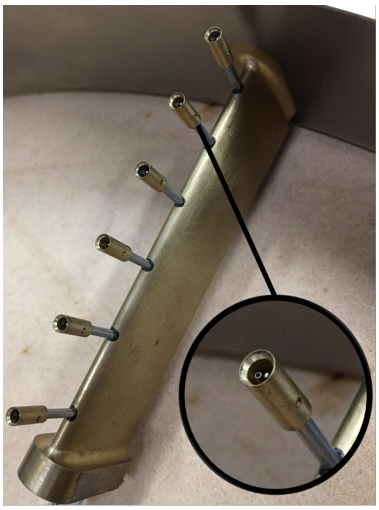

Figure 3.4: Stage inlet rake - Total pressure and total Temperature kiel head.

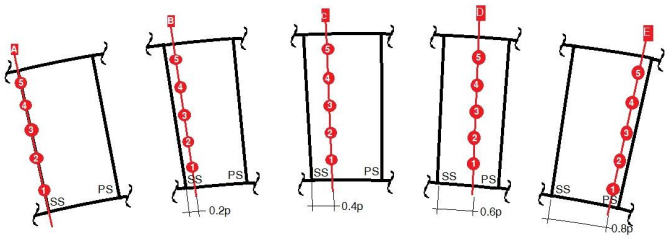

Figure 3.5: Total pressure and total temperature rake clocking in stage outlet section, with respect to the stator row.

3.1.3.2.2 Definition of an operating point

The operating point definition for the testing campaign refers to performance parameters measured or derived from the aforementioned rakes measurements such as : static to total pressure ratio, corrected mass flow, throttling parameter, flow coefficient and loading coefficient. Flow quantities were area averaged around the annulus. Mass flow averaging was not possible using rakes data since the rakes do have Kiel heads which are, on purpose, insensitive to the flow angle, in a given angle range depending on the head design. This is a greater concern in the Plane 4 (stage outlet) where the stator row flow deviation implies a non axial stage exit flow angle. As a result it was not possible to retrieve, the stage outlet mass flow distribution in the radial/azimuthal plane.

In each plane, ten static pressure taps were positioned at hub and casing. Like the rakes, their azimuthal repartition around the annulus was made such as the information over one average stator pitch is retrieved. For a given clocking and span, static pressure was either: (1) retrieved from a linear interpolation of the static pressure data at hub and casing, knowing the probe relative position to the stator blade; (2) evaluated from a linear interpolation of the two closest pressure taps pair around the annulus.

The stage mass flow was computed from the Mach number evaluated using the rakes and static pressure measurements in the test section inlet plane (Plane 0). Lumped performance parameters were defined based on mass flow averaged total quantities. Pressure ratios and isentropic efficiency computation follow the definitions given in Chapter 1. The total-to-total pressure ratio related uncertainty budget is estimated to be lower than 1% while the mass flow and the isentropic efficiency uncertainties are equal to 2.1% and 4% at nominal speed and for a near-stall operating condition.

In order to obtain repeatable data along the test campaign, an operating point was identified thanks to its static to total pressure ratio. The test rig being a dynamic system, with continuous performance fluctuation, the latter was the most stable variable in operation.

The operating points are defined in an increasing order of stage loading : Low loading (LL); Design loading (DL); Near stall loading (NS). The design loading point at nominal speed is the design point of the H25 stage. The H25 stage is robust to surge cycles which means that the real stability limit of the R4/H25 assembly can be explored in the experiments, at each rotational speed. Near stall operating conditions were then selected to be as close as possible to the stability limit while allowing measurements without any machine flow failure.

At fixed rotational speed, each point was consequently identified thanks to the vane or throttling parameter whose throttle law is given in equation 3.1.

$$\lambda = \frac{P t_{ref}}{W_r{}^2} * (\frac{P s_4}{P t_0} - 1) \tag{3.1}$$

The λ parameter was used to define LL, DL operating point at partial speed where the vane law in equation 3.1 crosses the performance curve of the H25 compressor. The Figure 3.6 displays the different operating points in the compressor map at nominal speed (100Nn) and partial speed (85Nn). At low loading, the throttle law is superimposed with a slow rpm acceleration of the compressor (in red) to highlight the match between the law chosen and compressor behaviour. A different definition of the near stall operating point was chosen. The vane law for the NS operating point at nominal speed coincides with the stall limit of H25 at 85Nn. This prevents sufficiently stable stage operating conditions at NS 85Nn to allow measurements. The NS point at 85Nn was defined based on the NS point at 100Nn as presented in equation 3.2. Operating points static to total pressure ratios are summarized in Table 3.1.

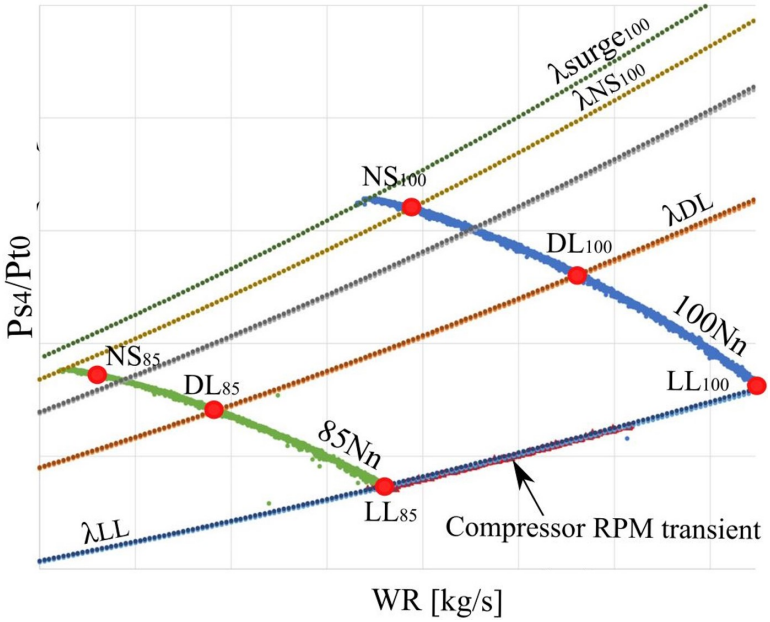

Figure 3.6: Operating point definition at nominal speed (100Nn) and partial speed (85Nn) in the stable range of H25 compressor - Operating lines of constant vane parameters - Plot of slow rpm transient at low loading vane parameter.

$$\frac{\lambda_{Surge85} - \lambda_{NS85}}{\lambda_{Surge85} - \lambda_{LL85}} = \frac{\lambda_{Surge100} - \lambda_{NS100}}{\lambda_{Surge100} - \lambda_{LL100}} \tag{3.2}$$

Operating points with and without injection were investigated. When injection was applied, the stage inlet corrected mass flow was kept constant. This ensured similar velocity triangle at rotor inlet between the cases. The injection conditions are presented further in section 3.1.3.8.

Operating Point	Static to total pressure ratio	ϕ	ψ
NS - 100Nn	1.025	0.922	1.066
DL - 100Nn	1	1	1
LL - 100Nn	0.958	1.078	0.878
NS - 85Nn	0.963	0.918	1.049
DL - 85Nn	0.945	0.982	0.973
LL - 85Nn	0.916	1.070	0.874

Table 3.1: Operating point definition at nominal and partial speed normalized with respect to the machine design point.

In Chapter 4, the operating points are also identified thanks to the stage loading ϕ and flow coefficient ψ respectively introduced in equation 3.4 and 3.5 where K is the rotor speed at mid span. Note that in equation 3.5, c_p is considered as constant in first approximation in view of the low temperature increase between H25 stage inlet and outlet. The values of the operating point stage loading and flow coefficient are given in Table 3.1 after a normalization with respect to the machine design point conditions. This convention is kept in the rest of this work.

$$\mathrm{K} = 0.5 * (\mathrm{R}_{0in} + \mathrm{R}_{0out}) * \frac{\mathrm{N}n * \Pi}{30} \tag{3.3}$$

$$\phi = \frac{\mathrm{V}_{ax}}{\mathrm{K}} \tag{3.4}$$

$$\psi = \frac{c_p * (\mathrm{T}_{t4} - \mathrm{T}_{t0})}{\mathrm{K}^2} \tag{3.5}$$

3.1.3.3 Main flow experimental means

The instrumentation described in this section was mounted prior to the modifications of the test section to accommodate for cavity flow studies. Thanks to those measurements, baseline data were collected and used as numerical methods boundary conditions, and main channel validation dataset. Details on measurement process and calibration methods are given in the further section on cavity flow specific instrumentation (see Section 3.1.3.5).

3.1.3.3.1 Traversing system

In each measurement plane, automatic radial probe traversing was possible thanks to compact carts equipped with step motors. In Plane 0, one azimuthal position was equipped with such access. In Plane 1, 2, 4, five azimuthal positions were used for radial traversing. In Plane 1 and Plane 2, the probe clocking with respect to the stator blade was similar for the five traverse access (see Figure 3.7).

The back section of the H25 assembly (light green in Figure 3.2) is supported by bearings. A dedicated motor allowed a rotation of the ring over one and a half stator pitch. Plane 4 data were then retrieved in a two dimensional map in both radial and azimuthal direction.

Before any traversing, probe installation were made with a typical safety mechanical margin of 0.02 [mm] between the probe's head and the hub. This value is added to the probe head size in the radial direction and defines the minimal span value that is accessible for each instrument.

Maximal flow cross section blockage induced by a probe is 0.6%. While testing, probes were split in groups to operate them in sequence thus limiting the blockage of the main channel. No probe could find itself in the wake of another. Typical radial traversing grid were performed in less than three minutes. The radial and azimuthal cartography of the outlet section was the most time consuming operation. It could take up to three hours to perform a 950 points map of the flow.

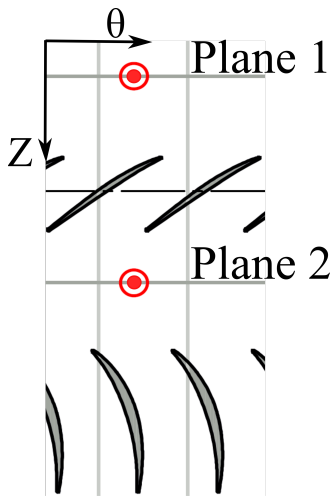

Figure 3.7: Plane 1 and Plane 2 traverse probes clocking (in red) with respect to stator blade.

3.1.3.3.2 Miniaturized total pressure probes and three hole probes

Miniaturized total pressure probes (Kiel) and miniaturized three hole probes were used to retrieve total pressure, Mach number, and flow angle in the main channel. The systematic uncertainty of the employed pressure scanners is the uncertainty item for the miniaturized total pressure probe. In fact, the recovery factor correction for Mach effects is falling within the systematic uncertainty of the transducer.

The three hole probes were angularly calibrated in the VKI - C4 calibration nozzle. The angular calibration consists in determining the Mach and angular dependency of the calibration coefficients through systematic testing. Each of the four employed probes were calibrated for a Mach number range spanning from 0.1 up to 0.5. For each of tested Mach number, the flow angle was varied between ±26° in steps of 2°. In Plane 4 data processing for radial and azimuthal cartography of the flow, since the probe crosses stator wake, holes positions were re-phased to correct for finite dimensions effects within steep gradients (Ligrani et al. (1989)). The fully propagated uncertainty of three hole probe measurements was assessed by considering the transducers systematic uncertainty and the angular calibration uncertainty. The latter was computed considering both, the systematic uncertainty of the transducers employed during the calibration phase and the fitting error for the calibration coefficients. The fitting error results from an estimation of the fitting accuracy weighted by the number of the degrees of freedom (number of calibration points). Further details on the methodology can be found in ASME (2005).

3.1.3.3.3 Miniaturized total temperature probes

The temperature probes presented in Figure 3.8 were designed with a Kiel head of external diameter 1 mm, in which a mineral insulated thermocouple of 0.25 mm in diameter was fitted in a parallel to flow arrangement. Two lateral vent holes of 0.3 mm give a ventilation ratio higher than 5. The same calibration philosophy described in the previous section was applied for the miniaturized total temperature. In order to apply the recovery factor calibration (see Fontaneto and Lahalle (2016)), the Mach number at the probe location must be known. To do so, processing routines automatically process firstly 3hole probes and then total pressure probes as both provide a Mach number distribution over their traversing path. When this is done, the closest pressure probes to the total temperature one was taken and the Mach number distribution was interpolated over the traversing path of the temperature probe. If no pressure probe were present during the same test on the same measurement plane of the temperature probe, then no recovery factor was applied.

Figure 3.8: Miniaturized total temperature probes in Plane 1 and Plane 2.

3.1.3.4 Unsteady measurement techniques

3.1.3.4.1 Fast response pressure probe

The probe used in the present test campaign is the one developed during the FACTOR (Full Aero-thermal Combustor-Turbine interactiOn Research) European project. It is built around a commercial Kulite sensor (XCEL 062-25psia). Probe and associated dimensions are given in Figure 3.9. The probe was used in the stage outlet measurement plane (Plane 4). It is important to note that the shape of the probe's head prevented measurement below 7% of the span. Calibration procedure is similar to the one of fast response Kulite inserts and fast response three hole virtual probe. The calibration is further detailed in the section 3.1.3.5. Typical fully propagated uncertainty level (i.e. taking into account calibration uncertainty (see Dell'Era et al. (2016)) and measurement uncertainty) were in the order of $\delta P = \pm 1.5$ [mbar] for this probe.

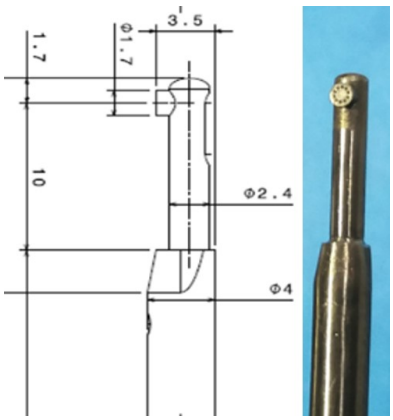

Figure 3.9: Fast response pressure probe used at H25 stage outlet.

3.1.3.4.2 Fast response casing inserts

Fast response pressure sensors were inserted in the casing. These Kulite inserts in the number of thirteen were positioned as presented in Figure 3.10. This feature allows to track the unsteady activity of the rotor tip leakage flow and to investigate pre stall behaviour of the H25 stage. Two additional sensors were present at the same axial location than sensor 1 but at different azimuthal positions around the annulus. The configuration presented above was used in the baseline H25 configuration. In the modified test section, specific to cavity flow analysis, twelve of the fifteen sensors were used for cavity flow investigation as presented in the next section.

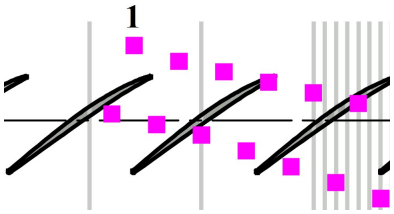

Figure 3.10: Fast response Kulite inserts position in rotor casing - Sensor 1 is duplicated three times around the annulus.

3.1.3.5 Cavity flow specific instrumentation

The modification of the test section and the instrumentation design was possible thanks to the guidelines obtained from preliminary numerical study (see Section3.2.2). The H25 test section was not originally designed to allow axial compressors cavity flow investigations.

With respect to some of the literature cases studied, this presents some limitations. The flexibility for experimental means modification was hindered by the compact size and complexity of the actual experimental facility. Furthermore, the C2 cavity design is presenting geometrical imperfections due to mechanical assembly as well as being used as an instrumentation routing volume for Plane 2 hub static pressure taps. These constraints were taken into account for the experimental setup update.

Nevertheless, the design studied presents some advantages concerning the outcome of the cavity flow experimental campaign. The complex environment described previously has been thought as an opportunity to provide results that contain the impact of: The blades, the rotor platform and pins, the stator sectors, limited labyrinth and platform clearance. The closed cavity configuration has been also a good platform to perform controlled leakage flow analysis thanks to an added injection system (see Section3.1.3.8.2).

3.1.3.5.1 Test section modifications

Cavity wall measurements

The presented setup was designed to retrieve the unsteady activity in the C2 cavity. Turbomachinery assemblies such as the one of H25-C2 produce complex flow regimes. There, the three dimensionality of the flow is such that instabilities propagate in the whole cavity volume. It is therefore easier to retrieve the cavity dynamics while measuring in one location only. However, with this approach it is more difficult to dissociate and identify the origin of the instabilities. In the study of Serre et al. (2001) the idea of the preponderance of the instabilities born in the stator boundary layer (or Bödewadt layer) on the cavity dynamics is mentioned. That is why, the H25-C2 experimental setup update includes measurement at that location.

The C2 cavity wall measurements were ensured by fast response pressure probes. The sensor used were Kulite XCQ-SL-062 pressure transducers. They are piezo-resistive sensors of absolute range 25 [Psi]. The sensors were flush mounted to the cavity wall thanks to special threaded brass inserts as shown by Figure 3.11 and Figure 3.15.

Twelve inserts were distributed at several azimuthal positions indicated on Figure 3.12. The associated test section modifications are presented in Figure 3.13. Table 3.2 gives the angular position retained for each of the Kulite insert as well as the sensor name.

In the modified platform, probe position was defined to allow cross correlation per sensor pair. The spatial discretization was : the interval [5°:15°], covered with steps of 5°; the interval [60°:125°], covered in steps of 5°; [170°, 175°,180°] were covered. Sensor position also produced repeated pairs of equal angular spacing.

The rotor row is constituted of 65 blades, and so 65 platforms. The minimal spatial resolution of 5° was then chosen in order to cover a wide angle range as well as being smaller than one rotor pitch (360/65 = 5.54[°]). Special care has been taken to position the sensor as far as possible from the instrumentation routing pipes (in the number of 10) introduced in Section 2.4 and visible in Figure 3.13.

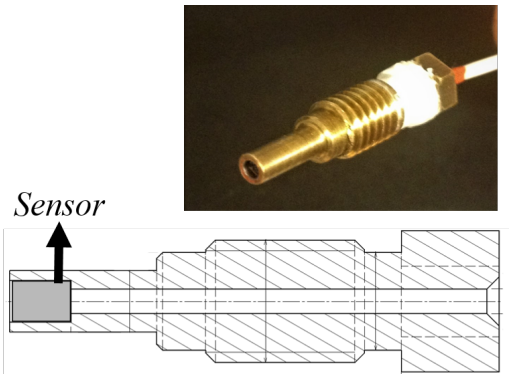

Figure 3.11: Cavity Kulite sensor integration in brass insert.

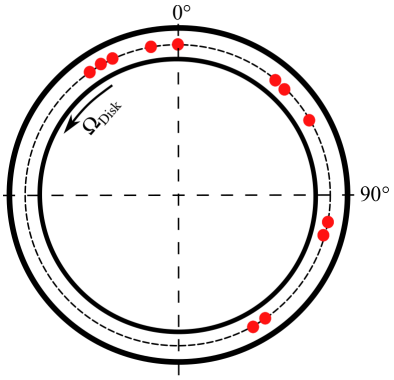

Figure 3.12: Fast response pressure inserts azimuthal positioning in stator hub cavity wall.

Static calibration of the sensors is performed for pressure and temperature. More information are available in appendix A.

The calibration uncertainty computation was performed according to the procedure presented in Dell'Era et al. (2016) and ASME (2005). For the twelve sensors, the maximal average fully propagated uncertainty, i.e. taking into account calibration uncertainty and measurement uncertainty, was of $\delta P = \pm 4.3$ [mbar].

The dynamic response of the insert was evaluated (see appendix A). Probe transfer function and system identification in Figure A.4 indicates a natural frequency of the cavity inserts of 73[kHz] and a non-dimensional damping evaluated from half power of 0.21.

Cavity main volume measurements

The H25 stator platform was also modified to offer radial traversing measurements in the C2 cavity, through the endwall, at three azimuthal positions. The traversed probes used the access in Plane 2. The modification is illustrated in Figure 3.15 in which a probe is maintained in its lowest position in the stator shroud cavity. Cylindrical probes that are designed specifically for the test campaign are used to guarantee platform sealing when the measurement is performed. An example is given in Figure 3.16 in which the probe is traversed through the stator platform and the probe's head is in the C2 cavity.

In order to use directional probes in the cavity, all the traversing carts of the facility in Plane 2 were re-

Figure 3.13: Holes for inserts in the stator platform - Instrumentation routing cable between two sensor sectors.

Table 3.2: Fast response pressure inserts label and corresponding angle in stator hub cavity wall - 0° indicates test section top.

Sensor name	Sensor Angle [°]
FP_{02}	0
FP_{03}	40
FP_{04}	45
FP_{05}	60
FP_{06}	100
FP_{07}	105
FP_{08}	145
FP_{09}	150
FP_{10}	325
FP_{11}	330
FP_{12}	335
FP_{13}	350

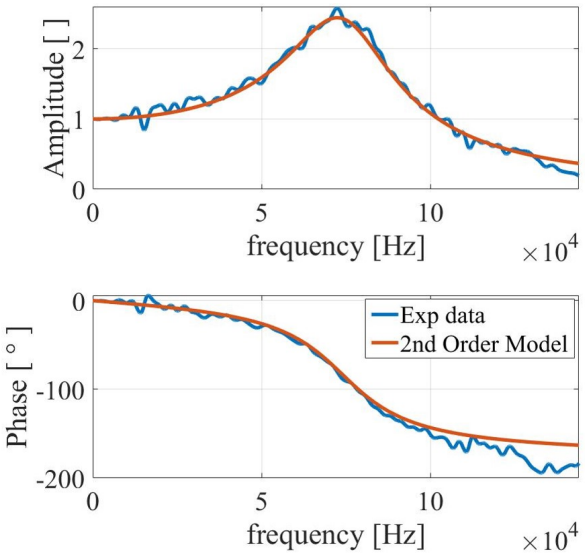

Figure 3.14: Kulite insert transfer function from experimental pressure step data – Second order linear model identification.

designed to allow yaw control of the probes, on top of the existing radial traversing capabilities. The final experimental setup (all planes) was composed of thirteen motors that were tuned and controlled independently.

The cavity instrumentation used both pressure and temperature measurements. Pressure measurements were performed by mean of an unsteady and a steady virtual three hole probes (Dell'Era et al. (2016)). These probes are composed of one measurement hole. The lateral hole measurement (as for a traditional three hole probe) were generated by rotation of the probe along its axis at the desired angle.

The fast response pressure probe was designed around a Kulite XCQ-SL-062 pressure transducer similar to the one used in the wall inserts. The sensor was mounted perpendicular to the flow in the probe stem as illustrated by Figure 3.17a. The miniaturized probe reached an external diameter of 2[mm]. When fully immersed in the cavity (cf. Figure 3.15), the probe occupied 8.5% of the cavity cross section.

The calibration procedure followed the methodology introduced in appendix A. The maximal uncertainty of the pressure measurement was computed at $\delta P = \pm 4.8$ [mbar]. Sensor integration was made to af-

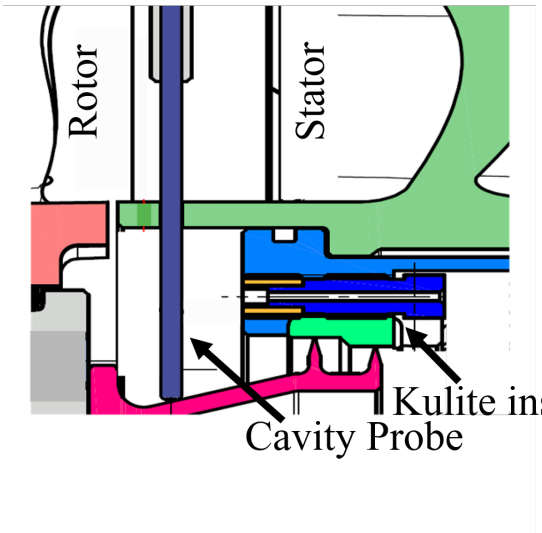

Figure 3.15: Instrumentation layout in C2 cavity - Integration of Kulite inserts in the stator platform - Modification of stator platform to traverse cylindrical probes in C2 main volume (here the probe displayed in its lowest radial position).

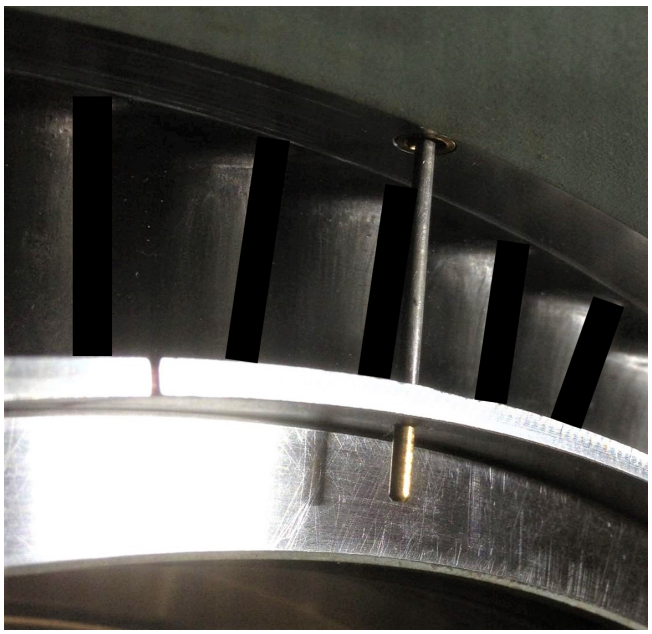

Figure 3.16: Cylindrical probe install in Plane 2, through the stator hub platform.

fect as less as possible the dynamic response of the probe. The line-cavity system presented in Figure 3.17a was designed to maximize the probe frequency response. The reader should refer at Persico et al. (2005) to have an in depth view of the high impact of probe cavity design on one sensor fast response pressure probes.

The design chosen was studied prior to manufacturing thanks to analytical model predictions of the natural frequency. The model used were the model of Hougen et al. (1963) and the model of Bergh, H., and Tijdeman, H (1965). The first one accounts for the compressibility effects that arises from the line volume being comparable with the probe cavity volume. Since the presented probe had a line aspect ratio (line diameter over length) of 0.3 (<1) , the Bergh, H., and Tijdeman, H (1965) model was implemented to model the sinusoidal fluctuations in the line-cavity probe system. In Table 3.3, analytical model results are indicated. The effect of the probe recess is also referenced to indicate the impact that probe manufacturing

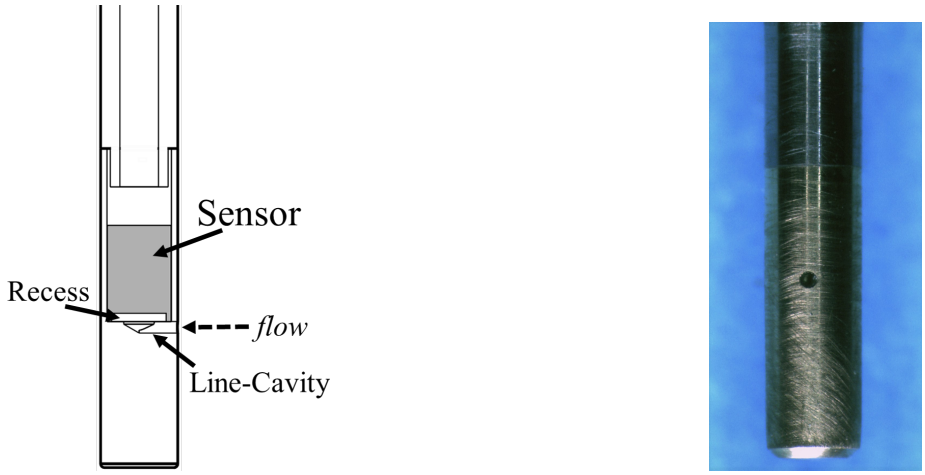

(a) (b)

Figure 3.17: (a) Fast response three-hole virtual probe side cut view sketch - Nomenclature of probe air volumes - (b) Fast response three-hole virtual probe front view used in the experiments.

and assembly could have on the final system response. The target for the design was to guarantee a natural frequency response at zero recess of at least seven times the blade passing frequency (70[kHz]).

Table 3.3: Comparison of analytical model prediction of Hougen et al. (1963) and of Bergh, H., and Tijdeman, H (1965) on three-hole virtual fast response pressure probe natural frequency (Ω_n) – Effect of membrane recess (see Figure 3.17a).

Recess Depth $[mm]$	$\Omega_n - Hougen$ $[kHz]$	$\Omega_n - Bergh$ $[kHz]$
0	77.3	71.5
0.1	44.9	38.8
0.2	34.9	29.5
0.3	29.5	24.8

Once manufactured, the dynamic response of the probe was evaluated. The probe transfer function failed at reproducing results in agreement with the analytical model used for its design. Nevertheless, second order linear model identification is successfully applied to model the obtained transfer function. As presented on Figure 3.18, the evaluated natural frequency of the probe was of 19[kHz].

Probe step response sensitivity to flow angle has been evaluated in a ± 10[°] range without observing changes in the probe transfer function.

The steady pressure measurement consisted in a pneumatic pressure probe whose design was inspired from the aforementioned fast response pressure probe. The pneumatic three-hole virtual probe was connected to a 5[Psi] pressure scanner whose systematic uncertainty was given for 0.08[%] of the full span.

The use of virtual three hole probes allowed flow angle measurements in the cavity. Angular calibration for Mach and Yaw angle was performed thanks to a Dantec Streamline Pro Automatic Directional Calibrator. Originally designed for hot wire calibration, the device has been adapted for the need of directional probe calibration.

For the presented probes, the calibration ranges were the following ones: from M = 0.1 to M = 0.5 by steps of 0.1 for the Mach number; from -80[°] to +80[°] by steps of 2[°] for the yaw angle. Figure 3.19a presents the pressure output obtained for the fast response pressure probe at a Mach number of M = 0.5. The pressure value is maximal when the aerodynamic zero angle was reached between the jet and the probe hole. Pressure increase at angle values far away from zero are caused by the probe hole passing the separation point and entering the probe wake. Around yaw value zero, the probe reading present a flat behaviour. This

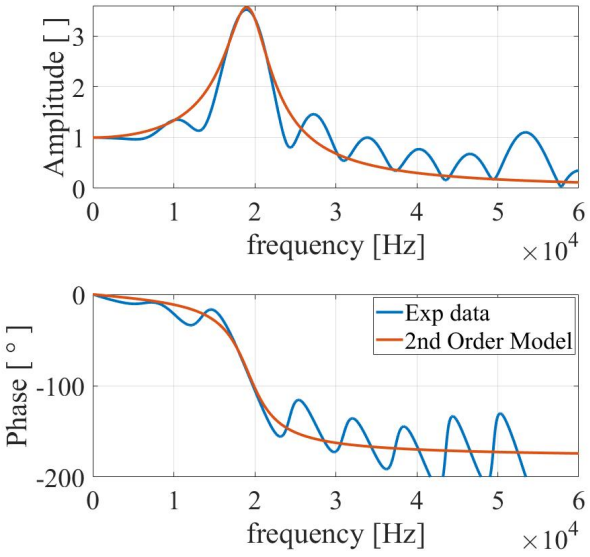

Figure 3.18: Fast response three hole virtual probe transfer function – Second order linear model identification.

traduces a small insensitivity region to the flow angle for the pressure reading. To obtain a better angular discretization, a polynomial fitting is applied to each pressure curve, from M = 0.1 to M = 0.5. The order of the polynomial used was the minimal order of convergence of the residuals between the fitting and the dataset.

In three hole virtual mode, the curve presented in Figure 3.19a was used as the central hole curve. The central hole curve was duplicated and translated in order to generate the voltage output given by virtual left and right holes, for a chosen hole spacing. Figure 3.19b illustrates for Mach 0.5 the output of the left, central, and right holes for a defined hole spacing of 30[°].

Flow quantities from cavity measurements were deduced from calibration data thanks aerodynamic coefficients. The coefficient K_{Yaw}, K_{tot}, and K_{dyn} are defined in equation 3.7, equation 3.8, and equation 3.9 respectively. P_{left}, $P_{central}$, P_{right}, indicates the pressure measured by left, central, and right hole respectively. P_s and P_t are the static and total pressure of the calibration jet. In the experimental campaign these coefficients were used in an iterative procedure on the Mach number (Gaetani and Persico (2020)) to retrieve total pressure, static pressure, and flow angle. The Figure 3.20 presents the aerodynamic coefficients for the three-hole virtual fast response pressure probe for a hole spacing of 30[°]. The coefficients were used following the chart displayed in Figure 3.21, for a given tolerance ϵ on the Mach number.

$$P_{avg} = \frac{P_{left} + P_{right}}{2} \tag{3.6}$$

$$K_{yaw} = \frac{P_{left} - P_{right}}{P_{central} - P_{avg}} \tag{3.7}$$

$$K_{tot} = \frac{P_t - P_{central}}{P_{central} - P_{avg}} \tag{3.8}$$

$$K_{dyn} = \frac{P_s - P_{avg}}{P_t - P_s} \tag{3.9}$$

Temperature measurements were performed in the C2 cavity by means of a K-type thermocouple. The probe is presented in Figure 3.22, the cylindrical probe head is built around the junction. It acts first as a shield to protect the sensor in the traversing process but also isolate it from the highly unsteady environment of the C2 cavity. The temperature probe was connected to the Scanivalve DT3250 temperature scanner mentioned in Section 3.1.3.2.

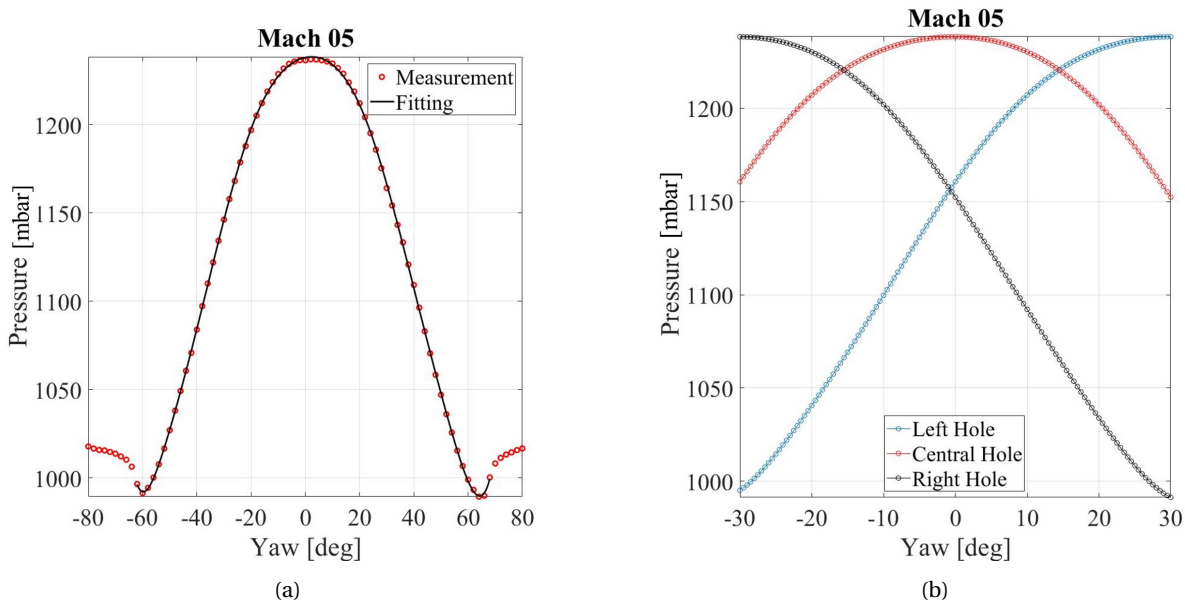

Figure 3.19: (a) Fast response three hole virtual probe pressure reading in calibration jet (red circles) - Mach 0.5 - Twelvth order polynomial fitting (black line) - (b) Fast response three-hole virtual probe left, central, and right hole reading at Mach 0.5.

3.1.3.6 Stator hub inlet boundary layer measurements

To assess the impact of C2 cavity flow on H25 performance and stability, data were collected in the H25-C2 cavity and in the main channel. The first location in which cavity flow effects were expected is the stator inlet hub boundary layer. Access to stator hub boundary was made through Plane 2 where the five available azimuthal locations were used (see Figure 3.23). One of the specificity of the H25 stage has been that rotor-stator axial spacing is large and not representative of real engine assemblies. As a consequence, in Plane 2, stator blade potential effect was limited. In Plane 2 and at design loading operating conditions, the typical average pitchwise hub static pressure non uniformity was of 4[mbar].

The cylindrical probes presented in Section 3.1.3.5 were also used to characterize stator hub boundary layer in three azimuthal positions. The extruded shape of each probe head (see Figure **??**, Figure 3.22a) allowed to perform measurement in the main channel while it ensures sealing of the stator hub platform. The distance from the probe measurement point to the bottom of the probe head was selected to ensure an overlapping with existing traversing data from previous experimental campaign. The overlapping interval ranged between 2% and 12% span. For the three cylindrical probes, the hole diameter being of 0.3[mm], the lowest measured point in the boundary layer stood at 0.6% span. This probe design also allowed to remove the traverse probes from the cavity which offers the possibility to limit measurement intrusiveness.

The remaining two azimuthal positions available for probe traversing were used to perform hot wire anemometry (Figure 3.23). Two single wire, straight sensors with an active length of 1[mm] were used in constant temperature anemometry (CTA). The equivalent circuit of the measurement chain was a Wheatstone bridge in which the sensing element (wire), maintained at a constant temperature, was one leg of the bridge. Temperature change of the wire (so resistance variations) linked the voltage output of the circuit to the convective heat transfer that took place between the wire and the flow. The use of CTA removes thermal inertia on the measurement but fluctuations of the flow temperature can affect the flow velocity estimation. Computed flow turbulence statistics can then be biased by temperature effects. To reduce temperature effects the wire temperature was kept as high as possible within the oxidation limit of the material used. To account for temperature effects in the measurements, non-dimensional calibration approach described in Cukurel et al. (2012) was used. It linked the bridge voltage ouput to the wire Nusselt number (Nu) that was then expressed as a function of Reynolds number (Re) and Mach number of the flow. The calibration was performed using Dantec Streamline Pro Automatic Directional Calibrator. The calibration curves for

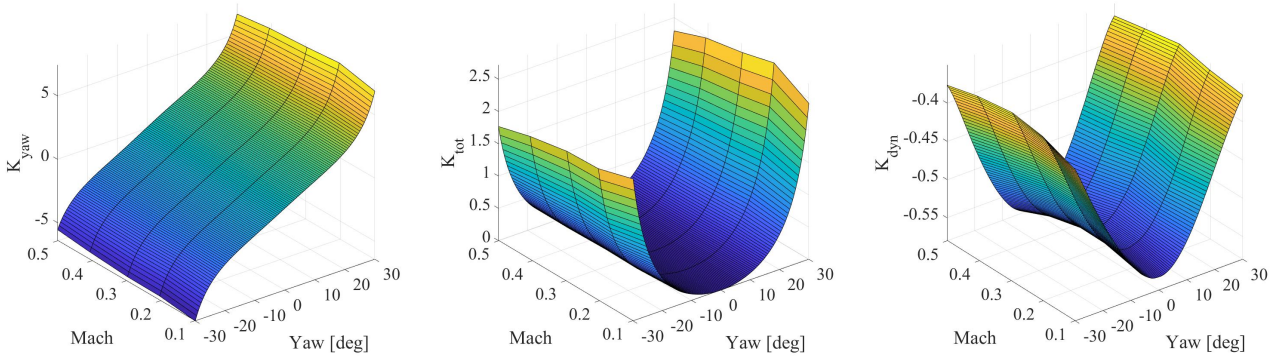

(a) K_{yaw} (b) K_{tot} (c) K_{dyn}

Figure 3.20: Aerodynamic coefficients for fast response pressure probe in three hole virtual mode - Hole spacing of 30[°].

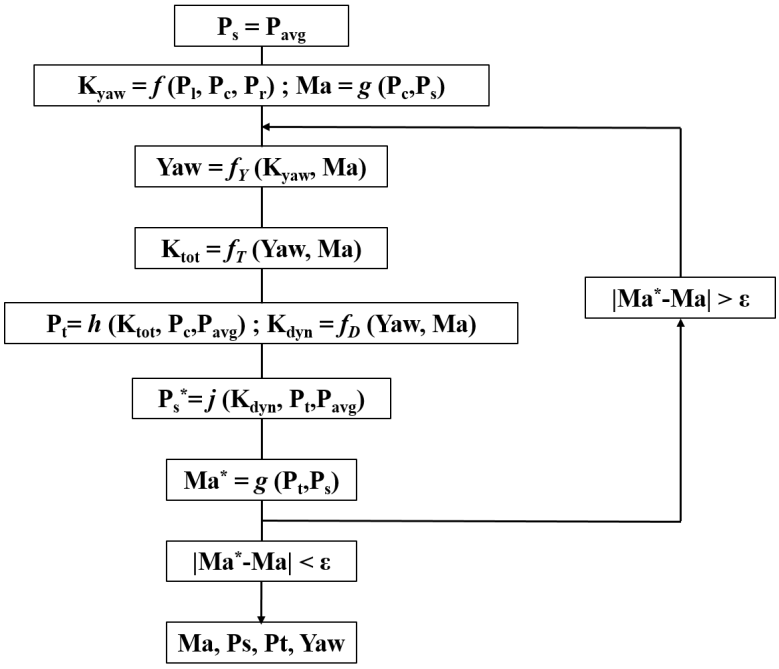

Figure 3.21: Schematic use of left, central, and right hole measurement along with aerodynamic coefficient for three hole probe post processing - Computation of Mach number, static pressure, total pressure, and flow angle.

different jet temperatures and Mach numbers (from M = 0.1 to M = 0.55) at reference angular position are presented in Figure 3.24. In the (Re,Nu) system, all the curves collapse on one fitting line. With the non-dimensional approach, the calibration was performed in the operational Reynolds number range. To use the fitting from the calibration, total temperature and total pressure of the flow as well as static pressure and wire voltage must be recorded in the experimental campaign. These variables allowed to retrieve local Nusselt and Reynolds number.

To deduce flow angle information from the hot wire measurement, an angular calibration was performed. The probe was calibrated for the angle in a range of ± 80[°]. The angular calibration map was created such as the wire can be used as a virtual two wire probe. The effective Reynolds number is the one driving the heat exchange at a fixed sensor angle with respect to the main flow direction. It is a combination of the normal and tangential Reynolds numbers to the sensor itself. Figure 3.25a indicates the angular dependency of effective Reynolds number for virtual wires at ± 30[°] from the reference angle direction. Respectively, Re_{eff1} and Re_{eff2} are the effective Reynolds number for each angular direction. The ratio

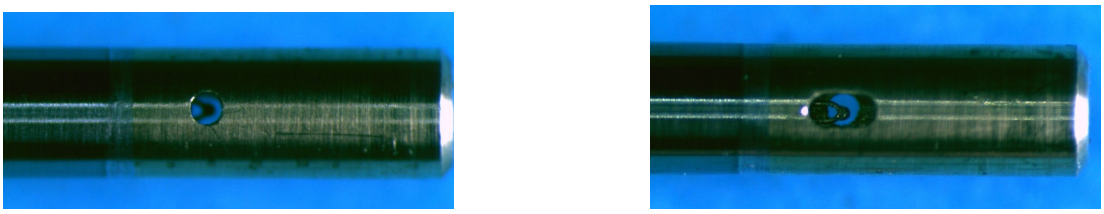

(a) (b)

Figure 3.22: Ventilated Temperature probe for cavity flow investigation - (a) Front View - (b) Back view.

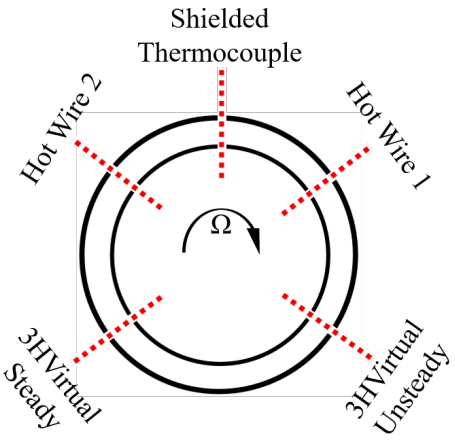

Figure 3.23: Experimental Plane 2 traversing probe disposition around H25 test section annulus.

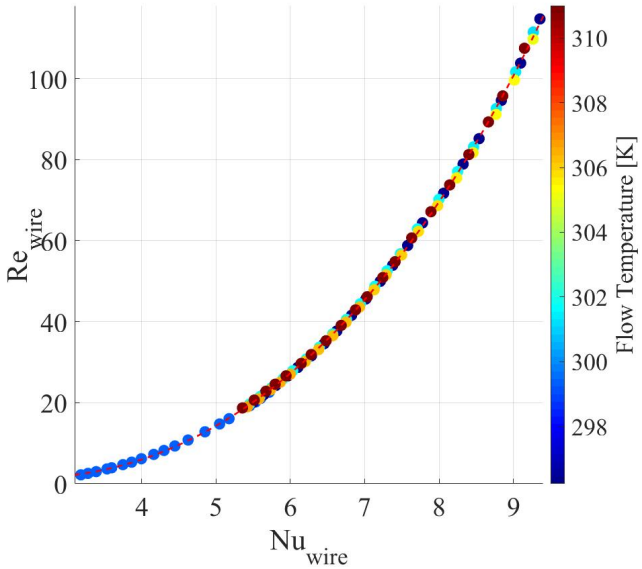

Figure 3.24: Nu-Re calibration for hot wire – Flow temperature and Mach number dependency – Temperature effects.

Re_{eff1}/Re_{eff2} is plotted on Figure 3.25b and allows to retrieve the flow angle from the experimental data independently from the Mach number. Figure 3.26 shows a schematic diagram that presents how flow angle α and velocity components were computed.

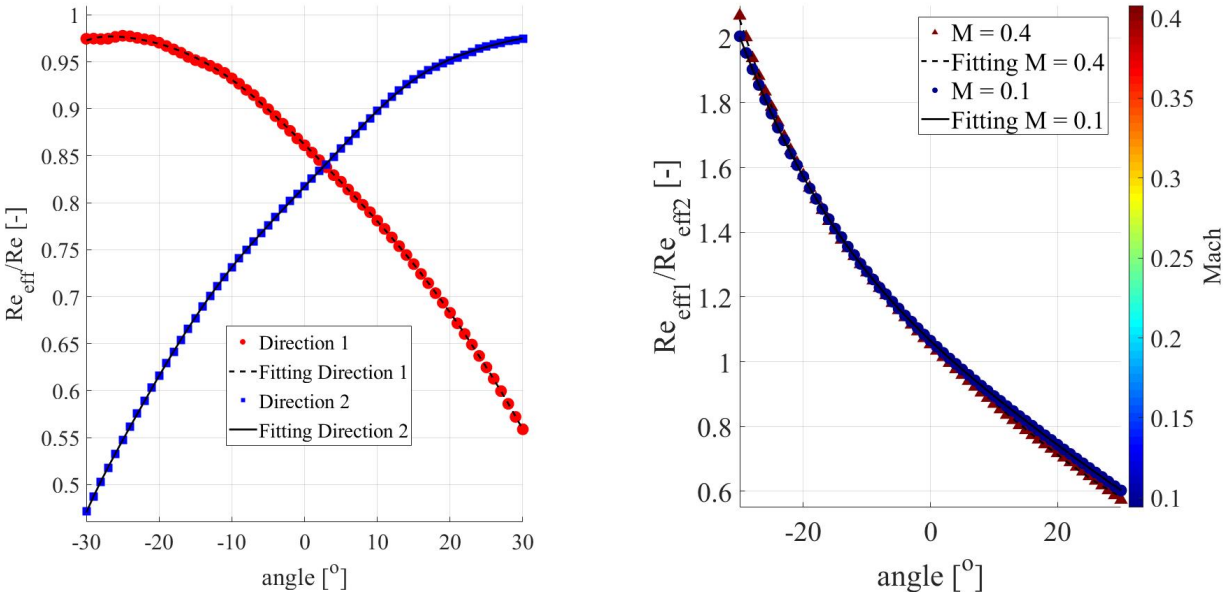

Figure 3.25: (a) Angular calibration for virtual two sensors hot wire probe with angular clocking of 30[°] – Effective Reynolds number at Mach = 0.4 - (b) Angular calibration for virtual two sensors hot wire probe with angular clocking of 30[°] – Effective Reynolds number at Mach = 0.4.

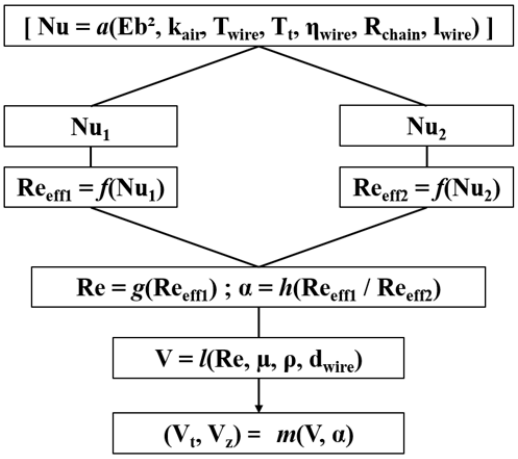

Figure 3.26: Use of hot wire data voltage (Eb) in the direction 1 and 2 with calibration data fittings to obtain flow angle α and tangential and axial velocity components respectively Vt and Vz.

3.1.3.7 Strategy for instrumentation use

3.1.3.7.1 Use of instrumentation in space

Prior to describe how the probes were used in space, probes limits are indicated. The span value for the radial coordinate was defined based on the main channel height. Span = 0 indicates the hub line, Span = 1 indicates the casing line in the investigated plane. This convention is kept in the cavity. Typically, the cavity volume extended radially between Span = 0 and Span = -0.96. In Plane 2, for the probe immersed in the cavity, the span range covered was from -0.12 (below the hub platform) to -0.76 (limited by the probe head shape). For the same probes, the span range in the main channel lied between 0 and 0.12.

Since the flow in the cavity is rotating due to the rotor disk action, the main flow direction and cavity flow direction differ on average. Figure 3.27 indicates the references direction and the sign for the main flow and the cavity flow. Note that the directions for the probes motor angles are opposite to that convention.

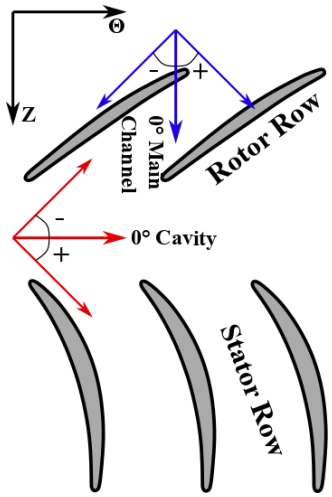

Figure 3.27: Reference angle direction and sign for the main flow (Blue) and the cavity flow(Red).

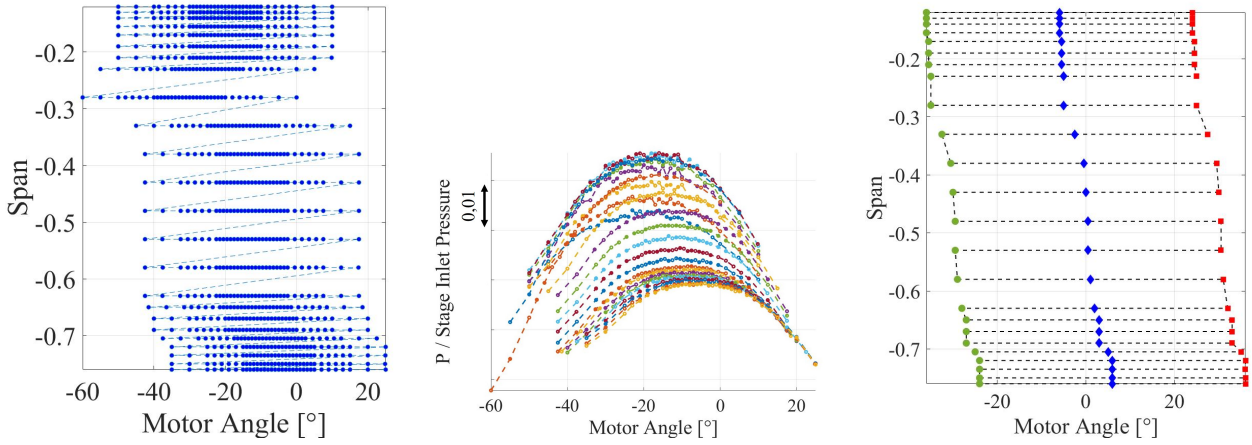

(a) (b) (c)

Figure 3.28: (a) Pitch/Yaw traverse grid for virtual probe average flow angle search mode - (b) Pressure reading obtained from search mode. One line corresponds to one span position of the probe - (c) Final traverse grid for three hole virtual probe in cavity measurements - Probes path: dashed line - Left hole: circle - Central hole: diamond - Right hole: square.

This section describes how the directional probes were used. As already mentioned, in virtual mode, a probe was maintained at a fixed span and multiple points were sampled for different yaw angle of the probe (ex : 3 points - left, central, and right if a three hole virtual probe was used).

To ensure that in virtual mode, the data collected fitted in the calibration range, probes had their central hole aligned with the average direction of the flow. In the cavity, the a priori unknown and complex flow organisation imposed to map for each operating condition the pressure field at every span position. The operation here called "search mode" was made for both steady and unsteady pressure probes. To illustrate how the search mode was used, an example is given for the steady three hole virtual pressure probe at H25 design loading operating condition.

A Span / Yaw traverse grid for the probe was defined and presented in Figure 3.28a. The pressure reading obtained at every span position is displayed in Figure 3.28b. Another advantage to the search mode was to inform on the mechanical offset between the different instruments. This allowed the comparison between absolute flow angles measured from different probes with minimal absolute referencing errors.

The maximal pressure at each span locates the average flow angle direction. Fitting was applied to the pressure curves obtained in order to smooth the behaviour at low probe to flow incidence to ease maxima detection. In the final measurement the traverse grid was designed to align all the probe central hole with

the angle corresponding the pressure maxima at each span position. In the example, the final traverse grid is indicated in Figure 3.28c which displays the probe path in a traverse procedure as well as the position of the left, central, and right holes of the probe.

The data collected in the search mode helped verify that the pitch angle effect is limited in the cavity. Under this assumption, the probe calibration has been made only to correct for the yaw angle (see example in Figure 3.20). Figure 3.29 compares for different span position in the cavity, the pressure measured in the search mode against the calibration data in the corresponding Mach number range. If pitch angle effects were important, the search mode curves would significantly depart from the calibration curve. The present data do not show such behaviour.

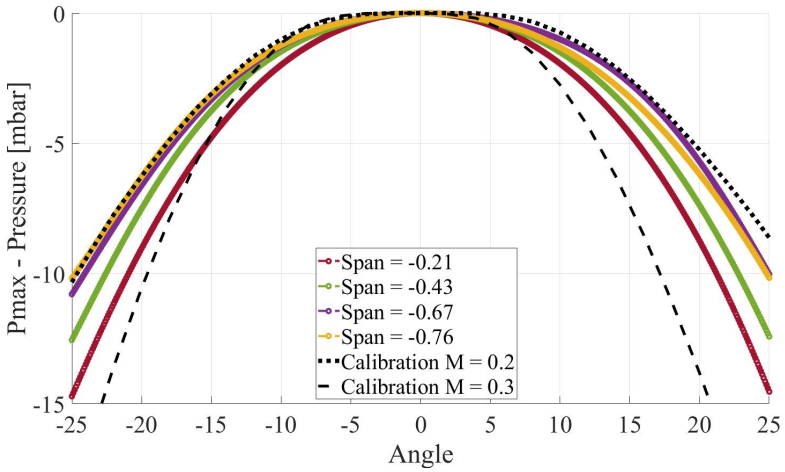

Figure 3.29: Search mode pressure angular sweep compared with angular calibration data in the Mach number range 0.2; 0.3 - Multiple span positions are indicated in the cavity.

With the new traverse grid defined, the central hole approached as much as possible the average flow angle. Using the search mode data it was possible to evaluate the sensitivity of the measured flow quantities to two parameters that were: 1- The central hole alignment with the average flow angle direction; 2- The angular spacing of the lateral holes in virtual mode. The effect of the central hole alignment with the flow is presented in Figure 3.30. The hole spacing was kept constant with a value of 20[°]. The variable plotted is the flow angle. Three curves are presented. The first one, is the flow angle corresponding to the pressure maxima in the search mode, at each span. The second plot gives the flow angle computed thanks to the probe calibration if the pressure for the central hole is taken as the maximal pressure from the search mode at each span. The last plot gives the flow angle if the central hole pressure is the pressure 10[°] off from the maximal pressure. The differences due to the different alignments remain on average below 1[°]. With an offset of 10[°] on the central hole, the flow angle evaluation is also more precise due to an increased sensitivity of the probe to the yaw angle (refer to Figure 3.19b). The other fields (Pressure, Mach, Temperature) were not presenting a sensitivity to the offset. Nevertheless, it was decided to keep the probes aligned with the average flow angle not to fall out of the calibration range during the acquisition, especially for the time resolved analysis.

The effect of the probe lateral hole spacing was studied on the same dataset as presented before. The central hole was taken as the middle point of each pressure bell in Figure3.28b. Figure 3.31 summarizes the sensitivity of the measurement to the holes spacing for the flow angle, Mach number, and total pressure. A hole spacing of 10[°] indicates that the virtual left and right holes were positioned at $\pm$ 10[°] from the central hole. The measurement highlight some differences that in absolute terms are on average of 2[°] for the angle, 0.015 for the Mach number and of $8 * 10^{-6}$ for the pressure ratio. To maximize the measurement range, a holes spacing of 30[°] was selected in the test campaign.

The definition of the traversing grids thanks to the search mode was made in the cavity and in the main channel, prior to the start of the test matrix. If between operating conditions the average flow angle direction do not present major changes, the traversing grids were kept identical.

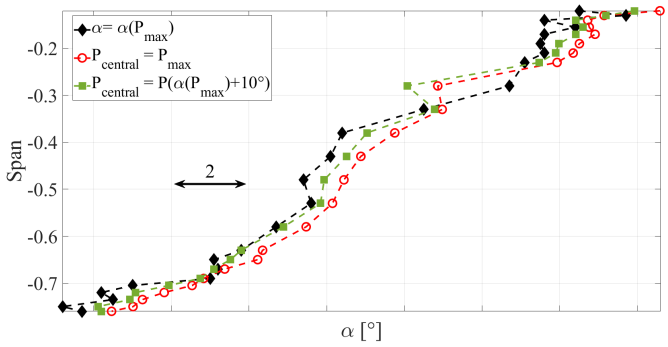

Figure 3.30: Flow angle - Position of central hole sensitivity with respect to flow direction - Flow angle reference with flow angle defined as the angle of maximal pressure in the search mode bells (see Figure3.28b)(black - diamond) - Flow angle from calibration with central hole in average flow direction (red - circle) - Flow angle from calibration with central hole in average flow direction plus ten degrees (green - square). Constant lateral hole spacing of 20[°] is used.

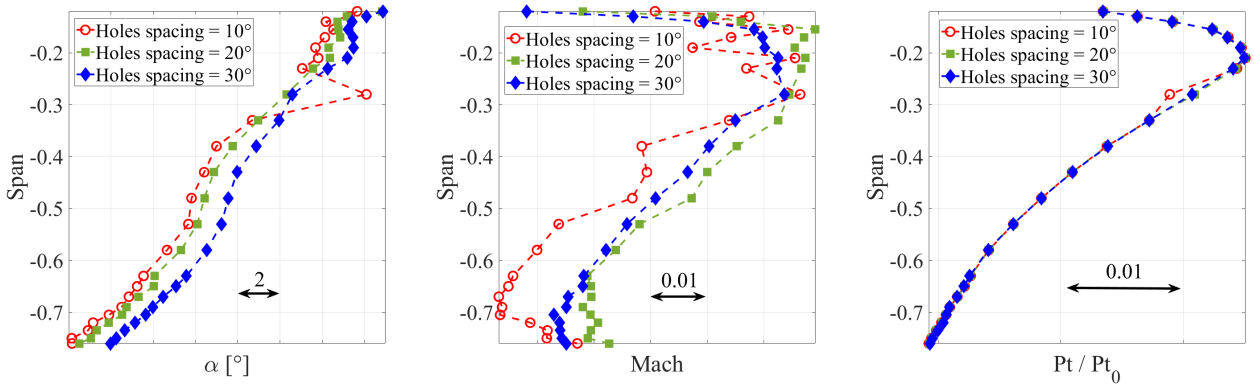

Figure 3.31: Effect of the probe lateral hole spacing in three hole virtual mode for cavity measurement - (a) Flow angle - (b) Mach number - (c) Total pressure ratio.

The use of multi hole probes in an environment such as the C2 cavity can be criticised on a few points. First, discussion can be set about wall proximity. The probe's virtual holes were positioned at a constant radius. However, central and lateral holes did not belong to the same plane with respect to the probe symmetry axis. As a consequence, the lateral and central holes were not at the same radial distance from the cavity endwalls, that are curved surfaces (same for main channel endwall). With a probe traversed in Plane 2, and at fixed span, the radial distance difference between an hole aligned with the flow and a lateral hole orthogonal to it was of 0.1[µm] with respect to the cavity bottom wall. For all the probes, this value was considered negligible in front of the measuring hole dimensions. At every span position, left and right holes were also effectively closer to the cavity lateral walls than the central hole. On average, with a hole spacing of 30[°], in a meridional view, the distance between the left and right hole represented 6% of the cavity width. A consequence of this shift was that in the case of a flow feature causing a strong pressure gradient at fixed radius, the measurement quality was affected by the relative position between the virtual holes and the flow feature.

3.1.3.7.2 Use of instrumentation in time

This section describes, using examples, the approach and post processing used for time resolved measurements. The different means of experiments put in place were used to ease an interpretation of the flow field. The expertise prior to the measurement campaign concerning compressor cavity flow in a realistic environment was limited. For that reason, a step by step increase complexity of the post treatment performed

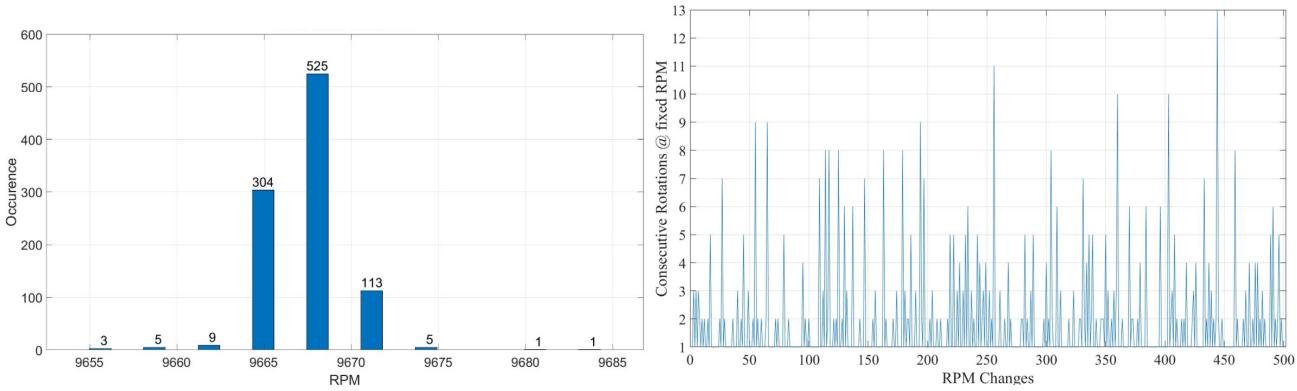

(a) (b)

Figure 3.32: RPM instability of H25 test section (a) Histogram of RPM occurrence during time resolved acquisition - (b) Change of RPM and number of consecutive rotations at same RPM during a typical acquisition.

allowed to access more and more information on the C2 flow field and its interaction with the main stream.

RPM fluctuations

Each collected time series contained a define number of disk rotations. If signals were acquired simultaneously, the rotor phase with respect to each acquired point was identical. However, to compare result from time series recorded at a different time (other spacial location, different testing condition, same condition but different day,...) rephasing of the signals with respect to the disk position was mandatory. The trigger from the test section phonic wheel was used at such extent to phase each test based on a known rotor position. During the acquisition, the rotor speed was fluctuating, even at fixed requested RPM. This was mainly due to the PID control of the motor that powers the compressor. As the information for the rotational speed was only detected once per rotation (1 notch on the phonic wheel), RPM changes were also happening in one rotation but could not be measured. Figure 3.32a indicates the histogram of measured rotation speed for a typical time resolved acquisition. Preferential rotational speed is highlighted. However, the consecutive RPM change, rotation after rotation that are illustrated by Figure 3.32b, required a treatment to analyse the full test. To phase each point in the time series with respect to the disk, data were interpolated along a defined grid for each rotation. The angular displacement of the disk between each point in the time series was then constant. The interpolated signal is superimposed over the original signal in Figure 3.33 for a time series acquired in the C2 cavity. The grid chosen for the interpolation was containing 4000 points in one disk revolution. In other words, the maximal frequency covered was of 4000 EO (Engine Order).

The change of disk rotation speed has been critical for the analysis of rotor stator cavity flows. As visible in the literature (c.f. Chapter 2), flow field organization is highly dependent upon the rotating Reynolds number. Speed up and speed down tests on academic cases show how much the flow field is sensitive to disc acceleration/deceleration phase. It is possible that the RPM fluctuations observed in the H25 facility modulated the flow field and especially flow structures that are non synchronous with the disc rotation. It is yet difficult to estimate the pollution in the measurement that arose from the RPM fluctuation, and evaluated if they were destructive for cavity coherent flow structures. It is still unclear how to include the role of the RPM fluctuations in the results interpretation given in Chapter 4.

Averaging procedure

The analysis of the instabilities in the H25-C2 configuration aimed to identify the phenomena that were clocked with the rotor disc, and flow structures that were non synchronous with the latter. To retrieve non synchronous instabilities, the signal ensemble average (called EA) was systematically computed. The computation of the EA was straightforward since all of the rotations are interpolated on the same grid. The EA was computed for a length set as a finite number of rotations (one rotation, five rotations,...). The EA

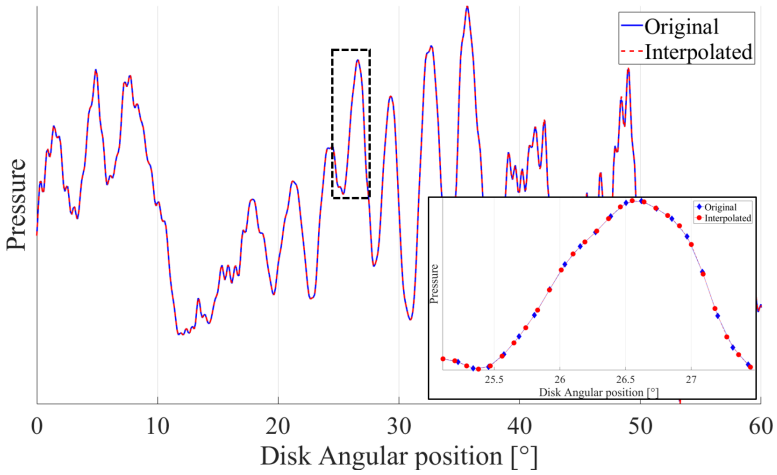

Figure 3.33: Example of original and interpolated pressure signal measured by the three hole virtual probe in the C2 cavity as a function of rotor disk angle.

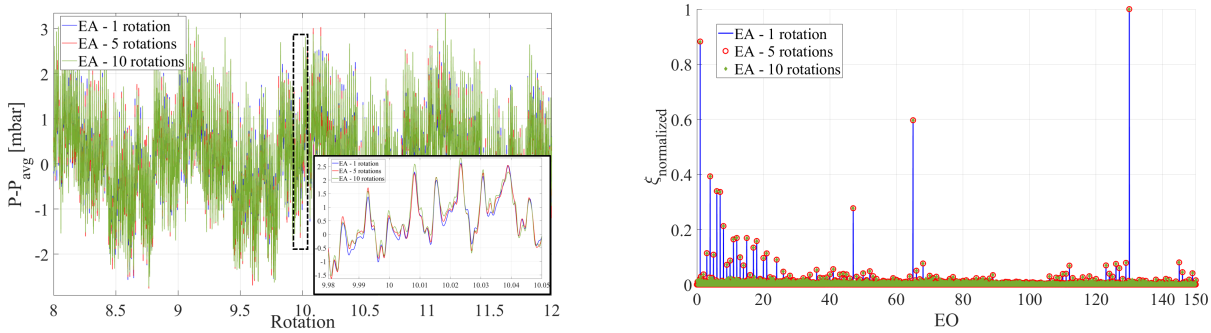

(a) (b)

Figure 3.34: Ensemble average sensitivity to number of rotations (a) Time series of ensemble average for averaging length of one rotation (blue), five rotations (red), ten rotations (green) - (b) Corresponding signal in the frequency domain with normalized energy content. ensemble average of size one rotation (blue) five rotations (red circles) and ten rotations (green diamonds).

spectral content was analysed in regard of the EA length in terms of rotations. For the different EA series generated, the root EA was duplicated to match the spectral resolution between the cases. The signal used as an example was extracted from one of the Kulite brass insert in the C2 cavity at design operating conditions, without imposed leakage. In Figure 3.34a, the EA based on one, five and ten rotor disk rotations are presented. It is noticeable how the time signal evolves with the size of the EA window. However, as suggested by Figure 3.34b, the spectral content based on normalized energy is independent from the number of rotations in the ensemble average.

The EA average do present the content of all the disc synchronous instabilities. Around the EA, temporal fluctuations (T_f) are present. Hence the analysis of non synchronous instabilities was made for the T_f component of the time series recorded. It was also verified that the spectra of these fluctuations remain insensitive to the EA window length. In the rest of this work, the window length for the ensemble average have been set at one rotation.

In order to have a better reading of the data, the signals spectral content (for EA and T_f) were extracted using Welch (1967) method's. This method is based on spectral averaging of the original signal cut in windows of same size. The number of windows (and so the length of the window) for each signal was defined as a compromise between stability and spectral resolution. A good compromise is to take a window length of $\sqrt{N}$ for a time series with N elements. Once the window length was defined (in terms of rotation), equation 3.10 and 3.11 indicates how are computed the actual number of windows length N_{window} based on the

requested number of rotations per window N_{rot} and the size of the overlapping regions between windows. To perform the computation, the length of one rotation L_{1rot} (in points) must be known.

$$N_{window} = log2(N_{rot} * L_{1rot}) \tag{3.10}$$

$$Overlap = 2^{N_{window}} * 0.5 \tag{3.11}$$

With the acquisition times set, the compromise window length discussed previously was too small (between 0.4 and 0.6 rotation). Parametric analysis on the window size was performed to evaluate the best compromise for the H25-C2 flow analysis. The dataset was the same than the one previously used. Ensemble average was removed to analyse the effect on the temporal fluctuations only. Figure 3.35 presents the signal normalized energy in the frequency domain for different window length in Welch's method. The bigger the window, the better the frequency resolution. Nevertheless, with a reduced window, peak detection in the signal is still easy. Local peak to noise ratio remain consistent independently of the window length for frequencies higher than 2 EO. Relative peak amplitude is also consistent between each series. As an example, between the peaks at 16.6 EO and 40.04 EO, the peak amplitude ratio is of 1.80, 1.81, 1.86, 1.84 for respectively one rotation, five rotations, ten rotations, and fifty rotations. Since the interest of the temporal fluctuations analysis was to detect regions (bumps of instabilities) of interest where the spectra could be sampled, a compromise has been taken with $L_{window} = 10$.

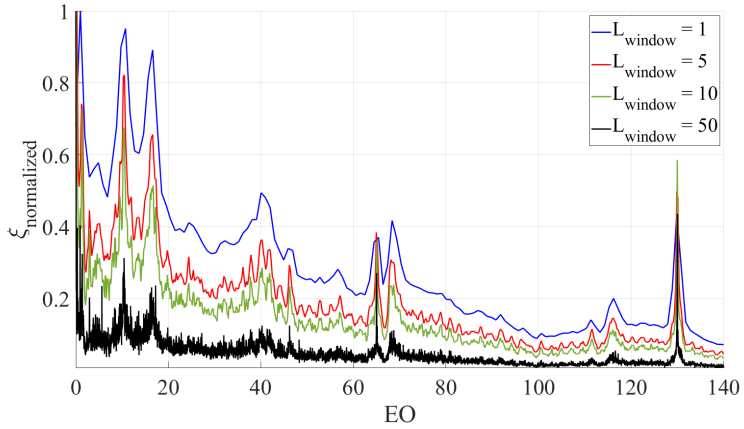

Figure 3.35: Welch's method applied on Kulite brass insert temporal fluctuations T_f - Effect of the window size L_{window} for the same total signal length.

When the analysis of the spectral content in time was done thanks to spectrograms, Welch's method was also used. In that case, the original signal was first cut in packs that contained a defined number of rotations called "trains". For each of this train, Welch's method was applied on a defined number of rotations, that was of course smaller than the train length. The train length and number of rotations used to generate the average spectra were defined to balance temporal and spectral resolution. The already used dataset was taken to show in Figure 3.36, as an example, the spectrogram for one of the Kulite sensor for an acquisition over 960 rotations.

Use of multi hole virtual probes

In the test campaign, multi hole virtual probes were used. Flow field measurement of this kind was used both in the cavity and in the main channel. The virtual mode was also used for the hot wires that investigated the H25 stator inlet boundary layer. The time resolved instrumentation was partly used to detect the spectral content at the probed location and to derive the average flow field. Three hole virtual probe signal from C2 cavity measurement in design operating conditions and no leakage is used as an example. The dataset is composed of three independent time series, i.e. sampled at different time, that corresponds to the left,

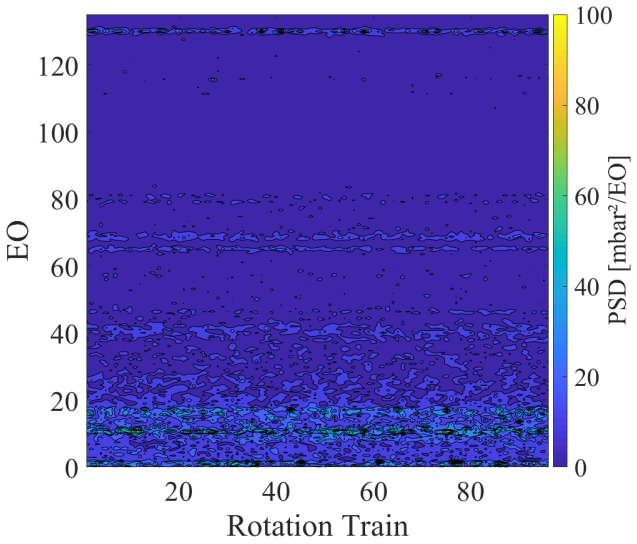

Figure 3.36: Spectrogram for trains of 10 rotations and Welch's method window length of 2 rotations.

central, and right hole of the virtual probe. Probe transfer function was applied to the signals independently. To extract the time resolved flow quantities from the measurement, these time series were phased with respect to the rotor disk. Aerodynamic flow angle time series, with respect to probe central hole, series is presented in Figure 3.37. Apparent peaks at +30° and -30° are identified. These values are the limiting values of the angular calibration range. In other words, points at ± 30° are out of calibration. The peaks are preceded by a smooth deviation from the mean value as visible in the zoomed window. It is not a random sharp peak. The reader should note that this behaviour was also found for the same probe while measuring in the stator hub boundary layer. It was also visible on the hot wire measurement at that location.

Two scenarios are possible to explain such behaviour. The first one is that there are effectively flow structure that present absolute flow angles out of the chosen calibration range. The second scenario is that the phasing of the time series with respect to the rotor disk only causes rotor non-synchronous flow structures to pollute the output signal for the flow angle. The value of the flow angle depends of the coefficients K_{Yaw} and K_{tot} (c.f. equations 3.7 and 3.8). With a bad phasing of non-synchronous flow structures, these coefficients deliver values out of the calibration range, which results in signal pollution. This signal pollution is not periodic. Different methods were tested to correct the signal without success. As an example, no major improvement in the flow angle signal has been visible after phasing the probe holes time series based on correlation of the most energetic frequency bands.

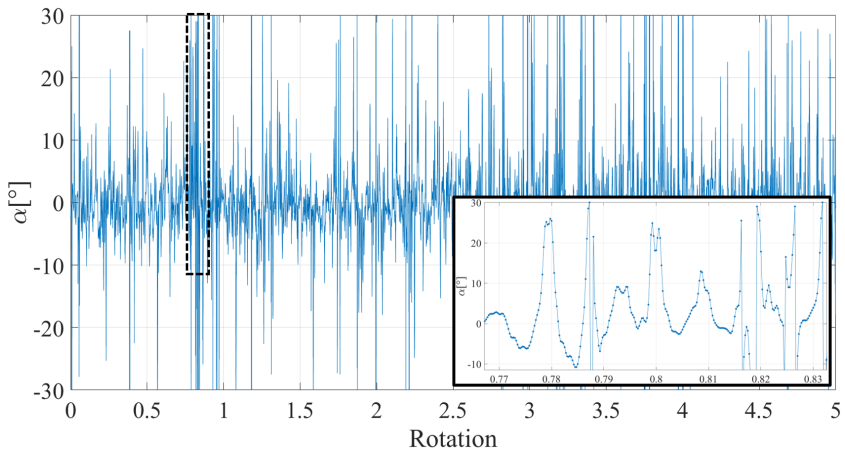

Figure 3.37: Time resolved aerodynamic flow angle at -43% span in the C2 cavity - Design loading, no leakage.

To evaluate the impact of the out of calibration points on the average flow field, the histogram for the aerodynamic flow angle and the total pressure are presented in Figure 3.38a and Figure 3.38b. On the flow angle distribution, the outliers are clear at 30° and -30°. For the total pressure, the effect of such outliers is to skew the distribution. As visible in Figure 3.20a and 3.20b for the aerodynamic coefficients, two opposite values of K_{Yaw} (so opposite flow angle signs), give a similar value for K_{tot}.

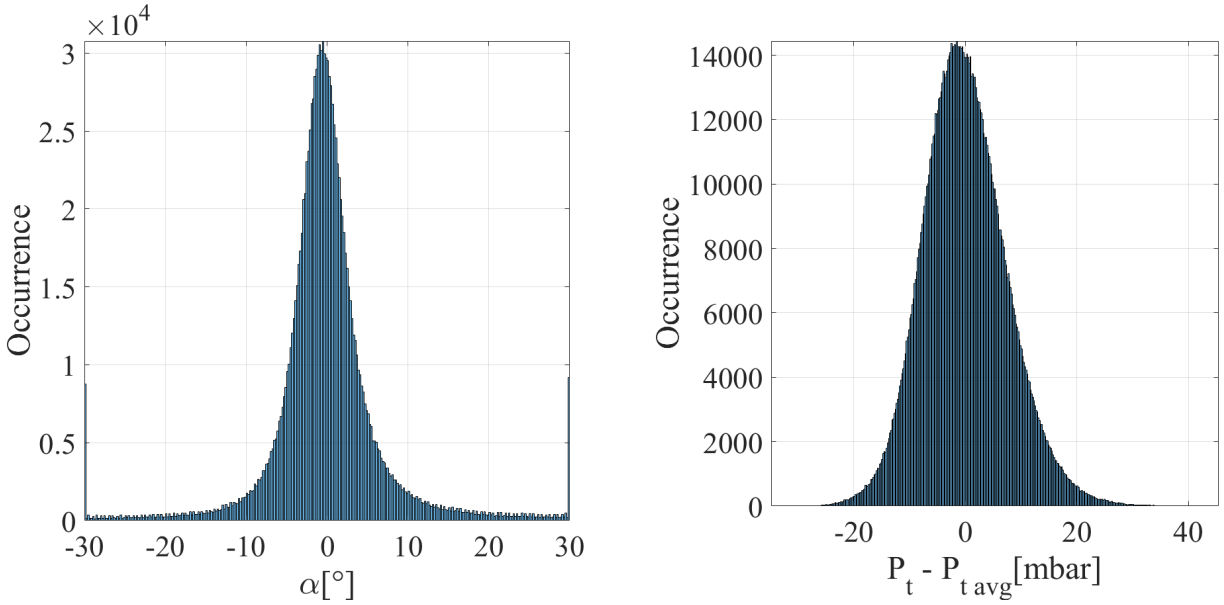

(a) (b)

Figure 3.38: Histogram of 300 rotor rotations for three hole virtual probe time resolved measurement at -43% span in the C2 cavity. Design loading, no leakage. (a) Aerodynamic flow angle - (b) Total pressure minus mean total pressure.

In order to choose the most reliable value to represent the average flow field from time resolved measurements, while ensuring quick processing of the database, the average procedure was evaluated for the flow gradients in the C2 cavity. The application of the angular calibration was time consuming for big time series where the scheme presented in Figure 3.21 is applied for each point. The number of operations to cover the whole database was then multiplied by the number of spanwise positions, and then by the number of operating conditions to analyse. Results for the total pressure and the absolute flow angle are presented in Figure 3.39a and Figure 3.39b respectively. These plots present: the profiles obtained after averaging the full pressure and angle signal, i.e. for all the rotations - two profiles of the mean of the EA signal over one and ten rotations - one profile where the angular calibration has been applied on the mean voltage outputs Vp and Vs from the measured time series. For each profile, the interval [-2σ:+2σ] is given where σ is the standard deviation of the time series. It is noticeable that this interval is reduced at lower span for the full time series (in blue rounds). When the time series used for the evaluation of the flow quantities is reduced to the ensemble average, the [-2σ:+2σ] is narrower. Differences in the mean value are identified, for both flow quantities depending on the type of mean. However, these differences remain below the sensor systematic uncertainty. To achieve low computation costs of the means profile, the mean value chosen for each spanwise position is the mean value from the ensemble average over one rotation.

Hot wire and offsets

Hot wires were used in Plane 2 boundary layer. These measurements have been subjected to offset drift during the test campaign. This paragraph details how the results obtained were used in order to compensate for the offset generated. Checks were also performed to evaluate the sensitivity of the measuring device to the operating conditions. The radial traversing grid of the hot wires covered the span interval [1%:60%]. The other traverse probes in Plane 2 were limited to 12% span due to the probe design. To get a comparison on

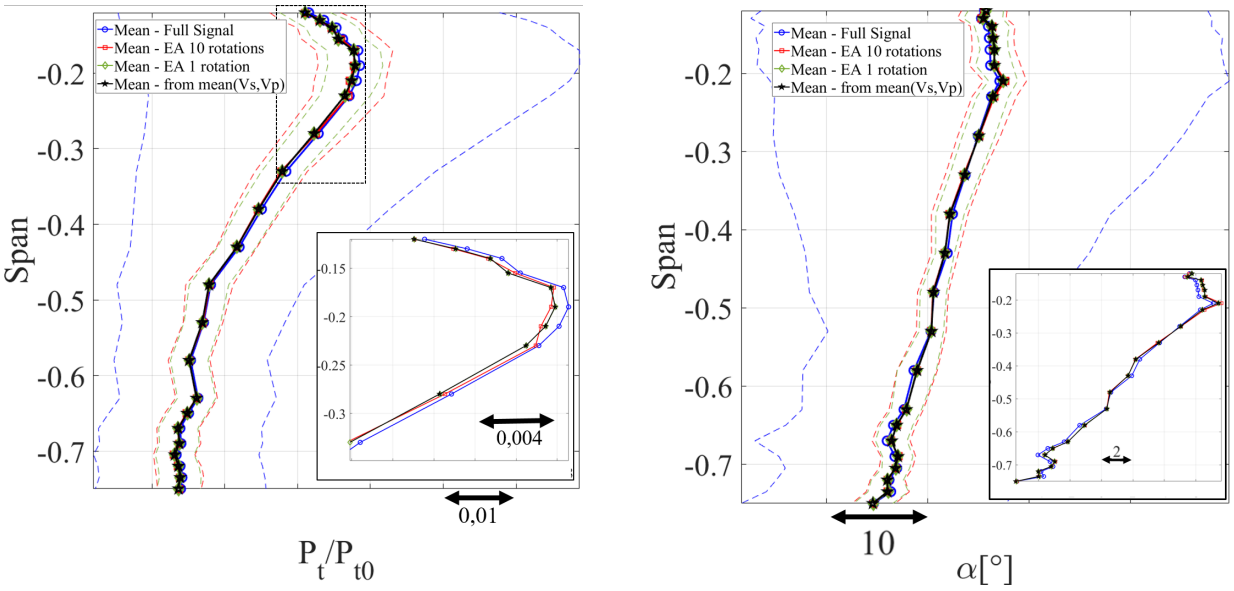

(a) (b)

Figure 3.39: Comparison of time averaged value for three hole virtual probe flow gradients in the C2 cavity - Design loading, no leakage - Area between the dashed lines indicates for each profile the 95% confidence interval - (a) Total pressure ratio - (b) Absolute flow angle.

the whole hot wire span range, numerical data (c.f. Section 3.2) were used. Velocity magnitude and absolute flow angle are compared in Figure 3.40a and 3.40b respectively. There is a big offset on the velocity profile in the amount of 25[m/s]. The absolute flow angle is consistent with the numerical result prediction giving less that 2.5[°] difference at midspan and do present a similar gradient. This gives confidence in the use of the angular calibration, i.e. the offset is constant and only present on the velocity profile.

The sensitivity to the operating point was evaluated at nominal rotation speed between the design loading and the near stall operating point. Figure 3.41a and 3.41b present the time averaged velocity profile and absolute flow angle. The velocity profile clearly indicates the velocity magnitude reduction between design and near stall. This is expected since an increase in loading is followed by a decrease in compressor mass flow. The incidence increase on the flow angle profile is also detected by the wire. The incidence increase on the stator is of four degrees at midspan between the two operating conditions. Figure 3.41c and Figure 3.41d show the sensitivity of the measurement to the leakage injection in the C2 cavity for the design loading operating point. The velocity low span blockage induced by the injection is captured by the hot wire. The midspan velocity magnitude remains similar with and without injection. Concerning the absolute flow angle, incidence increase is noticeable below 20% span.

The sensitivity of the hot wire measurement gave confidence in the use of the data collected. However, to compensate for the velocity magnitude offset when compared to numerical data, the profiles were plotted with respect to the midspan velocity magnitude.

Probe intrusiveness effect on unsteady data

Considering the dimensions of the traversed probes with respect to the cavity cross section area, the probe effect on the time resolved data required attention. In the first place, it was difficult to estimate the effect of the traverse probe on its own measurement. The effect of the probe would mainly induce flow structure disturbances upstream of the probe due to potential effect, and downstream due to wake generation. From the dimensions of the cylindrical probes used, the frequency of the wake at design operating conditions was estimated to be of 60 EO, using Strouhal number, which is similar to the one of the pressure tube routing pipes mentioned in Chapter 2 section 2.4. The interactions between the probe and the disk wall boundary layers were unknown. However, when an acquisition of the unsteady activity by means of

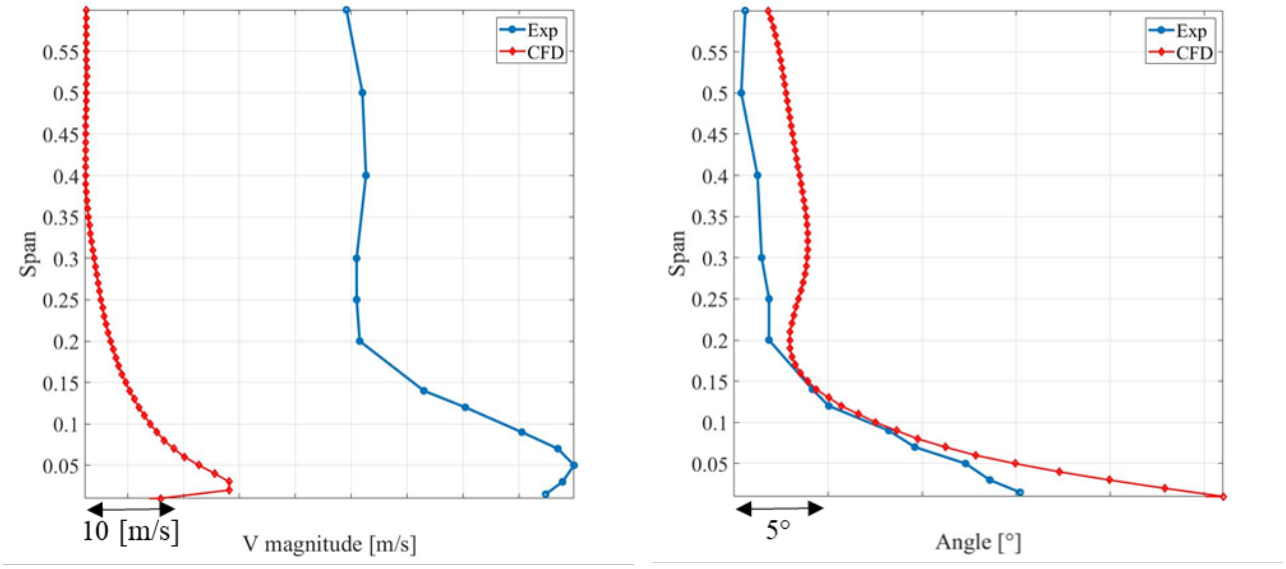

(a) (b)

Figure 3.40: Comparison between hot wire measurement in Plane 2 and CFD RANS results for the design loading point. (a) Velocity magnitude - (b) Absolute flow angle.

the wall Kulite inserts was performed, all the traversing probes were moved out from the cavity, while still sealing the stator hub platform hole. As a consequence, any probe induced effect have been removed from the dataset collected.

A test at design operating conditions where the three hole virtual pneumatic was immersed fully and one where there was no probe in the C2 cavity was performed. Acquisition results of the sensors FP08 and FP10 that are respectively at equal distance downstream and upstream from the probe is presented in Figure 3.42a and Figure 3.42b. The normalized power spectral density of the temporal fluctuations is plotted for both probe in and probe out case. The only visible difference is downstream of the probe on the FP08 spectra where spectral activity differs in the region 20 EO and 85 EO. The blade passing frequency (BPF), or rotor platform passing frequency is at 65 EO. It is possible that the instability at 20 EO is generated by the presence of the probe and the 85 EO (65+20) is a linear combination of this instability and the BPF.

Processing of fast response pressure sensors in stator disc boundary layer

This section describes the post processing of time series measured by the Kulite inserts in the stator disc boundary layer. The objective of the processing presented was to attribute to the most energetic flow structures in the frequency domain a physical description.

From the original pressure power spectral density, that can be the one of the full pressure signal, the one of the EA, or the one of the temporal fluctuations around the ensemble average (T_f), a frequency interval was sampled to isolate a defined frequency range (see Figure 3.43). From that point, the frequency interval will be indicated in the text as [a:b] where a and b are respectively the minimal and maximal frequencies in EO. Two approaches were evaluated for the sampling. The first one, called selective sampling, consisted to impose a null amplitude outside of the sampled frequency interval. The second one, called Butterworth, applied on the signal a band pass filter built of two fourth order low pass and high pass Butterworth filter.

As an example, the rotation 9 to 11 and 849 to 851 at design condition, no leakage, are extracted for the sensor FP_{10}. Figure 3.44 presents, for both of the method, the normalized pressure signal of the temporal fluctuations, obtained after sampling in the frequency band [8:12]. The reconstructed signals are in phase except for very local peaks. The selective method do not modify the original signal phase. The Butterworth method has a small effect on the phase. It is shown further that this behaviour has a small impact on the

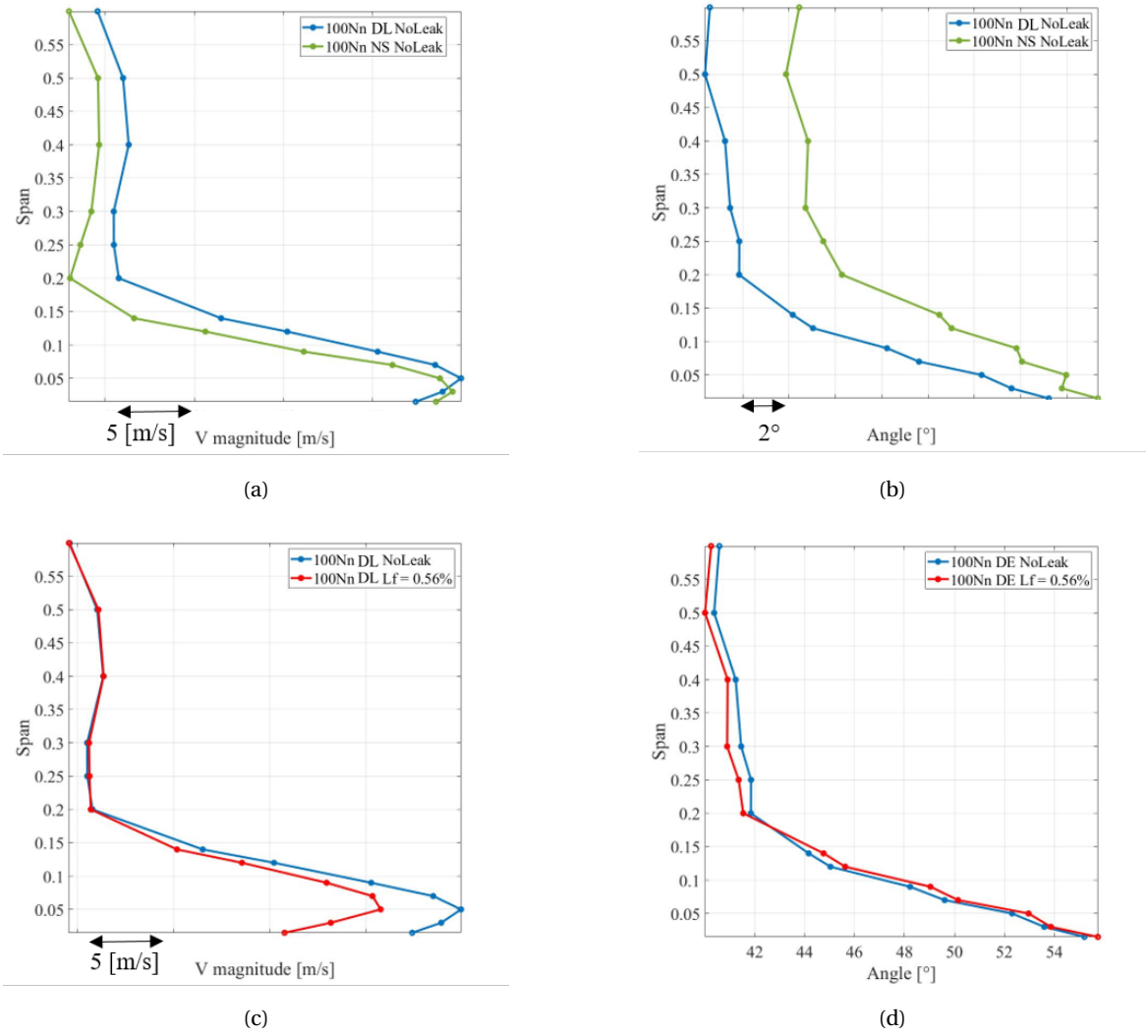

Figure 3.41: Hot wire measurement sensitivity to operating conditions in Plane 2 - (a) & (b) Velocity magnitude and absolute flow angle for the design loading (DL) and the near stall loading operating point (NS) - (c) & (d) Design loading. Velocity magnitude and absolute flow angle for no leakage (blue) and injection at leakage fraction of 0.56% (red).

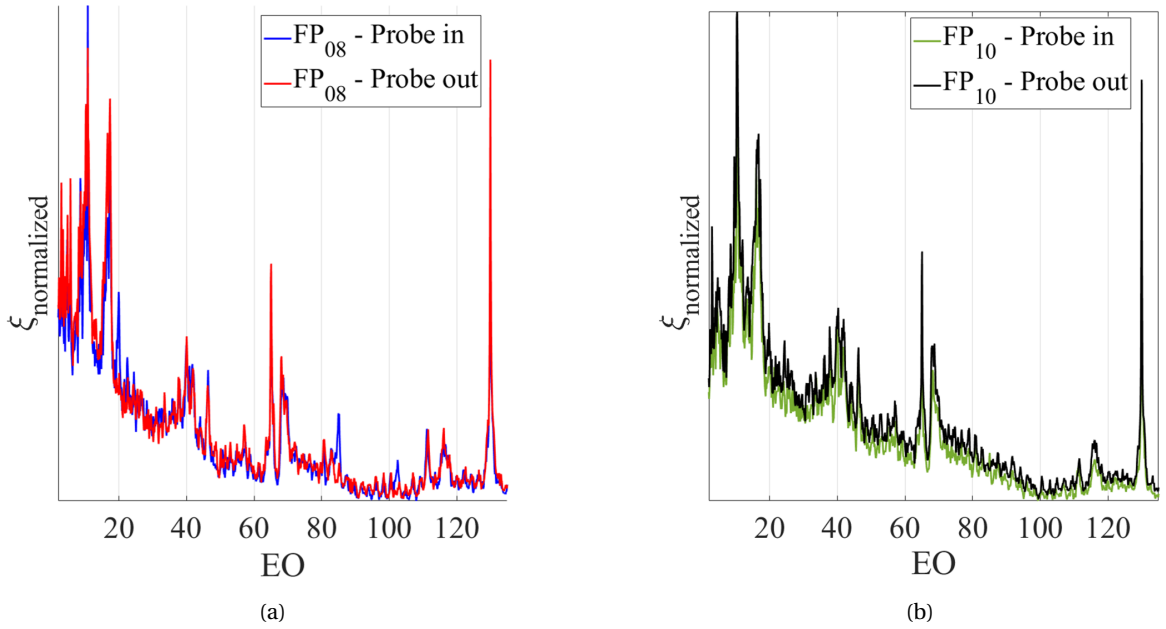

Figure 3.42: Cylindrical traversing probes intrusiveness in the C2 cavity - Acquisition of the wall flush mounted fast response pressure sensors - Normalized power spectral density of temporal fluctuations (a) FP08 sensor, downstream of the probe - (b) FP10 sensor, upstream of the probe.

results collected.

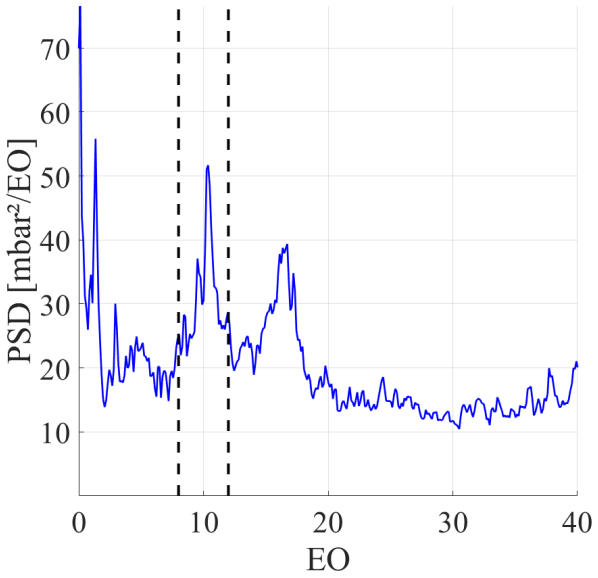

Figure 3.43: Definition of frequency interval to sample in cavity wall sensor analysis.

Once filtering was applied, sensors were analyzed by pair of angular spacing $\Delta\alpha$. In the case of the present study (12 sensors), a maximum of 132 pairs can be used. This number includes the pairs of similar angular spacing but at different position in the annulus to account in the analysis eventual azimuthal non uniformities / local behaviours.

Cross correlation was performed between the two sensors signal for each rotor disk rotation. The lag in number of points (see equation 3.12) between the two signals was used to derive the ratio between structure speed ω_s and disk speed ω_d following the equation 3.13. The correlation coefficient was normalized for each

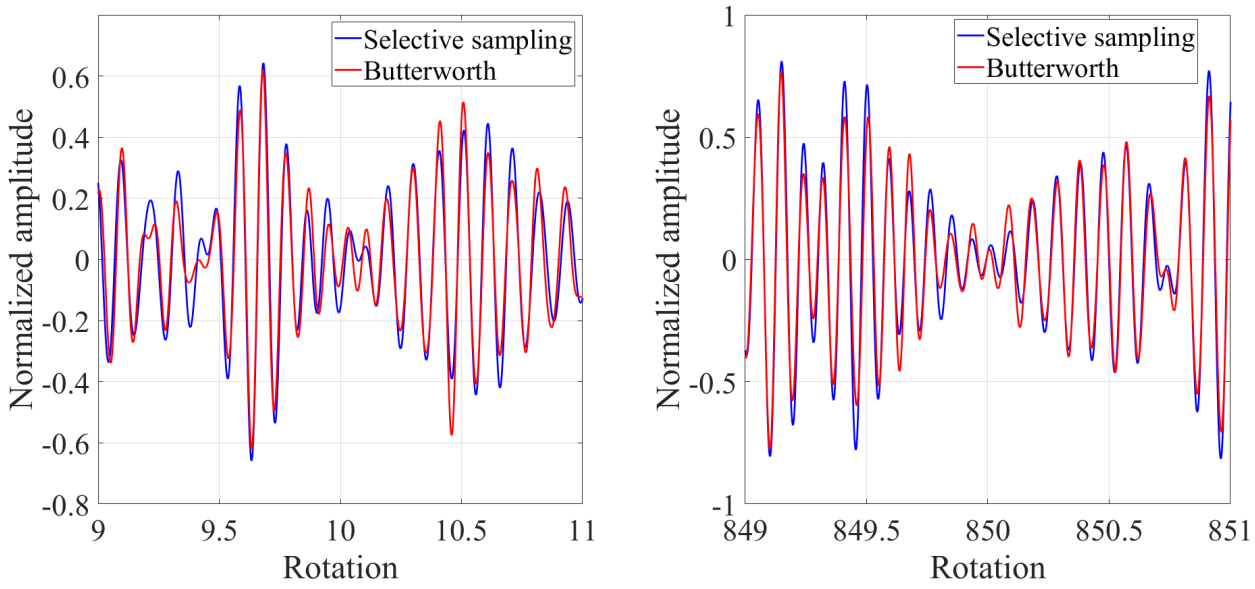

(a) (b)

Figure 3.44: Normalized pressure signal reconstructed after sampling in the frequency domain with selective and Butterworth method - (a) Rotation 9 to 11 - (b) Rotation 849 to 851 - These rotations are used to show that there were no phase shift between time series beginning and end.

sensor pair, for each rotation.

$$\omega_d = \frac{\Delta\alpha * f_{EO}}{360} \tag{3.12}$$

$$\frac{\omega_s}{\omega_d} = lag/\omega_d \tag{3.13}$$

For the design operating condition, cross correlation coefficient for the pair of probes FP_{10} and FP_{12} as well as the pair between probe FP_{10} and FP_{06} (see Table 3.2) is presented in Figure 3.45a. In this figure, the correlation of the ninth rotation of the time series is analyzed in the frequency range [8:12]. Note that this range, taken as an example, may not include coherent rotating structures.

The angle spacing for the pairs is of 10 [°] and 135 [°] respectively. The azimuthal range covered by the sensor pair has an impact on the structure speed resolution. As visible in Figure 3.45a and Figure 3.45b, larger angular spacing allows a wider window of velocity (see x axis). The drawback is that the velocity resolution between two sampled points is lower. To accommodate for that difference, the following approach was used. A grid of structure velocity was defined between the minimal and maximal possible velocity captured among all the pairs, i.e. this range is defined by the pair with the largest value of $\Delta\alpha$. The velocity grid also used the velocity precision of that pair. All of the other pairs correlation results were interpolated on that grid, with the aforementioned velocity precision.

Interpolated data were combined for all the pairs, in each rotation. To do so, the minimum correlation for each structure velocity was kept (Brandstetter et al. (2018)). In Figure 3.45c, the minimum correlation coefficient for the two sensor pair used is presented. When the results were combined for all the rotations, it was possible to have an overview of the evolution of the speed associated with the maximum correlation coefficient. In Figure 3.45d, such representation is presented for the test conditions and sensor pair used in this example.

The behaviour of the pressure signals in each sampled frequency range is different. If a frequency corresponds to a spatially coherent structure, a line of constant structure speed appears for a defined number of rotations. For the design loading condition, an example is given in Figure 3.46 for three frequency ranges. It is clear that the frequency range [38:42] presents a coherent behaviour for a structure speed of 43% of the disc speed. Analysis and interpretation of the results is done in Chapter 4.

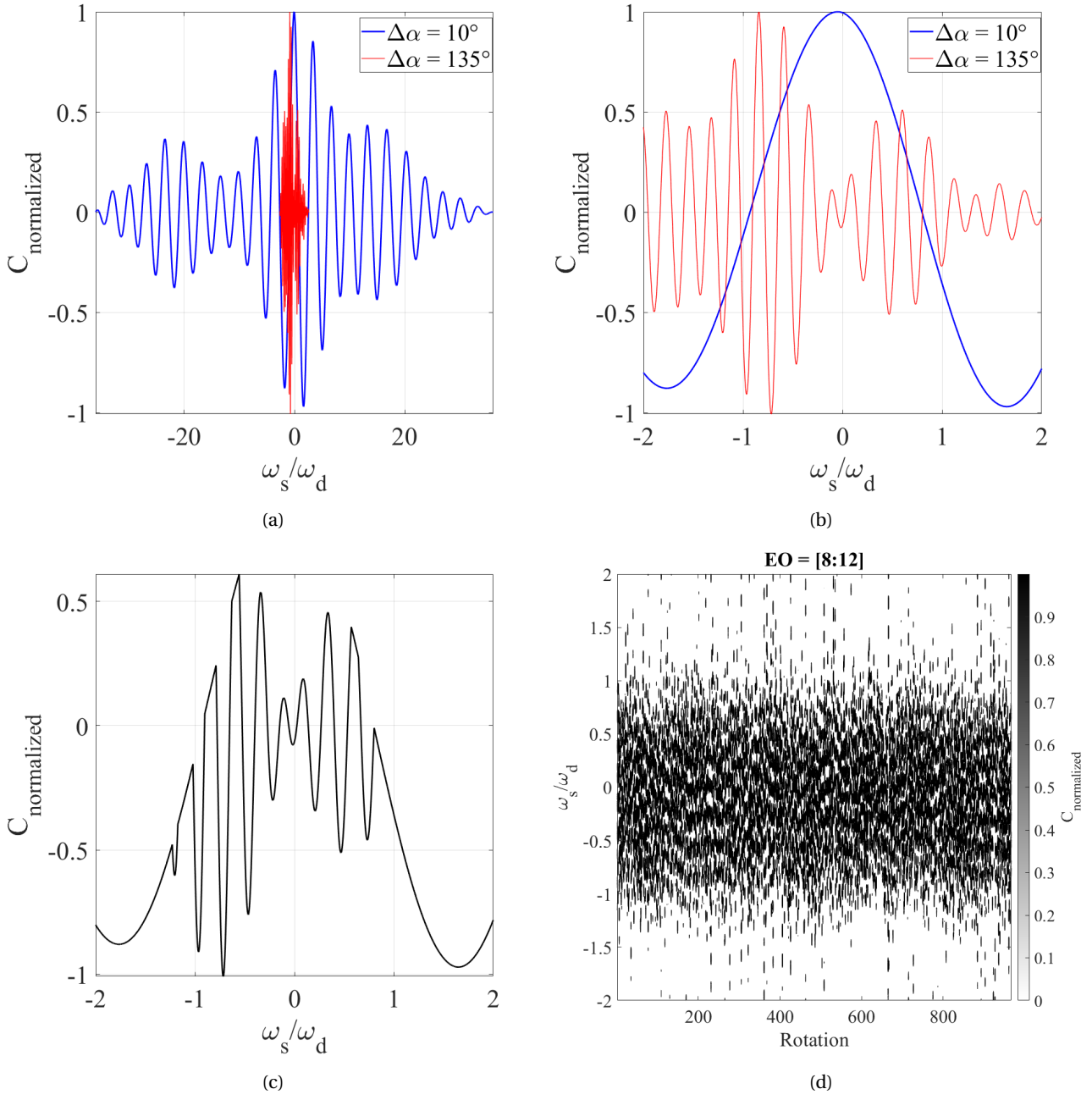

Figure 3.45: Example. Cross correlation of sensor pairs FP_{10} FP_{12} (blue) and FP_{10} FP_{06} (red) - (a) Normalized correlation coefficient for one rotation as a function of structure and disk speed ratio - (b) Zoom of (a) - (c) Correlation coefficient minimum between the two pairs for each speed in the rotation -(d) Combination of minimum coefficient between the two pair of sensors for all the disk rotations - x axis: Rotations (i.e. time); y axis: Structure speed; z axis: Correlation coefficient.

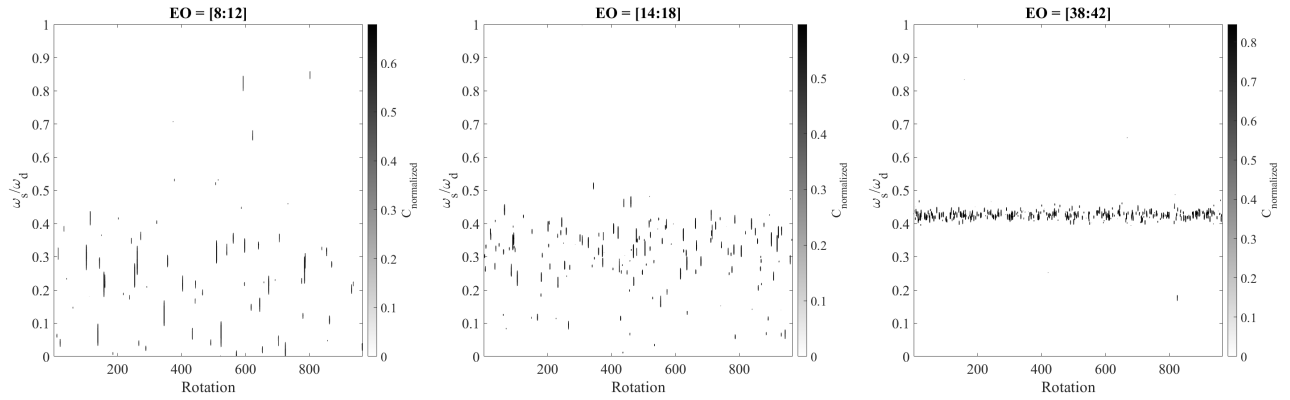

(a) (b) (c)

Figure 3.46: Result of cross correlation of eleven sensor pair at design loading, no leakage condition - (a) Frequency range [8:12] EO - (b) Frequency range [14:18] EO - (c) Frequency range [38:42] EO.

The sensitivity of the result obtained to signal processing was evaluated on the temporal fluctuations signal. The test case remain at design loading no leakage in the range [38:42]. The reference coherence map (in Figure 3.47a) is generated with: applied transfer function, selective sampling method, eleven pairs of probes using sensor FP_{10} as a reference. This reference case also uses time series of 4000 points per rotor revolution. In Figure 3.47b, the probe transfer function was not applied on the signal. No difference in correlation coefficient magnitude and structure speed are visible. In Figure 3.47c, the effect of the sampling method was evaluated. With Butterworth method applied, the coefficient values reduce and there is less dispersion around the average structure speed, which remains the same as Figure 3.47a. In Figure 3.47d, eleven pairs of sensors were used with sensor FP_{05} as a reference. The choice of sensor pairs has an effect on the normalized coefficient value but not on the structure speed. In Figure 3.47e, the sampling of the time series was done with 3500 points per rotation (instead of 4000). No change is visible from the reference given in Figure 3.47a. To conclude, the settings of the reference case were kept for the result analysis in Chapter 4.

3.1.3.8 Injection control

3.1.3.8.1 Measurement chain

The solution retained to allow controlled injection in the H25 test section was to pressurize the adjacent disk cavity (C1 in Figure 3.2). The injection in the C2 cavity was then made through the labyrinth seal. An injection port has been created at the back of the test section as illustrated by Figure 3.48. The injection line prior to the port was composed with two sonic orifices in parallel. Multiple diameter orifices combined with a maximal pressure supply of 40[bar] allowed to tune the mass flow injected in the disk cavity and pressurize it without exceeding the maximal axial load accepted by the disk bearings. Instrumentation was present along the injection path to compute live (2[Hz]) the injected mass flow in the main channel. Figure 3.48 informs on the measurements available along the injection line at different stations.

3.1.3.8.2 Selection and tuning of injection conditions

Section restrictions along the injection flow path set the mass flow injected in the C2 cavity. Aside from sonic orifice and injection line section, the labyrinth seal gap is a restriction. The labyrinth ring being cantilevered to the rotor disk, an evaluation of the labyrinth gap evolution with the C1 cavity pressure was done. The results are available in appendix B.

In the experimental campaign, different injection conditions were generated. The mass flow injected was defined based on 1 - the leakage fraction with respect to the stage corrected mass flow; 2 - the static pressure in the disc chamber B. The levels of injection are summarized in Table 3.4. The leakage fraction is

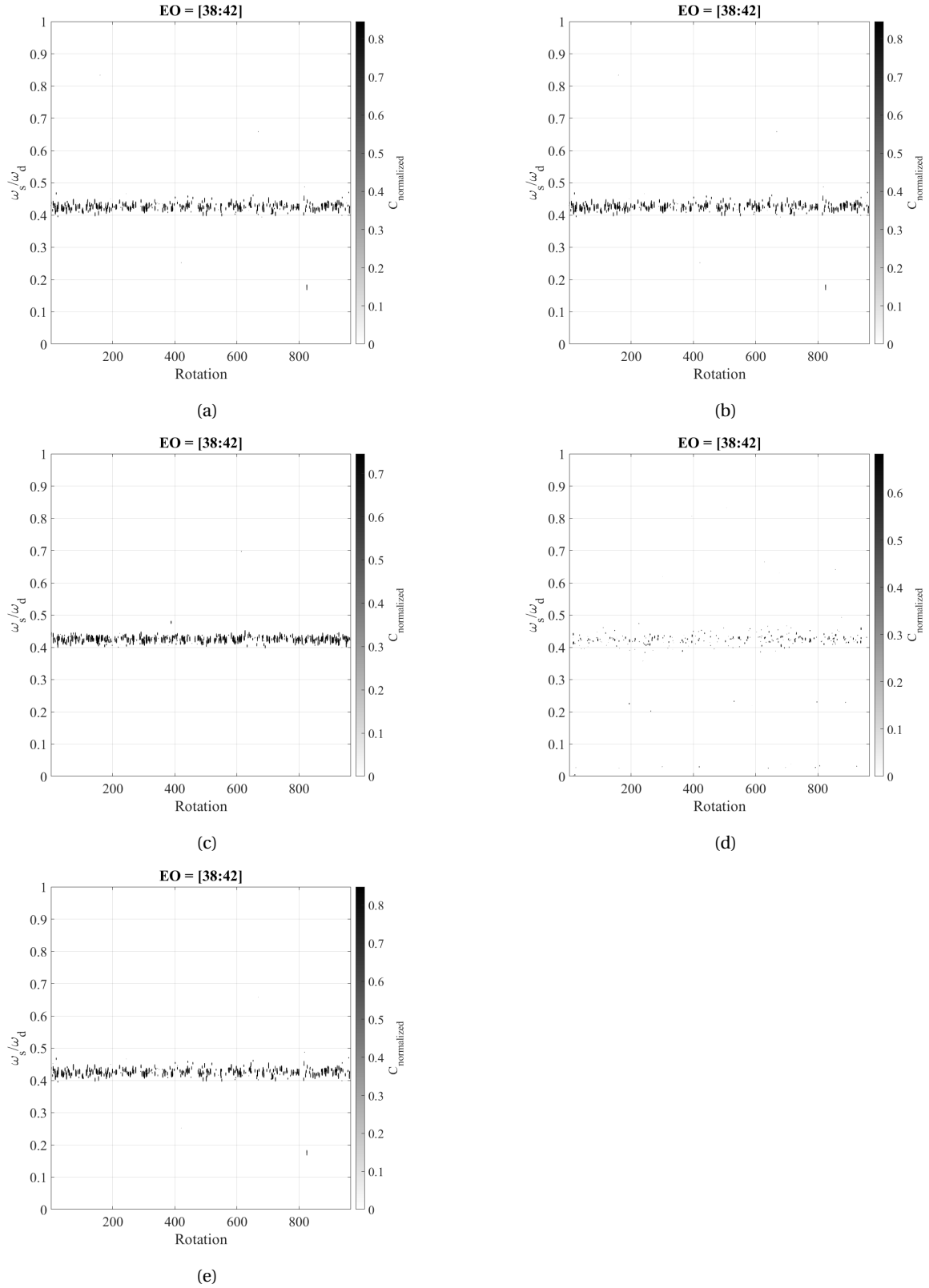

Figure 3.47: Sensitivity of coherence map to processing - (a) Reference case for eleven pairs of sensors - (b) No probe transfer function is applied - (c) Butterworth sampling instead of selective sampling -(d) Reduction of pressure signal sampling from 4000 points per rotation to 3500 points.

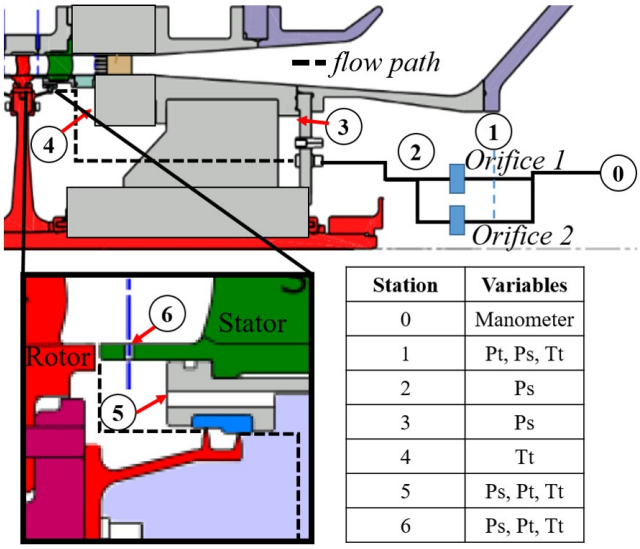

Station	Variables
0	Manometer
1	Pt, Ps, Tt
2	Ps
3	Ps
4	Tt
5	Ps, Pt, Tt
6	Ps, Pt, Tt

Figure 3.48: Injection line (in black) and measurement stations for leakage flow quantities evaluation.

computed at the sonic orifices, between station 1 and 2 in Figure 3.48. Injection 1 corresponded to a leakage fraction that exceeds the leakage flow rate given in the worst sealing case by the RANS cfd computation at design loading (see Figure 3.55b). The target value was of 0.56% of leakage fraction. Injection 3 was the injection given if the static pressure in the disk cavity chamber C1 equaled the average static pressure in the stage outlet (Plane 4). This condition was the closest from reproducing real engine recirculation for the H25-C2 cavity, hence it evolved with the operating point. Finally, the injection 2 was selected from being close to the leakage fraction given in the low loading point for the injection 3, at 0.3% leakage fraction.

Table 3.4: Injection conditions for the test campaign.

Condition	Leakage fraction [%]	Disk cavity pressure
Injection 1	0.56	-
Injection 2	0.3	-
Injection 3	-	Ps_4

During the experiments, the injection was performed while keeping constant the corrected mass flow measured in Plane 0. As already mentioned, it was possible to live tune the leakage fraction. Nevertheless, the test section is a dynamic system where performance fluctuations were present. Typically, at stabilized operating point, the compressor mass flow fluctuated of about ± 0.01[kg/s] around the target operating point.

When injection was performed, stabilisation time was required before measurement started. The operating point was considered stable on the base of the isentropic efficiency. As an indication, between two injection state, fifteen minutes were necessary to reach a stable state. In the same time, the total temperature at the inlet of the sonic orifices in Station 1 was monitored between the tests and kept as constant as possible to ensure repeatability of injection conditions.

The injection setup was designed around calibrated sonic orifices that allowed for the smallest uncertainty on the mass flow measurement. It was at first not clear if the measurements performed in the C2 cavity would be able to record clear differences between injection conditions. That is the reason why only the leakage fraction was controlled. The swirl ratio entering the cavity was driven by the rotor disk work. Finally, the injected air was not pre-heated. For that reason, the temperature in the disk chamber was decreasing with the leakage fraction. As an indication, the air temperature measured at station 4 (c.f. Figure 3.48) dropped of 16 [K] between no injection and injection 1 (max injection) at nominal speed and design loading

operating point.

To finish the discussion on the injection conditions selected for the C2 cavity test campaign, an evaluation of the H25 rotor disk pumping was done. The rotor disk was considered as a isolated rotating disk of radius R beneath a forced vortex where the fluid outside of the disk boundary layer rotates at a fraction of the disk angular velocity (rotating disk and rotating core in a Batchelor type flow). The forced vortex core velocity is represented with the swirl ratio S_f. Under the assumption that the disk boundary layer is turbulent from $r = 0$ and for the one seventh power law in the boundary layer, equation 3.14 gives the mass flow rate pumped by the disk (c.f. Sultanian (2018)). The massflow fraction ζ in equation 3.15 is a function of the forced vortex swirl ratio.

$$\dot{m}_{\text{disk}} = 0.219\mu r \left(\frac{\rho r^2 \Omega}{\mu}\right)^{0.8} \zeta \tag{3.14}$$

$$\zeta = (1 - 0.51 S_f)\,(1 - S_f)^{1.6} \tag{3.15}$$

The mass flow pumped by the disk is a function of the radius r and increases with it. In the case of the study, the focus was set on the radius interval between -0.63 span and 0 span. This interval is the radial extent of the C2 cavity corresponding to a rotor stator cavity configuration (see Chapter 2 section 2.4).

For three operating conditions investigated in the experimental campaign, the disk pumped mass flow was computed. For each condition, this mass flow was compared to the H25 compressor mass flow to express the result in leakage fraction. In the case of a Batchelor type flow in the C2 cavity, where a forced vortex of swirl ratio S_f is created between rotor and stator walls, the pumped leakage fraction was evaluated with respect to S_f. Results are presented in Figure 3.49. For each condition (Nominal speed design loading (black) - Nominal speed near stall loading (dashed red) - Partial speed design loading (short dash green)), leakage fraction envelope is indicated between the line at minimal radius and the line at maximal radius.

As seen in Chapter 2, when radial outflow is superimposed to rotor stator cavity flow, flow is detached from the stator boundary layer at the radius where the disk pumped mass flow exceeds added throughflow. With Figure 3.49, it is possible to estimate that with the injection conditions retained (i.e. inj 2 at 0.3% and inj 1 at 0.56%), the minimal swirl ratio in the forced vortex must be of respectively 67% and 55% of the disk rotating speed for the leakage fraction to exceed disk pumping demand.

In the case of the C2 cavity where the wetted stator surface was higher than the wetted rotor surface, thanks to the shroud surface, the stator torque is higher than the rotor torque. This condition imposes that $S_f < 0.5$, which indicates that the minimal swirl ratio for leakage fraction to overpass disk pumped flow for all radius was not reached in the tests.

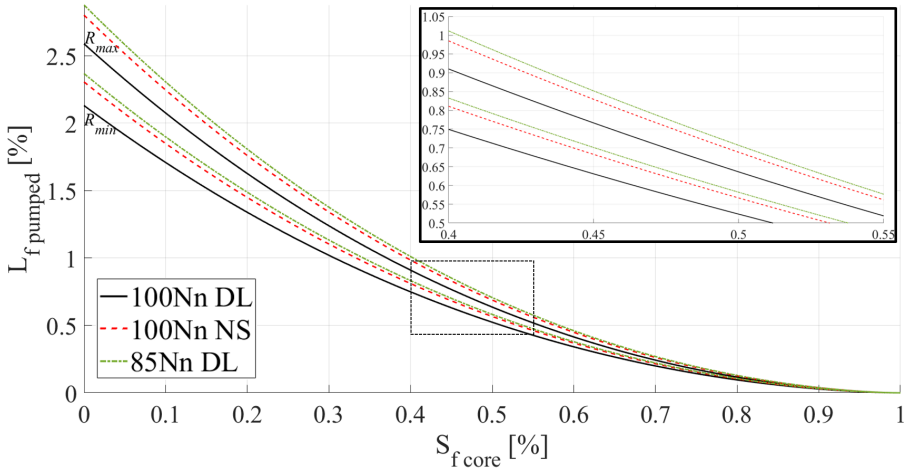

Figure 3.49: H25 disk pumped leakage fraction envelope in the radius interval where C2 behaves as a rotor stator cavity ($R_{min} = -0.63 span$,$R_{max} = 0 span$) as a function of sumperimposed forced vortex swirl ratio. Nominal speed design loading (black) - Nominal speed near stall loading (dashed red) - Partial speed design loading (short dash green).

To complete the introduction of the injection conditions and to locate the obtained results with available literature data, the reduced mass flow $C_w = \frac{\dot{m}_{leak}}{\mu * R_{max}}$ and the through flow parameter $\lambda_t = \frac{C_w}{Re_r^{0.8}}$ are computed. The results are presented for each operating point in Table 3.5. The through flow parameter should also be compared with the radially outward flow in the disc boundary layer that corresponds to $\lambda_t = 0.219$ (see Kármán (1921) and equation 3.14). The operating conditions investigated always presented a through flow parameter lower than this value.

Table 3.5: Leakage reduced mass flow and through flow parameter for the C2 cavity test campaign at injection 1 and injection 2 conditions

Operating point	L_f	C_w	λ_t
100Nn DL	0.56	5824.5	0.0430
100Nn NS	0.56	5421.1	0.0395
85Nn DL	0.56	4866.4	0.0396
85Nn NS	0.56	4538.6	0.0367
100Nn DL	0.3	3120.3	0.0231
100Nn NS	0.3	2904.2	0.0212
85Nn DL	0.3	2607.0	0.0212
85Nn NS	0.3	2431.4	0.0197

3.2 Numerical means

3.2.1 Introduction

The use of the numerical model to assess the effect of cavity flows on the H25 stage was done in different steps. First of all, the numerical tool helped the design and update of the experimental test section. The use of steady RANS simulation provided, for a limited computational cost, information regarding the ability of the test vehicle to be used for cavity flow analysis as well as selecting experimental probing locations. In a second time, the numerical tool was used to benchmark the steady RANS simulation against the database collected in the experiments. It informed on the robustness of such approach for preliminary design purposes. To finish, a numerical domain that isolates the C2 cavity was created. The simulations performed were unsteady RANS simulation. The objective of such simulation was to sample the unsteady activity of the C2 cavity for an injection condition, without technological effects (platform, pins,...) and blade effects. This sample was then compared with the time resolved database collected in the experiments. The interest there was to pinpoint the instabilities directly attributed to the C2 geometry and flow features. The simulation results helped also to state about the necessity to include such approach in the design practices for axial compressor stage.

3.2.2 Steady characterization of H25-C2 configuration

To give the reader more context, the steady numerical characterization of the H25 stage has been performed prior to the test section modification allowing any cavity measurement. The numerical tool acted mainly as a design tool for the experiments. Nevertheless, the chance has been taken to confront directly these preliminary numerical results against the experimental database in Chapter 4. Boundary conditions and geometrical representation in the numerical domain were constrained by the limited knowledge of the machine environment for cavity flow and cavity/main flow interaction analysis.

3.2.2.1 Numerical domain and mesh analysis

For the steady state simulations, the numerical domain shown in Figure 3.50 extends between the experimental Plane 0 and two rotor mid-span chords downstream of Plane 4. In the simulations, the hot geometries (i.e. in rotation) of the blades were used and the associated rotor tip gap was set to the averaged measured value. The estimation of the tip gap was done thanks to thickness measurement of rubbing gauges positioned around the rotor casing. Hub and tip fillets have been preserved in the numerical domain because of their crucial role on the junction flow field definition, in the area of interest for cavity leakage flows. Shroud cavities upstream and downstream the rotor row have been kept and closed. One blade passage per row was computed. The connection between the rotor and stator row was ensured by a mixing plane approach. The patches were linked with conservative coupling by the pitch-wise row method. The mixing plane was located between the rotor trailing edge and the cavity C2 trench connection with the main channel. Matching connections were used between cavities and main channel to allow better characterization of the flow exchange at their interface and to detect the presence of pitch-wise non uniformities.

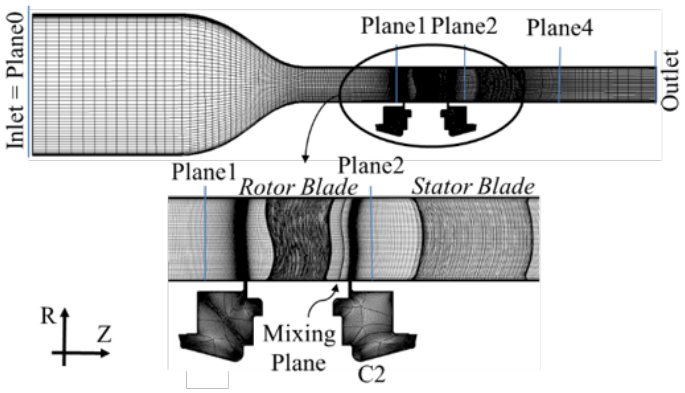

Figure 3.50: Meridional view of the finest grid for the baseline numerical domain.

The mesh was made with Autogrid5 and IGG software. A multi-block structured mesh approach could be chosen given the geometrical simplicity of the test section cavities. An O-4H mesh topology was used for both blade rows. The rotor tip gap region was meshed with OH topology and contains 22% of the rotor row stream wise number of points. The blade fillets were generated using a B2B section offset method. With this method, a 50 [°] minimal angle rule allowed a good balance between skewness level and number of cells consumption in these regions of the mesh.

In order to perform multigrid computations, three grid levels were built (Fine grid, Medium grid, Coarse grid) with respectively around 28 million, 3.6 million, and 0.5 million surface cells for the whole domain. The grid point balance, i.e. ratio between number of points in the cavity over the one of the associated row, was 0.75 in the rotor row and 0.87 in the stator row. When considering the shroud cavities, a non-dimensional wall distance (y^+) in the order of 1 was targeted to ensure a correct evaluation of the wall shear stress and its associated effects on the total temperature field. Average y^+ values are summarized in Table 3.6.

Table 3.6: Non dimensional wall distance y^+ for the fine and medium grid used in the steady RANS computation domain.

	Fine Grid	Medium Grid
Full domain average	0.391	1.005
Upstream cavity	0.331	0.490
Downstream cavity (C2)	0.850	1.240

The aim of the numerical domain presented was to: (1) Give a prediction of the H25 flow field under injection in order to support the feasibility of using a test vehicle equipped with closed cavities to achieve this

work objectives; (2) To benchmark the steady RANS fidelity to assess cavity flow effect on axial compressor stage.

To evaluate H25 leakage flow sensitivity different variations of the baseline numerical H25 domain were employed within the present study. They were all presented in Figure 3.51. The closed cavities configuration (CC - Figure 3.51a) coincides with the previously described baseline case and represents the ideal condition where the massflow recirculation falls into the numerical mass flow conservation uncertainty (e.g. high sealing performances). The opposite condition, called the natural cavity case (NAC - Figure 3.51b), was specifically designed to provide the H25 stator with the worst sealing performances. The natural recirculation cavity was built from the C2 cavity with a symmetry around stator stacking axis. It features a one rim seal configuration with a 0.8% gap to span ratio (cold R4 facility seal gap). In the end, the no cavity case (NOC - Figure 3.51c) helped in assessing the relevance of the other domains. Main channel refinement was independent from the cavity layout selected.

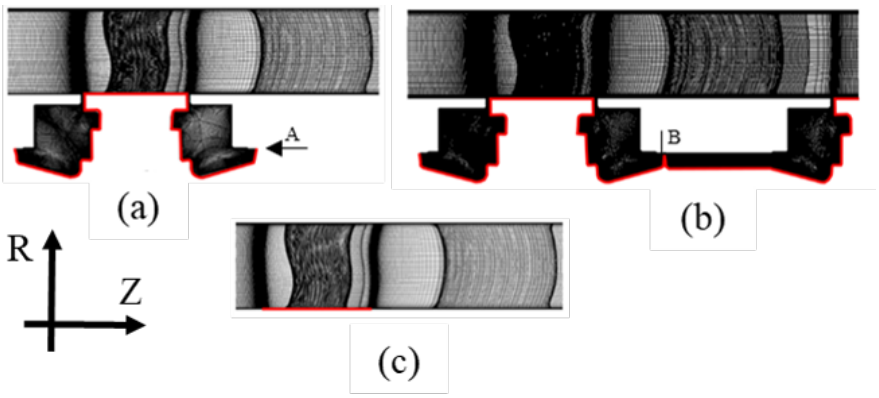

Figure 3.51: Numerical domain variations for steady RANS computations (a) Closed cavities configuration – (b) Stator natural recirculation – (c) No cavities configuration - (rotating surfaces in red).

3.2.2.2 Solver settings

Numeca's Fine/Turbo steady compressible RANS solver was used to run fully turbulent computations. The closure problem was solved using the two equation k-w SST turbulence model of Menter (1994). This model was chosen as the best compromise for complex flow and free shear flow prediction as for example illustrated in Bardina et al. (1997). The flow field was solved thanks to a second order central scheme. The CFL value chosen was kept at three due to the important mesh contraction and expansion close to the cavity matching connections. Time discretization was performed through four stage explicit Runge Kutta scheme.

3.2.2.3 Boundary conditions

Experimental boundary conditions have been employed from an existing database on the H25 test section. At the inlet (Plane 0), the azimuthally averaged total temperature and total pressure profiles were imposed while, at the outlet plane, a radial equilibrium condition was used to set the mid-span static pressure value. The value of the static pressure at the outlet was set so that numerical and experimental results can be compared for the same static to total pressure ratio in Plane 4. This condition has been selected as the cavity flow is driven by the static pressure increase in the stator row. As a result, flow coefficient differences may appear between the experimental and numerical operating point. The walls in the simulation were considered as adiabatic.

3.2.2.4 Grid sensitivity

A grid sensitivity analysis was performed to evaluate the impact of the domain spatial discretization on the computed quantities. This becomes even more justified when considering that the cavity region called

for a high cell counts. The grid convergence index (GCI), introduced by Roache (Roache (1994), Roache (1997)) and recently standardized in Celik et al. (2008), was adopted at such extent. The method targets the conservative evaluation of the spatial discretization related uncertainty of computations, so that the impact of the selected mesh could be automatically damped in the final result. The GCI approach requires at least three different grid levels to be generated and gives the relative difference between the CFD computed quantities and their asymptotic numerical value from the Richardson extrapolation. The GCI evaluation is more accurate with grids that are matching in terms of structure and with a homogeneous coarsening between them. In that extent, the three grid levels introduced previously suited well the required conditions. The grids were generated by an isotropic coarsening from the finest mesh in the 3 directions (i.e. 1/8th size ratio between each grid level). In conclusion, the solutions obtained must be in the asymptotic range of convergence to guarantee a correct evaluation of the GCI. In the present study, the mesh sensitivity on quantities such as the stage isentropic efficiency, mass flow and total-to-total pressure ratio have been considered. Table 3.7 presents the GCI values for the aforementioned quantities for both the fine and the medium grids. It also shows that the isentropic efficiency is the most sensitive quantity to the grid refinement, with an increase from 1% to 4.55% in GCI between the finest grid and the medium grid. It is important to note that the isentropic efficiency evaluation is more precise between the Plane 1 and Plane 4 rather than between the Plane 0 and Plane 4. This can be inferred to the presence of the convergent between the Plane 0 and Plane 1 (as showed on Figure 3.50) which, by common practice, corresponds also the coarsest mesh region. From the rotor inlet (Plane 1) and downstream, the mesh quality allowed to reduce the discretization error by a factor 2 for the aforementioned quantity.

Table 3.7: Grid Convergence Index for the fine grid GCI_{fine} and for the middle grid GCI_{medium}.

	GCI_{fine} [%]	GCI_{medium} [%]
η_{s04}	1.00	4.55
η_{s14}	0.50	2.47
Π_{st04}	0.01	0.02
Π_{tt04}	0.04	0.24
Wr	0.30	2.24

The grid effects on the stage isentropic efficiency profile are shown on Figure 3.52. On the most sensitive quantity, the areas of the flow field mainly affected by the grid density are directly highlighted. Beside the poor result of the coarse grid, the medium and the finest grid are in good agreement far from the endwalls. This suggests that the overall mass averaged performance will be well captured by both grid levels, still exhibiting a strong spatial discretization dependency in the flow field region of interest to the present analysis (hub region). As a consequence, the finest grid is used in the rest of this work.

3.2.2.5 Use of the different domains

Since the test section did not had leakage nor natural recirculation, the different numerical domain have been used to define the leakage conditions interval to impose. The NAC configuration defined the upper limit of the interval being the worst sealing conditions. This condition was used as a reference leakage conditions. From the conditions generated in the NAC domain at the labyrinth exit, boundary conditions were extracted to generate multiple leakage conditions. The extraction location is referenced in B in Figure 3.51b. These conditions were then used in the closed cavity domain where the labyrinth outlet patch is treated as an inlet. The injection location is indicated by the letter A and arrow in Figure 3.51a. With such domain, a parametric study for the leakage conditions was possible. The sensitivity to the leakage fraction and to the swirl ratio of the leakage flow was evaluated. The simulated leakage conditions are summarized in Table3.8 and Table 3.10 for the design loading operating point. The values for the low loading point are given in Table 3.9 and Table 3.11 The definition of the leakage fraction L_f and swirl ratio S_f used are presented in equation 3.16 and equation 3.17. The leakage fraction was computed as in the experiment comparing

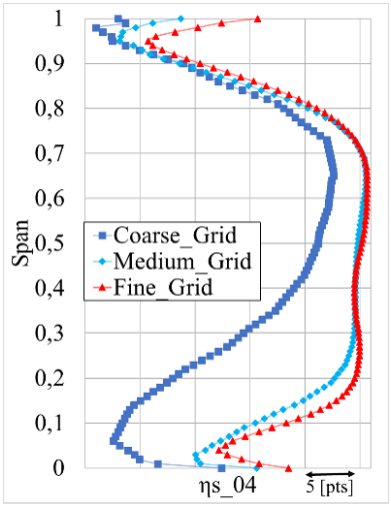

Figure 3.52: H25 stage isentropic efficiency at design operating conditions - Azimuthal averaged profile for the three grid levels.

the domain inlet corrected mass flow and the injected mass flow. The values labelled as Ref_x indicates the leakage conditions obtained for the NAC domain at the X operating point. The conditions imposed in the computations were derived from the reference values computed independently at each operating point.

$$L_f = \frac{Wr}{\dot{m}_{leak}} \tag{3.16}$$

$$S_f = \frac{V_t}{\Omega r} \tag{3.17}$$

Table 3.8: Leakage injection condition for the steady RANS numerical domain at design loading operating point - Leakage fraction sensitivity.

Case label	L_f [%]	S_f [%]
Ref_{DL}	0.46	49.6
L_{fLL}	0.39	49.6
L_{f0}	0.35	49.6
L_{f1}	0.23	49.6
L_{f2}	0.12	49.6
L_{f3}	0.06	49.6

3.2.2.6 Validation of the baseline configuration

The comparison between the experimental and numerical setup was made at first on global performance. Figure 3.53 shows that the RANS approach is capable to properly capture the static-to-total pressure ratio evolution over the selected operating range while overestimating by 1% to 2% the value of the isentropic efficiency. In order to provide a more detailed validation, a plane-by-plane approach was used. The comparison in each plane between the experimental and numerical data at DL operating conditions serves multiple purpose: 1. In Plane 1, the ability of the simulation to generate the correct boundary layer profile at the rotor inlet is assessed; 2. In Plane 2, measurements helped validating the stator row inlet conditions; 3. In Plane 4, thanks to the more complete experimental setup, the ability of the numerical setup in correctly identifying the flow field main features was evaluated. Figure 3.54 shows the total pressure profile

Table 3.9: Leakage injection condition for the steady RANS numerical domain at low loading operating point - Leakage fraction sensitivity.

Case label	L_f [%]	S_f [%]
Ref_{LL}	0.39	50.4
L_{f4}	0.27	50.4
L_{f5}	0.18	50.4
L_{f6}	0.09	50.4
L_{f7}	0.04	50.4

Table 3.10: Leakage injection condition for the steady RANS numerical domain at design loading operating point - Swirl ratio sensitivity.

Case label	L_f [%]	S_f [%]
β_1	0.46	0
β_2	0.46	12.5
β_3	0.46	25.0
β_4	0.46	37.5
Ref_{DL}	0.46	49.6
β_5	0.46	62.5
β_6	0.46	80.0
β_7	0.46	105.0

in the Plane 1 (rotor inlet). The numerical results show a thicker boundary layer at the casing for the design operating condition. The maximal pressure ratio difference between the experimental and numerical prediction is of one percent. The inlet flow remains axial and no incidence defect are detected in the rotor row inlet (data not showed).

The total pressure and absolute flow angle radial distributions in Plane 2 are plotted in Figure 3.55a and Figure 3.55b respectively. In particular, the experimental results there presented correspond to the average of two different measurements performed in as many azimuthal locations while the numerical data are pitch-wise averaged. As a matter of fact, part of the discrepancies are related to the poor spatial sampling of the experimental data. As previously mentioned, simulations have been run by imposing the average tip gap size measured by means of rubbing gauges. Given the small size of the H25 stage, this parameter is thought to provide an important impact on the solution, partially justifying the mismatch between numer-

Table 3.11: Leakage injection condition for the steady RANS numerical domain at low loading operating point - Swirl ratio sensitivity.

Case label	L_f [%]	S_f [%]
β_8	0.39	0
β_9	0.39	12.6
β_{10}	0.39	27.0
β_{11}	0.39	37.8
Ref_{LL}	0.39	50.4
β_{12}	0.39	63.0
β_{13}	0.39	81.0

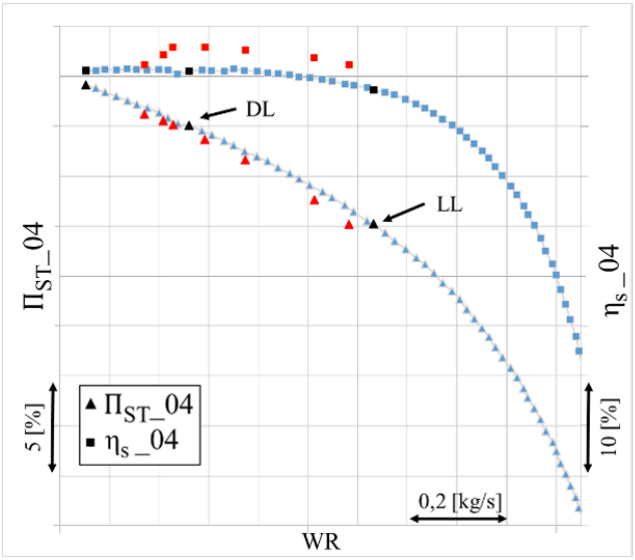

Figure 3.53: H25 stage performance comparison at nominal speed - Experimental (Blue) - CFD (Red).

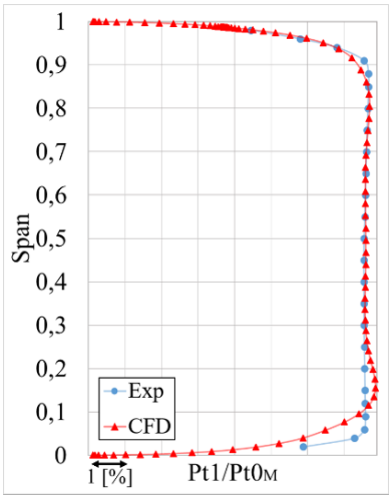

Figure 3.54: Plane 1 total to total pressure ratio - Design loading operating conditions - Experimental (Blue) - CFD (Red).

ical and experimental data in the upper part of the blade span (h > 0.7). Moreover, the use of a mixing plane at the rotor exit acts as a cut-off for the stream-wise mixing taking place in the end wall upstream of the rotor-stator interface (see Figure 3.50). As a consequence, further downstream at the measurement plane location, higher losses are expected in the measurements than in the numerical result, as shown in Figure 3.55a. In general terms, the average total pressure ratio matches within 1% in the free-stream conditions while, in the low span region, the flow angle shows an even higher validation rate, providing confidence on the prediction as far as the stator row inlet conditions are concerned. The traversing system of Plane 4 featured both, radial and tangential traversing capabilities, allowing to treat the data in terms of mass averaged radial distributions. The total temperature distribution on Figure 3.56a demonstrates that, in the free-stream region, CFD results are within the experimental uncertainty. In the end wall region, the best agreement comes in the low span region where CFD results fall beyond the experimental uncertainty range by less than 1 [K]. Still, discrepancies can also arise as a consequence of the choice of an adiabatic boundary condition in the numerical setup. As an example, the evident mismatch in the tip region can be justified by the aforementioned consideration: through the outer casing of the facility, heat is transferred to the laboratory environment, leading to the generation of a gentler temperature radial gradient, directly impacting on the predicted efficiency value. Still, the very high agreement in the low span region ($\Delta T < 1\%$) supports the

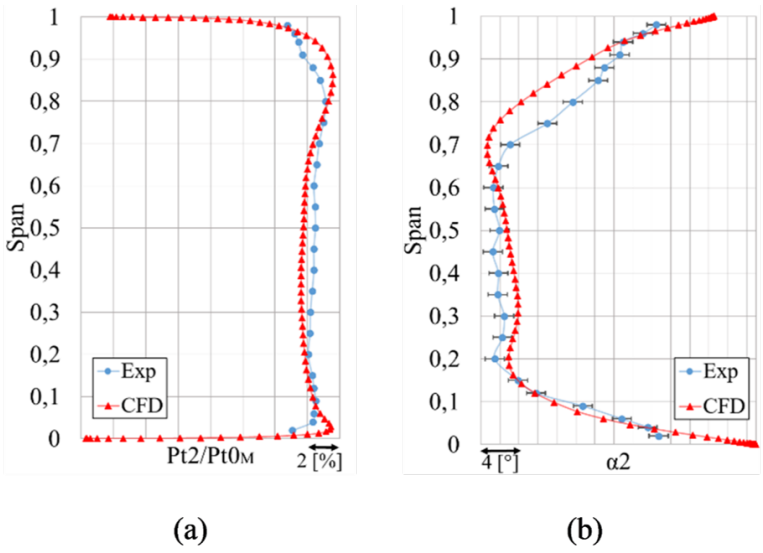

Figure 3.55: Stator Inlet conditions (Plane 2) - (a) Normalized total Pressure - (b) Absolute flow angle - Experimental (Blue) - CFD (Red).

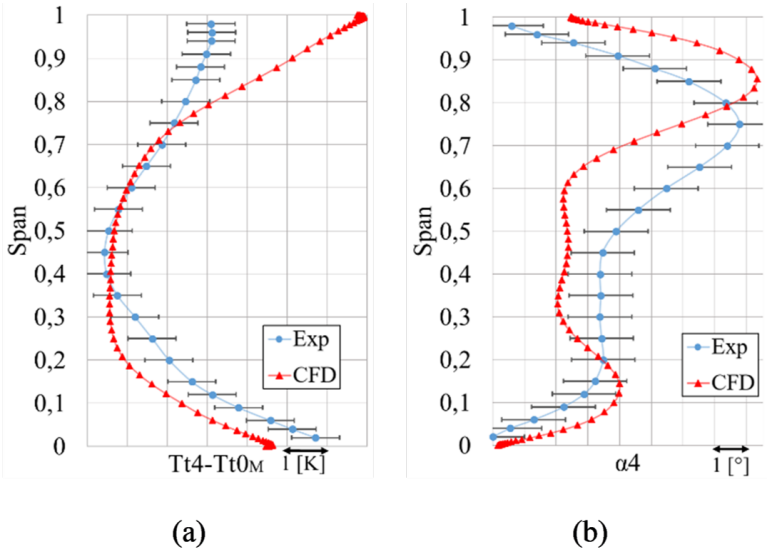

Figure 3.56: Stator outlet conditions (Plane 4) - (a) Total Temperature - (b) Absolute flow angle. - Experimental (Blue) - CFD (Red).

choice of the aforementioned boundary condition for the hub and gives confidence on the capability of the present numerical setup in predicting relative performance variations due to different cavity conditions.

Flow angle measurements in Figure 3.56b has the highest relative uncertainty, implying that numerical predictions tend to easily fall within the confidence interval. Nevertheless, the agreement with the experimental data in the region of interest (lower span) is high. While at casing the flow angle magnitude is well captured by numerical simulations, the radial organization of the flow is not properly predicted, with more than 10% discrepancy between corresponding features (e.g. overturning peak around 0.75 span (exp) and 0.90 span (cfd) in Figure 3.56b). The poor prediction close to the end walls has also to be put in perspective to the variation of the stator inlet conditions induced by the presence of the mixing plane as rotor-stator interface treatment.

On Figure 3.57, the normalized total pressure map of both experimental (a) and CFD (b) data are presented. The magnitude of the total pressure difference at stator outlet remains under 0.8% of the pitch-wise averaged values. The width of the wake (A) is correctly detected by the CFD. However, the RANS approach over-predicts the wake depth. In this position, the numerical data also shows a radial thickening of the wake

which results from the strong streamline contraction on the stator pressure side (cf. Figure 3.57c - PS). In the end-wall region, the wake signature is well described by both numerical and experimental data. Because of the presence of large blade fillets and of the forward-swept design of the H25 stator, no clear corner flow structure can be identified, while the suction side shear lines (cf. Figure 3.57c - SS) display the accumulation of low momentum fluid at the trailing edge location. The high lean angle of the H25 stator implies a strong transverse pressure gradient over the blade (c.f. Taylor and Miller (2017) and Chapter 1). It induces strong streamline radial migration and unloads the end wall region. The Lei criterion diffusion parameter (Lei et al. (2006)) for the design operating condition was computed to be equal to 0.17, a value in complete agreement with both the computed and measured flow topologies. The passage vortex is clearly identified in the middle of the blade passage on the CFD RANS data (marker B in Figure 3.57b) but no clear signature of its presence can be evinced in the corresponding experimental data.

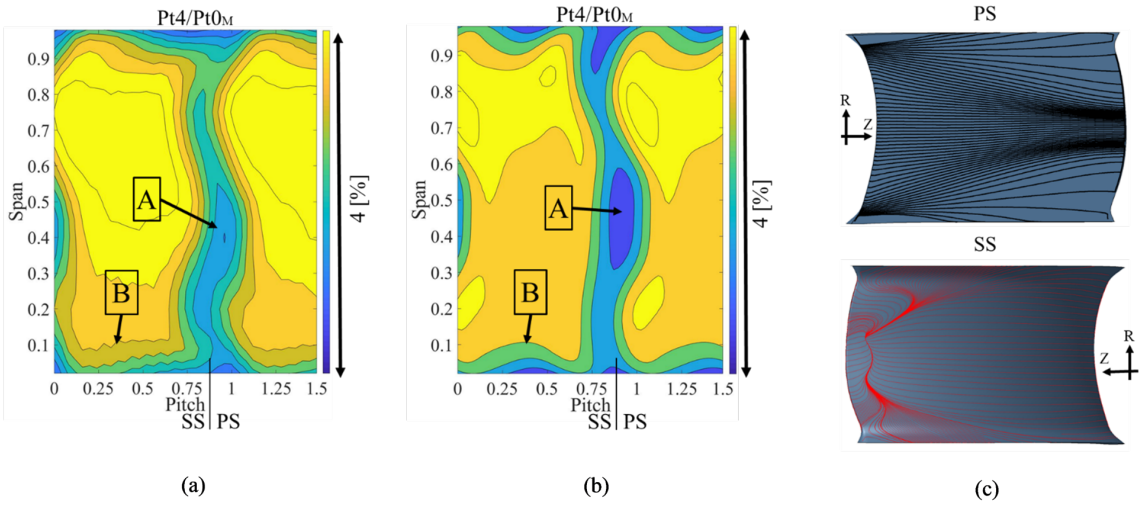

Figure 3.57: Stage Outlet normalized total Pressure map at design loading operating conditions - (a) Experimental data - (b) CFD - (c) Numerical friction lines on blade Pressure side and Suction side (profile not to scale).

The numerical baseline setup validates against the existing experimental database. The major discrepancies in the flow field can be explained by choices in the modelling strategy. The moderate cost of the steady RANS approach is then used as a platform for experimental design and to support the experimental database collected in this work (c.f. Chapter 4).

3.2.3 Unsteady characterization of the C2 cavity

3.2.3.1 Numerical domain

The computation of the time resolved C2 cavity flow was done for the full cavity. The domain used for the computation was framed around the cavity and covered the entire annulus (so 360°). Studies found in the literature agrees that the numerical domain angular sector width affects the quantitative results. To resolve the flow to 360° added issues such as: more computational cost, flow transients that are longer. Nevertheless, the influence to sector angle was then neglected. The numerical domain used for the unsteady RANS simulation is presented in Figure 3.58a. The axial extent of the main channel lies between H25 rotor trailing edge and stator leading edge. This choice was made so that multiple type of boundary conditions can be generated at the main channel inlet and outlet (to include blade effect for example). A view of the meridional mesh is presented in Figure 3.58b. A matching connection was kept between the cavity and the main channel. The mesh was made thanks to the unstructured meshing tool HEXPRESS. Multiple boxes of refinement were used to compromise between high mesh resolution in the cavity and limited computation costs due to a less refined higher part in the main channel. The refinement first layer was kept far enough from the hub boundary layer to limit the effect of cell distortion due to the change in refinement level. As it is visible in Figure 3.58c, the meshing tool imposed distorted cells locally between refinement levels to

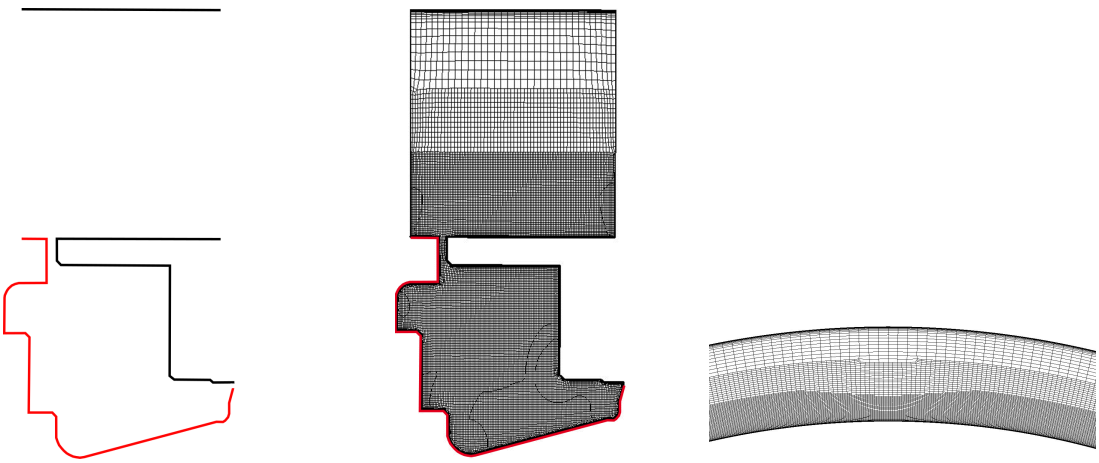

(a) (b) (c)

Figure 3.58: (a) Numerical domain for the URANS numerical simulations - (b) Meridional view of the mesh - Rotating surfaces in red - (c) View of main channel inlet mesh to highlight the cell distortion due to mesh boxing.

compensate for the hub curvature radius. The mesh used in this work presented a total of 44 million cells. For the hub boundary layer and all the cavity, the average non-dimensional distance is of $y^+ = 0.57$.

3.2.3.2 Solver settings

The solver used to perform the computation was Numeca's Fine Open solver. The turbulence model used was consistent with the steady domain being $k-\omega$ SST. Multigrid acceleration was used, thanks to the mesh presenting a minimum of four grid levels. Second order central scheme was used with a CFL number of 100. Nevertheless, the initialization procedure was performed at a limited CFL number of 2. Dual time stepping was used. Time discretization was performed through four stage explicit Runge Kutta scheme. The physical time step was set at a value of 650 Engine Order [EO] which is ten times the blade passing frequency of the H25 stage. The simulation was initialized from the result of a steady state simulation for the same operating conditions.

3.2.3.3 Boundary conditions

The computation performed aimed to reproduce the reference leakage conditions presented in section 3.2.2.5 for the design loading operating point. Figure 3.59 locates the patches used to impose the boundary conditions. Only averaged values were imposed. The boundary conditions values were extracted from the steady RANS computations of the H25 stage for the reference leakage conditions. At main channel inlet (Inlet 1), total pressure, total temperature, and flow direction were imposed. At main channel outlet, static pressure was imposed. For the leakage conditions (Inlet 2) total quantities and velocity direction were provided to the patch modelling the labyrinth seal gap. For simplicity, since the numerical setup was at its first steps, the walls were kept adiabatic in the simulation. Without a precise evaluation of the wall disc temperature, the choice has been taken to keep an adiabatic boundary condition. Otherwise, mistuned temperature difference could have caused artificial Rayleigh Bénard convection vortices that may have affected the results.

3.2.3.4 Grid sensitivity

A grid sensitivity was performed for the numerical domain presented. For this analysis, it has been chosen to only evaluate the effect of the azimuthal refinement. The flow in the cavity presents a toroidal shape so the sensitivity of the mesh to the preferential flow direction has been evaluated. The flow field was solved, on average, for three different mesh that have respectively 576, 288, and 144 points to discretize the annulus. The three mesh levels are displayed in Figure 3.60. The cut is showing the cavity mesh in the

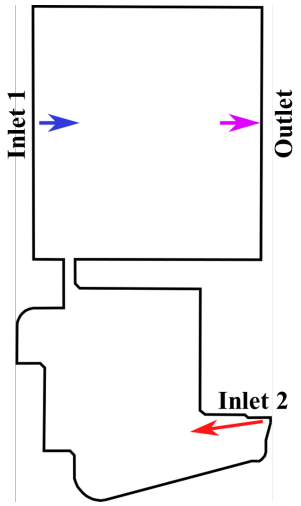

Figure 3.59: URANS simulation boundary conditions - Inlet 1: Main channel entrance - Inlet 2: Cavity injection - Outlet: Main channel exit.

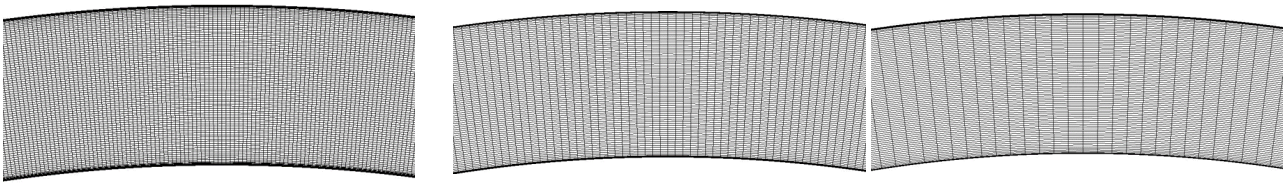

(a) (b) (c)

Figure 3.60: C2 cavity mesh for the URANS numerical setup - Mesh cut performed in Plane2 - (a) Fine mesh - (b) Medium mesh - (c) Coarse mesh.

Plane 2. The finest mesh was limited based on computation costs limitation for the unsteady simulation. In other words, true mesh convergence could have been evaluated but could not have been exploited directly in this work for 360° simulation. The angular spacing between to mesh points was of 0.625 [°] for the fine mesh. Average contour of entropy of the steady state computation are presented with the three mesh levels in Figure 3.61. The flow solver gives an axisymmetric solution for all of the cases. The average contour presented show a sensitivity to the mesh in the azimuthal direction. If the coarse grid solution clearly depart from the other mesh, the differences between the medium and fine grid are noticeable in the core flow in the middle and bottom of the cavity but also in regions where the tangential velocity component is reduced (e.g. leakage path, stator boundary layer). The finest mesh was kept for the rest of this work. The finest mesh was also selected in the eventuality of the presence of non-synchronous flow structure with the discs, to increase the spatial resolution for mode shape identification.

3.2.3.5 Result extraction and flow field convergence

The conservative quantities were extracted for each time step thanks to numerical probes positioned in the domain. The experimental setup presented in section 3.1.3.5 was reproduced to propose a direct comparison between the numerical and experimental instability content. Figure 3.62 indicates the numerical probe position. Three series of probes were positioned between 0.12 span and the cavity bottom in the

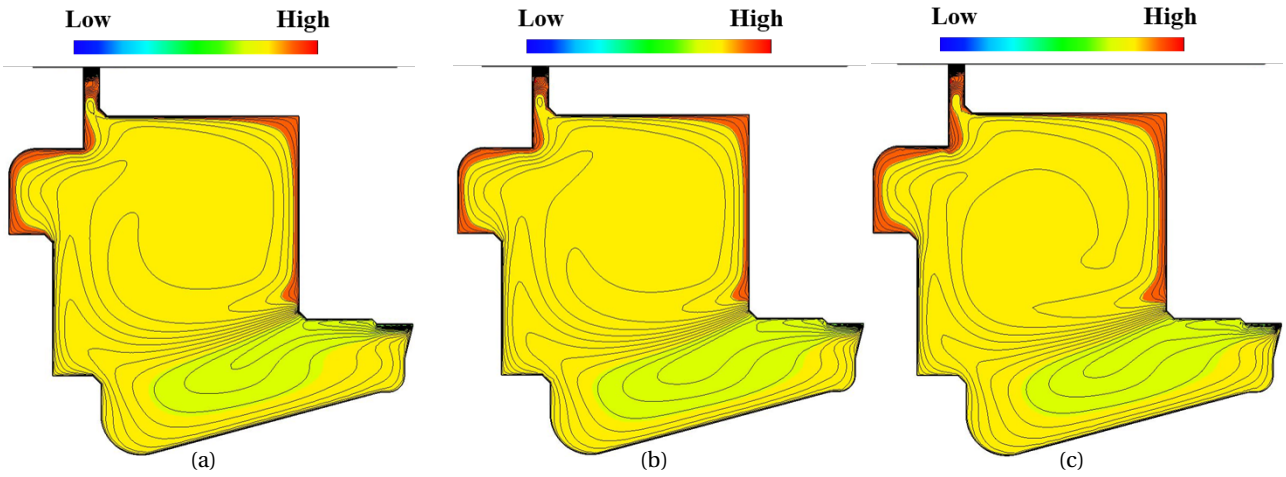

Figure 3.61: Iso contour of entropy for the fine, medium, and coarse mesh. Iso lines of 1.8 [J/K] - (a) Fine mesh - (b) Medium mesh - (c) Coarse mesh.

Plane 2 axial position for angles of respectively 0°, 144°, and 288°. These distribution in the cavity and in the main flow boundary layer matched the steady and unsteady three hole virtual probes as well as the shielded thermocouple from the experimental setup.

A series of twelve probes were positioned at the stator wall along the annulus. The angular positioning of this series matched the position of the Kulite brass inserts. Finally, a sector of the cavity trench and the direct downstream portion of the hub boundary layer was highly instrumented for multiple stator pitch width. This group of probes was used to detect if instabilities born in the C2 cavity were transported into the main channel.

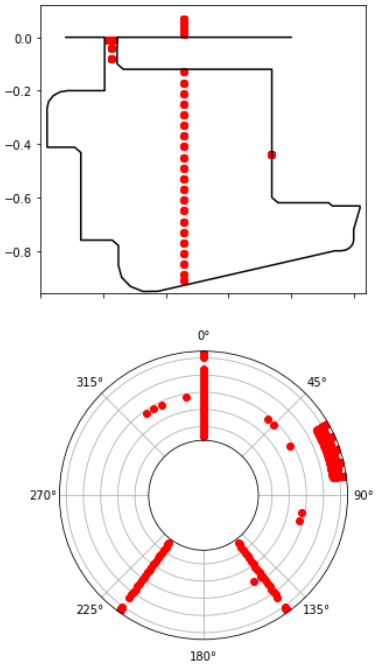

Figure 3.62: URANS simulation numerical probes position - Meridional view (top). Radius gives the spanwise position - Projection along machine revolution axis (bottom).

The flow field convergence was monitored thanks to the numerical probes presented. As mentioned in Chapter 2, the viscous diffusion time, which drive transient phenomena, required that the computations were performed on a important number of rotations to reach a stabilized state. In the case of the C2 cavity the computed viscous diffusion time indicates that, at compressor nominal speed, around 1700 rotations

are necessary to reach this state.

With the current numerical setup and with the time available, computations have only been performed for around seven rotations of the rotor disc. However, as it will be discussed in Chapter 4, the limited data recorded already helps to address the relevance of the approach that can be pushed further in a purely numerical work.

In Figure 3.63 an example of numerical probes signal belonging to the cavity and to the main channel is presented. The figure displays the variation of static pressure around the mean value taken for seven rotations after the beginning of the computation. The computation starts from a converged steady state simulation. The trigger of instabilities take one disk rotation. After the initial instability pulse, damping of the transient phenomena is observed in the signals. In the stator hub boundary layer and in the trench, pressure transient phenomena are damped quicker that in the cavity. There, after almost seven rotation, the solution is still showing a non-stabilized behaviour (green and grey curve). The pressure fluctuations in the hub boundary layer (blue curve) remain small with respect to the instabilities identified at other probing locations, for all the rotations. The same probe total temperature signals are presented in Figure 3.64. The temperature field is still in the transient phase at rotation seven. As for the pressure field, the fluctuations of temperature in the hub boundary layer are marginal. The lag between the temperature field and pressure field transient is minimal at the computation start. However, in the perspective of long run simulations, the thermal transient is the limiting factor for convergence.

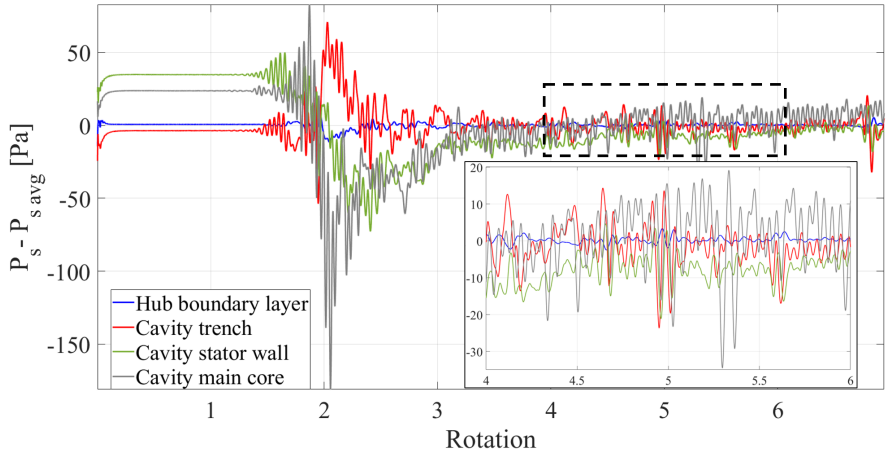

Figure 3.63: Static pressure fluctuation from the mean of numerical probes at different domain locations over seven disk rotations from computation launch - Probe in the stator hub boundary layer at 4% span (blue) - Probe in the cavity trench (red) - Probe in the stator wall at Kulite insert location (green) - Probe at -32 % span in the core flow of the cavity C2 at three hole virtual probe location (grey).

The time resolved analysis of the signal was made for the rotations where the transient behaviour were as damped as possible. Since the numerical signal did not present noise, any pre filtering is not necessary. The signals were extracted for three rotations between rotation 3.8 and 6.8 (c.f. Figure 3.63). Zero padding was applied to obtain the same spectral resolution than in the experimental data. Signal duplication (to increase peak to noise ratio) has also been tested (not showed here). However, the spectral pollution caused by the harmonics of the intersect between duplicated rotation was too important. Energy conservation of the half spectra was also considered. An example is given in Figure 3.65 a where the spectral content obtained for the numerical probe pressure signal represented in grey in Figure 3.63. In Figure 3.65a, the effect of the rotation window is presented. Regions of high energy content are better identified in the case of a large window. For completeness, Figure 3.65b presents the spectral content of the three successive rotations. It is visible that some frequency regions activate depending of the rotation (see region at 15 EO). It is then important to consider continuous signal of the largest number of rotations available.

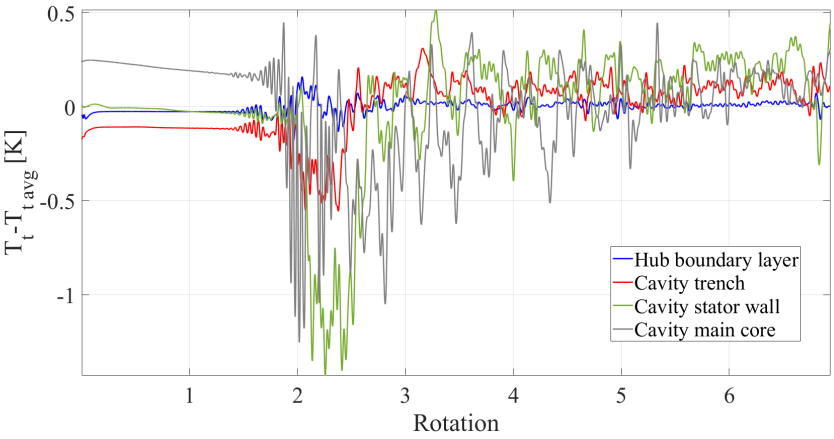

Figure 3.64: Total temperature fluctuation from the mean of numerical probes at different domain locations over seven disk rotations from computation launch - Probe in the stator hub boundary layer at 4% span (blue) - Probe in the cavity trench (red) - Probe in the stator wall at Kulite insert location (green) - Probe at -30 % span in the core flow of the cavity C2 at three hole virtual probe location (grey)

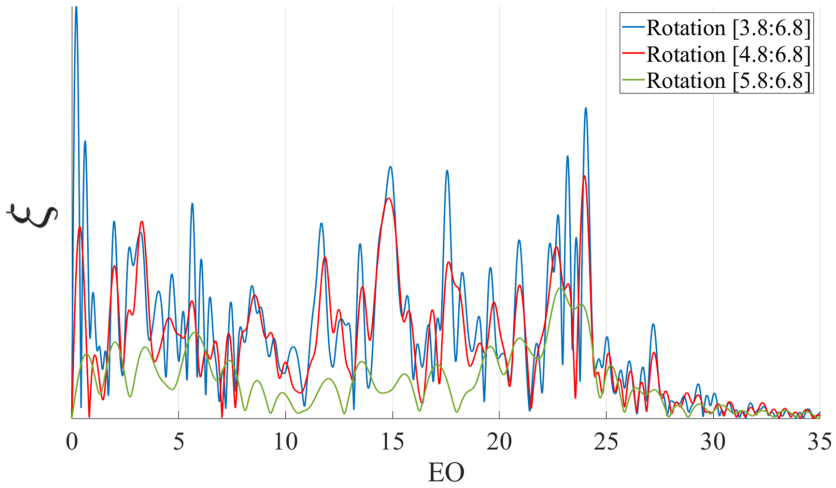

(a)

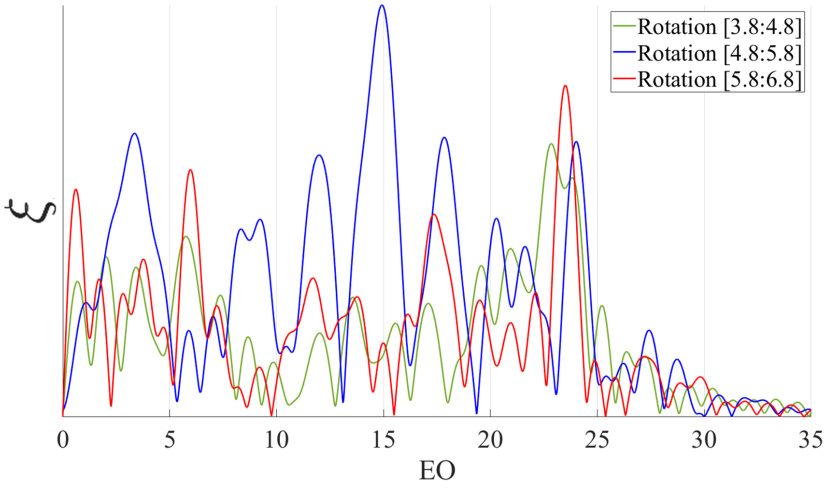

(b)

Figure 3.65: Spectral energy content of numerical probe located at (-32% , Plane 2) in the C2 cavity - Frequency in Engine Order (a) Signal length sensitivity - (b) Rotation dependence.

3.3 Conclusion

Chapter 3 presents the experimental and numerical approach used to evaluate the impact of cavity flow on axial compressor performance and stability.

In the first place, the existing H25 test section was modified to investigate the cavity flow field. There are few examples of cavity flow experimental characterization in realistic conditions for axial compressors as far as flow regime and geometry representativity were concerned.

Main channel flow has been updated to evaluate stage outlet unsteady flow field as well as stator inlet boundary layer. Access to the cavity main core steady and unsteady flow field was guaranteed by cylindrical probes, used in virtual mode, that traverses the stator hub platform. Unsteady data were also collected in the stator boundary layer. A bespoke injection setup allowed to fine tune the leakage flow injected in the stator hub cavity of the H25 stage. The operating conditions covered allowed to investigate the effect of the leakage fraction, the stage loading, and the compressor rotational speed.

To support the experimental activities, two numerical setups were used. The first one proposed, thanks to steady RANS computations, a help in design of experiments as well as a first comparison dataset. The setup was validated against data collected in a previous campaign to this work. Thanks to a numerical domain where parametric injection was generated, it is possible in Chapter 4 to status on the relevance of such approach for the study of cavity flows in axial compressors. The second setup was an unsteady simulation performed on a domain where the cavity was isolated. Numerical settings were selected to ensure the best physics description of the phenomena. The objective of such computation was to evaluate its interest for future studies through a direct comparison with the collected database.

Chapter 4

Results and discussion

THis chapter presents the results obtained on the H25 test section regarding the effects of cavity flow on axial compressor performance and stability. The results were obtained thanks to the instrumentation and numerical setups, for which respective calibration and validation have been presented in Chapter 3.

The first part focuses on the main channel flow without cavity flow analysis. It brings information to assess the impact of variable leakage fraction on the global performance, on the average radial gradients, and on the two dimensional flow field of the H25 stage. The second part of this chapter focuses on the cavity trench region and the stator inlet hub boundary layer. A description of the cavity and main channel flow interaction is made to complete the analysis of the first section. Section three and four consider the H25-C2 cavity flow only. There, an analysis is made on the average flow field (section three) and on the time resolved data collected (section four). The objective of these sections is to present the flow features attributable to the C2 configuration. In a larger extent, it allows to conclude on the contribution of the C2 cavity, and its instabilities, in the H25 stage performance degradation under forced leakage conditions. To finish, the last part introduces the response of the H25-C2 system induced by variations in the compressor rotational speed.

Contents

4.1 Impact of shroud cavity leakage on H25 stage main channel flow

In this part of the chapter, the main channel flow analysis is carried out to quantify the impact of the leakage flow forced injection on the main flow. The results start from the review of the stage performance to finish with a 2D flow field analysis at the stage outlet. An intermediate step is produced to understand the effect of the injection on the average radial gradients.

4.1.1 Global performance analysis

Performance with and without forced leakage in the C2 cavity is evaluated. The operating range investigated is between the low loading point (LL) and machine failure, so beyond the near stall operating point. Prior to the presentation of the results, information concerning the curve build and machine environment are provided.

4.1.1.1 Performance curve build

The H25 stage performance without leakage is obtained thanks to constant throttling of the control valve. The throttling is performed slowly enough, with a throttle valve closure speed of $2[\mu m/s]$, so that the machine remains in the range of thermal stabilization. The thermal stabilization is ensured thanks to the metal temperature measurement of machine casing inside and outside the test section, in the stage outlet plane.

Performance curves with injection are built with successive stabilized points. This is due to the obligation to manually adapt the injected mass flow to produce the targeted leakage fraction. To obtain a discretized curve between low loading condition and the stall limit of the machine, several operating points are sampled. Each point performance results from an average of the performance sampled over three minutes with the steady instrumentation (@2[Hz]).

At nominal speed, three stabilized points were equally spaced based on the stage static to total pressure ratio in the interval between the low loading and design loading operating point. In the same way, three stabilized points cover the interval between the design loading point and the near stall operating point. The repartition of the points with respect to the stage flow coefficient is visible in the Figure 4.2.

The investigation of machine failure under injection conditions, also called stall exploration (SE), was done thanks to constant throttling from the near stall operating point up to the first surge cycle of the test section. Due to the need to manually adjust the leakage fraction, the evaluation of the stability limit cannot be performed at constant leakage fraction. Nevertheless, the stall limit of the machine is close enough to the near stall operating point to obtain a limited change in leakage fraction between near stall and the last stable point. As an example, in the case of injection 1, if the leakage fraction at near stall operating point is of 0.56%, the leakage fraction at the stability limit is of 0.567%, at constant injected mass flow.

4.1.1.2 Performance curve collapse

The compressor test section and facility is a dynamic system that presents performance fluctuations even at stabilized operating point. When continuous throttling is applied to the compressor to measure performance curves, operating points do represent a “cloud” around the mean performance curve as shown in Figure 4.1a for the stage static to total pressure ratio. The operating point that limits the curve at lower corrected mass flow is the point prior the generation of the first surge event. After detection of the first and last point of the curve based on the throttling parameter λ defined in equation 3.1, the performance curve is divided in fifty λ classes from which the mean value of each flow parameter is retrieved.

The iso lines of throttling parameter are indicated in black in both Figure 4.1a and Figure 4.1b. Skewness and standard deviation in each class are computed. Collapsed data are presented in Figure 4.1b. It contains the mean value of static to total pressure ratio in each class as well as standard deviation intervals ($\pm\sigma$) for both corrected mass flow and pressure ratio. In this example, with the number of classes chosen, the average value of standard deviation on the mass flow is of 0.0055 [kg/s] and of 0.0005 on the pressure ratio.

The first point of the curve (λ_{min}) as well as the last stable point (λ_{max}) are kept out of any class. This allows to identify for each performance curve the flow coefficient corresponding to the last stable measured point.

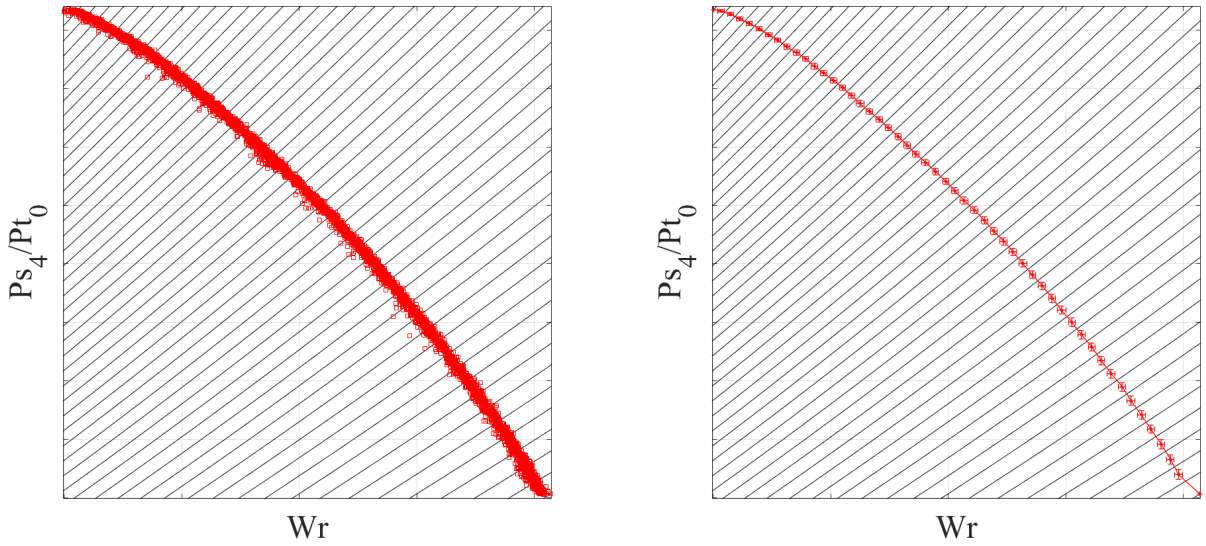

(a) (b)

Figure 4.1: H25 nominal speed performance curve collapse in throttling parameter classes. Static to total pressure ratio as a function of corrected massflow (a) Raw H25 performance map obtained after continuous throttling from low loading point to the first surge event (Red) – Iso lines of throttling parameter (Black) - (b) Final H25 performance map obtained after data collapse in throttling parameter classes (Red) – Mass flow and pressure ratio standard deviation in each class are indicated (Red error bars) – Iso lines of throttling parameter (Black).

4.1.1.3 Injection conditions

The leakage fraction conditions computed from the measured data along the injection line are presented in Figure 4.2. As introduced in table 3.4, three injection conditions are generated.

In the test campaign, for H25 nominal speed (100 Nn), injection 1, 2, and 3 are investigated. At partial speed (85 Nn), injection 1 only is studied (see Figure 4.2).

Injection 1 and injection 2 are respectively at targeted 0.56% and 0.3% of leakage fraction for the whole operating range. Since injection 3 imposes the static pressure at stage outlet in the C1 disc cavity, its leakage fraction increases when the flow coefficient reduces.

4.1.1.4 Annulus non uniformities – Impact on measured performance

Azimuthal non uniformities in total pressure and temperature are detected in the H25 stage both at the inlet and outlet of the test section. As a consequence, the evaluation of the stage performance, e.g. isentropic efficiency, is impacted by the position of the instrumentation with respect to the non uniformities.

The evidence of the annulus non uniformities is presented in appendix C.

Due to such behaviour, the measured efficiency curve as a function of the flow coefficient differs when the outlet stage instrumentation clocking changes. The motor controlling the clocking is called M1 and allows a rotation of the outlet rakes of approximately 1.5 pitch. The value of M1 ranges from -0.04 to 1.5 with 1 being one stator pitch width. A correction on the stage efficiency is proposed in appendix C for the operating points where a radial and azimuthal map of the flow is available at stage exit only, i.e. when M1 covers its full range.

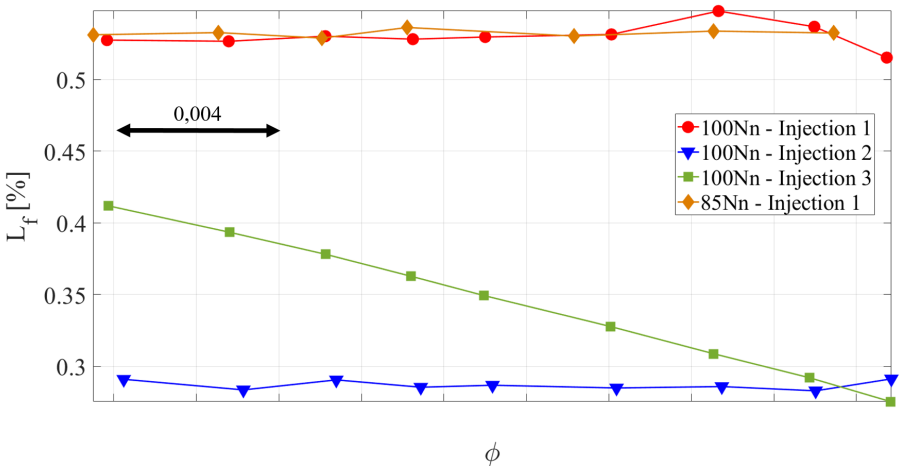

Figure 4.2: Leakage fraction imposed to evaluate injection effect on H25 performance at nominal speed (100Nn) and partial speed (85Nn).

Continuous throttling curves are compared between two stage exit instrumentation position M1 = -0.04 and M1 = 1.25. Figure 4.3a, presents the efficiency curves obtained. As mentioned, the curve shape is different as a function of M1. The curve at M1 = 1.25 has an efficiency peak around the design loading. For M1 = -0.04, peak efficiency is located between design and near stall operating point. When injection is applied, the differences in efficiency curve type remain as a function of M1.

Figure 4.3b presents the efficiency drop in % induced by the injection 1 condition from the no injection case as a function of the flow coefficient. Each curve corresponds to one position of the stage outlet instrumentation. Major differences (0.37%) in the predicted efficiency drop are noticed at high flow coefficients which indicates a high dependency of the measured efficiency to the M1 position. Unfortunately, no azimuthal traversing is available in this part of the curve to fully understand the reason for such differences, that also exists for the other injection levels. The smallest difference (0.05%) between the two curves in Figure 4.3b is reached for the design loading operating point (DL). When the flow coefficient is further reduced, the difference in efficiency drop prediction increases back to 0.1%.

Figure 4.3b is used here to present that the position of the outlet instrumentation affects the conclusions on performance degradation when injection is applied. To obtain an evaluation of the performance drop under injection, a performance curve should be measured for every position of M1, for every injection level, to obtain the corrected efficiency curve. This activity was out of the scope of the test matrix.

That is why, the quantitative evaluation of efficiency drop due to injection is performed on the points where corrected efficiency is available only (see table 3.1). When no quantitative considerations are presented, the data at position M1 = -0.04 are used.

4.1.1.5 Effect of injection on H25 performance

Performance curves trends and stall margin effect

The performance effect of injection is presented at rotor nominal speed. The detailed performance curves are provided in Figure 4.4 where the stage isentropic efficiency and loading are plotted for the different injection levels applied. The curves with injections are split in two parts to separate the stall exploration (SE) from the rest of the curve. On Figure 4.4a the injection level affects the isentropic efficiency on the entire investigated range. The efficiency drop from the no leakage is proportional to the injection rate. The maximum injection (injection 1) represents the maximum efficiency drop and the minimal injection (injection 2) the minimal drop. The efficiency drops are quantitatively defined further in the next section.

The expected trend of the variable injection 3 appears in Figure 4.4a. It matches, at high flow coefficient, the efficiency drop observed with injection 2, since leakage fraction coincides (see Figure 4.2). At lower

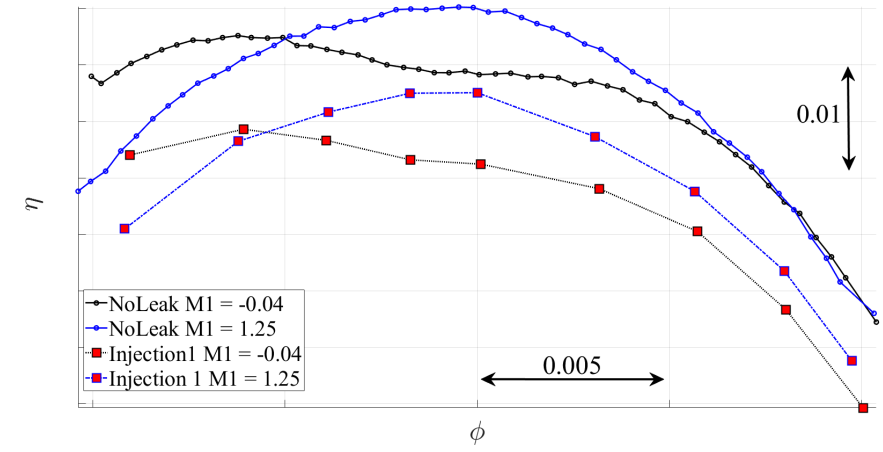

(a)

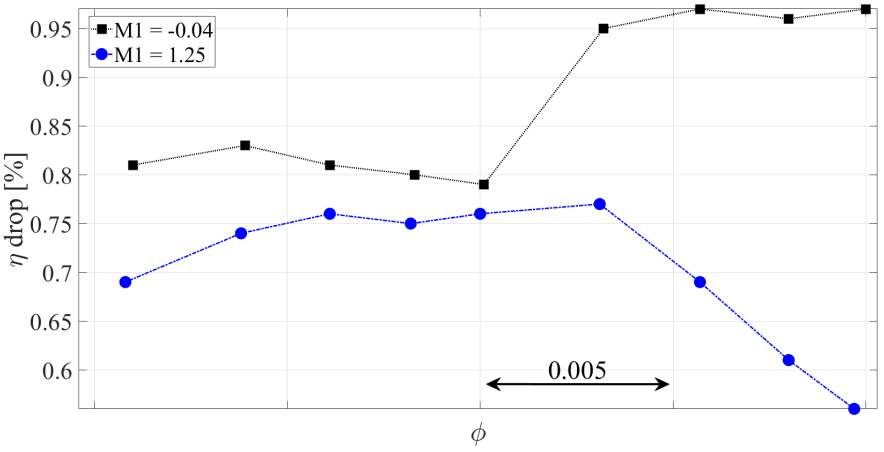

(b)

Figure 4.3: (a) Comparison of H25 stage efficiency curves at nominal speed for M1 = -0.04 and M1 = 1.25 – No leakage and injection 1 - (b) Efficiency drop in % from no injection to injection 1 for M1 = -0.04 and M1 = 1.25.

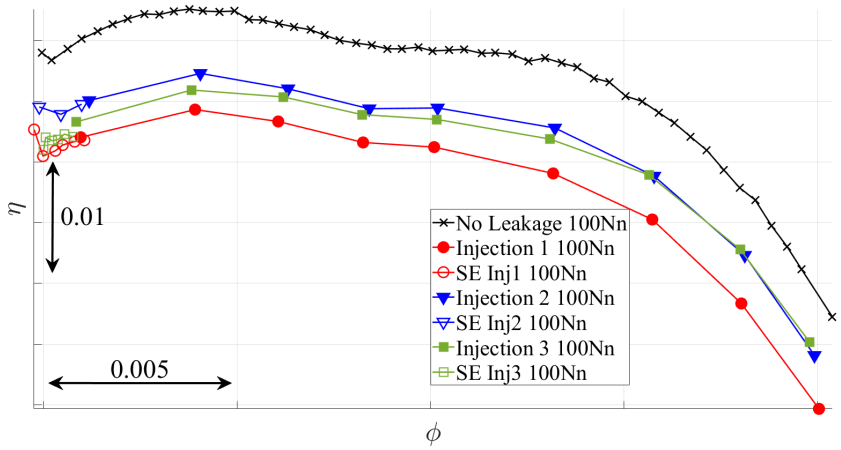

(a)

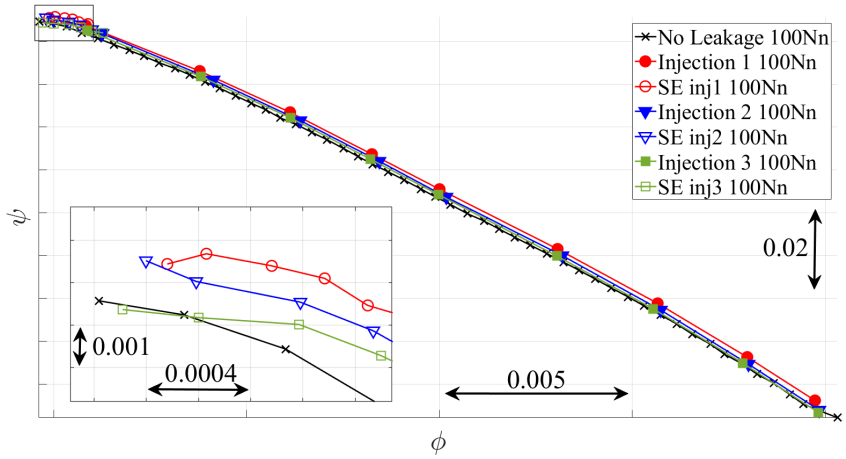

(b)

Figure 4.4: (a) H25 efficiency curves with and without injection – Nominal speed (100Nn) – M1 = -0.04 - (b) H25 stage loading with and without injection; zoom on the last stable point - Nominal speed (100Nn).

flow coefficient, the injection 3 leakage fraction increases. Its efficiency curve drifts towards the maximum injection (injection 1) as the performance degradation increases with the leakage fraction.

It is visible on the Figure 4.4b that the H25 stage loading ψ is few modified by the presence of the injection.

An important conclusion is that the last stable point flow coefficient is independent from the injection level. For stable operating points, i.e. no rpm or throttle transients, the injection level has no effect on the stall margin of the H25 axial compressor stage. This conclusion is eventually found in Wellborn and Okiishi (1996) for a multi-stage low speed axial compressor.

The behaviour observed and presented at nominal speed has also been found at partial speed, for the H25 stage.

Quantitative description of efficiency drop

In this section, a quantitative evaluation of the corrected efficiency drop caused by the injection is given. Table 4.1 summarizes the corrected efficiency drop for the operating conditions studied in the experimental database. The values are indicated with respect to the design loading value at nominal speed. At nominal speed, the largest performance degradation is measured at the design operating point with an efficiency drop of 0.97% for the maximum injection (L_f = 0.56%). At partial speed, the performance penalty for the

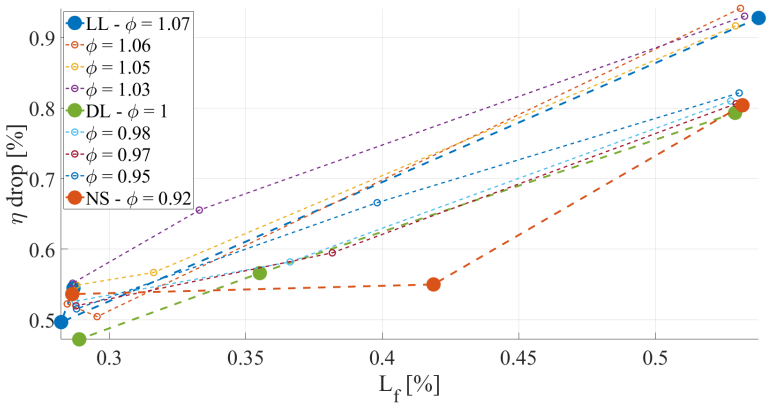

(a)

Figure 4.5: H25 stage isentropic efficiency drop with leakage fraction at rotor nominal speed - M1 = -0.04.

design point at injection 1, defined for the same λ value, is less important with 0.74% efficiency decrease.

The comparison between the near stall operating points at nominal and partial speed, evaluate that the efficiency drop due to the injection 1 is similar between the two rotational speeds investigated. From the definition of the operating points (see Figure 3.6) the data state that for a fixed leakage fraction, the efficiency drop is constant for points defined with the same stall margin.

At constant machine rotation speed, the nominal speed indicated that the efficiency drop is lower at high loading point at fixed leakage fraction, for both injection 1 and 2.

To complete the previous statement, stage performance drop with the flow coefficient is presented in Figure 4.5 for M1 = -0,04. The operating points investigated are referenced thanks to their flow coefficient. For that M1 position, the measured efficiency drop ranges between 0.47% and 0.94%.

What is seen in literature is that the stage loading has an effect on the slope of the linear relation between the leakage fraction increase and the stage efficiency drop. As an example, Wellborn and Okiishi (1996) show that, at low flow coefficient, the efficiency drop is higher than at design loading conditions, for a given seal tooth clearance (that is quite large 1% span). In the H25 stage, for M1 = -0.04, the measured efficiency drop is higher at high flow coefficient, than for low flow coefficient points. This behaviour is also the one of the corrected efficiency as presented in Table 4.1.

The trend in Figure 4.5 is similar to the one found in Wellborn and Okiishi (1996) for the third stage of their configuration. The near stall point presents a "kink" where the efficiency drop suddenly increases with the leakage fraction while the near peak efficiency point keeps a linear trend.

	100 Nn			85 Nn	
	No Injection	Injection 2	Injection 1	No Injection	Injection 1
DL	Ref = 0	-0.71	-0.97	Ref = 0	-0.74
NS	Ref = 0	-0.42	-0.80	Ref = 0	-0.79

Table 4.1: Corrected isentropic efficiency drop in % for the H25 stage under forced injection - For each operating point, the value is expressed relatively to the no injection case.

To support the findings of the experimental campaign Figure 4.6 references the combined corrected efficiency drop from the experimental and CFD RANS data as a function of the leakage fraction of the injected flow.

Numerical data are evaluated for a wider range of leakage fraction. As stated in Chapter 3, the simulation performed on the H25/C2 stage with injection do present a different flow coefficient than the experimental design loading point. The flow coefficient of the numerical data is lower by 1.7%. Numerical result present similar slope with respect to the experimental data in the range 0.2% : 0.4% leakage fraction. In leakage

fraction interval 0.3% to 0.4%, the numerical prediction falls within 0.1% from the experimental data. From this data, the use of steady RANS simulations shows its relevance in defining guidelines and performance degradation range in preliminary design phase for axial compressor stage and associated cavities.

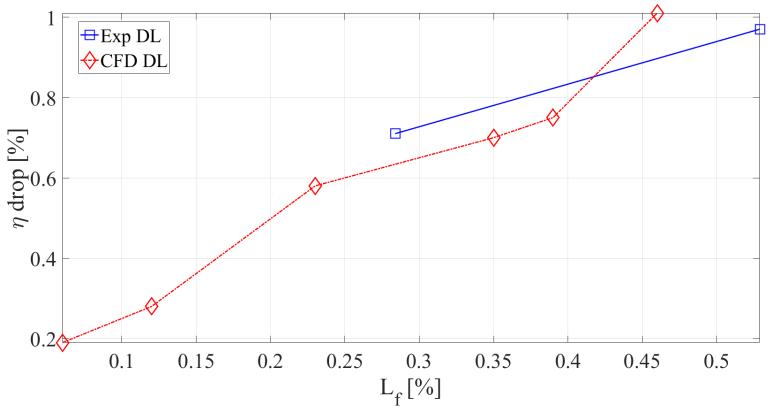

Figure 4.6: Stage isentropic efficiency drop as a function of leakage fraction at H25 compressor nominal speed – Corrected experimental data (square symbol, continuous line) – CFD steady RANS data (diamond symbols).

4.1.1.6 Labyrinth gap and leakage fraction

In classical turbomachine assemblies (i.e. multi-stage with natural recirculation), the under platform labyrinth seal gap drives the components of the leakage flow. Leakage fraction is one of them. The modifications performed in such machine to control the leakage fraction at a given operating point consist in changing the seal gap, to create bigger leakage fraction (large gap), or smaller leakage fraction (small gap). The obtained variation in leakage fraction depends also on the type of seal used (straight, stepped, ...) as shown in Sultanian (2018). Since seal gap opening and leakage fraction increase are corresponding, plots referencing seal gap opening to efficiency drop presents a decrease in efficiency with the increase of labyrinth seal gap (see Wellborn and Okiishi (1996)).

Such plot in the current study would be counter-intuitive and go against literature results. In the H25 test section, the leakage generation was made through adjacent rotor disc cavity pressurization (cavity C1 in Figure 1.16). Since the labyrinth seal is mounted cantilevered on the rotor disk, an increase in disk cavity pressure effectively closes the labyrinth seal as described in appendix B. The FEM analysis performed on the labyrinth seal teeth (c.f. Figure B.1) estimate the seal gap closing taking into account the pressure balance between the disk cavity pressure and C2 cavity pressure.

In Figure 4.7a and Figure 4.7b are indicated the labyrinth closing Δr, in percentage of the main channel span, of both teeth 1 and 2 (see Figure B.1) from the cold mechanical gap. The data presented include the operating points measured during the performance curve at nominal rotor rotation speed. On average, for tooth one, the seal gap closes by 0.03% of the main channel span. For the second tooth, the value averages 0.025% span. In the range investigated, the labyrinth closing is proportional with the leakage fraction for both teeth. Filled markers identify operating points at low loading, design loading, and near stall loading. At constant leakage fraction, when the stage loading increases, so ϕ decreases, the seal gap opens. Low flow coefficient operating points requires less injected mass flow to maintain the leakage fraction so less pressure in the adjacent disk cavity. The prediction of the gap closing is affected by the selected boundary conditions of the FEM analysis. These boundary conditions were known prior to the campaign detailed in this work. With the data collected along the injection line in the current experimental campaign, a more complete stress analysis can be performed in the future to fine tune the seal gap closing predictions.

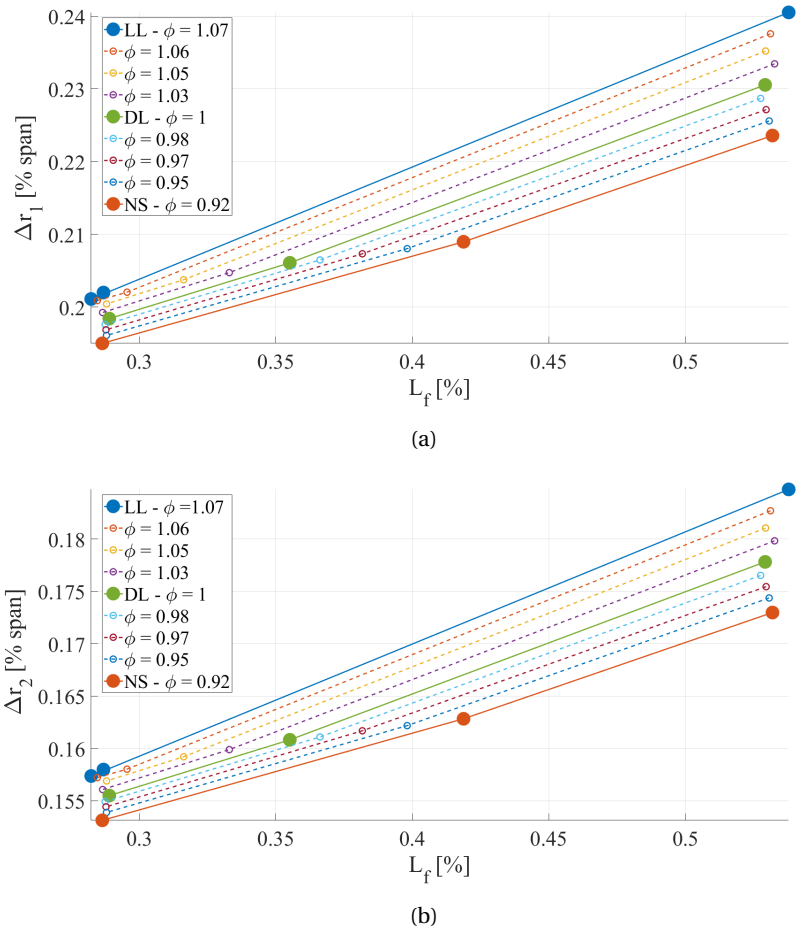

Figure 4.7: H25 stage labyrinth closing from the cold mechanical gap in % of main channel span. Result is indicated as a function of the leakage fraction and for multiple normalized flow coefficients - Compressor nominal rotation speed (a) Tooth 1 radial displacement - (b) Tooth 2 radial displacement.

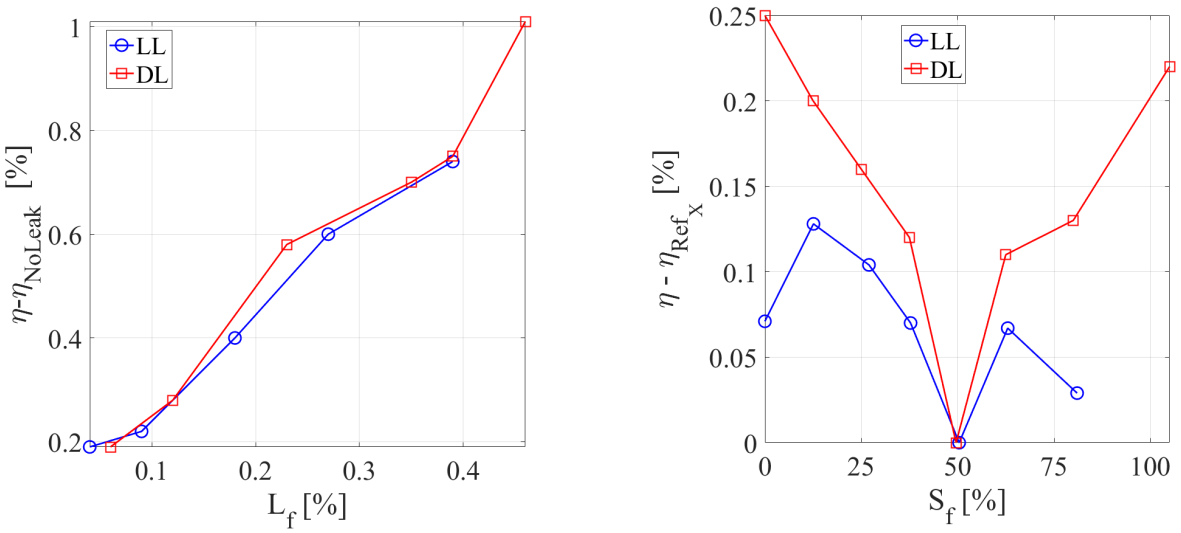

(a) (b)

Figure 4.8: Numerical prediction of the efficiency drop due to injection in the C2 cavity at low loading (LL) and design loading (DL) operating point for 100Nn rotational speed (a) Efficiency drop from no leakage case as a function of the leakage fraction - (b) Efficiency drop with respect to the reference leakage conditions generated by the NAC numerical domain as a function of the labyrinth exit swirl ration in %.

4.1.1.7 Comment on the results obtained in the steady RANS computations

From the previous paragraphs, the sensitivity of the H25 stage to the leakage fraction has been presented and is recalled in Figure 4.8a. The impact of the leakage flow swirl ratio at labyrinth exit is also evaluated. Results are presented in Figure 4.8b. The sensitivity to this parameter is evaluated against the efficiency value obtained for the reference leakage conditions. The reference leakage is the leakage given by the natural cavity domain presented in Section 3.2.2.1. The swirl ratio produced by the reference leakage is giving the minimal performance degradation for both low loading and design loading operating point. For both conditions, an increase or decrease of the labyrinth exit swirl ratio produces a lower stage efficiency. For the wide swirl ratio interval covered, the efficiency drop is limited to 0.2% from the reference. In other, words, from an experimental point of view, the effort that would have been engaged to produce a swirl ratio controlled injection may not have been rewarded by a dependence of the stage performance to this parameter. Eventually, in a different context, it has been showed by Schröder et al. (2020) that the swirl ratio has a small impact on the flow field. Demargne and Longley (2000) also presented that for cavity trench exit swirl ratios higher than 1 (or 100%), downstream stage performance improvement are observed. In the present case, the computation that evaluates a swirl ratio higher than 100% at the labyrinth exit do not produce such high value at the trench exit which explains the associated efficiency drop. Hence the conclusion of Demargne and Longley (2000) can not be verified here.

4.1.1.8 Partial conclusion

The analysis of H25 stage performance in injection conditions support the fact that the use of a closed loop facility and the methodology implemented in this work is suitable to generate realistic injection conditions, and so, to further answer positively to the objectives of the study.

When injection is applied, the stage isentropic efficiency drops with the increase in leakage fraction. On the H25 test case, a reduction of 0.97% efficiency is measured at design operating conditions for a leakage fraction of 0.56%. The link between injection, stage loading, and performance degradation do not follow a unique law in the database collected.

It is evidenced that the leakage fraction do not influence the stage stall margin for non transient operation of the machine.

To finish, it is presented that steady RANS simulations are relevant to quantify the performance degradation caused by the leakage flow injection. Based on these results it is also possible to identify that the compressor stage is second order sensitive to the swirl ratio and first order sensitive to the leakage fraction at the exit of the cavity rim seals.

The next sections describe the flow field in the main channel and in the cavity in order to point out the mechanisms leading to the measured efficiency drop caused by the injection.

4.1.2 H25 stage outlet flow details under injection

Stage outlet flow is investigated in this section. Time averaged and time resolved data are presented to track any change in the flow field induced by the presence of the leakage flow.

4.1.2.1 Labyrinth seal homogeneity

Appendix C highlights existing annulus non uniformities, mainly due to thermal stratification in the stage. The presence of such non uniformities lead the author to evaluate the possibility that non uniform injection may also occur.

When leakage is applied, the labyrinth clearance partly defines the leakage fraction. In the case of a non uniform clearance around the annulus, regions of high leakage and low leakage appear. If the mixing process in the cavity do not homogenizes the leakage flow, it results in a distortion (non uniform azimuthal flow) of the flow field felt by the downstream blade row.

Moulds from the H25 stage labyrinth seal were sampled to evaluate sealing uniformity. Two different sections labyrinth sections are analysed. The samples are presented in Figure 4.9. One sample is taken in a region where abradable is used but in a clean form. The second sample is extracted from a region where the abradable is damaged. It is clear that the clean region of the moulding presents sharp lines induced by the rubbing of the teeth in the abradable. In the damaged region, the abradable do not present the trace of a clear teeth rubbing so that the sealing effectiveness of the labyrinth may be reduced at that location.

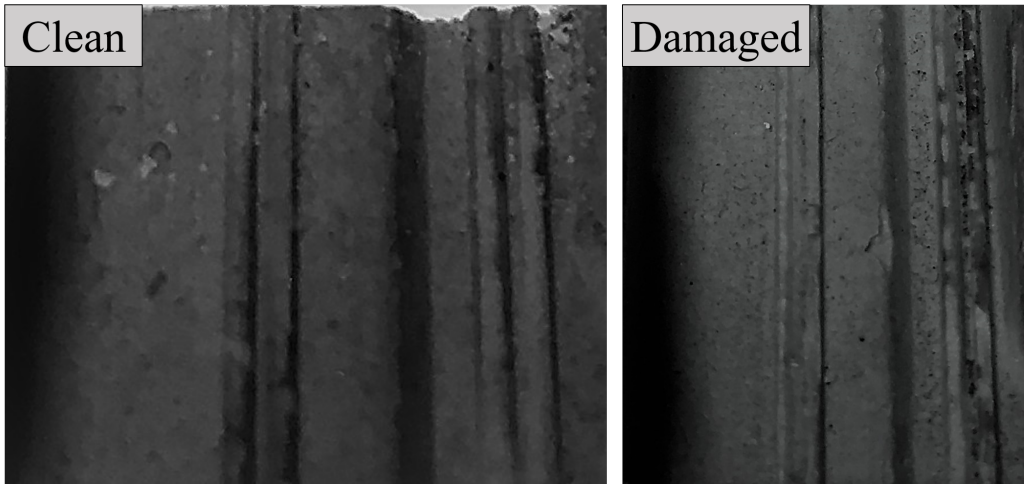

Figure 4.9: Negative mouldings of clean and damaged region of the abradable used in the two teeth stepped labyrinth seal of the C2 cavity.

Leakage uniformity is evaluated at stage outlet. The total temperature rakes are used to monitor the total temperature increase in forced injection condition with respect to the case where no leakage is applied. Their azimuthal position is used to track temperature field changes around the H25 annulus. The nominal speed design loading operating point is taken as an example. Figure 4.10a and 4.10b present, for the injection 2 and injection 1 (resp.), stage outlet to inlet temperature increase relatively to the no leakage case. The field computed in that way do not include the effects of the H25 thermal stratification. When injection is applied, the low span region (below 0.4 span) of each rake sector activates with higher temperatures than in

the no leakage case. In the high span region marginal changes in the order of 0.05[K] to 0.1 [K] are noticed (systematic uncertainty of 0.25[K]). Non uniformity between sectors is visible on both figures. Rakes sector on the machine top (i.e. A and E) do present less temperature increase for both injection levels. In the other sectors, the maximum temperature increase is always in sector D hub with 0.8[K] and 1.2[K] for injection 2 and 1 respectively. In Figure 4.10b, the temperature increase is noticeable for rake B hub region. It indicates a preferential region for the leakage flow to collect.

In the H25 stage, the aforementioned consideration informs that there are different levels of cavity to mainstream interactions for the same operating conditions.

With different level of local injection, in defined angular sectors, it is also possible that the cavity flow field exhibits simultaneously multiple topologies around the machine annulus.

4.1.2.2 Stage outlet flow field

Stage outlet measurement of the flow field with radially and azimuthally traversed fast response pressure probe is performed at angular position 72°. The azimuthal location of the probe is then close to rake B position, that showed high sensitivity to leakage. For each operating condition investigated, a radial and azimuthal cartography of the flow is performed with a minimum of 532 points for the intervals [0.077:0.8] span and [0:1.48] pitch.

The measured maps of entropy generation for the near stall loading operating point are presented in Figure 4.11a and Figure 4.11b, for the no leakage condition and the injection 1 respectively. The highest entropy region is located in the bottom part of the stator wake where secondary flow system is highly contributing to the loss by means of entropy generation.

The entropy difference between the map with and without injection is given in Figure 4.11c. When injection is applied, measured entropy increase is low on average and with no clear pattern. It is expected that the stator row interacts with the leakage flow and recovers from its effects (see Flores Galindo (2018)). It causes less traceability of the leakage flow one chord downstream of the stator row. The leakage flow is expected to remain close to the end wall, in the secondary flow system of the blade row. Nevertheless, as already mentioned in Chapter 3, the probe head size do not allow measurements below 7.7% span so that the leakage flow effect may not be detected, on average, also for that reason.

Stage outlet unsteady activity is presented in this paragraph. Dominant frequencies and the changes in flow field dynamics brought by the injection are highlighted.

The analysis of the time series collected at H25 stage outlet is done at three different locations indicated in Figure 4.12. The probe positions are set with respect to the stator wake identified on the pressure map. Location A acts as a reference point for the other probe positions. It is located at midspan and mid pitch, away from end walls and blade. Location B and C are chosen at the lowest span possible in order to detect the presence of the cavity flow that is convected in end wall secondary flow system. Mid pitch (B) and stator blade suction side (C) are selected as regions of interest thanks to the information gathered in section 1.5.3.

The ensemble average spectra of the three probes at design loading, no injection is presented in Figure 4.13. The energy content of the blade passing frequency (65 EO) dominates. However, spatial sensitivity is detected in frequency ranges below the blade passing frequency (BPF). The ensemble average spectra for the position A acts as a control and is subtracted from the ones at location B and C. This is done to present the local most energetic frequencies and track their evolution with the injection. Figure 4.14a and Figure 4.14b show the resulting ensemble average spectra for no leakage and injection 1.

The frequencies of the resulting spectra are sorted by energy content. Table 4.2 and Table 4.3 present for point B and C, the most energetic frequencies with and without injection, at compressor nominal speed, for the design loading and near stall operating point. The blade passing frequency and its harmonics are omitted on purpose if energy remains in the residual spectra. When peak detection is not clear (noise), the value of the following frequencies is not indicated (−). Linear combinations with the BPF are also indicated.

When no leakage is applied, the dominating regions are located for 3 EO and 21 EO. The frequency at 3 EO is predominant in point B where 21 EO is predominant at point C. Eventually, in point C, the presence of the peak at 24 EO (21+3) in three of the four cases suggests an interaction of the flow structures responsible for the 21 EO and 3 EO. The presence of the 24 EO frequency may also be linked with the downstream

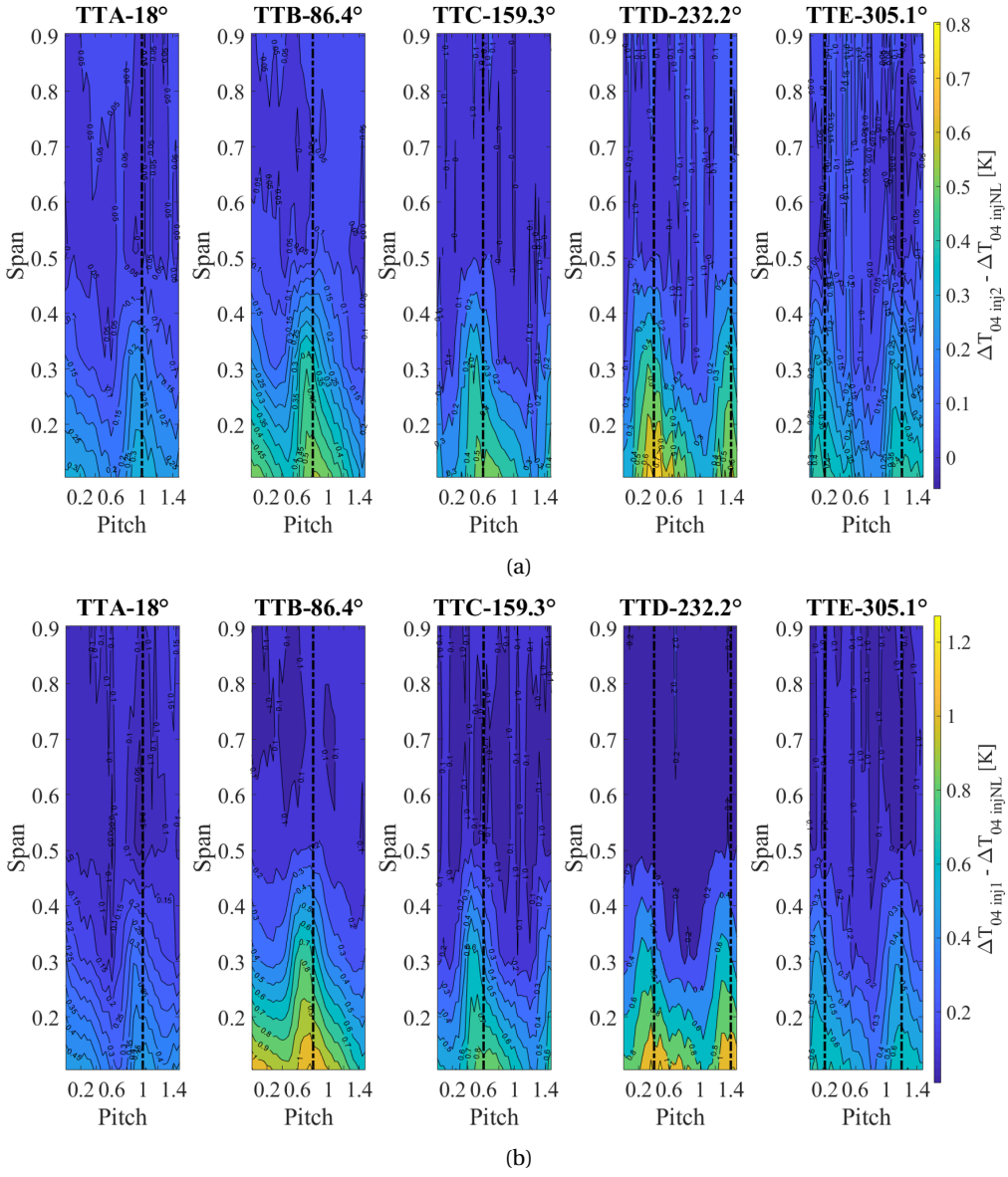

Figure 4.10: Total temperature rakes measurement at stage outlet for nominal speed and design loading condition. Stage inlet to outlet temperature increase under injection condition with respect to no leakage case. Black dashed lines indicates the stator trailing edge position (a) Injection 2 at $L_f = 0.3\%$ - (b) Injection 1 at $L_f = 0.56\%$.

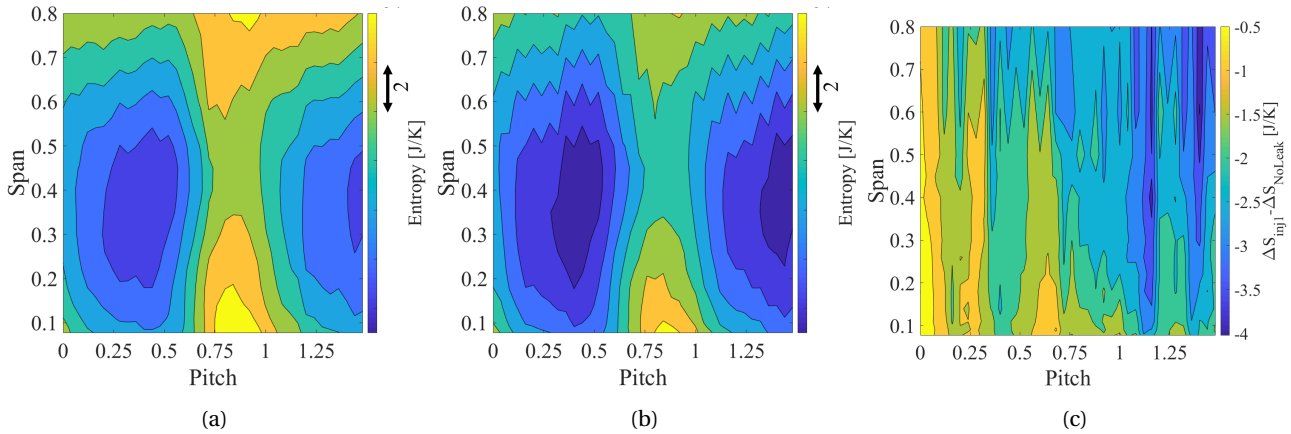

Figure 4.11: Measured entropy maps at H25 stage outlet - Nominal speed near stall loading operating condition - (a) No leakage - (b) Injection 1 at $L_f = 0.56\%$ - (c) Difference between the (a) and (b) maps.

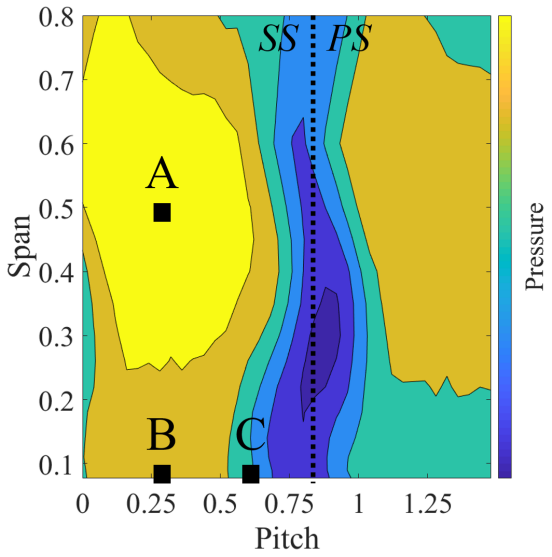

Figure 4.12: Location of probe position A, B, and C in the stage outlet pressure map for unsteady analysis - PS = Pressure side - SS = Suction side.

convection of the third stationary mode resulting from the interaction between the rotor platform and the stator sectors at the rotor stator interface (see table 2.3).

When leakage is applied at design loading, the frequency at 10 EO appears in both points. As presented in section 2.4, the estimated Helmoltz frequency of the C2 geometry is of 10.2 EO which fits that range. In general, there are not dramatic changes in the measured frequency content at stage outlet when leakage is applied.

The frequency content of temporal fluctuations, around the ensemble average, at position A, B and C is also presented in Figure 4.15. With a constant injection at 0.56% leakage fraction, the design loading point and near stall loading (on Figure 4.15a and Figure 4.15b resp.) do not show clear spectral activity uncorrelated with the rotor disk. The only clear peak present is a residual peak of the BPF.

In conclusion, the observation of the H25 stage outlet flow do not present clear differences from the no leakage to injection 1 leakage at varying operating conditions.

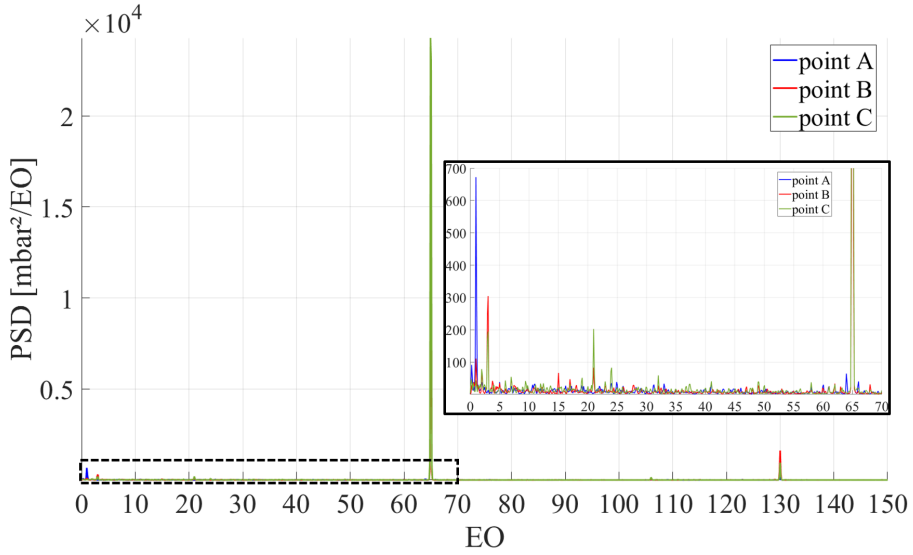

Figure 4.13: Spectra of ensemble average at probe location A, B, and C - 100Nn, Design loading, no leakage.

Table 4.2: Most energetic frequency ranking of residual spectra at position B (i.e. subtracting point A energy content) - compressor nominal speed.

f_B	DL NoLeak	DL inj1	NS NoLeak	NS inj1
1	3	3	3	3
2	21	2	BPF − 3	BPF − 3
3	15	15.4	BPF − 1	3.4
4	17	15	-	BPF + 3
5	3.78	10	-	57
6	BPF + 3	1.6	-	2 ∗ BPF − 3
7	BPF − 3	4	-	-

4.1.3 Stator inlet average flow field

The time average inlet flow field at stator row inlet (Plane 2) is detailed in this section. The objective is to understand the impact of leakage flow on the low span region downstream of the cavity trench. The resulting changes in stator inlet flow conditions are presented and discussed.

Velocity field is analyzed in the first place. The velocity components of the flow in Plane 2 are taken from hot wire measurement data. The hot wire data are collected up to 60% span in the main channel.

In the first place, the design loading operating point at nominal speed is analysed. As mentioned in Section 3.1.3.7.2, normalization or reference with respect to the midspan value is used in the flow gradient profiles. In Figure 4.16a, the axial velocity ratio with respect to the midspan value is plotted. Due to the injection, axial blockage is identified below 0.2 span. Mass flow conservation is balanced by an acceleration of the flow above that limit. In the tangential direction, blockage is also present. In Figure 4.16b the swirl ratio is computed with respect to the swirl ratio value at midspan. When injection is applied, the tangential velocity component is reduced below 5% span. Momentum balance induces an increase of swirl ratio from 5% to 20% span.

The axial and tangential momentum deficit in Plane 2 is caused by a change of the leakage properties at the cavity trench exit. In fact, at fixed operating point (DL), the steady RANS numerical data predicts that the meridional flow angle and the trench exit swirl ratio are highly dependent upon the leakage fraction. The results of the numerical analysis are presented in Figure 4.17. The meridional flow angle Φ increases of 40[°] from a no leakage case to a leakage fraction of 0.46%. For the same conditions a reduction of 16% in

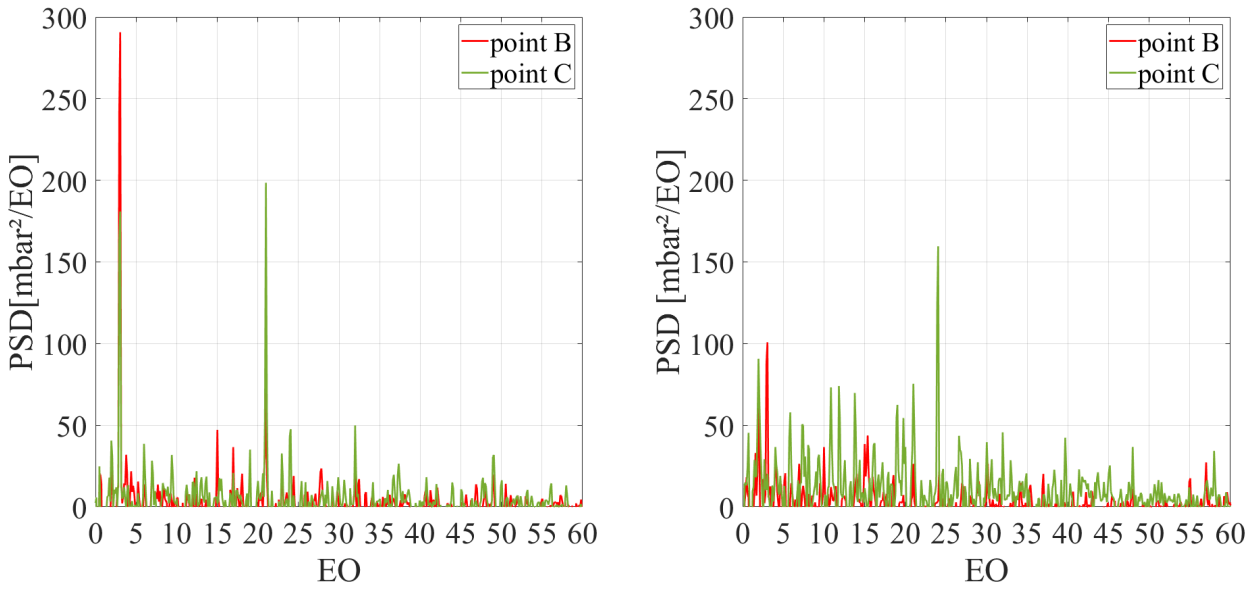

(a) (b)

Figure 4.14: Ensemble average spectra at probe position B and C from which spectrum at position A has been subtracted - Nominal speed, design loading operating point - (a) No leakage - (b) Injection 1 at $L_f = 0.56\%$.

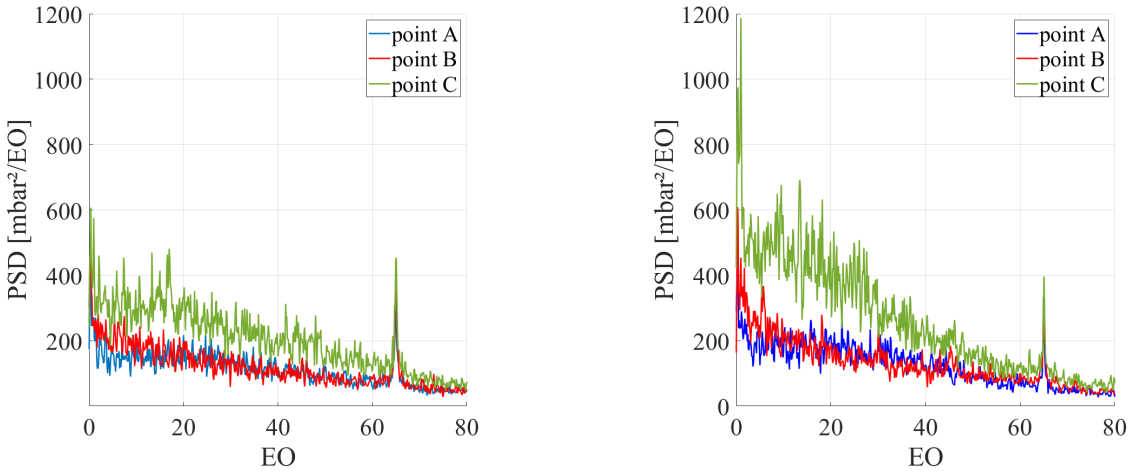

(a) (b)

Figure 4.15: Temporal fluctuation spectra at probe position A, B, and C - Nominal speed, injection 1 - (a) Design loading - (b) Near stall loading.

Table 4.3: Most energetic frequency ranking of residual spectra at position C (i.e. subtracting point A energy content) - compressor nominal speed.

f_C	DL NoLeak	DL inj1	NS NoLeak	NS inj1
1	21	106	21	BPF – 3
2	3	24	24	15
3	106	2	20	25
4	32	21	25	23
5	24	11.84	9	20
6	2	10.86	106	106
7	6	13.4	3	13

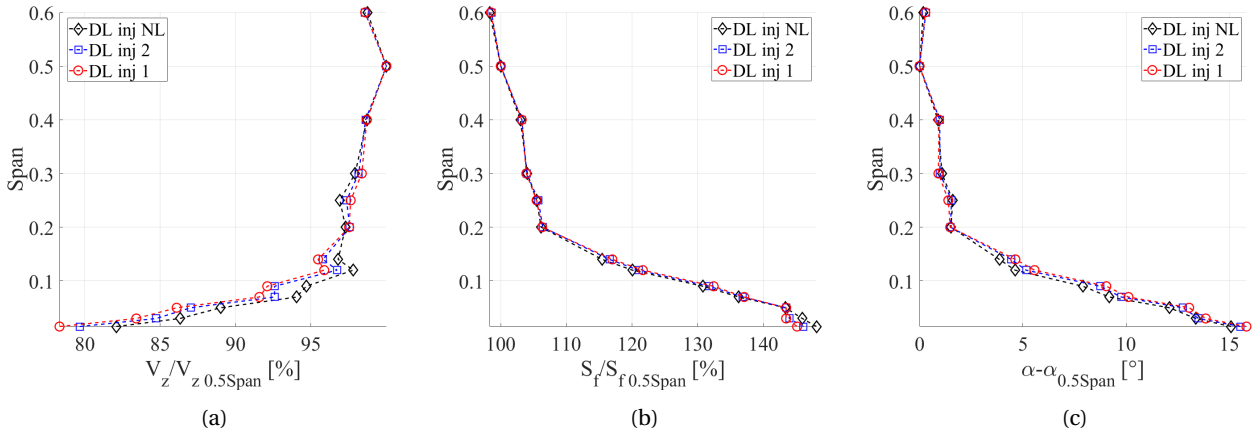

Figure 4.16: H25 stator inlet velocity profile and flow angle under forced injection at nominal speed design loading operating point (a) Axial velocity - ratio with axial velocity at midspan expressed in % - (b) Swirl ratio - ratio with value at midspan expressed in % - (c) Absolute flow angle relative to midspan flow angle.

swirl ratio is noticed. The C2 configuration is able to generate strong changes for the trench exit conditions in the leakage fraction interval covered in this study.

Flow angle is presented in 4.16c. The measured incidence increase attributed to the maximum injection is of 1.5[°] on the stator row, for the design loading operating point. The sensitivity of the flow angle to the injection is felt up to 0.2 span at Plane 2 which is located one fifth of rotor chord downstream of the cavity trench. The other operating conditions evaluated in the test campaign do not present incidence increase above 2[°] in the presence of injection, with respect to the no leakage case.

In order to present the effect of the operating point and the compressor rotational speed on leakage induced momentum deficit in Plane 2, the blockage factor introduced in equation 4.1 is used. It compares the velocity with injection to the one of the non leakage case at the same radius. The blockage factor is computed for both axial and tangential velocity components. If BF is inferior to 100%, blockage is increased.

$$BF_i(r) = \frac{V_i(r)}{V_{iNoLeak}(r)} \tag{4.1}$$

Figure 4.18 presents the axial and tangential blockage factors for different operating conditions in terms of compressor rotating speed and throttling. In Figure 4.18a, the injection always produces axial blockage in the low span region. When the stage loading is increased from DL to NS, the spanwise portion of $BF_z < 100\%$ increases towards higher span. It happens independently from the leakage fraction applied. The blockage generated below 12% span is smaller in the case of the near stall operating point at constant injection level. When stage loading is increased, the boundary layer downstream of the cavity trench is affected to a larger span range but axial blockage radial distribution is more homogeneous.

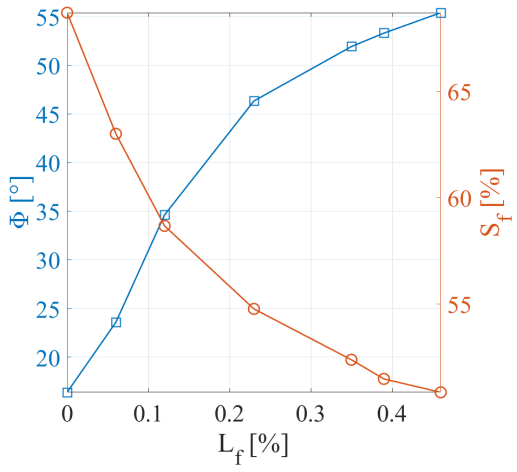

Figure 4.17: H25 design conditions. CFD steady RANS predictions of C2 trench exit conditions under forced leakage - left axis: Meridional flow angle Φ in [°] - right axis: Swirl ratio in %.

When the machine rotation speed is reduced from 100Nn to 85Nn at constant operating point ($\lambda = cte$) and constant leakage fraction, the axial blockage effect of the injection is reduced to lower span. Axial blockage factor also increases in the low span region.

The effect of the operating point on the tangential blockage factor is presented in Figure 4.18b. For both injection levels, an increase in stage loading leads to a more homogeneous blockage factor profile. When the rotation speed is reduced to 85Nn at design loading, the measured data present a tangential blockage factor higher than 100%. This indicates that, compared to no injection at similar radius, the leakage flow brings more momentum in the tangential direction. This counter-intuitive trend needs to be validated especially since the near stall condition do present a similar behaviour to all the other operating points.

Three hole virtual (3HV) probes are also used in the lower part of the Plane 2. These probes, that are used both in the main channel and cavity, could only be traversed in the bottom 12% span of the main channel. It is therefore impossible to obtain the flow quantities for the whole channel height using these measurements. The momentum deficit caused by the injection do contribute to the thickening of the stator inlet boundary layer. The total pressure measured by the steady 3HV probe is presented in Figure 4.19a. The reduction in total pressure caused by the injection is minimal in Plane 2. The measured total temperature profile is given in Figure 4.19b. An increase of total temperature is noted between the different injection cases. Two effects are superimposed that justify this trend. In the first place, conditions of injection are compared at same flow coefficient. In that extent, the rotor row produces more work to compensate for the blockage induced by the injection. On average, this shift in operating point implies higher rotor outlet total temperature. Then, the injection of the hot leakage flow from the cavity also thicken the thermal boundary layer at stator inlet. Due to the probe design limiting the traversing to 12% span, it is not possible to extract reference data at mid span to evaluate which effect is predominant in the low span region. A 1.6[K] increase in total temperature is noticed at maximum injection. The minimal increase in temperature from injection 2 to injection 1 is also justified by a total temperature decrease of the cavity flow as it is presented further in section 4.2.1.

To summarize the data collected in the experimental campaign, Figure 4.20 presents the total temperature increase in the stator hub inlet boundary layer for all the operating conditions investigated. The temperature is compared for each condition with the total temperature profile without injection at the same radius. From a general point of view, there are no big discrepancies among the data. The biggest temperature increase always appear at minimum span and varies between 0.82[K] and 1.6[K]. Temperature increase caused by the injection is always decreasing with the operating point loading at constant leakage fraction.

As a conclusion, the direct effect of the leakage flow in the on the main stream consists in increasing the axial and tangential blockage in the lowest part of the channel as well as increasing the local total temperature.

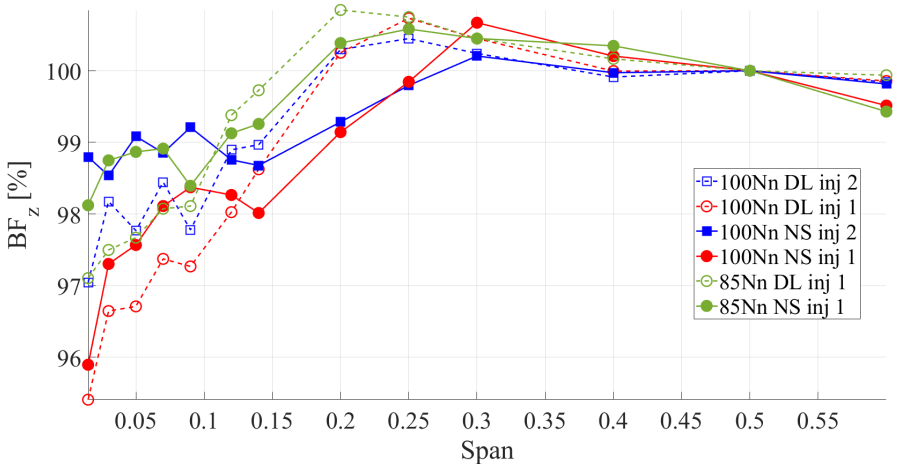

(a)

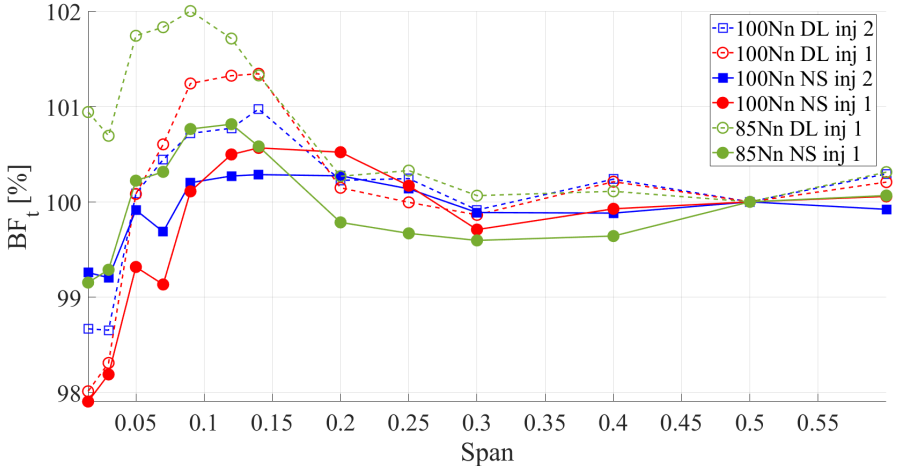

(b)

Figure 4.18: Stator inlet (a) Axial blockage factor - (b) Tangential blockage factor.

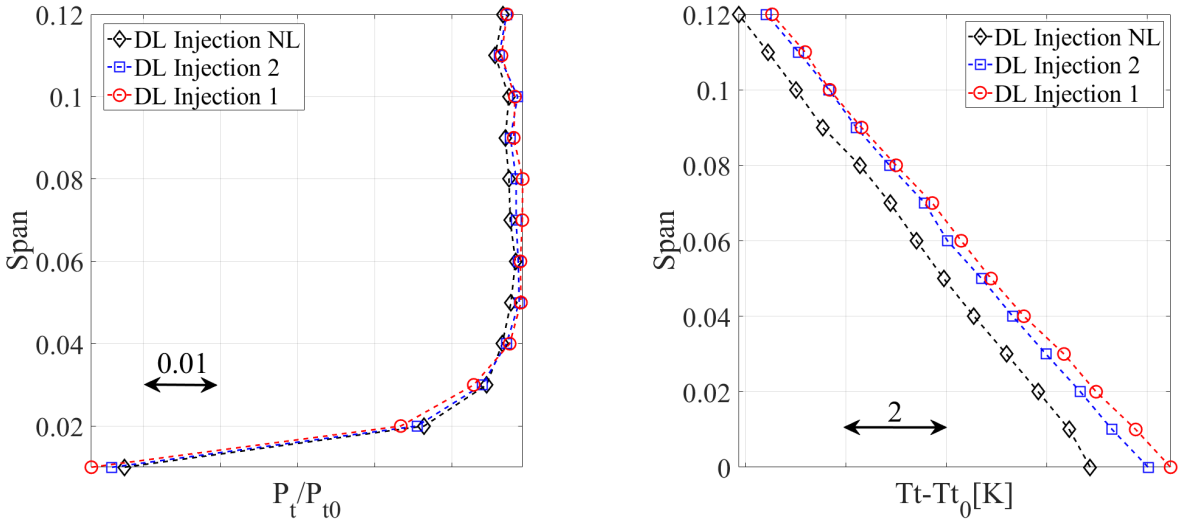

(a) (b)

Figure 4.19: 3HV steady measurement in stator inlet boundary layer at design loading operating condition (a) Total to total pressure ratio - (b) Total temperature difference with stage inlet.

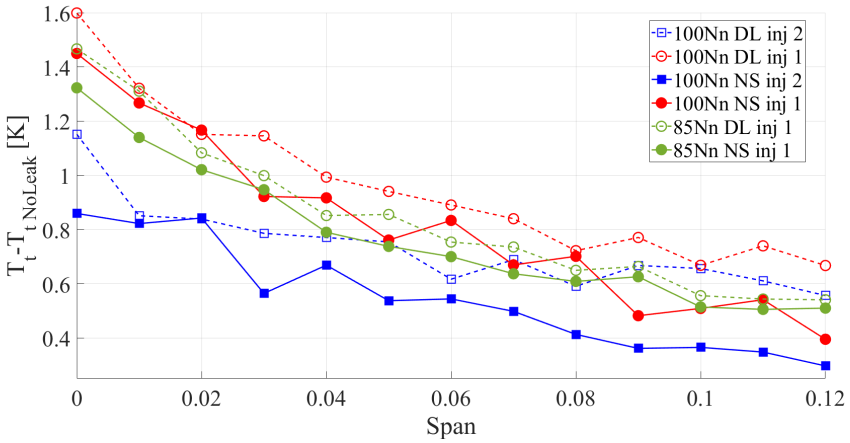

Figure 4.20: Experimental stator hub inlet total temperature increase with respect to no leakage case for the operating points studied in the database - refer to Figure 3.6.

4.1.4 Cavity flow and main flow interaction

This section investigates the cavity and main flow interaction. This interaction takes place in the cavity trench region. It is characterized by a strong mixing process between the main flow and the leakage flow, that is ejected from the cavity, at a defined average meridional flow angle and average swirl ratio. Azimuthal non uniformities are expected due to: (1) rotation driven ingestion in the cavity; (2) pressure driven non uniformities caused by blade effects. The upstream and downstream blade rows imposes preferential ingress and egress regions in the cavity as a consequence of potential effect and wake effect. Non uniformities and cavity trench topology are presented in the two following sub sections.

Downstream of the cavity trench, a new boundary layer is generated on the stator hub platform. This boundary layer is three dimensional and see its skewness changing as a function of the injection quantities. Quantification of the additional turning induced by the injection and dynamics of the flow in the stator inlet boundary layer are presented in the last sub sections.

4.1.4.1 Time averaged azimuthal non uniformities

In the experimental setup, azimuthal non uniformities monitoring is made between the cavity trench and the stator row inlet thanks to the hub static pressure taps. Results are given in Figure 4.21. Design operating point distribution of static pressure around the mean value over one pitch is plotted for both experimental and numerical data (Figure 4.21b). In the numerical datasets stator row potential effect is limited to 0.5[mbar]. In the CFD, the change in static pressure distribution due to the injection is almost not visible. The experimental dataset does present more dispersion around the mean value. The reader should remember that pressure taps are distributed around the annulus. In that extent they are exposed to the annulus non uniformities of the flow field in the test section which can blur the result presented here. Nevertheless, between injection cases, the highest sensitivity of the static pressure appears for points between 0 and 0.1 pitch in the region sensitive to blade potential effect (c.f. Figure 4.21a). The presence of the injection creates a higher pressure unbalance between 0 and 0.5 pitch.

4.1.4.2 C2 cavity trench

In the steady RANS analysis, the trench region is investigated. The first remark is that the computation do not show azimuthal non uniformities in the cavity trench. Regions of preferential ingress and egress do not appear (see Babin et al. (2021)). The cause for such behaviour is explained by the smaller potential effect detected at same axial location with respect to the experimental data (c.f. Figure 4.21b). The important axial distance between the rotor and stator row plays a crucial role in limiting the potential effect.

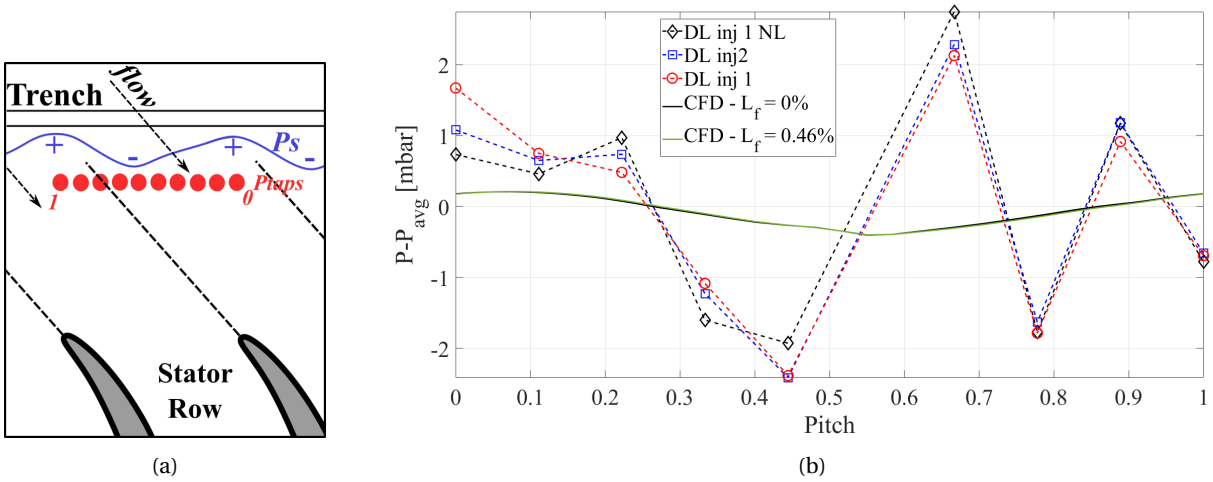

(a) (b)

Figure 4.21: (a) Sketch of azimuthal non uniformity of static pressure in Plane 2 (blue) under blade potential effect, at adapted incidence. Array of sensors combined to form one pitch (from 0 to 1)(red) - (b) Corresponding experimental and numerical stator hub inlet static pressure distribution at nominal speed, design loading operating condition - Downstream blade suction side at 0 pitch and pressure side at 1 pitch on the x axis.

In the computation, the C2 trench is located downstream of the mixing plane. As a result, no wake effect is visible (no wake transfer between rows). In the absence of azimuthal non uniformities, the C2 trench is studied with pitch wise averaged data.

Figure 4.22 presents the pitch wise averaged streamlines at design loading for different leakage conditions. At no leakage fraction, a trench vortex (TV) controls the interactions between the cavity and the main channel. The TV guarantees the equilibrium between disk pumping and pressure balance, between cavity and main channel. At $L_f = 0.12\%$, the TV is reduced but still present to satisfy the disc pumping effect. Once more leakage is applied, the trench vortex is progressively pushed out from the cavity. In the frame taken, the geometry effect of the cavity trench entrance is visible. The leakage flow that moves radially upward along the rotor surface faces a step at the transition between rotor and stator disk. A separation is generated at the step edge for all the leakage conditions.

By varying the relative radius height of stator and rotor disk, it could be interesting to study the effect of such flow feature on the aerodynamic blockage of the trench. Another geometry effect is visible at the trench exit. At high leakage fraction, the sharp edge of the stator platform also induces a separation. This feature presented in the simulation must be taken with care since the real platform do present a really small fillet radius. In fact, this radius is too small to be implemented in the current mesh at reasonable computational cost.

Along with the previously introduced streamlines, radial and azimuthal velocity components are extracted at -1% span in the trench. Figure 4.23a shows the swirl ratio distribution along the trench. The swirl ratio evolves between 0% on the stator disk and 100% on the rotor disk. As shown in Figure 4.17, the swirl ratio average value decreases with the leakage increase. The average swirl ratio profile is characteristic from Batchelor type flow between stator and rotor disc (see Childs (2010)). On the contrary, the radial velocity profile in Figure 4.23b is counter-intuitive with respect to a classical Batchelor flow (i.e. + on rotor side and - on stator side). The profile has to be put into perspective with respect to Figure 4.22 previously presented. The velocity profile is extracted at the edge of the trench at -1% span where typical "regimes" of rotor stator cavity flow are not the only driving phenomena.

For the no leakage case, part of the trench experiences negative radial velocity, mainly due to the presence of the trench vortex. When leakage increases, the main flow imposes a blockage for the leakage flow in the first axial part of the trench. The last part of the trench, close to the stator disc wall, becomes the preferential region for leakage flow egress. It is visible on the radial velocity profile how the trench width portion of high radial velocity grows with the leakage fraction. The direct consequence is the increase of meridional flow angle of injection in the main channel seen in Figure 4.17.

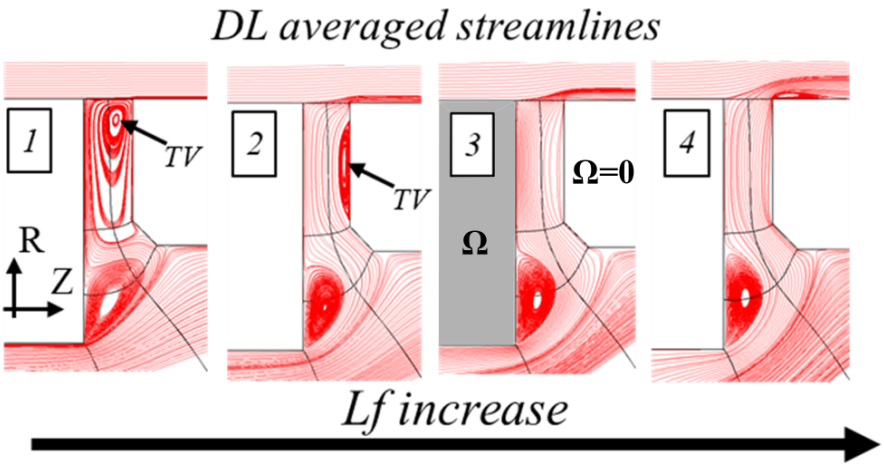

Figure 4.22: Meridional view of C2 cavity trench between rotor (Ω) and stator platform. Steady RANS streamlines at nominal speed design loading operating point for variable leakage fraction - (1) L_f = 0% - (2) L_f = 0.12% - (3) L_f = 0.23% - (4) L_f = 0.46%.

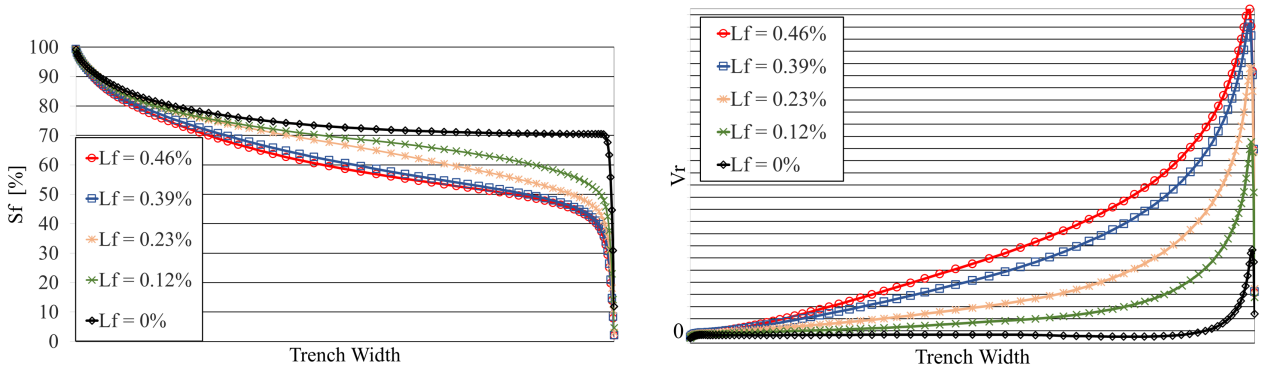

(a) (b)

Figure 4.23: Pitch wise average flow quantities from steady RANS simulations at -1% span in the C2 cavity trench. Nominal speed, design loading operating point - (a) Swirl ratio in % - (b) Radial velocity.

4.1.4.3 Stator inlet boundary layer skewness

The change in reference frame from rotor to stator platform as well as the injection conditions have an impact on the hub boundary layer skewness at stator inlet. The steady RANS computations where forced leakage is applied allow to evaluate the cross stream and streamwise velocity components in Plane 2.

Figure 4.24a presents the skewness hodograph for the cross stream U_n and streamwise U_s velocity components normalized with respect to the velocity at boundary layer edge Q_e. When the leakage fraction is increased at C2 labyrinth exit, the stator inlet boundary layer skewness is changed. The maximum cross stream velocity is increased with the leakage fraction. The additional turning angle $\Delta\gamma$ induced by the skewness (see section 1.5.3.2 Figure 1.11 and Figure 1.12) is presented in Figure 4.25a. The additional turning is given with respect to the case computed without leakage. In the leakage fraction range investigated, a leakage point always present additional turning with respect to the no leakage case. Skewness induced turning angle increases with the leakage fraction to reach a value of 9.1[°] at 0.46% L_f. The rate at which the turning angle increases suddenly reduces passed L_f = 0.35%. This coincides with the vanishing of the trench vortex and the generation of a separation pocket at the trench exit (see Figure 4.22, case 3 and 4). Figure 4.25b plots the radial position of the maximum cross flow velocity as a function of the leakage fraction. The results indicates that the proportion of skewed region in the stator inlet boundary layer increases of 10% between L_f = 0.06% and L_f = 0.46%. To summarize the findings, the numerical results show that an increase in leakage increases both the skewness of the boundary layer as well as the skewness induced turning.

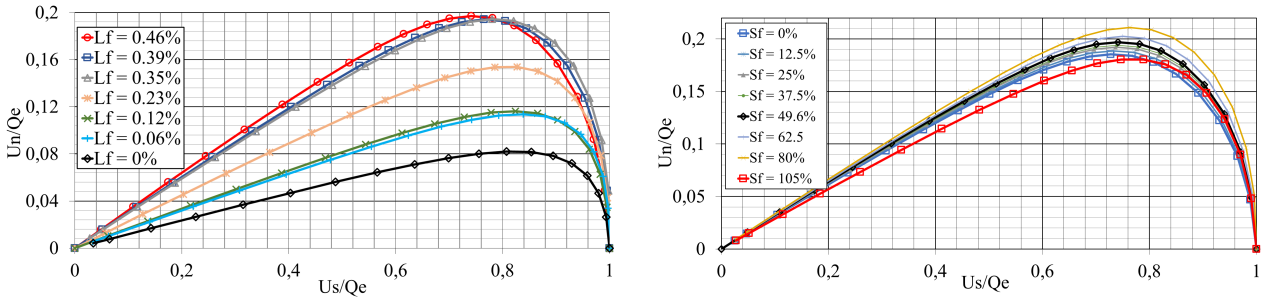

(a) (b)

Figure 4.24: Hodograph of streamwise U_s and cross stream velocity component U_n of the three dimensional hub boundary layer at H25 stator inlet - CFD steady RANS data at design loading point - (a) Sensitivity to leakage fraction - (b) Sensitivity to the swirl ratio of injected leakage at C2 labyrinth exit. Constant leakage fraction of 0.46%.

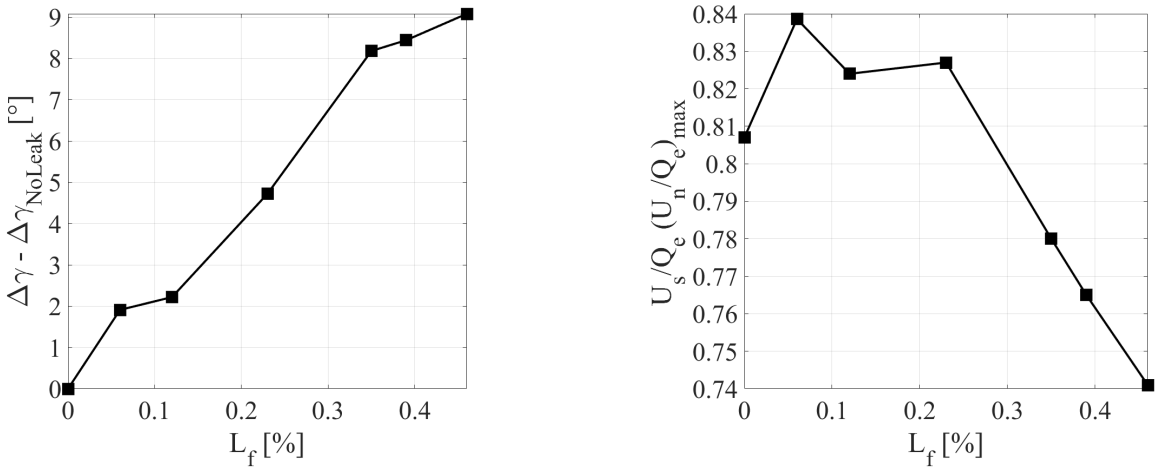

(a) (b)

Figure 4.25: (a) Skewness induced additional turning angle in stator inlet boundary layer as a function of injected leakage fraction in the C2 cavity - Numerical data - (b) Radial position of peak cross flow velocity $(\frac{U_n}{Q_e})_{max}$ in stator inlet boundary layer as a function of injected leakage fraction in the C2 cavity - Numerical data.

Figure 4.24b presents the effect of the injected flow swirl ratio, at labyrinth exit, on the Plane 2 boundary layer skewness. The sensitivity of the skewness to this parameter is less important than for the leakage fraction and displays grouped hodographs. This confirms the second order sensitivity of the stage flow field and performance to C2 labyrinth exit swirl ratio.

The conclusions taken for the skewness sensitivity still need to be considered in view of the flow modelling limitations of the chosen turbulence model k-w SST. In three dimensional turbulent boundary layers (3DTBL), the misalignment of stress and strain due to the turbulence anisotropy is not taken into account with a model that uses the Boussinesq approximation, so isotropic turbulence. Information concerning the limitations of such models can be found in Johnston and Fiack (1996) and in Lynch (2016).

At compressor nominal speed, design loading, the boundary layer thickness predicted by the numerical data in Plane 2 ranges from 2.1% span at no leakage, to 4.6% with $Lf = 0.46\%$. The location of the minimal radius where hot wire measurement is performed is 1.5% span. With the velocity profiles collected in the experiments, it has been possible to extract part of the skewed region. The results at design loading operating point are presented in Figure 4.26.

Under injection, Figure 4.26a experimental slopes indicates that the additional turning angle of the external streamline always reduces with the increase in leakage fraction (see γ_e in Figure 1.12). The numerical data presented previously valid this trend in the leakage fraction range of concern. A local zoom of the ex-

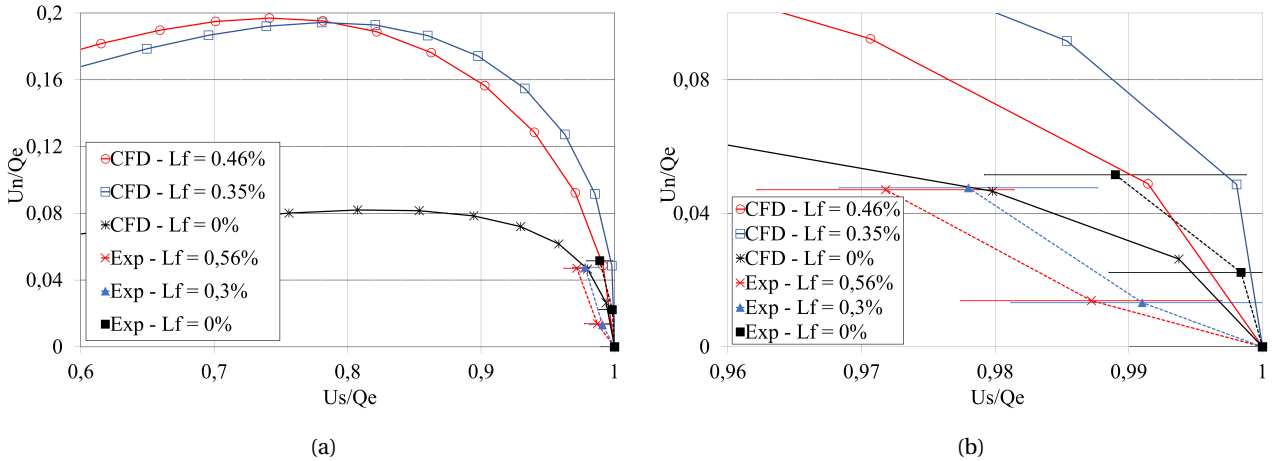

Figure 4.26: (a) Numerical and experimental hodograph comparison at compressor nominal speed and design loading operating point under injection conditions - (b) Zoom on the region where experimental data are available.

ternal region of the boundary layer is plotted in Figure 4.26a. The experimental uncertainty of the cross stream and stream wise velocity ratios is computed at 0.99%. This value has been computed thanks to the results presented in Boufidi (2017) and Boufidi et al. (2020) . In the measurement region, the experimental data falls within 2% of the numerical data. However, the measured local trend with injection is inverted with respect to the numeric, when injection is applied. The comparison clearly indicates a limitation of the current experimental set-up in exploring the stator inlet boundary layer structure. However, it shows the sensitivity of the measurement to the leakage and encourage a more focus work on the topic.

4.1.4.4 Comment on hot wire measurement of stator inlet hub boundary layer dynamics

The unsteady activity measured in Plane 2 is first analyzed thanks to hot wire measurements. The hot wire is traversed radially in stator inlet plane between 1.7% and 60% span. For the design loading at injection 1, the temporal fluctuations of axial velocity are presented in Figure 4.27 for different span positions. Similar to the results seen at stage outlet, no clear frequency emerges from the temporal fluctuation around the EA, for all the conditions investigated. Note that the peak at 65 EO is a also residual from the blade passing frequency.

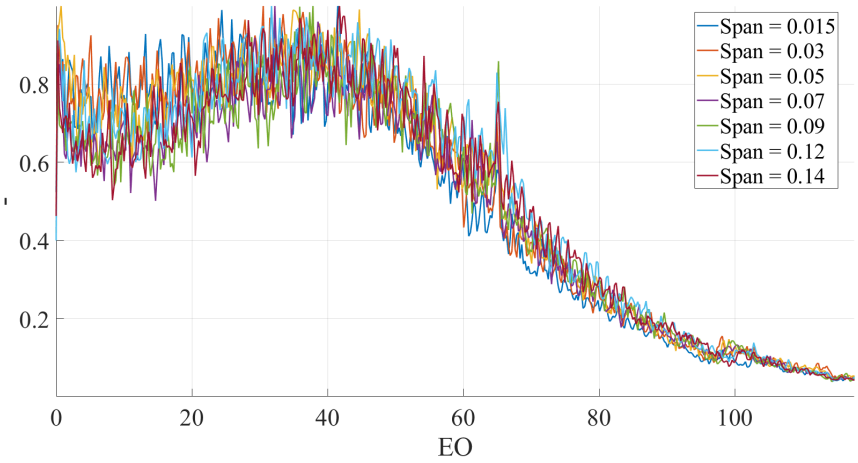

Figure 4.27: Spanwise normalized power spectral density of axial velocity temporal fluctuations at stator row inlet - Hot wire measurement - Design loading injection 1.

The analysis of the ensemble average spectral content is then performed to evaluate changes induced

by the leakage flow. A comparison is done between operating conditions at no leakage and at injection 1 ($L_f = 0.56\%$). In the ensemble average, a band stop filter is applied on the BPF and its harmonics to ease the identification of spectral activity below the blade passing frequency. For each spanwise position of the wire, a spectrogram of the filtered spectra is produced with a Welch window length of four rotor rotations. Power spectral densities are then normalized in each spectrogram to limit the energy between 0 and 1.

To obtain a quick comparison between the no leakage case and the injection case at fixed radial location, the difference between the spectrograms is computed. As an example, if for a radial position, a frequency is present in both no leakage and injection 1 condition at a normalized amplitude of 1, the result spectrogram indicates 0 for that frequency band.

The spectrograms are combined to represent the frequency content, in time, for every span wise position of the hot wire. The operation is performed for the axial velocity and for the absolute flow angle. This allows to identify the preferential direction (azimuthal, axial) of each frequency range.

The resulting spectrograms are plotted in Figure 4.28 and Figure 4.29 for the design loading and near stall loading operating point. In the figures, the horizontal axis indicates the span wise grid used. For plot clarity, spectrogram at constant spanwise position are plotted on an interval of 51 rotations.

At design loading, the low span region presents three frequency bands at 7 EO, 24 EO and 32 EO. The high level of energy in the 24 EO band indicates that it is amplified by the presence of the leakage. this frequency is present for all of the spanwise positions in the axial velocity spectrogram. The reader should remember that this frequency is also found at stage outlet, in the stator suction side corner when injection is applied at design loading (c.f. Table 4.3). From 5% span on, the frequency at 21 EO, also visible at stage outlet, appears as well as its first harmonic at 42 EO.

The behaviour of the flow at near stall condition in Figure 4.29 is different. The low span region presents a much richer content. Here also it is possible to identify multiple frequencies and their harmonics, that are activated by the leakage and also present in the stator low span suction side region in the stage outlet plane (see point C in Table 4.3).

The different normalized energy levels between flow angle and axial velocity informs that part of the leakage induced energy is discharged in the tangential velocity component. The balance between meridional flow angle and swirl ratio at the ejection point of the cavity trench is driving such an energy distribution.

4.1.4.5 Comment on unsteady three hole virtual probe measurement of stator inlet hub boundary layer

The fast response three hole virtual probe is also used in the stator inlet boundary layer. These measurement present the same behaviour as the hot wire measurement regarding the point that no frequency peaks of temporal fluctuations is found for the different operating conditions. Figure 4.30a shows the aforementioned spectral content for the design loading injection 1 case at different span position of the probe above 2% span. Since the probe is traversed through the end wall, it is possible to effectively measure down to 0% span, i.e. with the center of measurement hole at 0% span. Figure 4.30b plots the spectra of temporal fluctuations from 0% to 2% span. A peak at 6.71 EO is clearly visible with an amplitude decreasing with the span. This peak is induced by the measurement himself. The probe diameter is equivalent to 10% span and the measuring hole diameter is of 1% span. The probe is measuring its own potential effect at low span. When the probe measuring hole is positioned at more than 3 times the hole diameter (i.e. from 3% span and above), this behaviour disappears.

4.1.4.6 Partial Conclusion

In this section it is found that the current experimental setup is not able to clearly detect azimuthal pressure non uniformities that are on average attributed to the stator blade potential effect. It can not be excluded that close to C2 cavity trench, the stator potential effect is limited due to the long axial distance between H25 rotor and stator rows.

The use of steady RANS simulation is effective to point out the flow topology in the cavity trench region as well as the changes in boundary layer skewness caused by the presence of the injection. It is evidenced

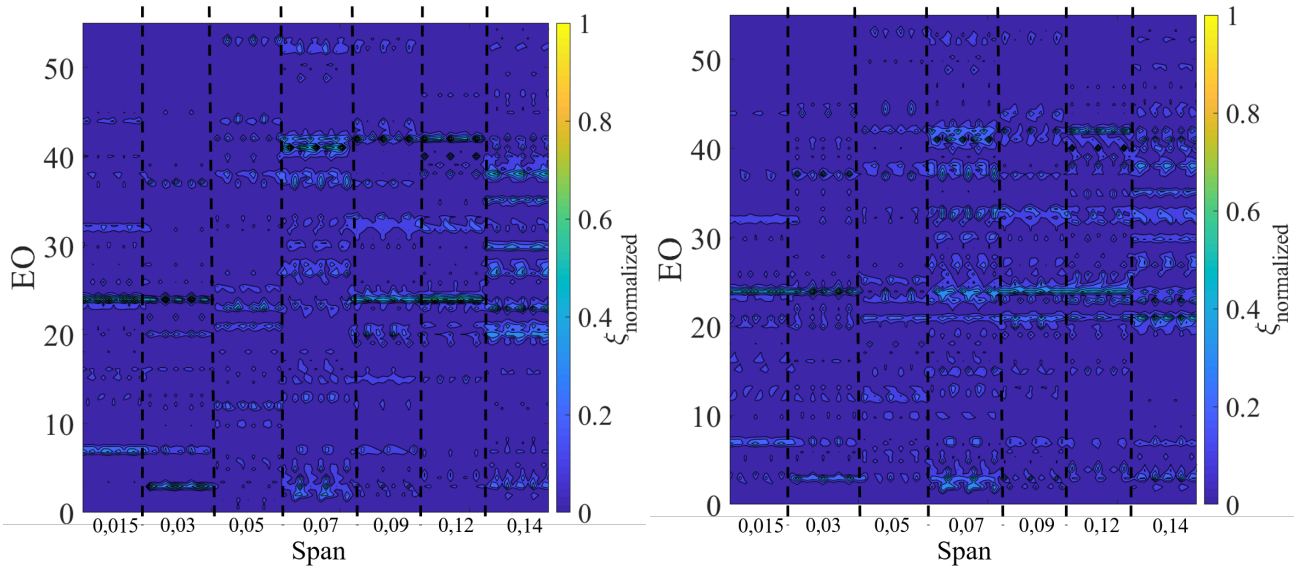

(a) (b)

Figure 4.28: Differential spectrogram of normalized energy between injection 1 at L_f = 0.56% and no leakage, at consecutive constant spanwise position of the hot wire from 0.015 span to 0.14 span. For each span position, 51 rotations are plotted in the spectrogram - Nominal speed, Design loading -(a) Absolute flow angle - (b) Axial velocity.

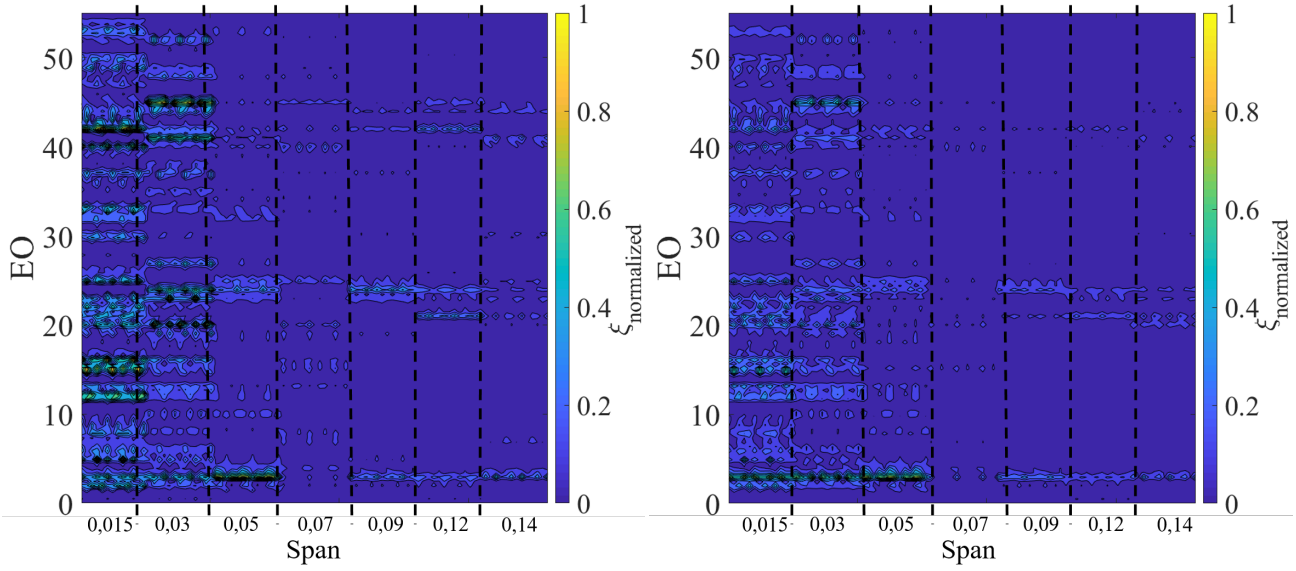

(a) (b)

Figure 4.29: Differential spectrogram of normalized energy between injection 1 at L_f = 0.56% and no leakage at consecutive constant spanwise position of the hot wire from 0.015 span to 0.14 span. For each span position, 51 rotations are plotted in the spectrogram - Nominal speed, Near stall loading -(a) Absolute flow angle - (b) Axial velocity.

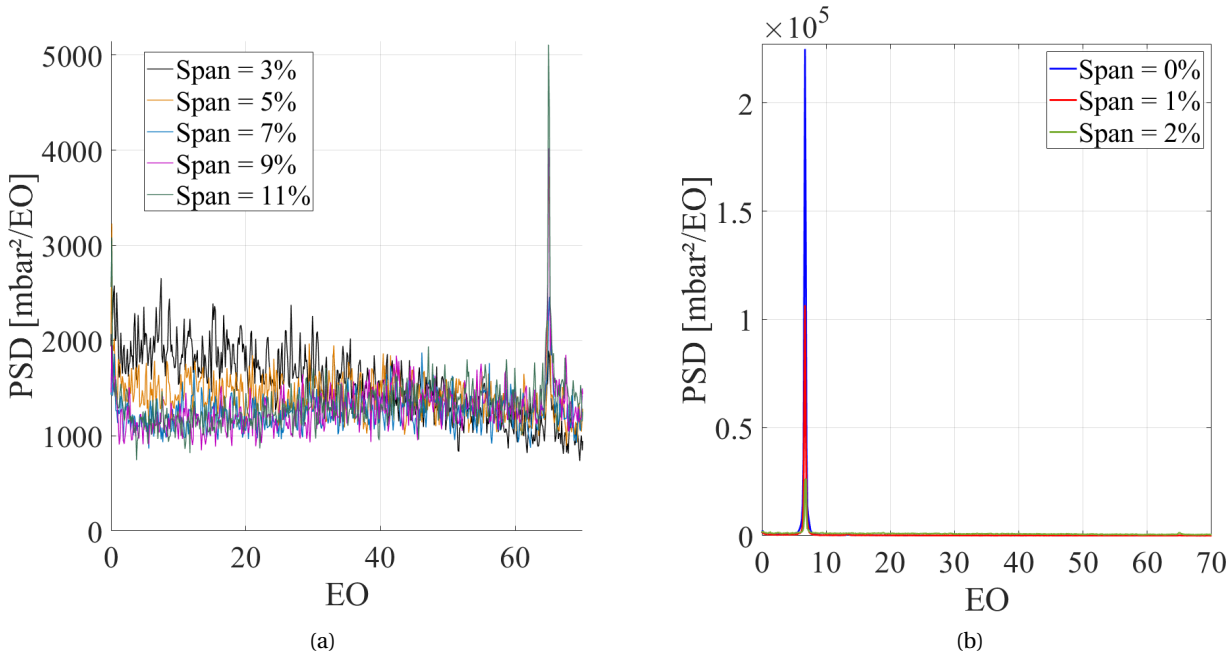

Figure 4.30: Span wise spectra of temporal fluctuations measured in stator inlet boundary layer - 3HV fast response pressure probe - Design loading, injection 1 at $L_f = 0.56\%$ -(a) Above 3%span - (b) Below 3% span.

that the trench geometry has an effect on the aerodynamic properties of the flow in the interaction region (trench vortex, separation regions,...). Additional turning at stator inlet of 1.5° is computed for design operating conditions for a leakage fraction of 0.56%. Under the precision offered by the experimental setup, 3.5° additional turning is measured for the same operating point at 0.56% leakage fraction.

The analysis of the stator inlet boundary layer dynamics shows unsteady activity in the ensemble average that is also present at stage outlet. At this point of the analysis, it is still not clear if the frequencies identified can be: (1) attributed to flow features convected from the rotor row; (2) rotor disk synchronous flow features that are emerging from the cavity; (3) the result of an interaction between the two precedent phenomena. As such, the cavity flow field must be investigated.

4.2 Time averaged flow field in the C2 cavity

The time averaged flow field in the C2 shroud cavity is detailed in this section. The analysis is made in three steps. The effect of the injection is presented first. Then, the effect of the stage loading at fixed rotational speed is analyzed. To finish, the effect of the disk rotation speed on the cavity flow is studied.

4.2.1 Effect of the leakage fraction

The machine operating condition is fixed at compressor nominal speed and design loading operating point. Levels of injection at 0.3% leakage fraction (injection 2) and 0.56% leakage fraction (injection 1) are generated at the C2 labyrinth exit in the experiments. In the steady numerical simulations, the injection ranges from 0% to 0.46% leakage fraction, and the swirl ratio is kept constant at the injection point.

The meridional averaged streamlines from the simulations are presented in Figure 4.31a. Thanks to this representation, it is possible to understand, on average, if the geometry of the cavity imposes a spatial organisation of the flow. The C2 geometry splits in two local regions separated by the radius of the labyrinth seal, called injection radius. This could be anticipated from the literature and non-dimensional number analysis presented in Chapter 2. When leakage is applied, a schematic view of the flow field is given in Figure 4.31b where the red line highlights the jet line of the flow travelling from the labyrinth exit to the trench. Above the injection radius, the largest vortex structure is identified as the cavity main core. It is

characteristic from Batchelor type flows and separates rotor and stator turbulent boundary layers where the flow is respectively moving radially upward and radially inward.

In the main core region, the flow field predicted by the simulation homogenizes with the increase in leakage fraction. On the average streamlines is visible the merging of the two cores into a single vortex for leakage fraction equal and higher than 0.23%. In Figure 4.32, the swirl ratio of the main core is presented. As expected from the cavity characterization done in Section 2.4, the swirl ratio at no leakage is below 50% due to the superior stator wetted surface, and associated torque. The swirl ratio decreases with the increase of leakage fraction with a quasi-linear trend. An increase of 0.1% in leakage fraction induces a decrease of swirl ratio of 1.7%.

Below the injection radius, another vortex core is detected in Figure 4.31. It is labelled as secondary core. In the absence of leakage, the secondary core is limited to the region where the rotor disc and stator disc are parallel to the machine axis. In fact, as showed in Chapter 2, this region of the cavity can generate Taylor-Couette type instabilities. At zero leakage, the shear induced by the two parallel disks gives to the secondary core a swirl ratio of 52.5 % as presented in Figure 4.32. For all the leakage range, secondary core swirl ratio is always higher than the injected swirl ratio of 49.6% at labyrinth exit.

When leakage is increased, two effects are superimposed in that region. The first one is geometrical. At labyrinth exit, the axial velocity component encounters a backward facing step. The higher the leakage, the larger is the extension of the separated region as well as the distance, from the seals, of the reattachment point of the flow to the rotor disc . The visible increase in swirl ratio up to 0.3% leakage fraction results from the second effect. When the secondary core is moved axially by the leakage, the radial limits of the core are the rotor disk on the bottom and the jet line on the top, instead of the stator disk. As a result, there is less friction applied by the stator surface on the secondary core with a direct increase of the swirl. Passed 0.35% leakage fraction, a decrease in secondary core swirl ratio is computed. As visible between state 3 and 4 of Figure 4.31a, the secondary core reaches the maximum space available in the under leakage radius cavity. This is also indicated by the jet line reattachment point reaching the first step of the rotor disk. When, due to the geometrical confinement, the vortex can not expand any more, the leakage has the same effect than for the main core where an increase in leakage fraction reduces the swirl ratio.

The reader must keep in mind that the flow is highly tangential, which means that the spatial organization around the machine annulus is in fact resulting from the interaction between toroidal structures.

The measured flow quantities radial distributions in the C2 cavity are presented in the rest of the current section. The traversed probes in Plane 2 ranges from -0.12 span to -0.76 span. Probes were designed in order to cross the jet line in the lowest part of the traverse grid. Figure 4.33a presents the total pressure ratio between the cavity and the stage inlet. The injection increase induces a better homogeneity of the profile between the top and the bottom of the cavity. When leakage is applied, the profile also rotates around a pivot point at -0.58 span. The location of that pivot almost coincides with the injection radius and the sudden enlargement of the cavity, which stands at -63% span. Below the leakage radius, the total pressure ratio increases when the injection is applied.

The static pressure gradient of the cavity flow under no leakage conditions is plotted in Figure 4.34a. The static pressure distribution is plotted around the mean value in traversing range from -0.12 to -0.76 span. Radial equilibrium balances the cavity flow which induces an average linear profile from cavity bottom to top, with high pressure on the top. The gradient profile is separated by regions of different slopes. The radial position of the slopes intersections coincides with increase or decrease in local cavity aspect ratio (Figure 4.34b). Pressure gradient slope is increased when local cavity aspect ratio is reduced. The pressure balance in the cavity is affected by geometrical constraints but also by the toroidal flow features highlighted in the streamline analysis. As an example, the predicted radius for the main core by the numerical data also coincides with the -40% span slope change. The presence of the main core and secondary core generates local regions of radial equilibrium in the cavity. Using radial equilibrium equation and pressure data, it is possible to evaluate the speed of the rotating fluid structure associated with each slope region, using forced vortex assumption. The experimental results present two main region, one corresponding to a rotating core at 82% and one at 45% disc speed. The numerical profile for the same operating conditions is given in Figure 4.34c. The pressure balance point is predicted at lower radial position than in the experiments. The

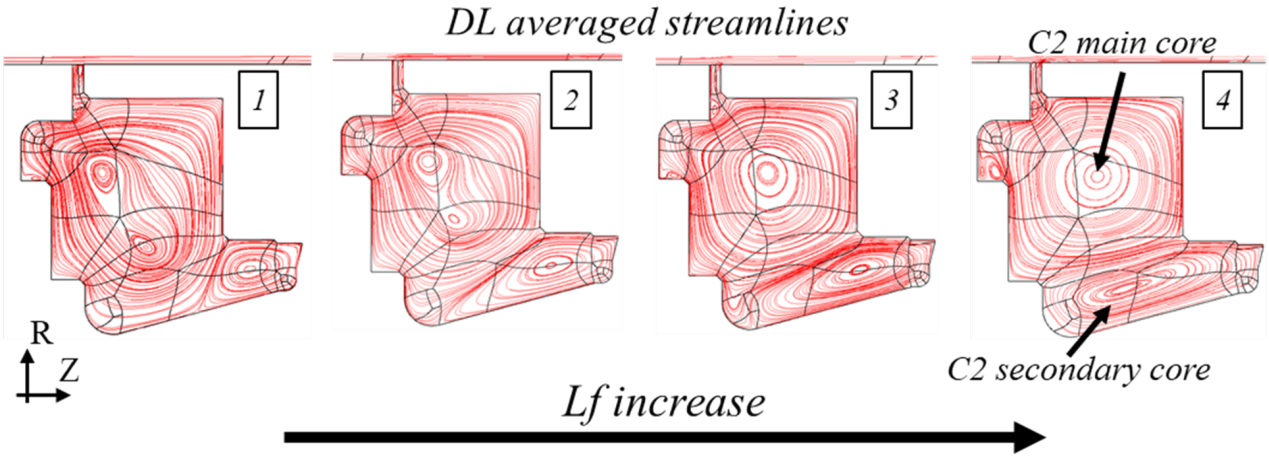

(a)

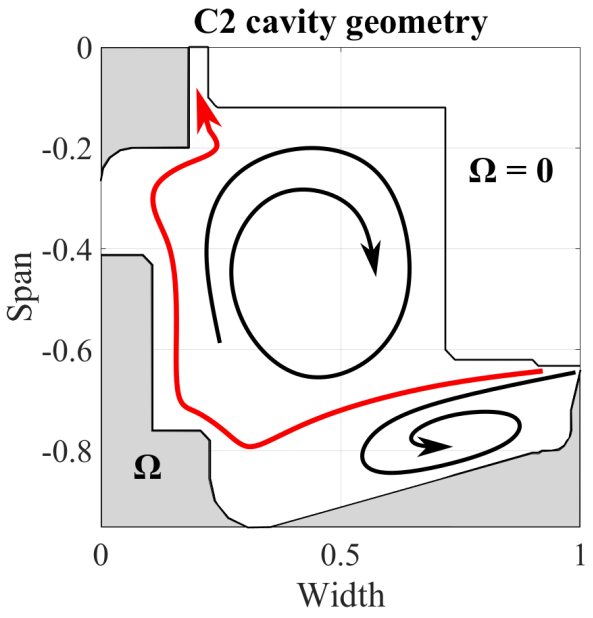

(b)

Figure 4.31: Steady flow organization in the C2 cavity - (a) Meridional averaged streamlines from steady simulations where leakage is applied. (1) L_f = 0%.(2) L_f = 0.12%. (3) L_f = 0.23%. (4) L_f = 0.46% - (b) Schematic representation of the flow with main core and secondary core (black). Identification of the jet line and leakage path in the cavity (red).

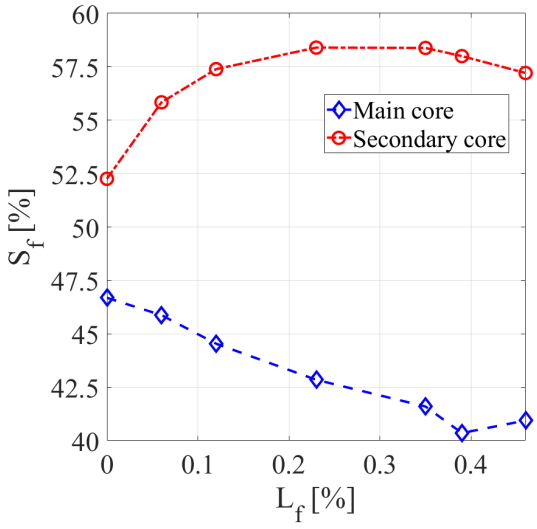

Figure 4.32: CFD RANS prediction of C2 cavity swirl ratio (in %) of the main core and secondary core in the C2 cavity as a function of leakage fraction.

pressure maximum and minimum values around the mean differ respectively by 4[mbar]. The slope change is less obvious in the numerical data but the mid cavity intersection point is at a similar location than in the experiments. Tangential speed of the rotating cores indicates that the numerical prediction at low cavity span get close to the prediction of the experiments with a computed speed of 47% disc speed. However, the upper cavity span pressure gradient is underestimated with respect to the experimental dataset. For both cases, an abrupt change in pressure distribution is noted above -20% span. Aside from the reduction in aspect ratio, the presence of the step induced vortex visible in Figure 4.22 also have an impact on the static pressure distribution at that radial location.

The effect of the injection on the static pressure gradient is presented in Figure 4.35a. On average, the static pressure in the cavity increases with the leakage. However, the representation around the mean value of static pressure eases the comparison between the cases. The increased leakage fraction produces a better homogeneity of the cavity pressure distribution. However, it is visible that the static pressure profile "rotates" around a pivot region at -36% span. The slope change between the flow regions separated by the pivot point is similar between the injection cases. This lead to think that it is effectively due to a geometrical effect. The change in slope previously presented in the upper part of the cavity is reduced by the presence of the leakage. The reduction of the step vortex size when injection is applied (see Figure 4.22) may contribute to the increase in pressure gradient in this region of the cavity.

The temperature of the leakage flow that exits the cavity trench is critical for the performance degradation of the entire stage since it contributes to the local entropy generation. The total temperature gradient, relative to stage inlet temperature, measured in the cavity, indicates a strong stratification of the flow (c.f. Figure 4.35b).

Total temperature reduces strongly for the points above -50% span. Without injection, the two extreme points of the traverse grid indicates a total temperature difference of 17[K]. The highest temperature gradient is reached for the injection 2 at $L_f = 0.3\%$ with 21.5[K]. When the maximum injection at $L_f = 0.56\%$ is applied this difference drops down to 18[K]. The injection 1 and injection 2 profiles overlap above -20% span. With the measurement taken, it is possible to compare channel and cavity temperature measurement. The complete differential temperature profiles at design point and nominal compressor speed are presented in Figure 4.2.1. The stator hub platform lies between 0 span and -0.12 span. Since the probes traverses through the end-wall, the 0 span and -0.12 span positions are effectively measured. Unfortunately no acquisition has been performed with the thermocouple between -0.12 and 0 span. Between the upper point in the cavity and the lowest point in the main flow, the temperature gradient is of 11[K], 15[K], and 16[K] for the no leakage, injection 2, and injection 1 respectively.

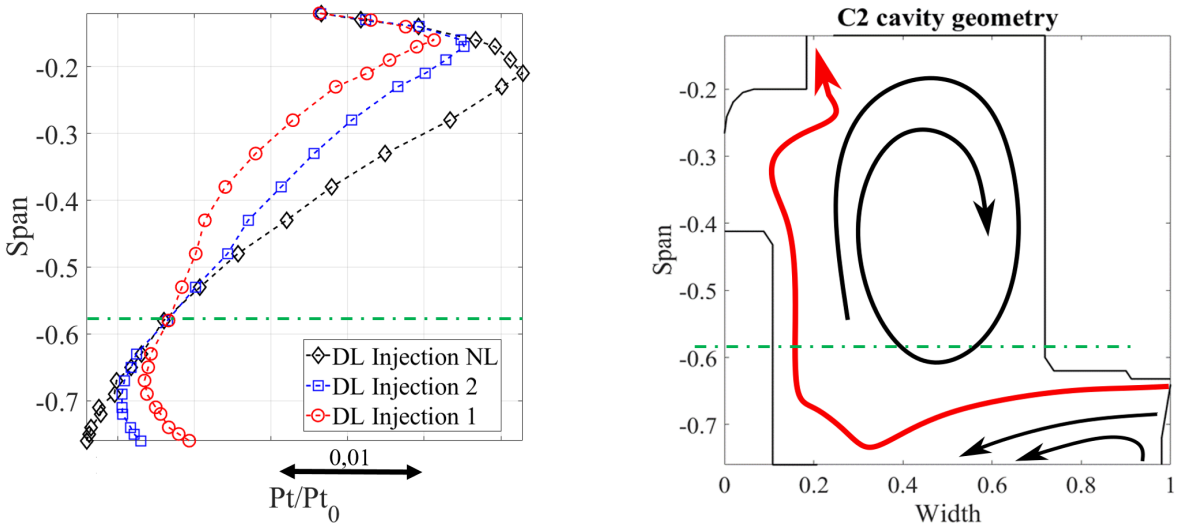

(a) (b)

Figure 4.33: Total pressure ratio in the C2 cavity at nominal speed design loading conditions - (a) Impact of the leakage fraction - (b) Schematic representation of the flow field.

The last flow quantity presented is the absolute flow angle. The sensitivity of the flow angle to the leakage fraction is introduced in Figure 4.36a. The flow angle is plotted in the cavity reference frame where 0[°] indicates a fully tangential flow and where the positive angles indicate that the flow is oriented with the compressor main stream. The experimental flow angle is distributed around a fully tangential flow that expands from -0.38 to -0.55 span, in the middle of the cavity. The behaviour measured at this location coincides with the presence of the main core. The radial extent of this region is not impacted by the forced leakage applied in the cavity. Outside from the core region, flow angle skews in the positive direction at the top. There, flow angle increases with the leakage as more fluid is entrained in the stator disc boundary layer. The flow angle is increased by 4[°] when the injection 1 at L_f = 0.56% is applied from a no leakage condition. When the probe measures in the leakage path at low span, the flow angle decreases when injection is applied. Nevertheless, the flow angle reduction observed is still limited. This suggests that the probe may not cross the average jet line in the experiments.

As a comparison, experimental and numerical data are superimposed in Figure 4.36b. The effect of injection 1 and 2 is well captured in the top part of the cavity. However, the flow angle value differs between numerics and experiments, especially in the lower part of the cavity.

At low leakage fraction, i.e. 0% and 0.12%, the numerical data also presents the vertical part of fully tangential flow previously seen in the experiments. When leakage is increased, the flow angle gradient increases and the large portion of the cavity at full tangential flow disappears - Note that it is also visible that the flow reorganisation is done around a pivot point at -0.39 span - The vanish of fully tangential flow coincides with the change of topology in the main core presented in Figure 4.31. When the flow angle profile is flat, the numerical solution indicates a main core flow composed of two vortices. For high leakage flow (above 0.12%) a single vortex is visible in the averaged numerical streamlines and the flow angle distribution do not present a vertical span portion at 0[°].

If the previous consideration is taken into account, the time averaged experimental data indicate a flow organization close to the two core solution, for all the leakage conditions studied. In the top part of the cavity, the measured flow angle falls within 3[°] of the numerical prediction for equivalent level of injection except for the no leakage case. In the low span region, the measured flow angle fits better the numerical distribution at low leakage, in which the jet line is still impinging close from the labyrinth exit (see 2 in 4.31). At high leakage, the numerical probe crosses the jet line. As a consequence, a local minimum in the flow angle is reached at around -0.68 span.

This section highlighted that, At fixed operating point, the leakage fraction has a strong impact on the

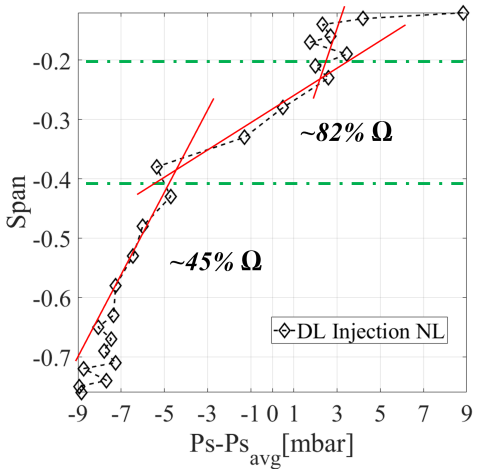

(a)

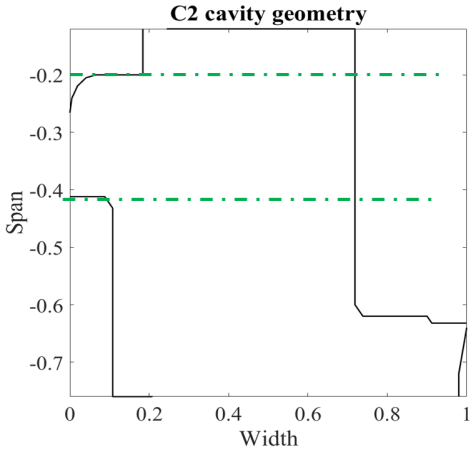

(b)

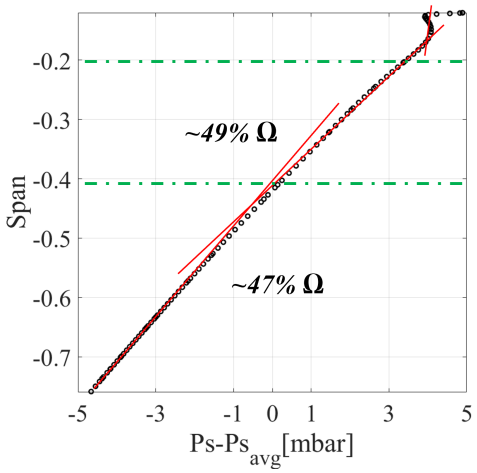

(c)

Figure 4.34: Static pressure gradient in the C2 cavity at nominal speed design loading conditions - (a) No leakage condition superimposed with trend lines - (b) Cavity related geometrical features at trend lines slope changes - (c) Steady RANS simulation results.

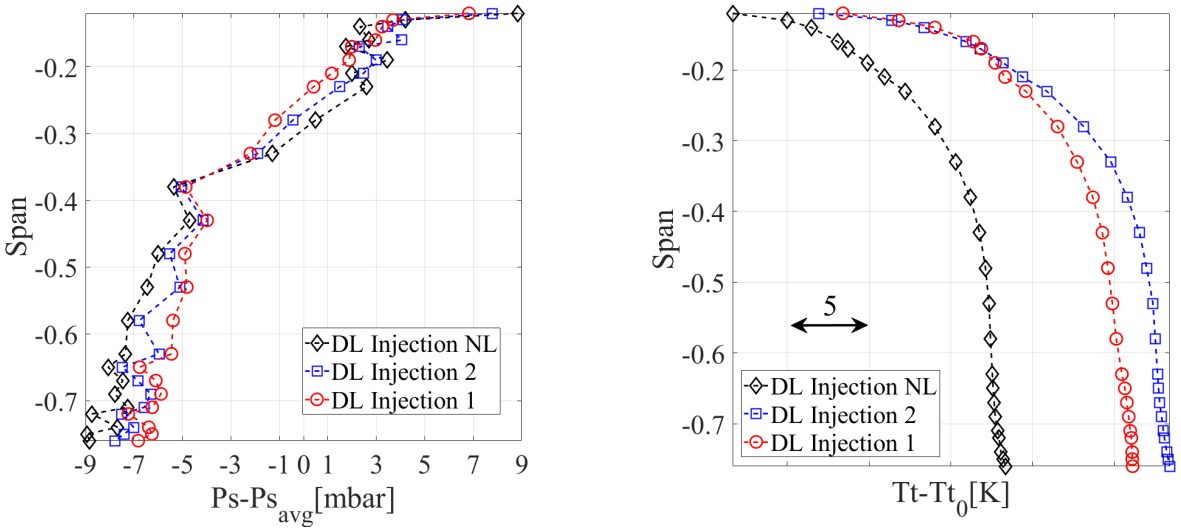

(a) (b)

Figure 4.35: Effect of the injection at nominal speed design loading conditions - (a) Experimental static pressure gradient in the C2 cavity - (b) Experimental total temperature difference with respect to stage inlet - gradient in the C2 cavity.

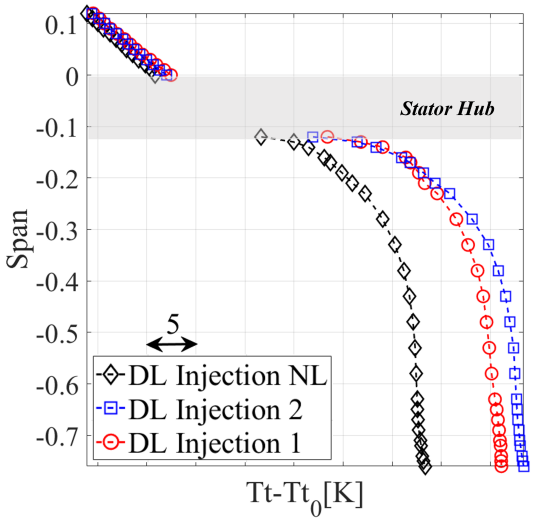

total temperature difference with respect to stage inlet in C2 cavity and main channel - Nominal speed, design loading

average flow organization of the C2 cavity. Markers of the geometry are found in the flow gradients which indicates a strong dependence of the flow to the geometry. The detected trends and flow interpretation are reinforced by the use of steady RANS simulations as a comparative dataset. It has been presented that the injection homogenizes the pressure field in the cavity but produces a higher flow gradient. Temperature increase directly caused by the injection are measured in the cavity core in the excess of 17[K] with respect to a no leakage conditions. The use of three hole probes in virtual mode is of enough quality to provide an evaluation of the average flow field in such a highly confined environment.

4.2.2 Effect of the operating point

The sensitivity of the C2 flow to the operating point is presented in this section. When, at fixed rotational speed, the stage loading increases, the cavity flow system experiences higher flow Reynolds number. Changes in the flow field at nominal speed from the design operating point to the near stall operating point

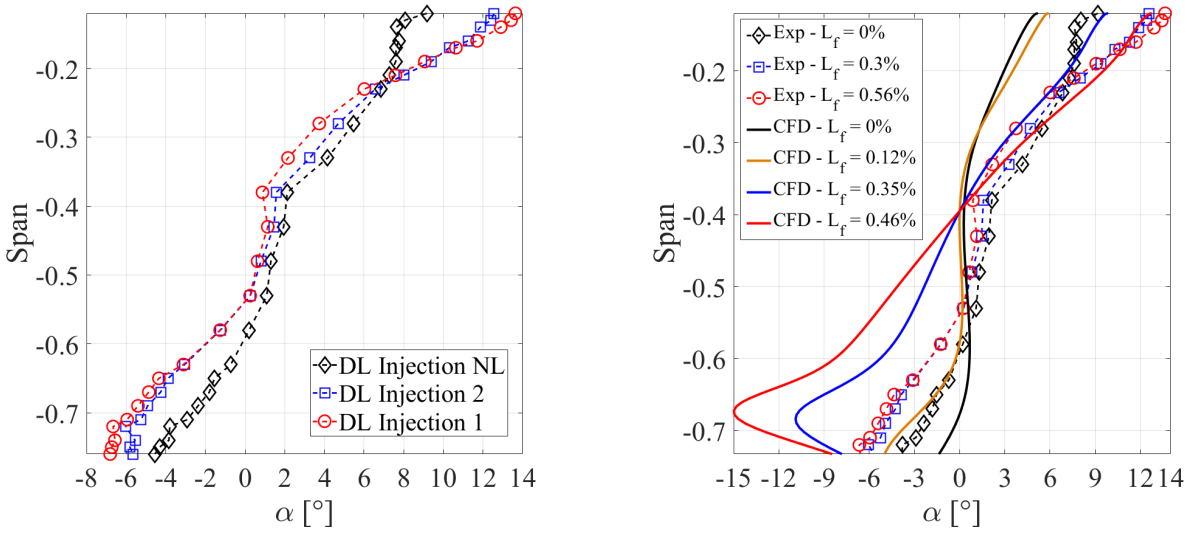

(a) (b)

Figure 4.36: Absolute flow angle in the C2 cavity at compressor nominal speed, design loading conditions - (a) Impact of the leakage fraction on experimental measurements - (b) Comparison with numerical data.

are evaluated in the light of the previously introduced results.

Figure 4.37 presents the experimental data collected. From a general standpoint, the stage loading does not affect the cavity flow topology, both with and without injection. An increase in stator disc boundary thickness layer with the operating point is noticeable in the top part of the Figure 4.37a for the total pressure profiles. The pivot point of the profile remains at the same radial position independently of the stage loading when injection is applied. For the gradient total temperature (Figure 4.37c), an increase in the average flow temperature is detected caused by the higher rotor row work at near stall condition (with respect to the design point). However, the temperature stratification is similar at DL and NS. Concerning the static pressure and flow angle (Figure 4.37b and Figure 4.37d) no significant change is detected. As a result, the operating point effect is minimal on the flow organisation in the H25-C2 cavity.

4.2.3 Effect of the compressor speed

To finish the analysis of the time averaged flow field, the RPM dependence of the C2 flow is presented. Measurement at compressor nominal speed (100Nn) and partial speed (85Nn) are performed. When the compressor speed is reduced, the Reynolds number based on the rotation speed is also reduced. Nevertheless, at 85Nn a type IV flow regime is still expected in the cavity main volume with turbulent separated boundary layers (see Figure 2.5). Figure 4.38 plots the gradients of total pressure (a) static pressure (b) total temperature (c) and flow angle (d).

The average total pressure drops due to the stage loading reduction with the machine RPM.

When injection is applied, the 85Nn profile of total pressure present a pivot point as it is the case at 100Nn. Eventually, this behaviour is also found in near stall conditions. At partial speed, the measured pivot point is detected at higher span and the total pressure in the cavity is more homogeneous than at nominal speed.

At partial speed, the effect of the injection presents the same behaviour than at nominal speed. The pivot point at -36% span is also present as well as the geometry induced slope change. However, for the same injection level, it is noticeable that between two compressor speed there is a shift in static pressure distribution below -0.25 span. At partial speed, disk pumping effect is reduced and the radial equilibrium in the cavity imposes a more homogeneous static pressure distribution. The thermal stratification amplitude is reduced by half due to the lower windage heating produced by the disk. The temperature increase caused by the injection is also scaled down with respect to the nominal speed.

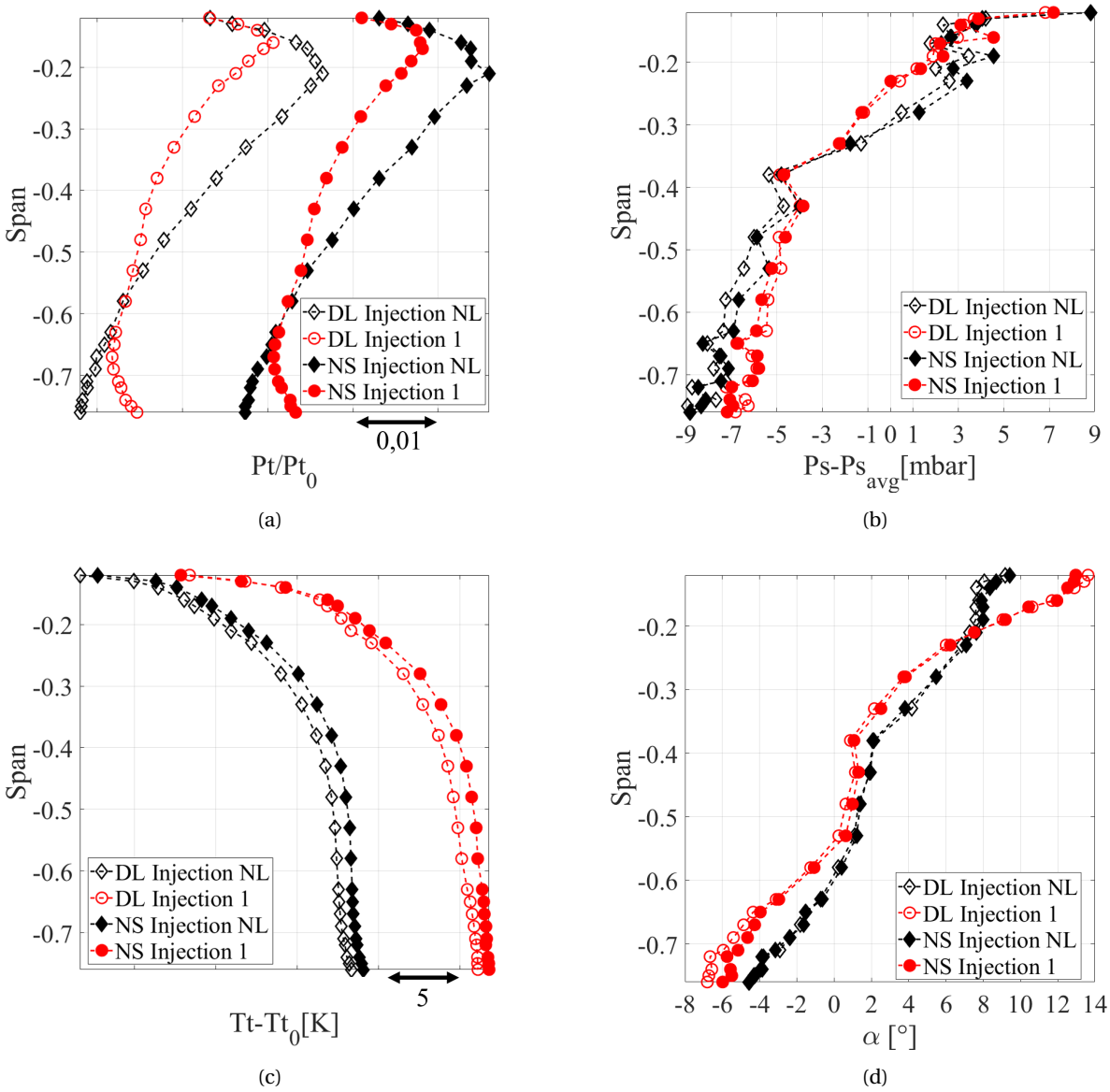

Figure 4.37: Impact of the stage loading on C2 cavity average flow - with and without injection 1 at L_f = 0.56% applied - (a) Total pressure ratio - (b) Static pressure - (c) Total temperature - (d) absolute flow angle.

To finish, the absolute flow angle matches for the top part of the cavity, for the two rotation speed. For the no leakage case, no flow angle change is measured on all the traverse grid. This implies that the average flow topology do not change, in the region measured, with the compressor RPM. As mentioned in the non-dimensional number analysis of the C2 cavity, the flow regime down to -0.6 span is expected to be similar at nominal and partial speed (i.e. based on the rotational Reynolds number and the rotor stator regime classification) which could explain the previous consideration.

The measurement collected at these two operational speeds indicate that the topology of the cavity flow is on average not impacted by changes in rotational speed. In the lowest part of the cavity, the direction of the flow goes towards the rotor disc when injection is applied. This flow deviation is higher at higher rotational speed, for the same injection level. This behaviour can be explained by two phenomena. The first one is due to the probe approaching the injection jet line where cavity flow effectively progresses towards the rotating disk. The second effect is caused by reduced rotor disk pumping effect when the compressor speed diminishes which leads to a more tangential fluid.

4.2.4 Partial conclusion

The time average flow in the C2 cavity evidenced the link between the geometry and the flow structures organization in the cavity main core. As an example, it has been presented that static pressure and flow angle gradients in the cavity do present inflexion points that coincides with sudden increase in cavity aspect ratio.

At a fixed operating point, the presence of the leakage flow homogenizes the cavity pressure field. Concerning the total pressure, it is homogenized around a pivot point that radially separates two local regions of the cavity that, by design, suggest to different flow organization. The existing total temperature stratification in the cavity is few affected by the leakage increase while its average value evolves with the injection conditions. The results given by steady RANS computations are interesting for design purposes as they are able to inform on flow induced effects on gradients for varying leakage conditions. It also helps put the experimental data into perspective concerning the meridional average flow organization.

Changes in operating conditions by mean of stage loading at fixed compressor rotational speed has been investigated. It results that average flow gradients are similar from the design to near stall point at nominal speed. To go further, the flow field response to the same leakage fraction, at different stage loading for the same machine speed, shows an identical behaviour.

Changes in operating conditions by mean of change in compressor rotational speed informs that the consequent reduction in rotating Reynolds number: Do not affect the average flow structures and their response to injection since the cavity remains in regime IV; homogenizes the static pressure radial distribution; reduces the thermal stratification in the cavity as well as the temperature increase caused by the windage in injection conditions; mitigate the disk pumping effect in the lowest part of the cavity, close to the shaft.

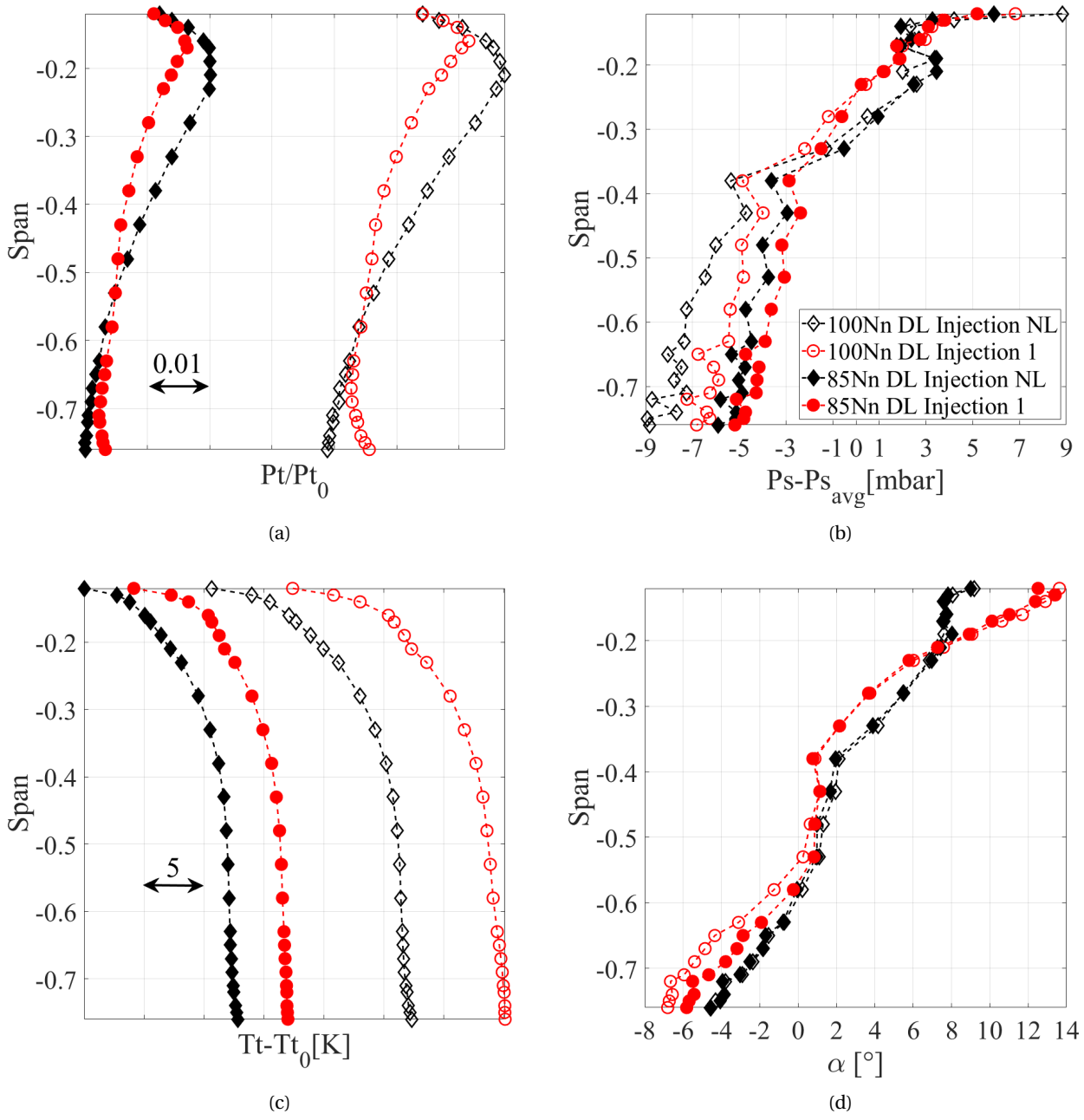

Figure 4.38: Impact of the compressor rotation speed on C2 cavity average flow - with and without injection 1 at L_f = 0.56% applied - (a) Total pressure ratio - (b) Static pressure - (c) Total temperature - (d) absolute flow angle.

4.3 Time resolved flow field in the C2 cavity

In this part of the chapter, the results from time resolved analysis of the C2 cavity flow are presented. Two types of instrumentation are available to analyze the flow field as a function of the leakage fraction, the stage loading, and the compressor rotational speed. In the first part, flow field data from the fast response three hole virtual probe traversed in Plane 2 from -0.12 span to -0.76 span are presented.

The second part of the analysis focuses on the unsteady activity from wall flush mounted fast response pressure sensor immersed in the Bödewadt layer of the C2 cavity. When it brings some valuable information, the experimental data are compared with the numerical result from time resolved simulation of the isolated cavity under injection.

The previously discussed results show that there are no unsteady activity uncorrelated with the disk rotation in main channel measurements. The information presented here investigates the presence or not of such flow feature in the cavity. Coherent flow structures are identified and their dependence to the compressor operating conditions is given.

4.3.1 Unsteady activity in the main core region

4.3.1.1 Ensemble average spectral content

The ensemble average over ten rotations is computed from the traversed 3HV probe data. The objective is to identify in the cavity some frequencies that are correlated with the disc rotation, and present if some also appear in the main channel.

The power spectral density of the ensemble average at three spanwise position (-14% span, -43% span, and -76% span) is presented in Figure 4.39 for the design loading operating point. The positions are selected to be (respectively): in the upper part of the cavity close to the trench and in the cavity casing boundary layer, in the main core region in the middle of the cavity, and at the bottom of the traverse grid at the closest position from the jet line and secondary core. No leakage is applied in Figure 4.39a. The blade passing frequency at 65 EO and its first harmonic appear clearly, along with the 1 EO. Aside of these frequencies, the region below the BPF presents a strong energy content where multiple peaks appear. There is a spanwise dependence to the frequency content and amplitude which indicates the presence of local sources of instabilities. As a comparison, the power spectral density for the design loading point with injection 1 is plotted in Figure 4.39b. The low frequency region energy, below 20 EO, dramatically increases. The spanwise variations are also visible when leakage is applied.

Table 4.4 gathers the most energetic frequencies in the range 0 EO - 150 EO for the near stall operating point and the design loading operating point, with and without injection, at the three span position selected. For all the cases the blade passing frequency and its first harmonic are present. It is also interesting to note that most of the time, the 130 EO (2BPF) has a larger energy content that the BPF.

It is not obvious that the blade passing frequency and harmonics appear in the bottom of the cavity if it is thought that they appear due to pure blade effects. In fact, as introduced in section 2.4, the presence of the rotor blade platform and junction pins on the rotor disk surface is expected to be at the origin of this behaviour. The flow travelling upward in the rotor disc boundary layer is affected by the rotor assembly on the disc. In other words, the BPF is not appearing in the measurement due to the blades but due to the technological choice retained for the blade assembly on the disc. If the 2BPF is the most energetic component, it is also due to the combination of platform(65) and pins(65). These "technological effects" on the cavity wall highly contribute to the flow field and are convected in the cavity boundary layer system (see section 4.3.2).

The presence of the 1 EO as main energy contributor is also questionable. In fact, this behaviour is independent from the ensemble average window used nor signal acquisition. It is presented in section 4.1.2.1 that the labyrinth abradable shows non homogeneous rubbing marks nor depth around the annulus. It informs on the presence of eccentricity of the disk with respect to the stator casing. The exact consequences of this mechanical behaviour on the flow field are not known in the current state of the experimental database exploration, but it could lead to the activation of low frequencies (typically 1 EO) where leakage flow pulses

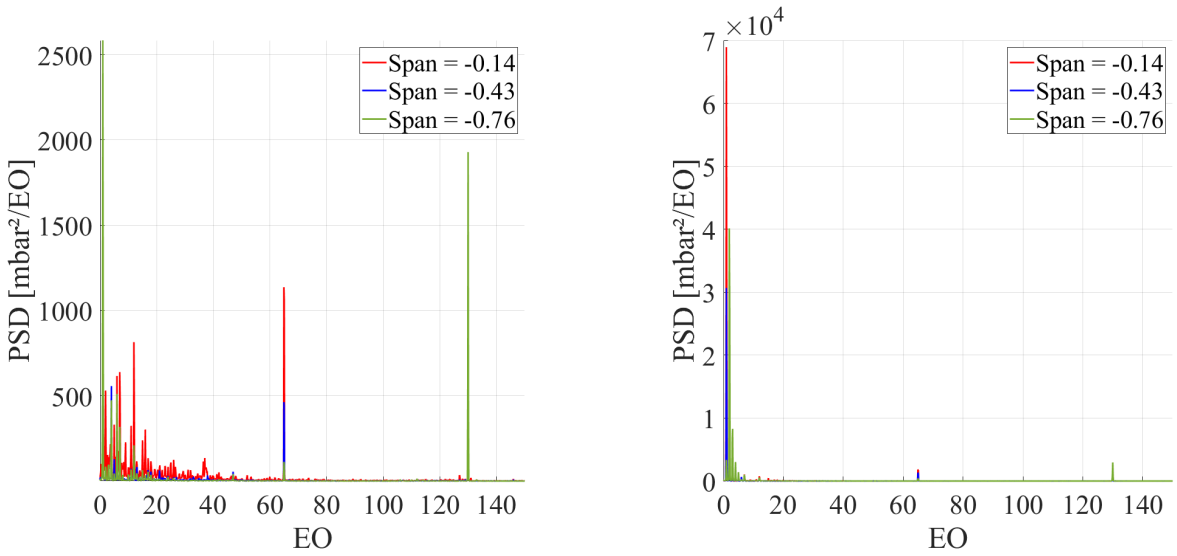

(a) (b)

Figure 4.39: Ensemble average spectra in the C2 cavity at three spanwise position - Nominal speed, design loading operating point - (a) No leakage - (b) Injection 1 at $L_f = 0.56\%$.

with the eccentricity at the labyrinth exit.

Among the four cases presented, the most energetic frequencies fall within the same range. Aside from the BPF and 2BPF, the majority of the frequencies involved are below 15 EO. Linear combinations of high energy frequencies are possible to find the components of higher rank. Some of the frequencies at the highest span position are also present in the stator inlet boundary layer (c.f. Figure 4.28 and 4.29). This indicates that the source of these instabilities is really energetic that there is effectively instability transport between the main channel and cavity which is correlated with the disc rotation. A selection is operated in the trench which filters the frequency content.

Table 4.4: Most energetic frequencies in the ensemble average at three span wise positions in the C2 cavity at compressor nominal speed.

Condition	Span	f_1	f_2	f_3	f_4	f_5	f_6	f_7	f_8	f_9
DL_{Noleak}	-0.14	1	2*BPF	12	7	6	2	5	11	46
	-0.43	1	4	BPF	6	2*BPF	12	7	5	13
	-0.76	1	2*BPF	6	4	7	12	3	2	11
DL_{inj1}	-0.14	1	2	2*BPF	BPF	7	12	6	15	3
	-0.43	1	2	4	3	6	12	7	5	11
	-0.76	2	3	1	4	2*BPF	5	7	12	BPF
NS_{NoLeak}	-0.14	1	12	6	7	2*BPF	9	15	8	BPF
	-0.43	1	4	3	6	7	12	BPF	2*BPF	5
	-0.76	1	2*BPF	3	6	4	7	12	BPF	5
NS_{inj1}	-0.14	1	2*BPF	6	3	7	12	15	BPF	4
	-0.43	1	3	4	6	BPF	12	7	11	2*BPF
	-0.76	1	2*BPF	2	4	6	3	7	BPF	12

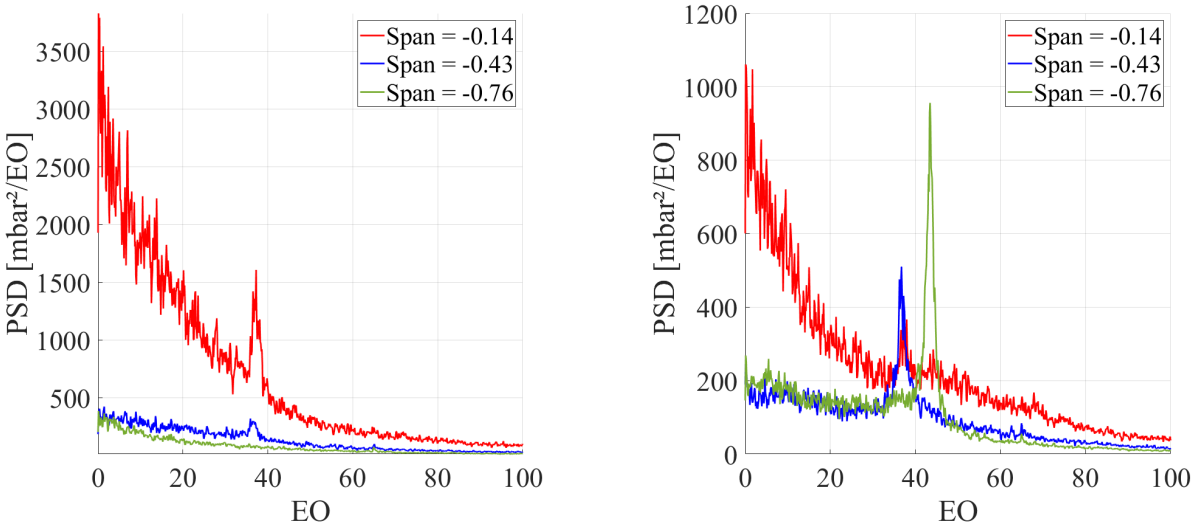

Figure 4.40: PSD of pressure temporal fluctuations in the C2 cavity - Design loading no leakage - (a) Virtual probe central hole - (b) Virtual probe right hole.

4.3.1.2 Temporal fluctuations around the ensemble average

The temporal fluctuations of the flow around the ensemble average are computed. The power spectral density for the nominal speed, design loading point is presented in Figure 4.40a. The removal of the ensemble average and of the synchronous structures with the disk leads to the identification of one residual frequency peak at 37.2 EO, at 14% span . The peak amplitude is decreasing with the span and its maximum frequency of the peak is changing from 37.2 EO to 36.5 EO at -43% span. When the probe is close to the source of the instability, the relative amplitude of the frequency attached to this flow feature increases. From high to low span, it is seen that the probe moves away from the source at 37.2 EO.

The angle of the unsteady probe used is based on the average flow direction at each span evaluated in the search mode procedure using steady three hole virtual probe (see section 3.1.3.7.1). The spectral content collected in the cavity main core is evaluated against the probe direction to assess if some instabilities present some direction preferences.

Figure 4.40a plots the measurement of the virtual probe central hole. For the same conditions, the probe right hole is plotted in Figure 4.40b. The energy of the spectra at 14% span is reduced and the amplitude of the 37.2 EO is now below the amplitude of the 36.5 EO at cavity midspan. In the lowest point of the traverse grid, a dominant frequency at 46 EO that was not present in the central hole measurement appears. Added to the spanwise sensitivity, the results collected also present a dependence to the probe orientation.

The frequency contents at each span position are grouped to locate sources of instabilities in the cavity volume. The impact of leakage fraction on the spanwise instability distribution is presented in Figure 4.41. Design loading power spectral densities of temporal fluctuations with and without leakage is presented for the central, left, and right position of the measuring hole. The left position means that the probe faces towards the rotor disk at 30° from the average flow direction. The right hole is at the opposite, facing the stator disk wall at 30° from the average flow direction.

The map for the central hole at no leakage (Figure 4.41a) presents a high energy region in the low frequency range for the upper part of the cavity. The frequency peak already seen at 37.2 EO reach a maximal energy for -17% span. Its amplitude quickly decreases downwards. It indicates a highly local phenomena. This component is found in all the data presented. Its amplitude is higher when the probe hole is oriented towards the rotor disc (Figure 4.41e). Either, the preferential direction of this structure is better captured by the left hole, either, the lateral displacement of the hole put the source closer to the sensor. From what has been seen in the previous sections, it is possible that the vortex generated at the step between rotor and

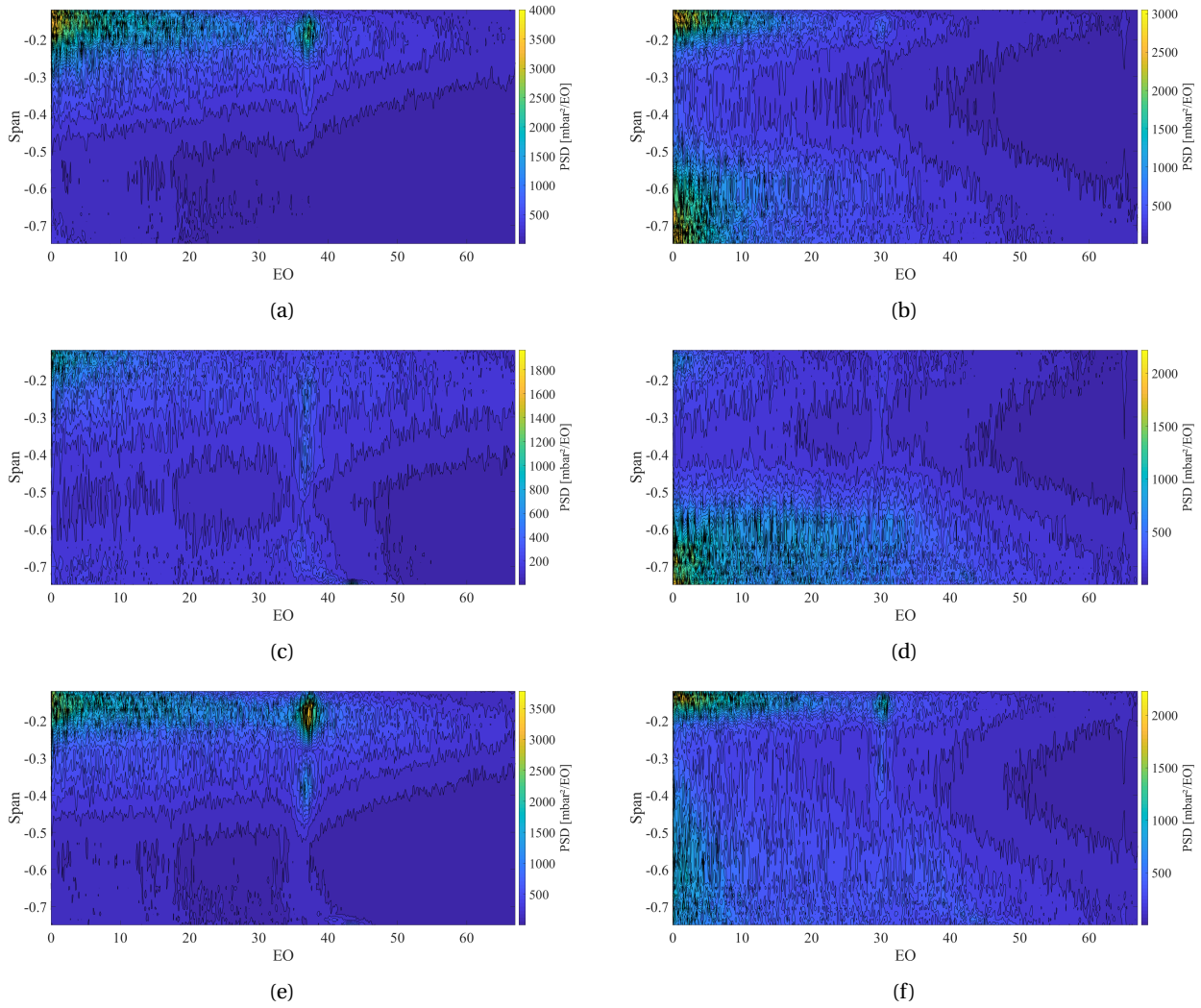

Figure 4.41: PSD of pressure temporal fluctuations in the C2 cavity along the span - Design loading nominal speed - (a) Central hole no leakage - (b) Central hole injection 1 - (c) Right hole no leakage - (d) Right hole injection 1 at $L_f = 0.56\%$ - (e) Left hole no leakage - (f) Left hole injection 1 at $L_f = 0.56\%$.

stator disc in the top part of the cavity is the source of the fluctuation.

When leakage is applied (Figure 4.41b), the cavity frequency content at low span activates for the low frequency range. Between -55% span and -20% span (parallel disks), the low frequency range energy is highly reduced. With the injection increase, the 37.2 EO frequency shifts down to 30.3 EO.

The maps for the right hole (Figure 4.41c and Figure 4.41d) highlight at no leakage the presence of maximum energy at the lowest measured point, for a frequency of 43.5 EO. When the probe is moved from the top to the bottom an energy band at 36.6 EO see first its frequency reduced at 35.7 EO at -65% span and then increased to 43.5 EO. The measuring right hole in the bottom part of the cavity is directly facing at the leakage jet and secondary core pulse. When leakage is applied (Figure 4.41d), the low frequency energy content is only increased in the bottom part of the cavity. The left hole position presents the opposite trend from the right hole. In fact, the maximum energy content is kept at high span with and without injection. The shift in frequency for the local instability at high span is also noticed but the position of the maximum energy in that band is opposite to the one of the right hole.

Figure 4.42 presents the same contour plots for the design loading point, with injection, but at partial speed. The central hole position shows the same behaviour than in the nominal speed case where the top and bottom of the span range gather the highest energy content at frequencies below 20 EO. Since injection is applied, the reading of the right hole in the bottom part of the cavity is blurred by the low frequency high

energy content induced by the leakage. However, it is still possible to distinguish on the left hole map the spanwise frequency shift previously introduced etween 30EO and 40 EO. At partial speed, from no leakage (not shown) to injection 1, the high span instability originally at 37.6 EO shifts down to 30.7 EO.

4.3.1.3 Comparison with numerical data

Numerical simulation results are used to evaluate the experimental data against a configuration without blade effects and with smooth cavity walls. The operating condition in the numerical analysis is taken at nominal speed, for the design point, and for a leakage fraction at L_f = 0.46%. The comparison with the experiments is done for the design loading injection 1 at L_f = 0.56%.

The spectral content of numerical probes positioned in the main cavity volume at the same location as the three hole virtual probe is plotted in Figure 4.43a. Each probe is at a different radius. A span wise dependence of the frequency content is visible, like in the experiments. For that reason, the span wise frequency map of the results is built in Figure 4.43b. The most energetic frequency found in the simulation is at 24 EO and remain for most of the spanwise positions. This frequency has also been found in the main channel in the experiments, at both stator inlet boundary layer and stage exit. The second frequency range of interest is located at low span only and at a frequency of 46.7 EO. The frequency and spatial localization correspond to the low span frequency seen in the three hole virtual probe measurements in the cavity.

4.3.1.4 Partial conclusion

The previous section identifies the dominant instabilities measured in the cavity main volume. The blade passing frequency and harmonics have dominant energy. The presence of these frequencies in the cavity is induced by the rotor mechanical assembly. In general, most energetic frequencies in the cavity are below the BPF. Even when leakage is applied, the most energy is found below 12 EO, for disc synchronous instabilities .

The analysis of the temporal fluctuations presents the sensitivity to the span position and orientation of the probe in the measurements. The combination of these parameters is used to evaluate the presence of local instability sources that are non-synchronous with the rotor disc as well as their preferential convection direction in the cavity. In summary, it is showed that when the probe is oriented toward the rotor disc, the highest energy content is located below 40 EO and in the cavity bottom, i.e. below -0.6 span. On the contrary, when the probe is directed towards the stator disc, high instability region is located below 25 EO, and in the cavity top part, i.e. above -0.2 span. Nevertheless, high span localized instability source between 30 EO and 50 EO is also detected.

4.3.2 Unsteady activity in the stator disk boundary layer

Wall flush mounted fast response pressure sensor were used to measure the unsteady activity at -43% span in the stator disk boundary layer. Thirteen sensors were available around the machine annulus. The signal acquisition was performed with all the traverse probes out from the cavity.

The power spectral density of temporal fluctuations for the design loading point at injection 1 is presented in Figure 4.44a. The thirteen sensor data are displayed. Around the annulus, there are no discrepancies in the most energetic frequencies. The spectral content below the blade passing frequency is composed of three main regions around 10 EO, 16 EO, and 40 EO. For a similar condition, the numerical probes (in Figure 4.44b) present a bump of rotating instabilities centred in 16 EO and composed of multiple peaks such as 12 EO, 15 EO, 17 EO, 21 EO and 24 EO. These frequencies were previously highlighted in the ensemble average spectral content of: the measurements performed in the main core, the measurements in stator inlet boundary layer, and some (see 24 EO) at stage outlet. At this point it is also important to remember that the C2 geometry characterization predicted a cavity Helmoltz frequency of 10.2 EO. Furthermore, when the leakage flow follows the leakage path, it is pushed radially upward on the rotor disc that acts as a radial compressor with a BPF of 65 EO due to the platform assembly. Then, the leakage that is not ejected in the cavity, collects in the stator boundary layer. It has been presented that the stator platform wall is non smooth. In

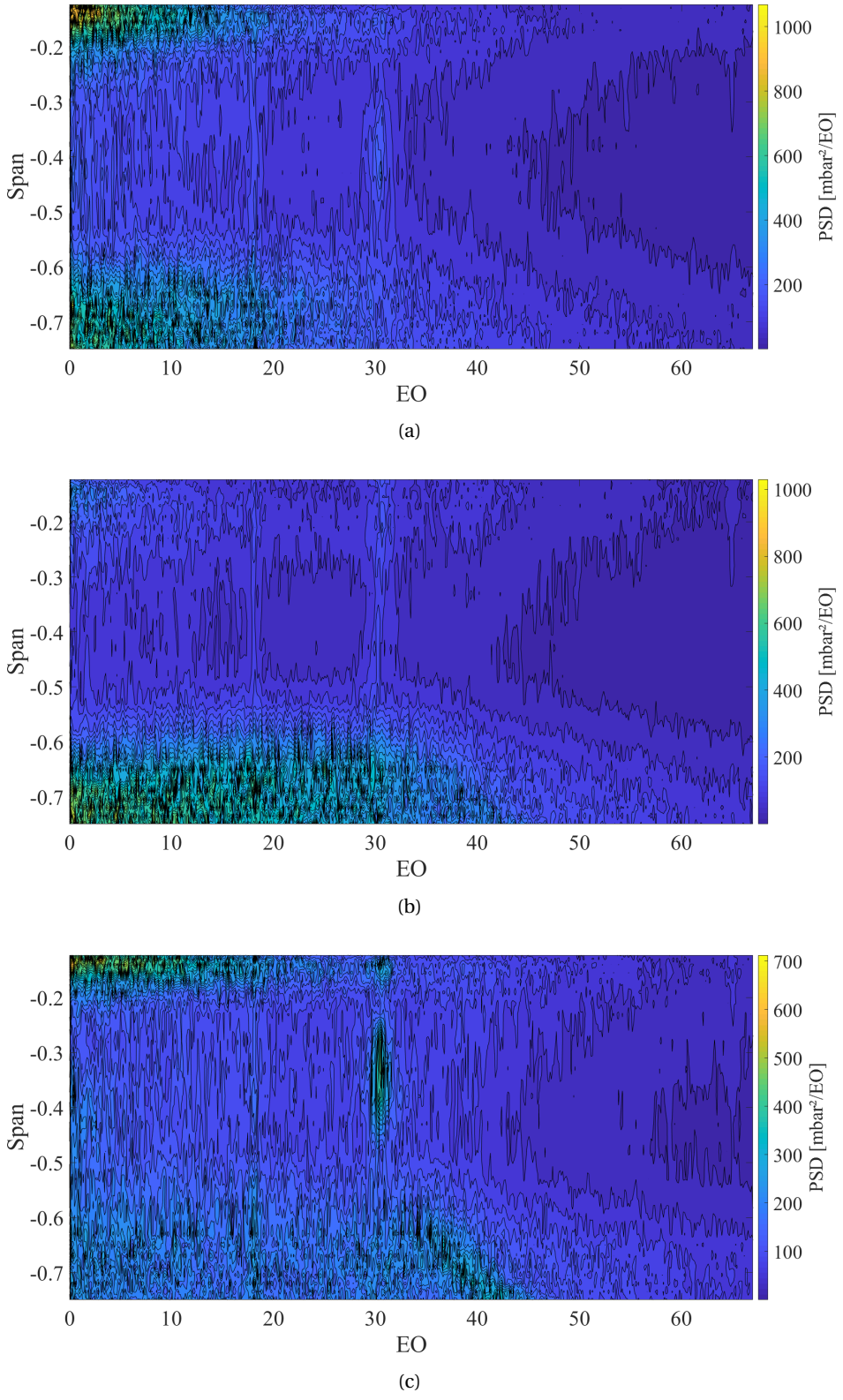

Figure 4.42: PSD of pressure temporal fluctuations in the C2 cavity along the span - Design loading partial speed and injection 1 at $L_f = 0.56\%$ - (a) Central hole - (b) Right hole - (c) Left hole.

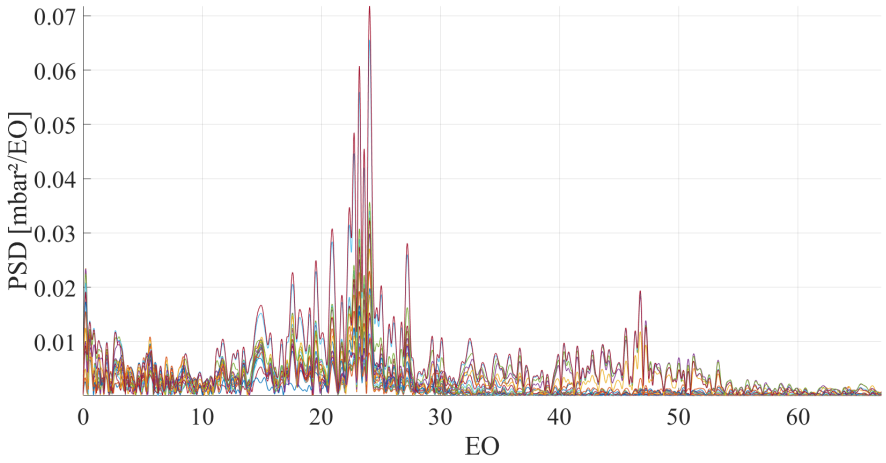

(a)

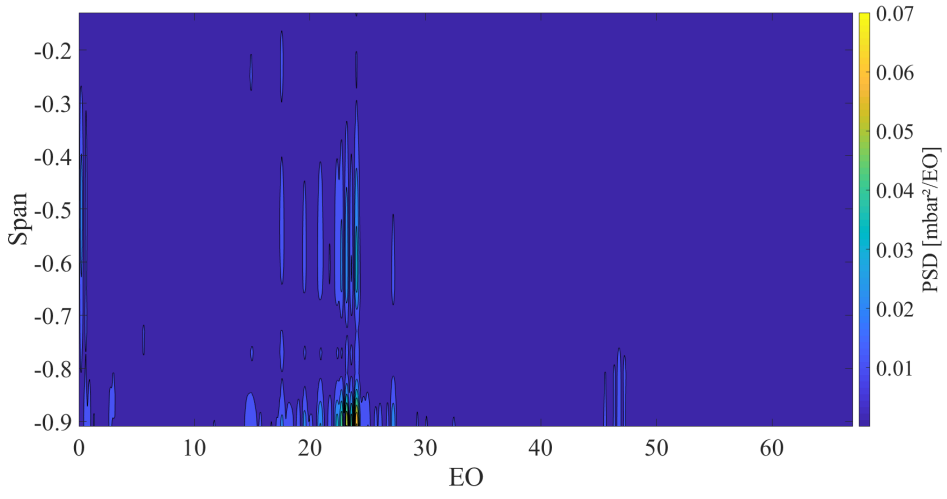

(b)

Figure 4.43: Unsteady numerical results of main core instability at nominal speed, design loading, 0.46% leakage fraction- Spectra and spectrogram collected along a probing line in Plane 2 to match experiments sampling - (a) Spectra for an array of numerical probes radially distributed in the numerical domain at the location of the 3HV probe in the experiments - (b) Corresponding span wise frequency map.

fact, it presents the junctions of the 8 stator blade sectors equally spaced around the annulus. The leakage flow sees rotor stator interaction from 65 rotor blades and 8 stator blades. The computation of Tyler and Sofrin modes done in Chapter 2 for the same number of blades indicates stationary modes (so visible in the temporal fluctuations) M(0,2), M(0,3), M(0,5)of respective value 16 EO, 24 EO and 40 EO. The frequency ranges perfectly fits with the frequency regions activated in the stator boundary disc layer. However, the numerical data predicts similar frequency ranges while having totally smooth walls which goes against the aforementioned argument.

The experimental power spectral density is averaged between all the sensors to evaluate the most representative frequency content for each operating condition. The obtained average spectra are displayed in Figure 4.45 for three operating conditions (100Nn DL, 100nn NS, and 85Nn DL) and two leakage fraction (0% and 0.56%). For all the cases residual components of the BPF and 2BPF are present.

At nominal speed design loading (Figure 4.45a), the frequencies at 10.62 EO and 16.6 EO are not affected by the leakage. The 10.6 EO is close from the estimated 10.2 EO Helmoltz frequency at this operating condition taking into account the trench as a pressure line attached to the cavity volume. Similarly, the measured 16.6 EO is close from the computed 16.9 EO Helmoltz frequency of the cavity, taking the last labyrinth tooth as the pressure line attached to the cavity volume (see Table 2.1). Above 20 EO, the frequency bump at 40 EO shifts to higher frequency at 41.3 EO. The peak at 46.3 EO remains at the same frequency when leakage is applied. These frequency ranges eventually coincides with the 3HV measurements in the low span region of the cavity. Their origin may be explained by a pulsing effect of the jet line that separates the main core and secondary core which causes shear layer instability. This hypothesis would need to be confirmed in future work. To finish, the energetic component at BPF+3.2 EO disappears when leakage is applied.

When the operating point is changed to higher loading (c.f. Figure 4.45b), the sensitivity to the leakage fraction is similar than at design loading. No major change in flow structure is induced by the leakage (except for the BPF + 3EO). However, with respect to the design point, new frequencies are activated. A frequency peak is created at 27.6 EO and the amplitude of the 46.7 EO increases.

When the rotation speed is reduced, flow features remain similar but are shifted and changed in their energy hierarchy. The list of interesting spectral content region is the following one: 11.1 EO, 18.2 EO, 39.6 EO, 55.1 EO.

In the frequency range below the blade passing frequency (65 EO), the presence of the injection does not significantly impact the amplitude of the most energetic modes that are non-synchronous with the disc rotation.

The ensemble average signal are presented in Figure 4.46 for a test with and without injection at nominal speed and design operating conditions. In this operating point, the instability at 47 EO disappears with the injection which indicates the presence of an instability directly controlled by the leakage fraction. The localisation of the instability source is not possible with the current measurement. However, its amplitude is almost equal to the amplitude of the BPF which indicates a strong driver for the cavity flow topology. In the current knowledge of the experimental database, this behaviour has only been detected at that operating condition.

4.3.3 Space-time analysis of instabilities in the stator disc boundary layer

In this section, instability spatial coherence is investigated using the method presented in section 3.1.3.7.2. The objective is to identify the mode structure and rotating speed associated with the most energetic frequencies introduced in the previous parts of this work.

Results at nominal speed, design loading, no injection

The method presented is applied first at design loading, no injection. The spectra of the full pressure signal ($EA + T_f$) is plotted in Figure 4.47a for the FP_{10} sensor in the stator disc boundary layer. For the same test, the spectra of temporal fluctuations around the ensemble average is indicated in Figure 4.47b.

In this part, eleven pairs of sensor are used in the cross correlation with the same reference probe being FP_{10}. As a reminder, the minimal angle spacing used is of 5° which means that a structure with 72 lobes

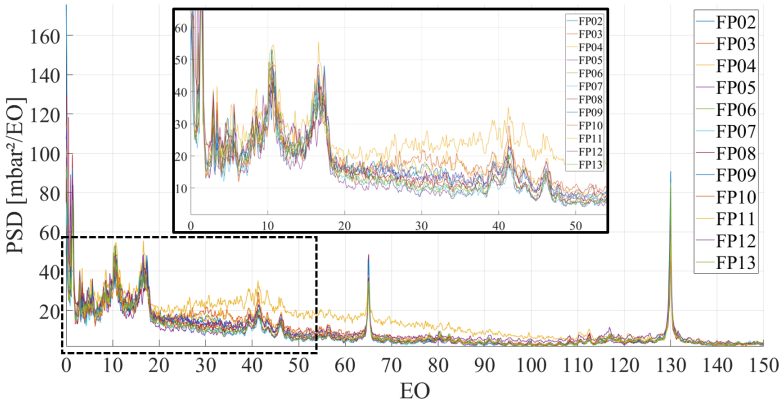

(a)

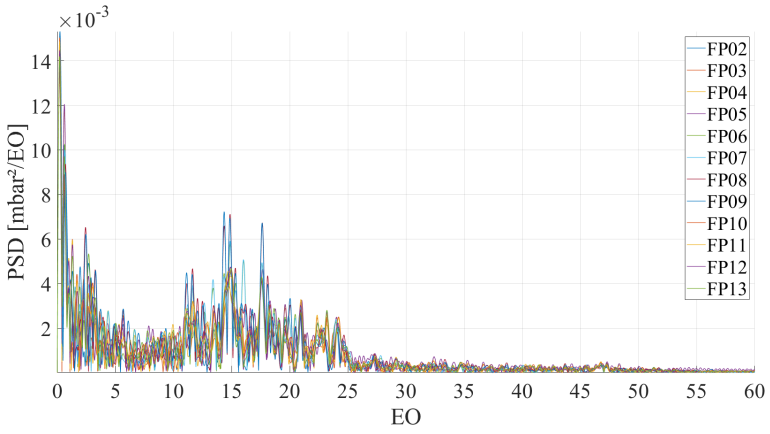

(b)

Figure 4.44: Spectral content of pressure temporal fluctuations in the stator disk boundary layer - Nominal speed, design loading - (a) Measurement with fast response pressure sensor at injection 0.56% leakage fraction - (b) Numerical probes at same location than fast response sensors. Injection at 0.46% leakage fraction.

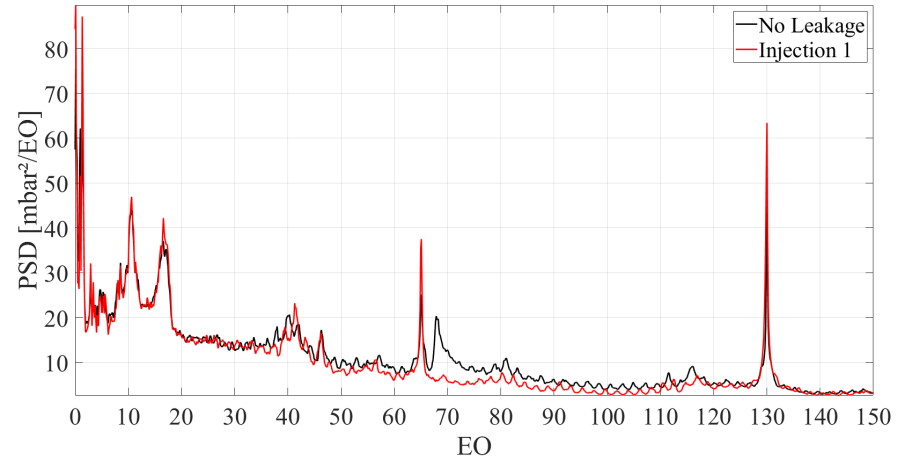

(a)

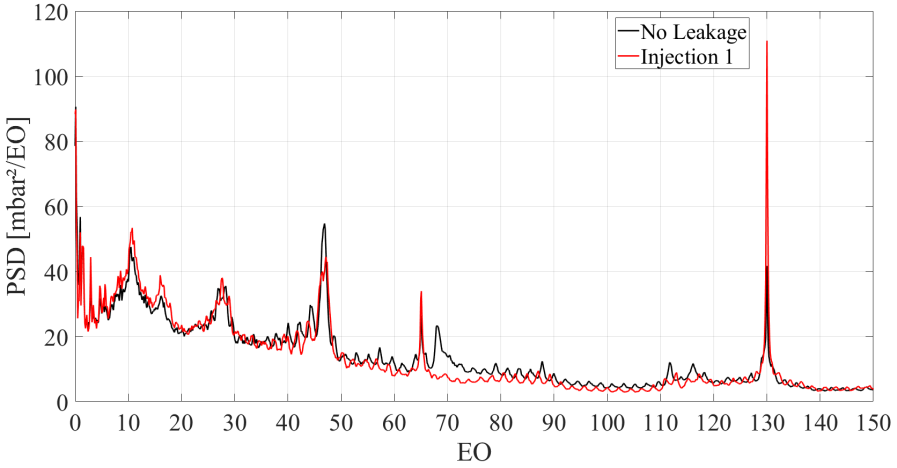

(b)

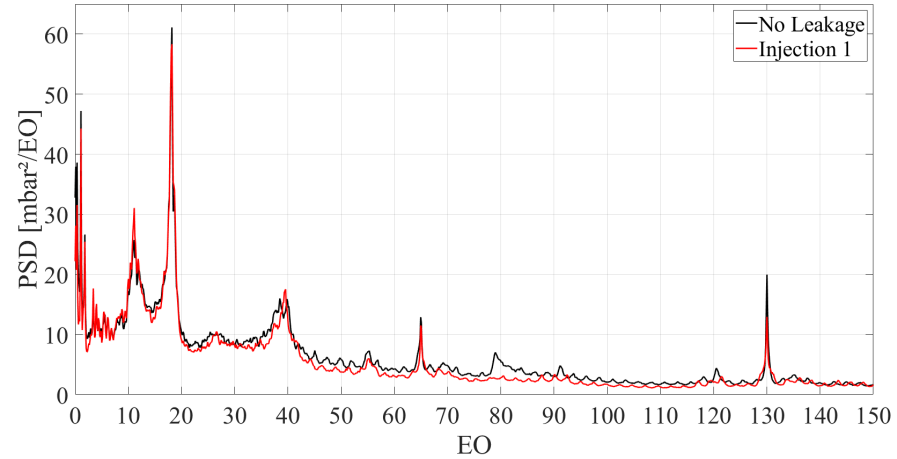

(c)

Figure 4.45: Average of PSD between the fast response pressure sensor in stator disk boundary layer - Temporal fluctuations - Effect of the leakage fraction - (a) Nominal speed design loading - (b) Nominal speed near stall loading - (c) Partial speed design loading.

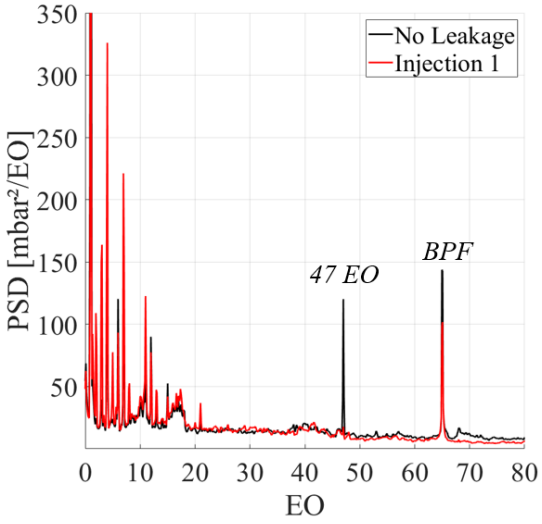

Figure 4.46: Average of PSD between the fast response pressure sensor in stator disk boundary layer - Ensemble average - Nominal speed, design loading - Effect of injection.

($\frac{360}{5} = 72$) just find one period of the phenomena between two sensors. If the number of lobes found is higher, aliasing issues arise.

In the first place, the correlation maps are extracted in a 0.2 EO frequency interval around the most energetic peaks present in the spectra in Figure 4.47a.

In Figure 4.48, frequency intervals sampled are organized by increasing frequency. In the low frequency range, below 15 EO, the interval sampled present coherent behaviour for structure speed close to the disc speed. Visualisation suffers from space-time precision. Most of the frequencies investigated inform on modes that are rotating at the disc speed in the low frequency range. The only departing case is in the interval [3.92:4.12] where a 95% structure speed is computed with a correlation of 0.55. This is converted to a non natural number 4.2 lobes.

At high frequencies, an interesting behaviour appears. The peak present at 47 EO, already seen in Figure 4.46, which coherence map is indicated in Figure 4.48h gives a correlation coefficient of 0.65 for a mode rotating at 83.3% of the disc speed. A corresponding number of 56 lobes is computed. The rotating speed of the mode comes close to the 82% disc speed deduced from the Figure 4.34a pressure gradient in the cavity upper part.

The case of 65 EO and 130 EO that respectively are the BPF and $2 * \text{BPF}$ are presented in Figure 4.48i and Figure 4.48j. It is interesting to note that from the coherence maps, these frequencies are not correlated with the disc speed. The 65 EO map indicates a speed of 45% disc speed. The 130 EO indicates two bands, one at 39% disc speed and one at 95% disc speed. For the structure speed mentioned, there is an aliasing problem with the sensor position. The period of 65 EO at the disc rotating speed is on the edge of the measurement reading but is still bigger than the minimal sensor spacing. The method should be able to partially track this instability speed if it is measured by the sensors which it appears not to be the case.

Similar analysis is done for the spectra of temporal fluctuations in Figure 4.47b. Most energetic regions of the spectra are analysed for an interval of 0.6 EO. Results are presented in Figure 4.49. For all the maps that present a coherent behaviour, the main wave speed is estimated at 44.5% of the disc speed.

There is no clear explanation of that behaviour. The transport of instability in the cavity may be at the origin for such structure speed, inducing a cavity group velocity. Here also, the mode computed velocity is close to the measured core velocity deduced from Figure 4.34a, in the cavity lower part. The preliminary CFD RANS data also indicates for that operating conditions a main core swirl ratio close to 46%. The regions activated in the spectra, e.g. 10EO, 16EO (both close to Helmholtz frequencies), 40EO, are "resonant" modes of the cavity geometry. It is visible since, these frequencies are excited, non-correlated with the disc rotation, and they are also excited in all the operating conditions visible (see Figure 4.45), at varying loading,

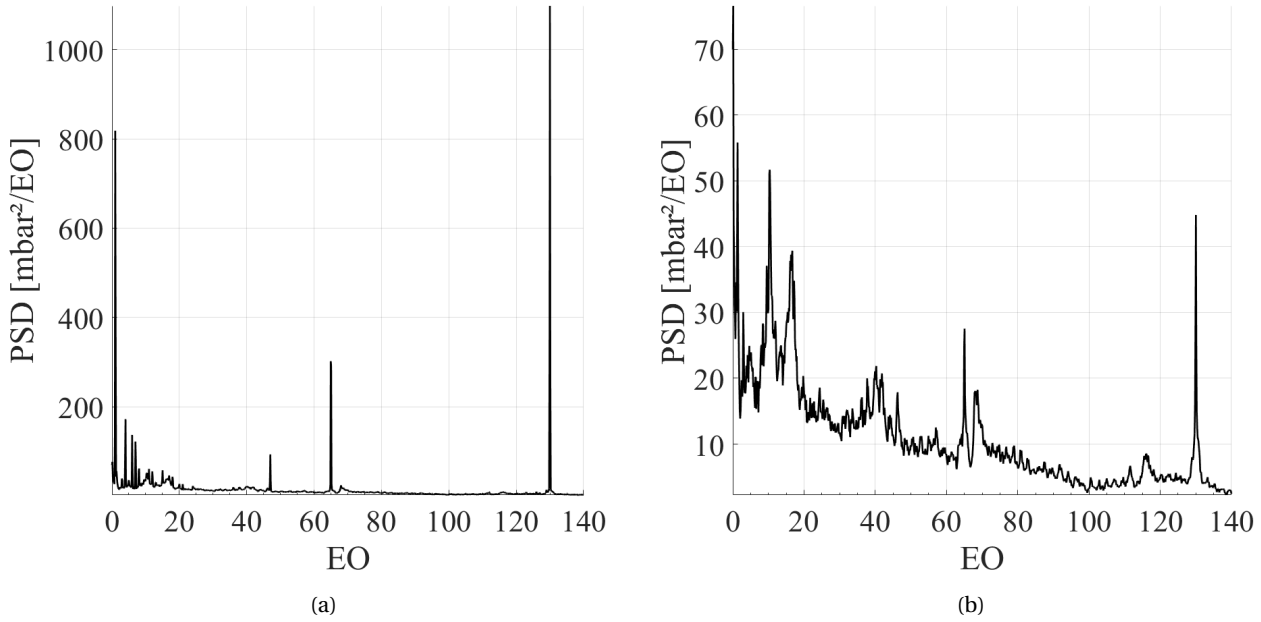

Figure 4.47: PSD of pressure fluctuations for sensor FP_{10}. Design loading, no leakage - (a) Full signal - (b) Temporal fluctuations around the EA.

leakage fraction, and rotational speed. In other words, if at rest, a uniform pressure wave is applied to the cavity, these modes are excited, and the coherence map should display a 0% structure speed. However, if these axial modes are excited by an instability transported in the main core cavity vortex, the frequency response is visible in the vortex frame of reference, hence at 45% disc speed. This could explain why they all present the same main wave speed in the correlation results.

The aforementioned assumption should be verified in a future activity with the evaluation of the cavity geometry fundamental modes.

Effect of stage loading

The stage loading effect is evaluated between design loading and near stall loading. Changes are small concerning the coherence maps.

The 47 EO peak presented in the full pressure signal analysis remains and has the same wave speed at 83.3% of the rotor disc speed.

In the temporal fluctuations, the behaviour is identical at near stall and at design loading. All of the most energetic frequency range do present a similar main wave speed. Nevertheless, this speed decreases from 44.5% at design loading to 43% disc speed at near stall loading.

Effect of the rotation speed

The effect of the compressor speed has been evaluated thanks to RPM transient tests. In the literature, clear evidences of flow reorganization in the Bödewadt boundary layer appear during spin up and speed down tests. This is mainly due to flow regime changes in the stator and rotor disk boundary layers, caused by a drop or increase in rotational Reynolds number. In the work presented here, the speed up and speed down tests were performed between 95%Nn and 100%Nn. This range was selected to be sufficiently wide to observe the flow response while keeping a reasonable data weight.

The compressor speed was changed manually in the speed interval. In that sense, acceleration was not constant and test repeatability was not possible. The test section was not designed to run at more than nominal speed which imposed to approach this value with extreme care under acceleration. An example of

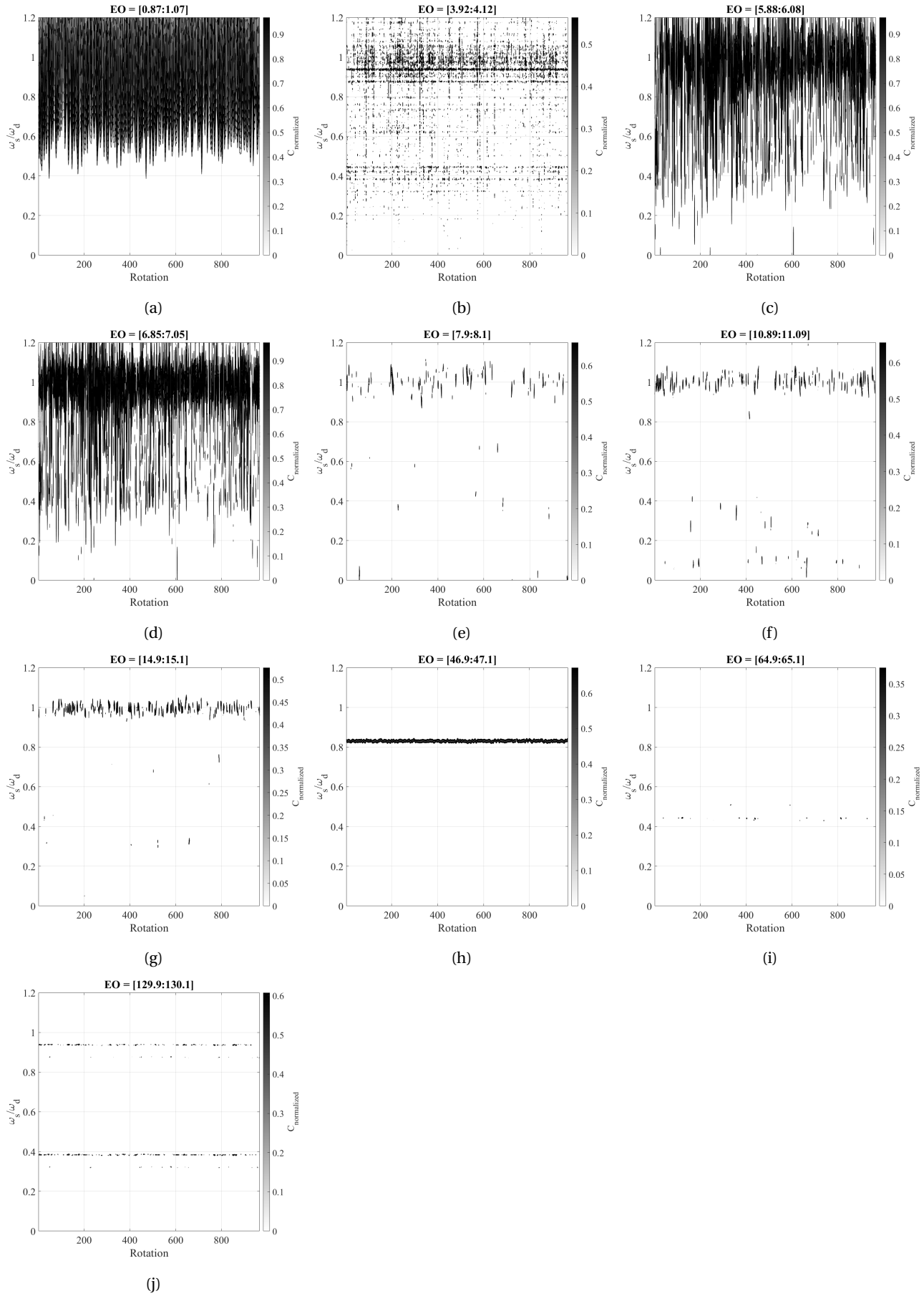

Figure 4.48: Coherence maps for most energetic regions in full signal spectral density. Eleven sensor pairs at nominal speed, design loading, no leakage - BPF = 65EO.

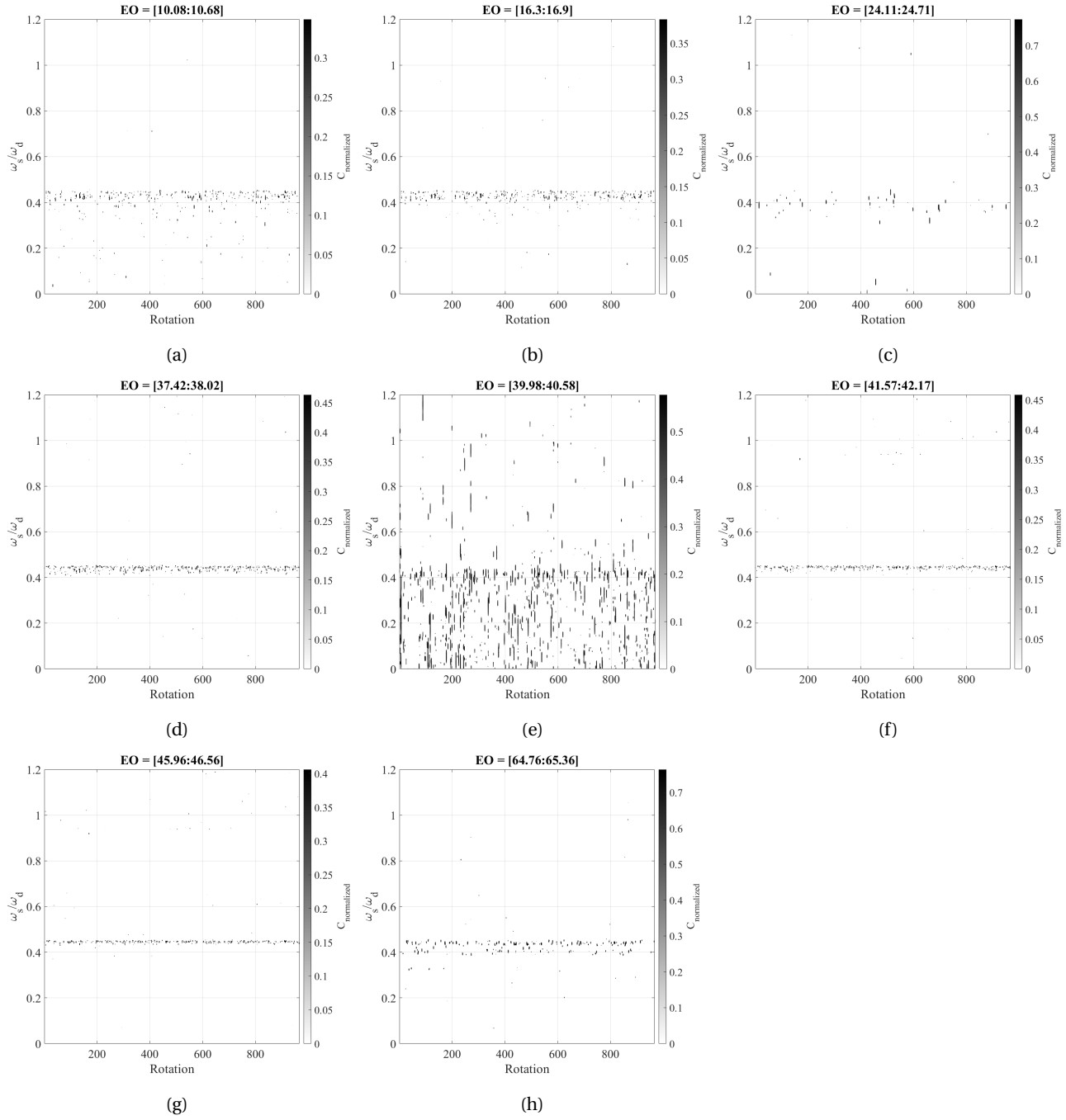

(a) (b) (c)

(d) (e) (f)

(g) (h)

Figure 4.49: Coherence maps for most energetic regions in pressure temporal fluctuations spectral density. Eleven sensor pairs at nominal speed, design loading, no leakage - BPF = 65EO.

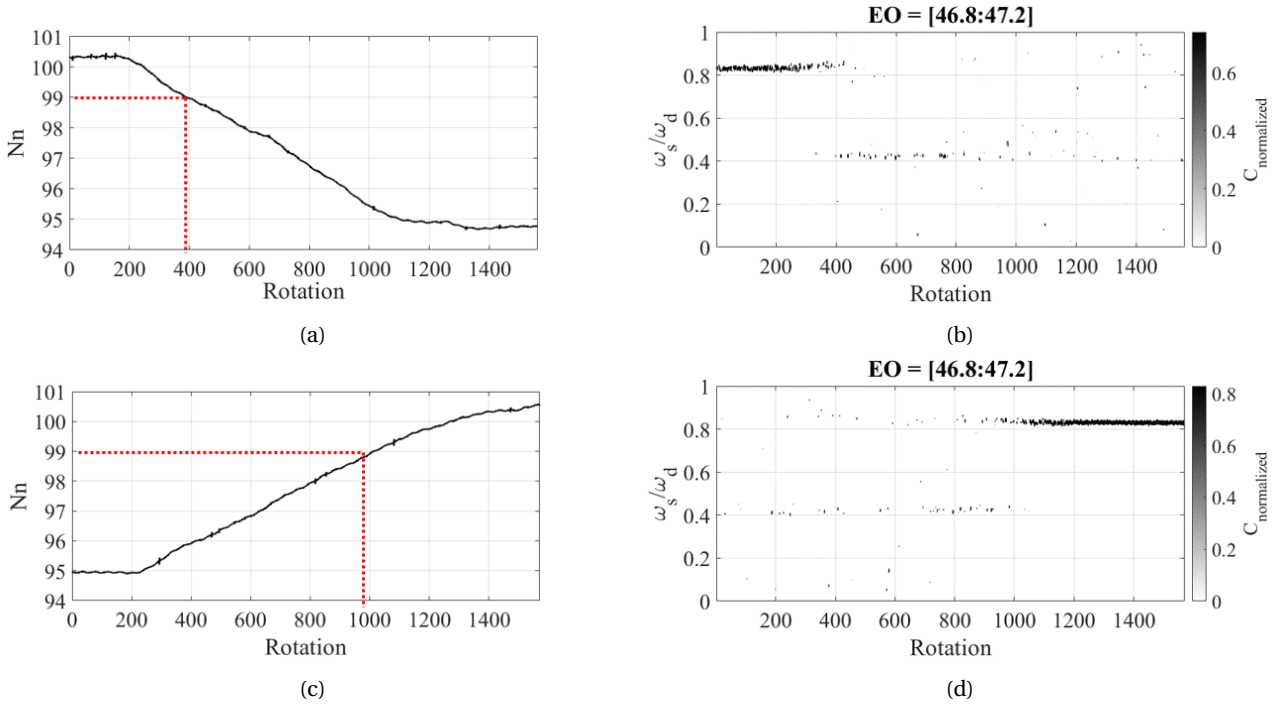

Figure 4.50: Coherence map for the interval [46.8:47.2] in the full pressure signal during RPM transients at design operating vane parameter - (a) Speed down test compressor rotational speed - (b) Speed down test coherence map - (c) Speed up test compressor rotational speed - (d) Speed up test coherence map.

speed down ramp generated in the experimental campaign is presented in Figure 4.50a.

For the full pressure signal, focus is set on the highly correlated peak at 47 EO, visible in Figure 4.48h. The coherence map in the range [46.8:47.2] is presented in Figure 4.50 for speed up and speed down tests of the compressor. In a speed sown operation of the compressor, Figure 4.50b indicates that the 47 EO mode speed changes brutally in rotation 400 for a compressor speed of 99Nn. In the speed up test, in Figure 4.50d, the inverse phenomena occurs, for the same rotation speed of 99Nn. There is no hysteresis in the generation of this mode. With a mode speed reduction of almost 50%, with approximately 43% disc speed below 99Nn, the 47 EO frequency enters in aliasing for the sensor spacing.

It is noticeable that the flow phenomena associated with this frequency is highly RPM dependent. It is also possible that this phenomena is changing of frequency range when the speed of the compressor changes. Nevertheless, at stabilized operating point at partial speed, no similar behaviour than the 47 EO at 100Nn can be found in any frequency interval, which indicates a flow structure only present above 99Nn of compressor speed.

In the temporal fluctuations, the main wave speed is analyzed in the range [37:43] for the speed down and speed up tests presented in Figure 4.50a and Figure 4.50b respectively. The main wave speed appears to be RPM dependent. In that frequency range the correlation coefficient is above 0.7 and is constant during the transient phase. Figure 4.51a and Figure 4.51b report that during speed down and speed up tests, the structure speed follows the evolution of the compressor rotation speed. The main wave speed evolves between 40% and 44% of the disc speed with no lag time perceptible.

To validate the hypothesis that the wave speed measured can be attributed to the cavity main core speed, a verification should be performed to evaluate the impact of the rotor speed on the swirl ratio of the aforementioned flow structure.

Comparison with numerical data

Data from the unsteady simulations are extracted to investigate the presence of azimuthal non uniformities in the cavity. In the CFD computation, leakage is applied at a leakage fraction of 0.46%.

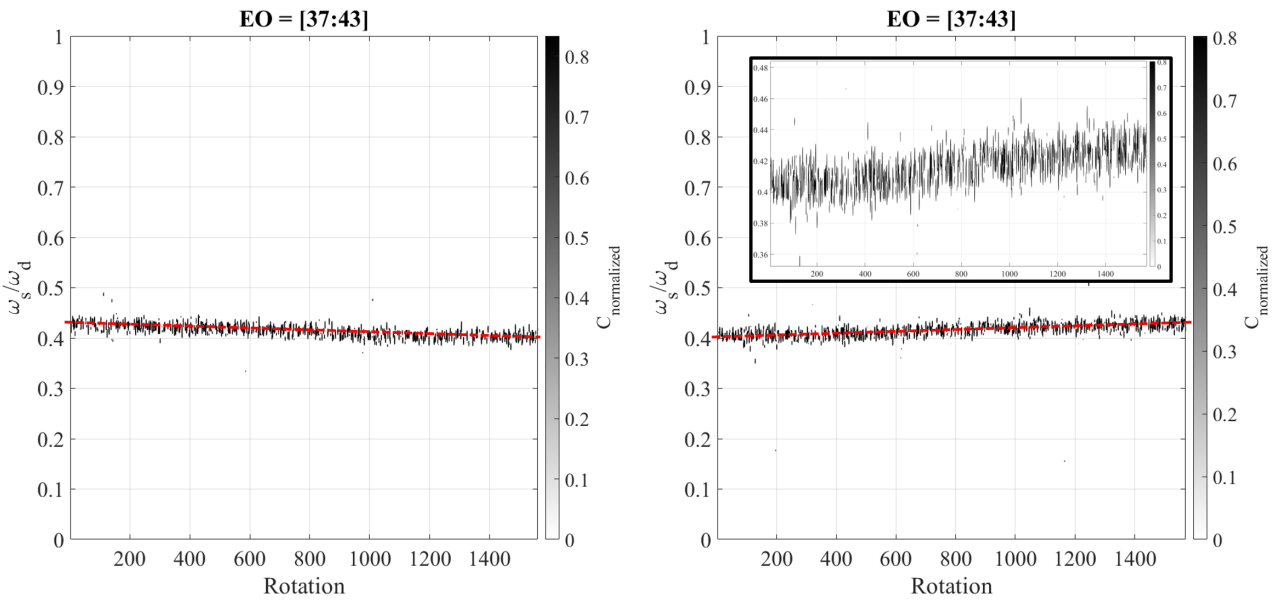

(a) (b)

Figure 4.51: Coherence map for the interval [37:43] for the temporal fluctuations during RPM transients at design operating vane parameter - (a) Speed down test - (b) Speed up test

The meridional average streamlines over one rotor revolution are plotted in Figure 4.52a. Similar to the Figure 4.31, the solution predicts the presence of two main vortical structures being the main core (biggest vortex) and the secondary core (close to the labyrinth exit).

Cuts in the domain are done at position A and B to investigate the flow field over the machine annulus. Cut A passes through the stator disc boundary layer and crosses the region of the secondary core instability. Section B cuts the cavity trench in half and approaches the rotor disc boundary layer.

The static pressure in cut A is plotted in Figure 4.52a. The secondary core region presents a vortical disturbance around the machine annulus. The number of lobes of this disturbance is of 47. The computed mode speed is of 46.8% disc speed. As a consequence, the corresponding frequency in the stationary frame of reference is of 23 EO. The presence of this secondary core instability forces the jet line to pulse, which also influences the main core dynamics. The previously introduced spectra and spectrogram in Figure 4.43 show this trend where the most energetic frequency is of around 23 EO from the bottom of the cavity (where the secondary core is) up to -0.3 span (top of main core vortex). Nevertheless, it is important to note that the static pressure numerical probes in the stator disc boundary layer, whose spectra is presented in Figure 4.44b, do not clearly show traces from this instability.

To complete the analysis, the flow radial velocity in cut A is presented in Figure 4.52c. In the region of secondary core instability, alternate positive and negative radial velocity of the flow is visible which corresponds to the secondary core toroidal structure. The radial velocity in cut B is added in Figure 4.52d. It shows that the instability created in the jet line imposes a pattern for the flow travelling upward in the rotor disc boundary layer. Forty-seven local regions of accelerated flow are present. This dynamic is also found in the trench region.

4.3.4 Partial conclusion

The time resolved flow field in the C2 cavity has been investigated in this section. The measurement setup used in this work allowed to identify and locate the most energetic regions of the cavity. Cavity traverse grid top and bottom positions presents the most energetic content in a frequency range below the blade passing frequency. The instability balance is perturbed by the presence of the injection which homogenizes the unsteadiness of the cavity, thanks to an increased flow recirculation in the disc boundary layers. A

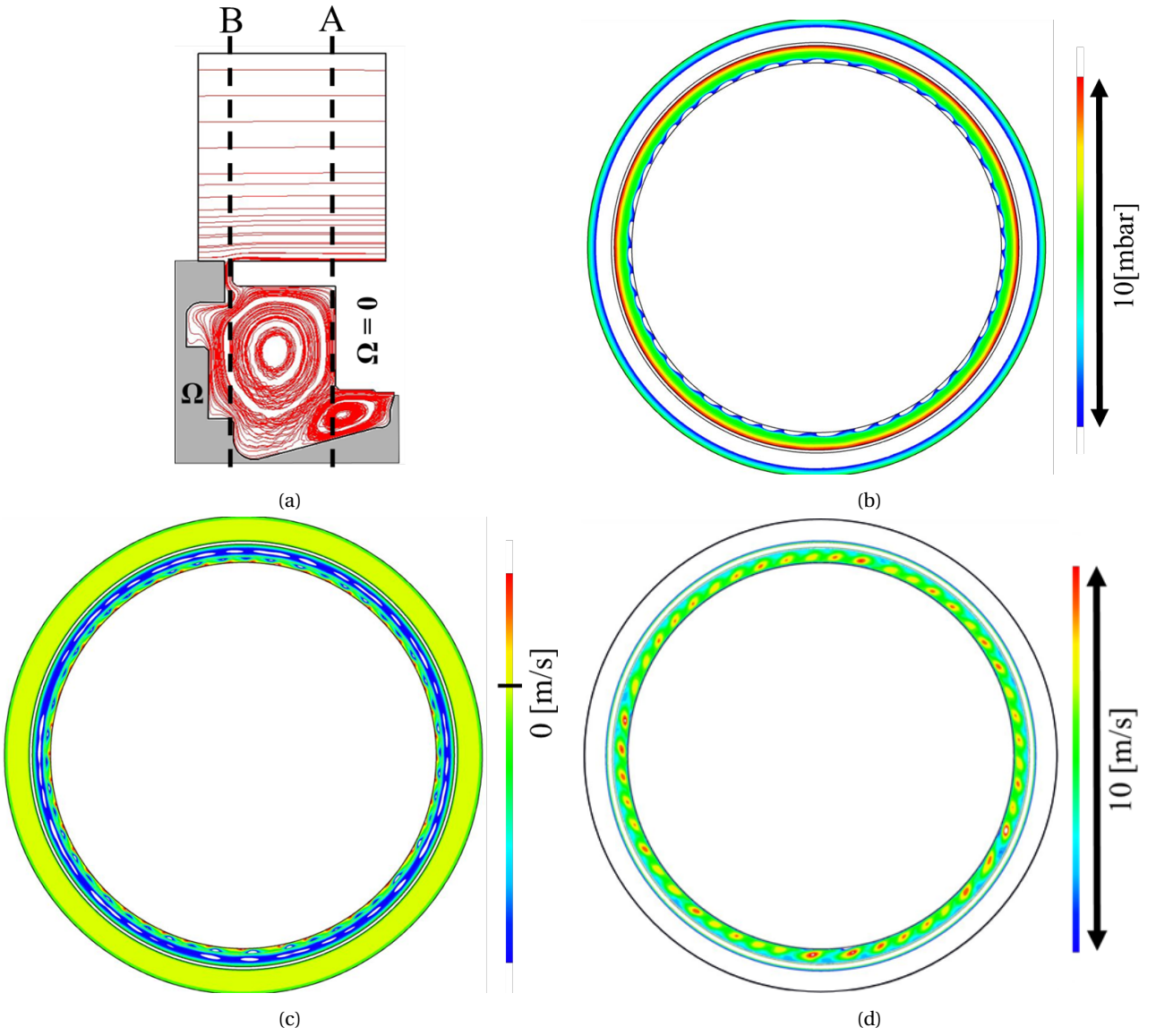

(a) (b) (c) (d)

Figure 4.52: URANS simulations flow field investigation - Nominal speed, design loading, leakage fraction of 0.46% - (a) Azimuthal averaged streamlines over one rotor rotation. Definition of cuts A and B for flow field visualisation - (b) Static pressure field in cut A - (c) Radial velocity in cut A - (d) Radial velocity in cut B.

first comparison with unsteady RANS data gave comparable frequency range activation with respect to the experimental data. This gives confidence in a possible follow up for the numerical activities on the C2 cavity.

The evaluation of the flow field in the stator disc boundary layer informed on the presence of non-synchronous instabilities that are few affected by the leakage fraction but evolve with the compressor operating conditions.

A deeper analysis of the 47 EO frequency that show a high sensitivity to leakage in the full pressure signal, indicates the presence of a 56 lobes rotating flow structure at 83.3% of the disc speed. The mode activation is also RPM sensitive with no hysteresis. This further confirm the high coupling that exists between the machine operating conditions and the cavity flow regimes. Further analysis of the temporal fluctuations indicates a group velocity of around 44% disc speed for the cavity instabilities that are non-synchronous with the disc. The group velocity is also rotor speed dependent.

The complementary analysis of the numerical unsteady computations reveal that in the case of a smooth cavity the secondary core instability drives the dynamics of the flow along the jet line. As a consequence, the 47 lobes flow pattern found at the labyrinth exit is also found at the trench exit.

Both in the experimental and numerical data, local dynamic behaviours has been evidenced. The limited current knowledge of the data and of the instability transport mechanism do not allow to justify fully the measured disturbances in the stator disc boundary layer.

4.4 Conclusion

The results presented in this chapter traduce the current knowledge of the experimental database collected in this work. Conclusions can be derived from the analysis of the H25-C2 cavity system both from a numerical and an experimental approach.

From a methodology point of view, at equivalent leakage level, the discrepancies between the experimental results and the numerical results are limited. The use of steady RANS simulations with controlled leakage allows to draw a good understanding of the average flow in the H25 stator shroud cavity. It is also a conservative way to evaluate, at minor cost, the performance degradation induced by cavity leakage at design operating point. The use of unsteady simulation of the isolated cavity is effective to target the main frequency ranges attributable to a geometry.

The use of time averaged and time resolved instrumentation in the test campaign bring that it is possible to measure highly turbulent confined environment such as the C2 cavity. The use of three hole probes and hot wires in virtual mode is a good practice to reach compact measurement devices. In complex environment such as the C2 cavity, the use of directional probes coupled with a yaw control capability of the traverse system is requirement. It allows to perfectly tune the alignment of the probe with the average flow direction to obtain results within the calibration range. The use of a closed loop facility equipped with closed cavities is a good platform to analyze the effect of cavity flows on axial compressor performance. The leakage conditions can be tuned independently of the operating point. This is an advantage to cover a wide spectra of injection properties and for multiple operating points and rotation speed in a limited amount of time.

Concerning the effect of cavity flow on the H25 stage, the performance degradation of the stage caused by forced leakage is measured. A reduction in efficiency is observed at nominal speed and partial speed for all of the operating points. For a leakage fraction of 0.56%, the compressor design isentropic efficiency is decreased by 0.97% at the design point. At stabilized operating point, the leakage fraction does not affect the stall margin of the compressor. this result is valid at nominal speed and partial speed. The leakage flow that exits the cavity induces a reduction of the axial and tangential momentum of the main stream. As a consequence, additional turning is felt by the downstream row due to the increase in inlet hub boundary layer skewness. A cost effective way to model the cavity flow effect on a compressor stage (in design phase for example) is to focus on the change applied by the leakage on three-dimensional boundary layer profile downstream of the trench.

In the main stream, frequencies that are not correlated with the disk rotation are not found. This suggest that the cavity leakage flow is convected in the stator row stream in flow structures that are in phase with

the rotor. The analysis of the trench region (stator row inlet) set the same conclusion.

In the cavity, the added injection reduces the pressure gradients. The leakage flow tends to homogenize the flow field. An important temperature stratification is found in the C2 cavity. Thermal effects are a key component to the flow generated in the shroud cavities. The average flow field organization is driven by the shape of the cavity where trends can be explained thanks to the non-dimensional numbers. The average flow field show limited effect of the operating point and rotation speed except for the total pressure distribution.

Spatial and temporal organization of the flow in the cavity is detected by the instrumentation put in place. It is possible to provide operating condition sensitive measurement of cavity flow in unexplored regimes, at high confinement levels, in a turbomachine like environment.

The impact of technological features such as non-smooth disc walls, due to rotor platforms and pins, is huge in the cavity flow dynamics. As a result, spectral signature from the technological effects is found at high energy content in the whole cavity. A similar configuration with smooth end walls would give crucial information, as a comparison case, to evaluate the flow disruption induced by cavity technological effects.

Uncorrelated frequencies with the disk are found in the cavity. Instability transport along the leakage flow path is identified thanks to the traversed probes. The effect of the operating conditions is such as stage loading and rotational speed induce changes in the disk synchronous and non-synchronous instabilities.

Findings and trends from this work could also be compared with turbine seal flow studies as far as flow and geometrical non dimensional numbers coincide. In the trench region, azimuthal non uniformities, ingress and egress mechanisms have similar origin between compressor and turbine test cases. However, a comparison of cavity and main flow interaction should be taken with care, as compressor cavity exit flow faces adverse pressure gradient, contrary to turbine seal exit.

Chapter 5

Opening to new research

THis chapter closes the manuscript with an outlook to future activities following or directly inspired from the presented work. Thematics for a deeper use and analysis of the generated experimental database are investigated. In the first place, the influence of the mechanical assembly of the rotor disk on the cavity flow is evaluated. In the same section, the necessity to take into account cavity geometrical effects is discussed. In a second section, the use of cavity flow measurement is done to evaluate its implication in axial compressors flow working beyond the stability margin. To finish, considerations about cavity flow low order modelling are given following the work presented in this manuscript.

Contents

5.1 Impact of rotor mechanical assembly and geometrical effects

5.1.1 Impact of rotor disk assembly

This section evaluates the possibility that the data collected contain information and flow disturbances induced by the rotor mechanical behaviour. Similar to fluid structure interactions in the compressor main channel between blades vibration modes, acoustic modes and vortical disturbances, the cavity flow and cavity/main flow interactions are expected to contain traces of rotor disk induced perturbations.

Potential sources of mechanical induced instabilities are presented. In the first place, the eccentricity between the rotor disk and the stator is able to generate azimuthal non uniformities in the cavity since it locally affects the cavity geometry. Figure 5.1 defines three types of eccentricity. The first one, called static eccentricity is caused by a misalignment between the rotor and stator symmetry axis. The second type of eccentricity is dynamic. Here, rotor and stator have the same symmetry axis but the rotor is not concentric to the shaft. To finish, mixed eccentricity presents the two previous behaviours.

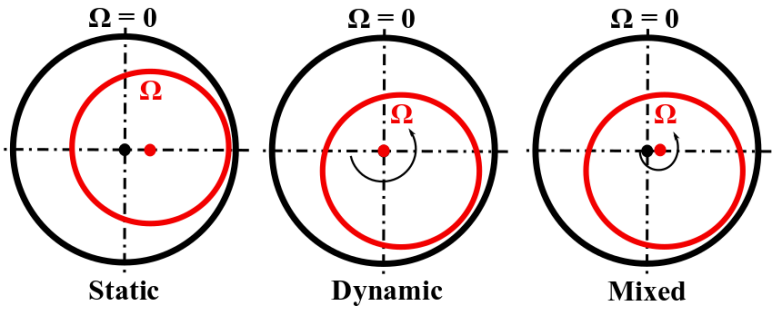

Figure 5.1: Static, dynamic and mixed eccentricity for rotor-stator assembly.

In stator shroud cavities using labyrinth seal as a clearance management technology, the eccentric behaviour of the rotor causes a non uniform seal gap around the machine annulus. As a consequence, the leakage fraction in the cavity is not uniform.

With a static eccentricity, flow distortion at cavity trench exit and at downstream row inlet boundary conditions is created.

In the presented work, labyrinth seal abradable moulding clearly indicated the presence of a non uniform clearance in the C2 cavity (see Figure 4.9). In the experimental stator inlet total temperature increase with an increase in leakage fraction in the cavity (see Figure 4.19b). Nevertheless, with the used experimental setup, it was not possible to track temperature distortion at stator row inlet. As a consequence, low span total temperature level was used to detect the presence of cavity flow, at H25 stage outlet. In Figure 4.10 an average non uniform temperature field in the low span region is detected between cases with and without injection. There is clear evidence that under injection, the low span stage outlet flow is separated between a region of high and low total temperature increase. Static eccentricity of the H25 rotor seal assembly can be at the origin for such behaviour.

To go further, dynamic eccentricity is considered as well as rotor vibration. The rotor disk assembly modal activity is driven by the mass distribution around the center of rotation as well as the rotational speed of the compressor. The work of Jia et al. (2020) demonstrates the impact of rotor disk vibration in a turbine rotor stator cavity. In this numerical study, the frequency of disc vibration do not affect the topology of the baseline flow field. However, traces of rotor vibration are found in the cavity dynamics. The detection of the disk vibration frequency shows stronger amplitude in the seal region where the flow enters the cavity. The flow amplitude response to the vibration is also dependent upon the disk vibration frequency.

In the present work, it has been found that in the cavity, the most energetic frequency always coincides with the 1 EO (see Table 4.4). Dynamic eccentricity can be at the origin for such behaviour. When injection is applied, the energy associated with the frequencies below 4 EO is increased. It is also visible that when injection is applied, the amplitude of temporal fluctuations around the pressure ensemble average for low frequencies increases in the low part of the cavity, close to the seal. This is visible in Figure 4.41 from the

probe traverse measurement in the C2 cavity.

The rotor disc static assembly and dynamics also impact on the cavity/main flow interaction due to its effect on cavity trench geometry. For simplicity, an orthogonal trench is considered here. In Figure 5.2, the geometry change from an aligned configuration is presented. Disk radial expansion, or contraction, can create a step at the trench exit. Rotor disk flex can also reduce or increase the trench aspect ratio. The relative axial position of the rotor and stator assembly can be azimuthally non uniform in static but also in dynamic.

The consequence of trench geometry changes would then affect the mechanisms of cavity flow ingress and egress, as well as the downstream stator hub boundary layer generation.

In the lowest part of the cavity, labyrinth seal flutter could occur. Local flow unsteadiness is then created and could affect the cavity flow dynamics.

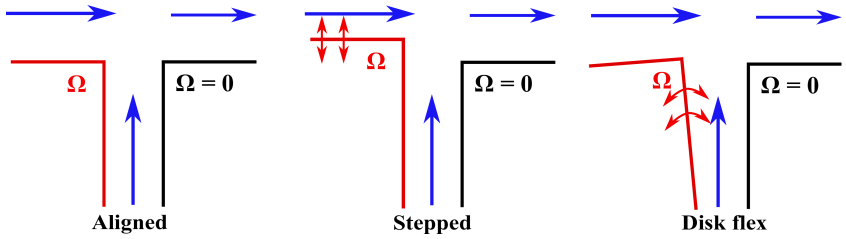

Figure 5.2: Orthogonal trench rotating disk induced deformation.

This section covered the possible effect caused by the static and dynamic mechanical assembly irregularities between the rotor and the stator disk. To further understand the cavity flow dynamics measured in this work, it could be of interest: to measure static and dynamic eccentricity of the current labyrinth seal; to evaluate the rotor assembly structure modes either by performing a modelling analysis of the isolated rotor, and to include obtained structural modes into cavity only numerical setup (as one presented in this work); to mature the existing test section with the ability to evaluate fluid structure interactions.

5.1.2 Geometrical effects and representativity

This section discusses the validity of cavity flow studies in non representative environment for turbomachinery applications. The representativity in question here concerns the geometrical effects that are present in an engine-like configuration but that can be missing in low TRL (Technical Readiness Level) applications.

It is often presented in the literature canonical configurations that are composed of two smooth discs, one rotating, the other one fixed. In reality, turbomachinery applications can present protrusion, such as bolts, either in the rotating or fixed frame of reference. Studies that consider these geometrical effect demonstrate they are not only increasing the rotor work on the cavity fluid (if on the rotor), but also contribute to the global dynamics of the flow (see Moghaddam (2015)). In the present work, evidences of flow disturbances caused by the non-smooth nature of the cavity walls were indicated. As an example, the rotor assembly composed of platforms and pins provides to the cavity flow a high energy content to the 2*BPF component (see Table 4.4). The presence of rotor and stator sector junction along the cavity flow path also induces disturbances from rotor and stator interaction.

By including the rotor blade assembly in cavity flow studies, the inter platform leakage flow and its effect on axial compressor performance could also be taken into account (see Taylor, D. J., Longley, J. P. (2019)).

To finish, it has been presented in section 2.4 that instrumentation routing pipes are present in the C2 cavity. It is for the moment not clear to the author if the measurement collected include detectable traces of these pipes wakes, and what is their contribution into the measured cavity unsteadiness.

As a conclusion, for the experimental activities, results obtained on the flow physics and cavity dynamics can bias the generalisation of the analysis towards engine-like configurations. Concerning the numerical activities, a cost balance should be found between the numerical domain angular size, that affects the cavity mode resolution (see Chew et al. (2019)), and the inclusion of geometrical effects from engine-like environ-

ments. If the numerical domain angular size is favored, specific wall boundary treatment can be created to take into account periodic geometrical effects.

As a last comment, the present database can be used to compare smooth and engine like C2 cavity configurations to evaluate the destructive versus non-destructive behaviour of geometrical effects on the cavity dynamics.

5.2 Leakage flow contribution to stall inception

The VKI R4 facility and the H25 stage offer the possibility to go over the stability limit of the machine and study machine failure mechanisms at fixed rotor rotational speed. In the test campaign, multiple stability tests have been performed at different machine rotational speed. One of the possible follow up to this work is the study of the cavity flow contribution to the stall inception of the H25 stage. In this section, a first overview of what the measurement setup offers is presented.

The analysis of the machine failure mechanism mostly rely on the Kulite sensor inserts that are present in the test section and introduced in Chapter 3. Sensors names and azimuthal positions are recalled in Table 5.1. Sensors FP_{01}, FP_{14}, FP_{15} are located in the main channel in front of H25 rotor leading edge, at tip. The other sensors are positioned in the C2 cavity stator disk boundary layer. With the current arrangement, no sensor is found at the same azimuthal position than another one which prevent the visualization of instability axial convection.

Table 5.1: Fast response pressure inserts label and corresponding angle in main channel casing in front of rotor leading edge (FP_{01}, FP_{14}, FP_{15}) and in stator hub cavity wall(FP_{02} to FP_{13}) - Rotor rotation is in the direction 40°–>0°.

Sensor name	Sensor Angle [°]
FP_{01}	38
FP_{14}	158
FP_{15}	258
FP_{02}	0
FP_{03}	40
FP_{04}	45
FP_{05}	60
FP_{06}	100
FP_{07}	105
FP_{08}	145
FP_{09}	150
FP_{10}	325
FP_{11}	330
FP_{12}	335
FP_{13}	350

Typical H25 machine failure recorded from the rotor leading edge sensor FP_{01} and cavity sensor FP_{03} is displayed in Figure 5.3a. These sensor are chosen because of their close clocking position in the machine (see Table 5.1). Pressure is normalized based on the maximal pressure in each time series to ease the reading. The rotation label 0 indicates the position of a spike event detected both in the main channel and in the cavity. The spike event is detected in the cavity few instants before being detected in the main channel due to sensor different azimuthal alignments. When the instability passes in front of the cavity sensor, it indicates a pressure drop while the opposite is noticed in the main channel. After 1.3 rotations, the compressor enters in unstable mode and a surge cycle is triggered.

To evaluate the type of stall inception of the H25 stage, the spectral content of the FP_{01} sensor is given in black in Figure 5.3b. As a comparison, the measurement of sensor FP_{03} in the cavity is also indicated, for

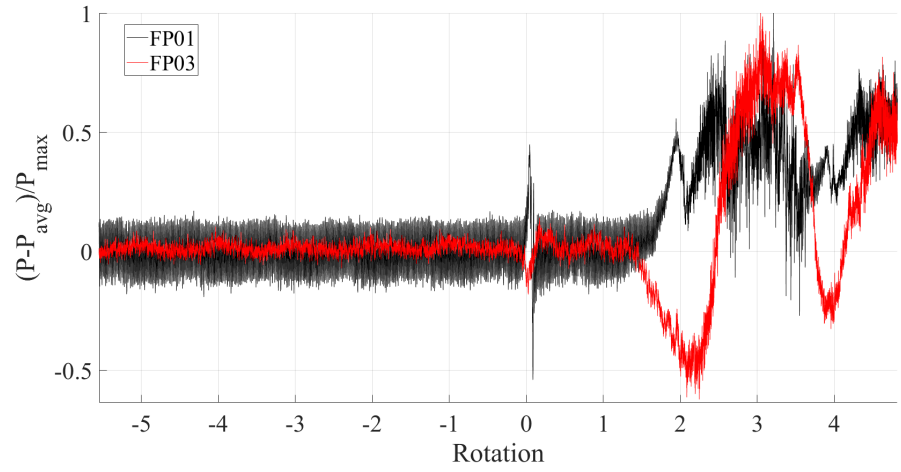

(a)

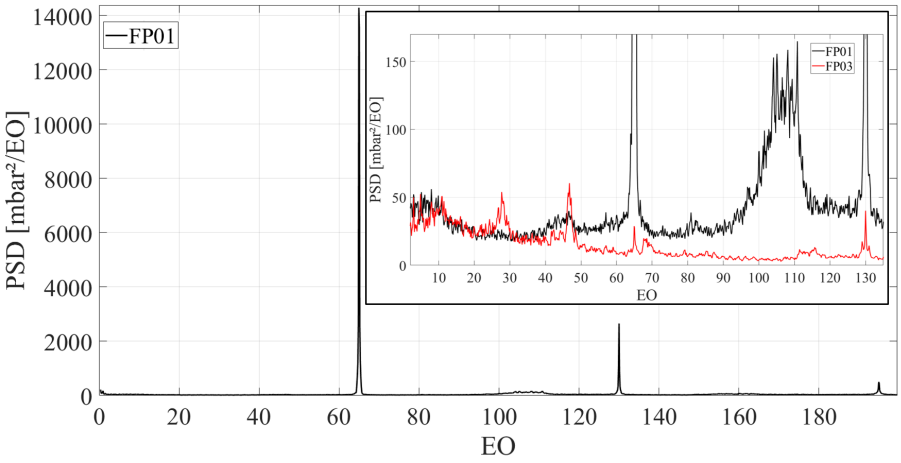

(b)

Figure 5.3: H25 stage machine failure at nominal speed - Comparison between pressure signal at rotor leading edge (Black) and C2 cavity stator disk boundary layer (Red) at respectively 38° and 40° clocking - (a) Pressure signal normalized with respect to maximal pressure in each time series. Spike event identification at rotation 0 - (b) Pressure temporal fluctuations around the ensemble average for 550 rotations prior to spike event.

the same test. The signal treatment method is similar to the one introduced in section 3.1.3.7.2.

Residual content from the BPF (65 EO) and 2*BPF remain with a lot of energy in the main channel. However, frequency humps that are, in the literature, associated to rotating instabilities (see Baumgartner et al. (1995) as an example) are visible and centred around 7 EO, 45 EO and 108 EO. It is interesting to note that the main channel second instability bump overlaps with the bump visible in the cavity between 40 EO and 50 EO. Second order bump in the cavity spectra is also visible between 110 EO and 120 EO, not far from the previously introduced 108 EO bump in the main channel.

The spike event rotating speed is also evaluated thanks to the sensor in the main channel and in the cavity. Sensors located in front of rotor leading edge measure a structure speed of 73.2% of the disc rotating speed, with only 3 sensors available. Using the cavity sensors, the computed speed is of 74% disc rotating speed. This information indicates that it is possible to use cavity sensors to detect spike type events and characterize their speed in the current experimental setup. All of the phases of the H25 stage instability behaviour are detected in the cavity, including phases of rotating stall prior to surge event (data not showed here).

To finish, the cavity mode at 47 EO discussed in section 4.3.3 is studied in the presence of a H25 surge event. Figure 5.4a plots for sensor FP_{10} a self-stabilized surge event in which the spike event is indicated

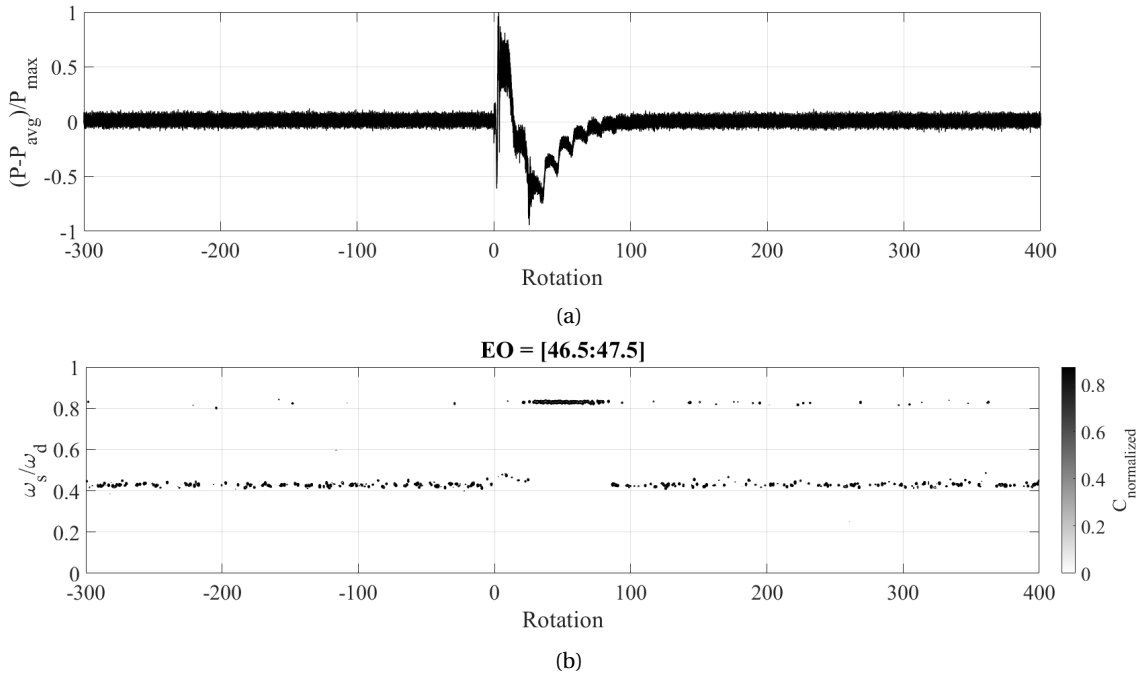

Figure 5.4: H25 stage machine failure at nominal speed - Analysis of cavity 47 EO mode speed - (a) Pressure signal of sensor FP_{10} normalized with respect to maximal pressure. Spike event identification at rotation 0 - (b) Coherence map for mode speed identification in the frequency interval [46.5:47.5] EO for the cavity Kulite sensors.

at rotation 0. It is possible to reconstruct the mode speed during the machine surge cycle as illustrated by Figure 5.4b. The 47 EO mode rotating at cavity group velocity of 43% disc speed sees its velocity changing when the stage instability is initiated. The mode speed is then accelerated to 48.2% disc speed when the cavity pressure reaches its maximal value between 4 and 12 rotations after the spike event. A reduction of the mode speed to 44% disc speed is noted between 12 and 20 rotations. After rotation 20, the mode speed peaks with a strong correlation at 83.3% disc speed until the pressure level is re-adapted to the pre-spike event value.

As a conclusion, this section illustrated the possible interest for the study of cavity flow during machine failure events. Aside from being a possible location to measure compressor stage behaviour beyond the stability limit, this puts into perspective the possible contribution of cavity modes in this working phase of the machine. This preview encourages to consider in the design phase, cavity eigen modes as destructive for the mechanical, acoustic, and aerodynamic modes that participate to the machine failure.

5.3 Cavity flow low order modelling

The information contained in the literature and in this manuscript, about the effect of cavity flow on axial compressor, highly suggest that cavity flow should be included as early as possible in the compressor design process. This point is even more relevant for machine with blades that tend towards low aspect ratio values, which increases the proportion of secondary flow losses in blade row loss decomposition.

In early design phases of turbomachinery components, low order modelling is used since it provides, for a limited computational cost, information regarding blade design ability to work in a defined operating range. If low order modelling approaches are updated to take into account technological effects such as the stator shroud cavity, the design process becomes more robust with an early inclusion of engine-like environment, and more efficient since less iterations are needed further in the design process.

Concerning the inclusion of cavity flow, the designer objective is to obtain, for a fixed cavity geometry and operating conditions, a correct evaluation of the flow field in the cavity to main flow interaction region. Beyond this point, a connection is done to the modelling of the flow field in the adjacent blade rows.

However, a prerequisite to this is the correct evaluation of the cavity main core flow.

The evolution of the flow quantities in the cavity are dependent upon the geometry and the operating conditions. These two elements are connected, thanks to the definition of non dimensional numbers (see Chapter 2 section 2.4) that gives a general view of the cavity flow topology expected. In any low order modelling approach, it is then advised to conduct first a complete non-dimensional analysis of the cavity system.

Engine-like cavities often present complex geometries that are far from canonical cases. It has been demonstrated that these complex geometries trigger local flow behaviour, on average, but are also source of local and global unsteadiness. That is why, prior to any cavity flow breakdown, it is advised to include in the modelling a step where the cavity geometry is split into elementary blocks or regions. An example is given in the next paragraph for any cavity geometry.

Cavity split

The cavity discussed in this section is half of the cavity found in typical stator shroud cavities. The cavity is bounded by the labyrinth seal exit and by the cavity trench exit. A schematic representation is given in Figure 5.5 where rotating surface are in red and fixed surfaces are in black.

The cavity presents three main regions to model. In Region A focus is on the modelling of the retained sealing technology, e.g. labyrinth. Region B is the cavity trench. Finally, region C is the main cavity volume.

Modelling of section A is deeply covered in the literature. The prerequisites for region A are a correct evaluation of the seal geometry as well as the pressure balance between seal inlet and outlet. Since the seal outlet conditions can evolve due to cavity flow topology, the seal equation (see for example Sultanian (2018) Chapter 5), can be computed iteratively in the modelling loop that evaluate the cavity flow conditions.

The modelling of the trench region (B) needs to take into account, on average, the mixing of two jet at different enthalpy (see Denton (1993)). The blade effects, and azimuthal non uniformities in this region can be evaluated thanks to an orifice-spoke web as it is suggested in Sultanian (2018) (Chapter 4). The unsteady prediction of the flow field at the exit of the trench should also consider approach such as the one of Rossiter (1964), to take into account the effect of the trench geometry on the shear layer instability generated between the rotor and stator platform. The modelling of the trench as a filter for instabilities should also be considered as it has been presented that few of the cavity modes are apparent in the main channel for the H25 - C2 configuration.

The evaluation of region C is specific to the cavity volume geometry. To simplify the problem, a split approach can be used to model independently local regions and associated flow behaviours.

To perform a first split of the cavity, any type of cavity is considered in Figure 5.5 as an assembly of two base cavities that are: rotor stator cavity, i.e. parallel disks; coaxial cylinder cavity, i.e. Taylor Couette type flow. In any cavity, the seal radius is indicated by R_s between the minimal radius R_i and maximal radius R_o. In an analogue definition, the stator disk main vertical plane location Z_x is presented between minimal and maximal axial location (Z_{min} and Z_{max} respectively). Specific configuration arises for $Z_x = Z_{max}$ (full annular cavity) and for $R_s = R_i$ (full rotor stator cavity). Otherwise, the presented cavity can be decomposed in: a region of flow between two coaxial cylinders of radius ratio $\frac{R_i}{R_s}$ over a length of $Z_{max} - Z_x$, a region of rotor stator cavity flow of aspect ratio $\frac{Z_x - Z_{min}}{R_o}$ between the seal radius and the maximal radius.

It is important to note that in the splitting process, buffer regions may appear, as the one delimited by $[R_i : R_s, Z_{min} : Z_x]$ in this example. There, a special treatment should be considered to take into account of the mixing between the leakage jet and the flow travelling inward in the stator disk boundary layer.

After cavity split, most important local regions are identified. It is then possible to build a low order modelling strategy with multiple levels of complexity being: The computations of the 0-D cavity flow thanks to lump parameter modelling, the computation of cavity flow gradients (i.e. 1-D flow field), and the evaluation of the cavity dynamics (unsteadiness). The following paragraph evaluates each of the aforementioned level of complexity.

Prediction of cavity flow field

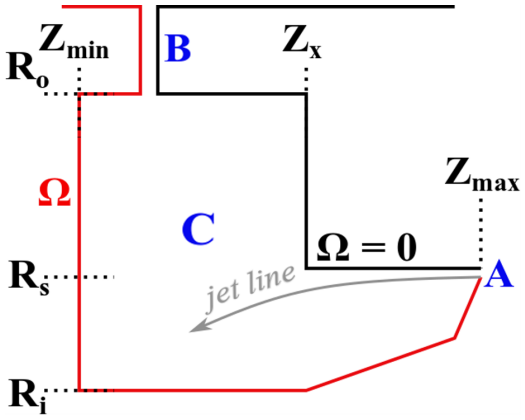

Figure 5.5: Cavity model general representation for cavity split in low order modelling approach.

The 0-D evaluation of the cavity flow is directly deduced from the non dimensional number analysis. After cavity split, each region independently can be evaluated thanks to the type of geometry (Rotor-Stator, Taylor-Couette,...) and flow regime based on average non dimensional numbers.

The computation of cavity flow gradients as 1-D profiles is also impacted by the non-dimensional analysis in each sub block after the cavity split. In fact, this step allows to identify the average flow topology but is also crucial to correctly define the work coefficient and torque coefficient for both rotor and stator disks. It is then possible to compute a 1-D steady flow field of the cavity using angular momentum balance equation on small control volumes as it is presented in Sultanian (2018). Such approach can be used as a starting point and further completed taking into account heat transfer between cavity walls and the fluid. The low order modelling of cavity instabilities is complex by the nature of the flow but also by the already discussed impact of geometrical effects on the cavity dynamics. Chapter 2 indicates the existence of complex flow regimes and local source of instabilities, especially in the working range for turbomachinery components. The analysis of the C2 cavity raised questions concerning the dominant instability generation in this type of cavities. The idea behind the low order modelling of the cavity unsteadiness is to be able to estimate the most representative spectral content of the cavity flow. To do so, global, e.g. cavity Helmholtz frequency, and local sources of instabilities must be identified.

As an example, it has been seen that at the labyrinth exit, below the jet line, there is the interaction between Taylor Couette type flows and backward facing step flow (in a referential given by the labyrinth exit swirl ratio). It could be interesting to evaluate what are the instabilities created in this two types of flows independently, on canonical cases, to see if the physics of the flow in the under jet line cavity can be modelled like this. In other words: Is it possible to breakdown the instability generation into canonical cases such as backward facing steps, mixing - shear layer interactions...?

What has also been identified in the numerical work on the C2 cavity is that the under jet line part of the cavity volume is creating predominant unsteadiness for the flow following the leakage path where flow is travelling upward on the rotor disk, and exiting the cavity through the trench.

Further along the jet line, the shear layer interaction between jet flow and flow travelling inward on stator disk boundary layer is also a source of instability. However, it is not clear if the turbulence created in this layer participates to a large extent to the cavity unsteadiness.

As a final comment, the cavity flow instability transport in the low order modelling approach would be difficult to estimate since these mechanisms are still unclear nowadays.

This section briefly discussed area of interest for cavity flow low order modelling based on the physical knowledge brought by Chapter 2, and the study of the C2 cavity. The objective of the modelling here described is to propose a simplification of any cavity geometry into elementary/canonical cases on which basic fluid mechanic approaches can be applied. Nevertheless, the description of the geometry and operating condition of the studied cavity through non-dimensional numbers analysis is a prerequisite to obtain

a good prediction of the time average and unsteady flow field.

5.4 Conclusion

In Chapter 5, an opening on new research activities on the topic following this work, or directly inspired by it, has been presented. Three area of interest have been detailed concerning: the rotor mechanical assembly, the contribution of the cavity volume in axial compressor flow failure phases, a possible approach and strategy for cavity flow low order modelling.

These elements, as well as the four preceding chapters, underline that the increasing integration of technological effects in the axial compressor design process requires a deep comprehension of the physics involved with each element. To improve the design process efficiency, experimental data are required to develop new modelling approaches. The perspective of the results presented in this thesis are multiple, since few experimental data of the kind have been collected in stator shroud cavities, in the case of axial compressors.

In the first place, such data could be beneficial to compressor modules manufacturers. The database collected can be used as a benchmark for design tools and methods of design. It can also be used to derived guidelines for a better aerodynamic integration of the shroud cavity in the blade / cavity combination.

To the scientific community, this work can be used as a reference for the design of instrumentation in the frame of cavity flow characterization, e.g. test rig or simply probe layout. The data collected can also be used as a benchmark for high fidelity numerical methods in complex flow regimes. In general, this approach will also lead to a better comprehension of the cavity flow physics for axial compressors.

Appendices

Appendix A

Fast response pressure sensor calibration procedure

In this appendix, fast response pressure sensors are described. In the first part, the operating principle of such measuring device is presented. The static calibration procedure is introduced in a second section. To finish, the method used to define the dynamic behaviour of the fast response probes is showed.

A.0.0.1 Operating principle

Fast response pressure transducers are piezo-resistive sensors. The measurement device makes use of a membrane on which four strain gages are glued (silicium piezoresistors). When pressure is applied on the sensor diaphragm, the strain gages deform. It results in a variation of their electrical resistance. Those items are electrically connected to form a Wheatstone bridge in which the aforementioned resistance unbalance maximizes the voltage output of the circuit. The measured voltage output offset is then proportional to the pressure variation felt by the sensor.

Strain gages resistance variation is also affected by the temperature changes of the media in which the sensor is immersed. The measurement chain in this work includes an active compensation for the temperature. The principle described in Brouckaert (2004) is that the sensor equivalent resistance is part of a Wheatstone bridge from whose voltage output is proportional to the temperature fluctuations.

Figure A.1 shows the two voltage outputs obtained from the measurement, Vp (function of pressure and temperature) and Vs (mainly function of temperature).

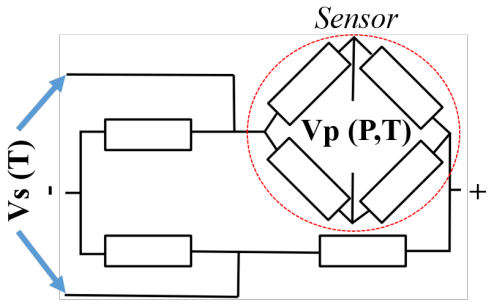

Figure A.1: Active temperature compensation circuit for piezoresistive transducers.

A.0.0.2 Static calibration

Static calibration of the sensors is performed to find the relation between Vp, Vs , Pressure , and Temperature. All the sensors are immersed simultaneously in a closed chamber where pressure and temperature

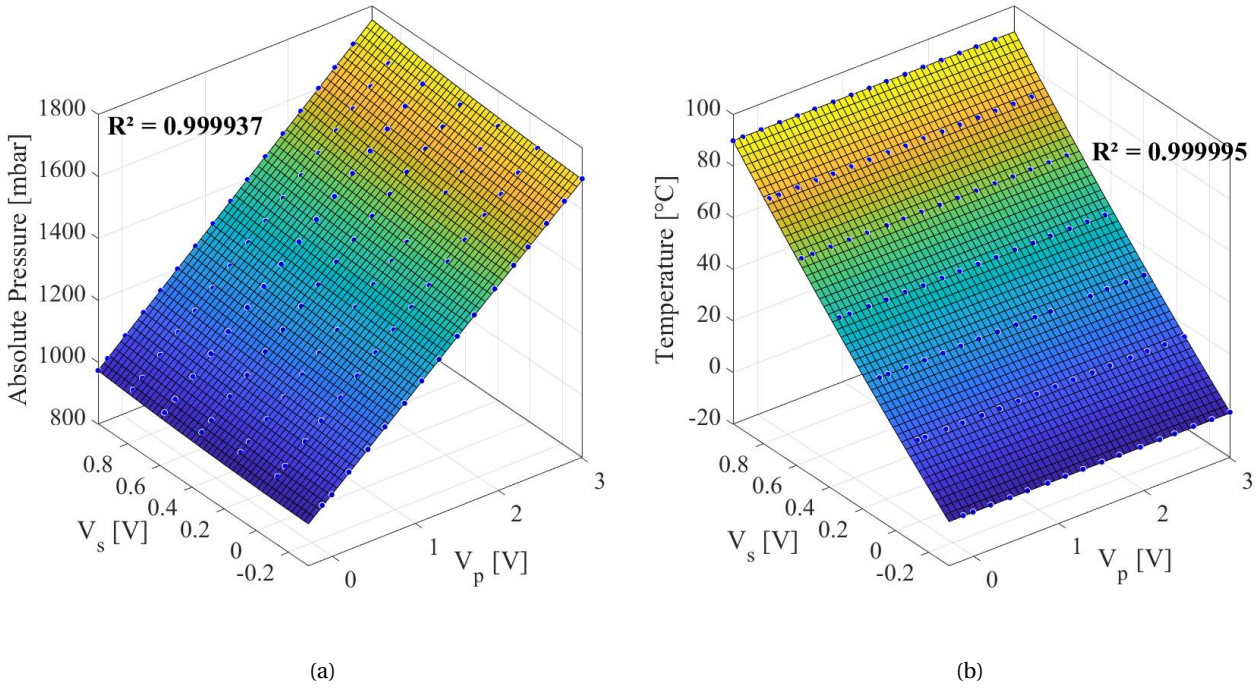

(a) (b)

Figure A.2: (a) Pressure fitting for one piezo-resistive sensor - (b) Temperature fitting for one piezo-resistive sensor - Fitting error is indicated by R^2.

are controlled. The calibration maps obtained for one of the sensor used in the C2 cavity are presented in Figure A.2a and Figure A.2b.

A fourth-order polynomial fitting is applied with coefficients *a* and *b* to retrieve the Vp and Vs contribution to pressure and temperature, as expressed by equation A.1 and equation A.2.

$$\mathbf{P} = \mathbf{a}_{00} + \mathbf{a}_{10}\mathbf{V_p} + \mathbf{a}_{01}\mathbf{V_s} + \mathbf{a_{11}}\mathbf{V_p}\mathbf{V_s} + \mathbf{a}_{02}\mathbf{V_s^2} \tag{A.1}$$

$$\mathbf{T} = \mathbf{b}_{00} + \mathbf{b}_{10}\mathbf{V_p} + \mathbf{b}_{01}\mathbf{V_s} + \mathbf{b_{11}}\mathbf{V_p}\mathbf{V_s} + \mathbf{b}_{02}\mathbf{V_s^2} \tag{A.2}$$

A.0.0.3 Dynamic response

To serve as a sensor protection as well as accessing the measurement location, probes are used. The probe assembly integrates the sensor. The dynamic response of the probe is evaluated to apply a correction on the measured raw signals, hence removing probe induced effects on the amplitude and phase. The probe used as an example in this appendix are the Kulite inserts mounted in the C2 cavity stator wall.

The natural frequency of the bare sensor in use is about 240[kHz]. To estimate the response to a pressure step of the probe, the von Karman Institute shock tube is used. More details of the facility and method are available in Boufidi et al. (2019) and Gaetani and Persico (2020). In this work, the probes are positioned to mimic the final experimental setup. As an example, if the probe is flush mounted to the wall in the experiment, it is also flush mounted in the shock tube.

The response to one pressure step of 200[mbar] sampled at 1[MHz] is measured. Figure A.3a presents the obtained raw signal for one of the Kulite insert with normalized voltage as a function of time.

To be statistically consistent, a minimum of fourteen repeated steps are performed for the calibration. Figure A.3b presents the repeated Vp response of one Kulite insert to fourteen pressure steps. From the raw signal, digital filtering is applied with a cut off frequency of 120[kHz] to damp perturbations linked to sensor resonance. The signal is normalized (0: value at test beginning; 1: value at test end). The signal is cut after the dynamics of the probe has been excited to remove traces of post shock disturbances in the spectral

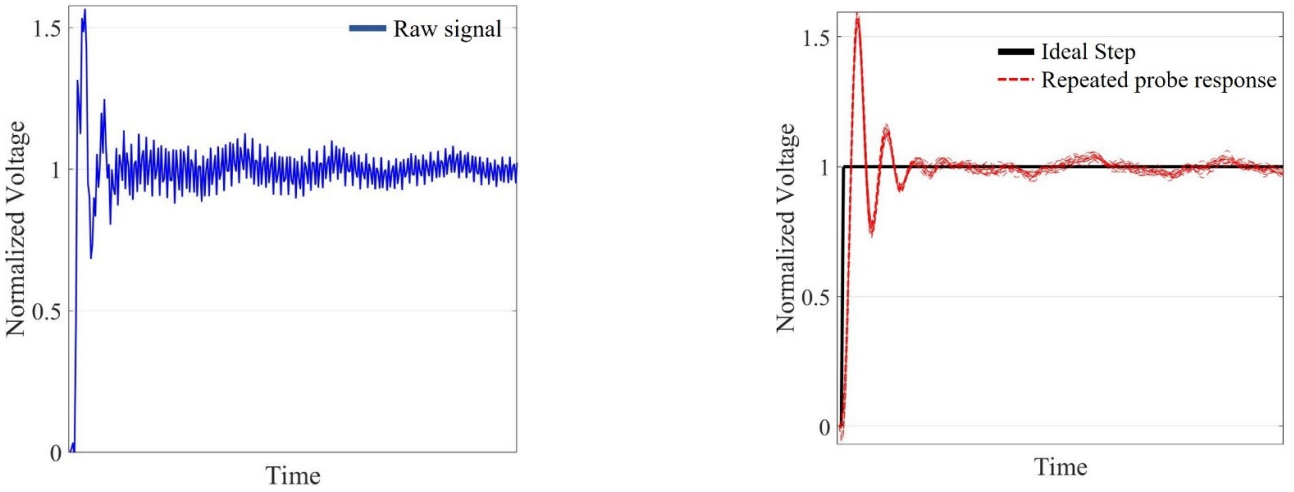

(a) (b)

Figure A.3: (a) Kulite insert raw Voltage output (Vp) from one 200[mbar] pressure step response test - Sampling frequency of 500[kHz] - (b) Kulite insert voltage output (Vp) response to fourteen pressure steps after filtering / normalisation/ windowing – Sampling frequency of 500[kHz].

domain. To finish, signal is elongated with the mean voltage value to obtain the desired spectral resolution and a half Hamming window is applied at the elongation point to create a periodic signal. Averaging is performed in the frequency domain and the sensor transfer function is established with respect to the ideal step visible in Figure A.3b.

The correction of experimental data in the experiments is done by applying the probe transfer function, modelled through system identification with a linear second order system.

The amplitude and phase from the shock tube tests as well as the model fitting for the transfer function are presented in Figure A.4. In this example, the average estimated natural frequency of the cavity inserts is 73[kHz] and the non-dimensional damping evaluated from half power is 0.21.

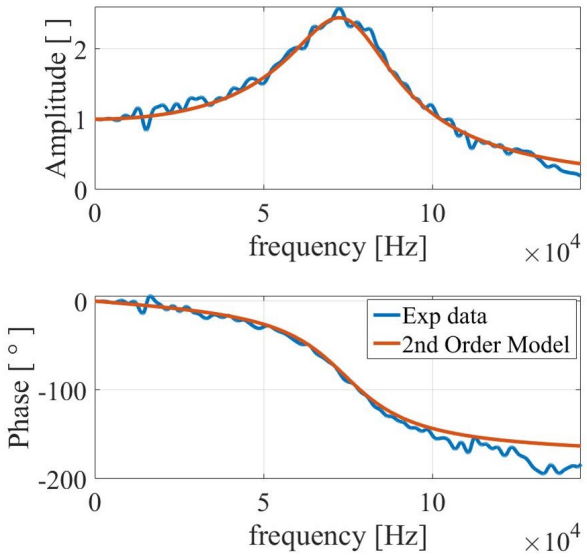

Figure A.4: Kulite insert transfer function from shock tube experimental pressure step data – Second order linear model identification.

Appendix B

FEM analysis of H25 stage labyrinth seal ring

The control injection system used in the experiments makes use of the pressure difference upstream and downstream of the C2 cavity labyrinth seal to generate the leakage conditions. With such approach, it is important to guarantee the mechanical integrity of the stage over the whole range of injection conditions. The present appendix focuses on the radial displacement of the labyrinth seal teeth when injection is applied.

The H25 stage labyrinth seal uses abradable tracks in which two teeth in a cantilevered assembly rub to generate as less clearance as possible (see light green part in Figure B.1a). The minimal clearance is obtained for the maximal radial displacement of the teeth. In other words, this is the case for one operating condition only.

From the disassembled machine, the abradable tracks are measured thanks to sections moulding at two azimuthal positions. An example of such moulding is presented in Figure B.1b. The moulding present two traces from the labyrinth seal (double tracks). This is due to multiple dismount and assembly of the rotor ring where axial alignment can vary slightly. Labyrinth teeth displacement are summarized in Table B.1 for the sections investigated. The data from the double tracks are averaged. The maximal difference in track height is of 0.05[mm] which is in the order of magnitude of the measured eccentricity of the rotor assembly.

The labyrinth seal opening is a function of the centrifugal force on the disk, the temperature of the material and the pressure forces acting on the disk wall. A Finite Element Method computation of the disk ring is performed to establish the link between labyrinth opening and disk cavity pressure at running conditions. The goal is to quantify the mechanical displacement caused by the pressurisation of the C1 cavity when leakage is applied.

Open source Calculix software is used at such extent. The numerical domain consists in a 72 degree sector of the labyrinth ring. Figure B.2a presents the mesh used.

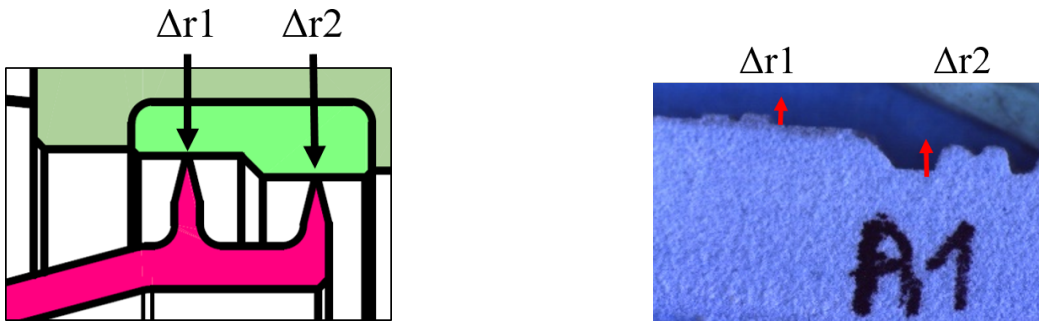

(a) (b)

Figure B.1: (a) H25 labyrinth seal configuration - Radial gap numbering for tooth one and two - (b) Corresponding abradable moulding section cut under microscope - two dents induced by two mounting of the H25 test section.

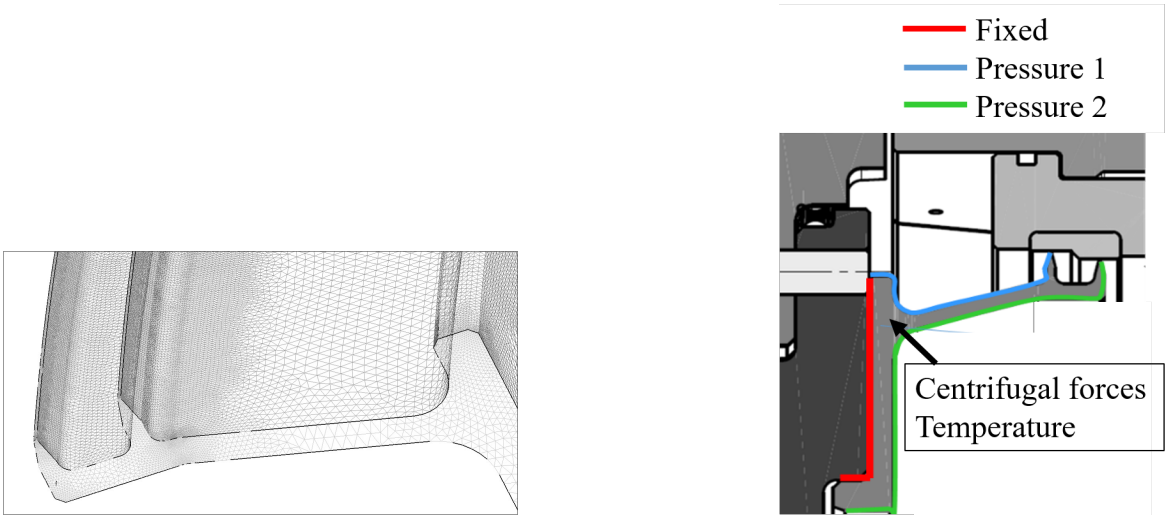

(a) (b)

Figure B.2: (a) Labyrinth seal FEM analysis domain mesh - (b) FEM domain boundary conditions.

The operating condition for the rotor is the design point at nominal speed. The H25 rotating speed never exceeded nominal speed in the tests. This allowed to compare the results with the moulding measurements that indicates the maximal labyrinth radial displacement. The boundary conditions used in the analysis are presented in Figure B.2b. Temperature condition is the temperature obtained in the disk cavity (c.f. Figure 3.48 station 4) after thermal stabilization of the stage. The pressure 1 condition is imposed equal to the static pressure measured at hub between rotor and stator row. Pressure 2 (Ps2) condition is changed between the static pressure measured in the stage outlet at design condition (baseline) and a pressure ratio of 3.5 with respect to the stage inlet total pressure (Pt_0). In the experiments, the pressure 2 maximal value is limited by the use of a 50[Psi] differential pressure scanner (3.45[bar]).

As indicated by Table B.1 for the baseline case, the $\Delta r1$ value is comparable with the moulding measurements with an error of 0.04[mm] when the $\Delta r2$ value is underestimated by 45%. This can be explained with the computation not including teeth/abradable rubbing effects on temperature and material integrity. The results on the trend of labyrinth closing with the disk cavity pressure increase are presented in Figure B.3 and inform that the labyrinth gap scales with the disk cavity pressure. The fitting obtained is used to associate injected mass flow and gap opening for each of the operating conditions covered in the test campaign.

Table B.1: Labyrinth teeth displacement contribution of centrifugal forces, temperature and pressure at H25 design operating conditions, nominal rotor speed

Test Conditions	$\Delta r1$ [mm]	$\Delta r2$ [mm]
Mouldings	0.308	0.700
FEM-Baseline	0.262	0.380

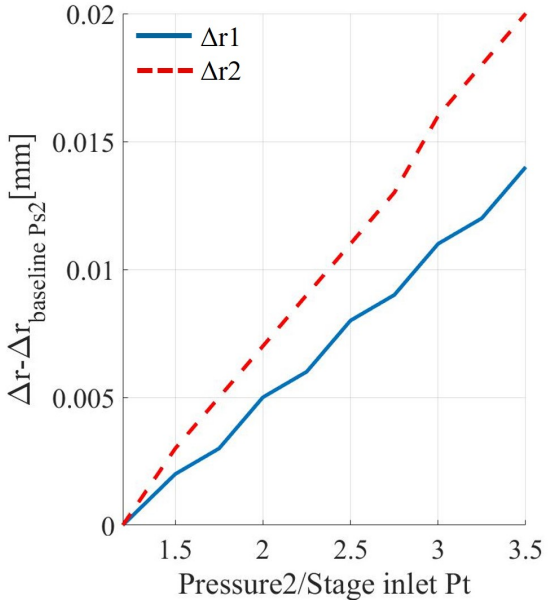

Figure B.3: Labyrinth teeth displacement from baseline pressure case in function of disk cavity pressure- design operating condition, rotor nominal speed.

Appendix C

Annulus non uniformities and efficiency correction in the H25 stage

The present appendix details the azimuthal non uniformities that were measured in the H25 stage. For the compressor working at nominal speed, the effect of these non uniformities on the performance measurements is quantified. To finish, the method to give a correction to the measured isentropic efficiency is described.

C.0.0.1 Non uniformities and effect of H25 stage performance measurement

As mentioned in Chapter 3, stage performance is measured by means of total pressure and total temperature rakes. In Figure C.1, the stage inlet rakes are identified in grey. They are equally spaced around the machine annulus. The 0[°] position corresponds to the top of the machine (between rake A and rake E).

Azimuthal non uniformities exist in pressure and temperature at stage inlet. This is visible in Figure C.2a and C.2b. In Figure C.2b, the thermal stratification that exists at stage inlet is such that the machine bottom is more than 1.5[K] hotter than the machine top. As a general rule, the machine sectors between 180[°] up to 324[°] (rakes C, D, and E) see hotter inlet flow. This may be caused by a stratification in the upstream heat exchanger (see Figure 3.1) caused by less flow efficiency in its bottom part.

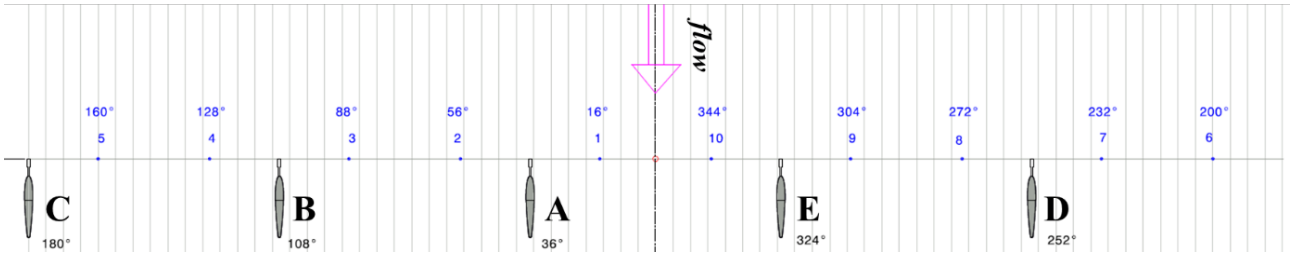

Figure C.1: Rakes of Total pressure and total temperature clocking at stage inlet (Capital Letters) – Plane 0 – Test section top is at 0[°].

In the test campaign, at defined operating points, the stage outlet instrumentation is rotated of one pitch and a half to allow radial and azimuthal probe traversing. In this manipulation, the stage outlet total pressure and total temperature rakes also rotate with respect to the stator row. The motor that control this rotation is called M1. M1 ranges from 0 to 1.5.

In Figure C.3, the clocking of the stage outlet rakes is presented for the position M1 = 0. The rakes pair (total pressure, total temperature) are labelled with A, B, C, D, and E.

Since the rakes are clocked differently with respect to the stator, a given position of M1 combines rake measurements to give a radial and azimuthal outlet map of flow quantities. Performance of the stage is computed using an average of the aforementioned map. In the case where the machine does not present non

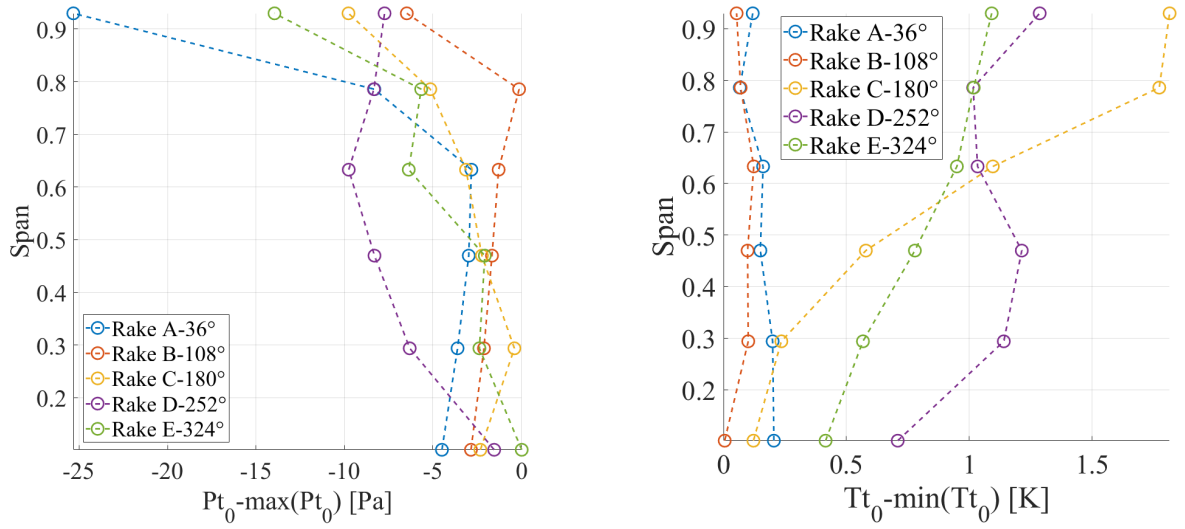

(a) (b)

Figure C.2: Stage inlet non uniformities. Rakes measurement at nominal speed for Near stall operating conditions - (a) Inlet total pressure distribution with respect to the maximal inlet total pressure measured - (b) Inlet total temperature distribution with respect to the minimal inlet temperature.

uniformities in the outlet plane, the performance retrieved from the experiments should be independent from the value of M1.

Figure C.4, displays the stage isentropic efficiency curves as a function of flow coefficient for two positions of the outlet rakes (so two different values of M1). Curves are obtained thanks to constant throttling between the low loading point and the stability limit. At high flow coefficient, the measured efficiency curve is independent of the motor M1 position. Differences in the isentropic efficiency curve shape appear when flow coefficient is reduced. In the design loading point neighborhood (i.e. DL), a difference of 0.5% in efficiency prediction is visible. In the near stall region this difference increases up to 0.8%.

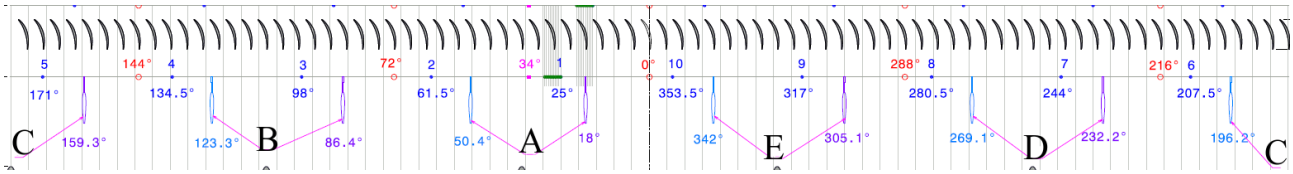

Figure C.3: Total pressure (Blue) and total temperature (purple) rakes clocking in stage outlet plane.

C.0.0.2 Isentropic efficiency correction

The efficiency correction is available for the points where a radial and azimuthal traversing of the outlet stage instrumentation is done. To obtain the corrected efficiency full curve, i.e. for each flow coefficient, the traversing must be performed for a consequent number of point. This was out of the scope from the present thesis.

In order to present how the corrected value of efficiency is computed, an example is taken from the dataset recorded at compressor nominal speed. The operating point is stabilized at near stall condition (NS). M1 varies from 0 to 1.5.

The measured value of isentropic efficiency, total to total pressure ratio and outlet to inlet stage temperature difference are plotted in Figure C.5. The measured performance drop associated with change in M1 value is highlighted. From the definition of isentropic efficiency, the efficiency drop is a function of measured temperature and pressure variation at the outlet of the stage.

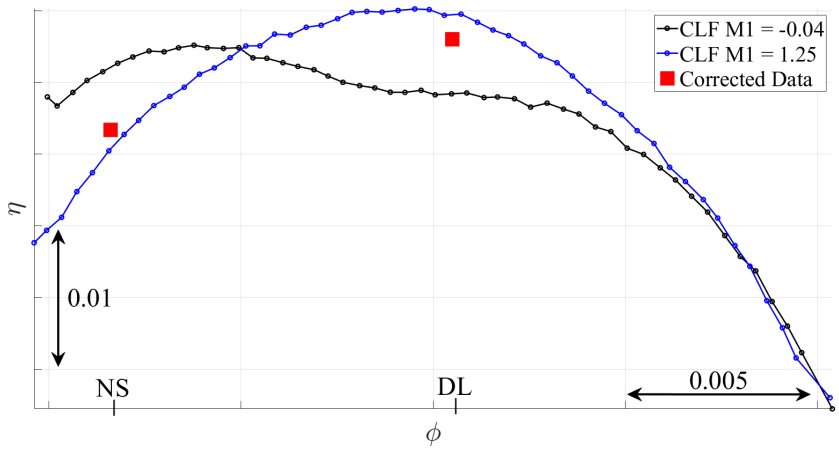

Figure C.4: Nominal speed H25 stage isentropic efficiency computed for two azimuthal positions of the stage outlet instrumentation M1 = −0.04 and M1 = 1.25 – Correction applied on data at design loading and near stall loading where test data are available for M1 covering its full range (red square).

The sensitivity of the isentropic efficiency is evaluated against average stage outlet total pressure and total temperature. In Figure C.6, iso lines of isentropic efficiency are plotted for varying outlet total temperature and total pressure. Stage efficiency measured as a function of M1 is also indicated as a reference? (blue curve). In Figure C.6a, from the initial value of efficiency at ring motor position M1 = 0, each line gives the efficiency that would be obtained if the average stage outlet total temperature increases by 0.05 [K]. An increase of 0.35 [K] in the average stage outlet total temperature induces a 1.2% drop in efficiency. The temperature scanner systematic uncertainty is of 0.25[K]. It corresponds to a 0.86% efficiency drop. If only the temperature increase effect is taken into account, the efficiency decrease noticed with M1 varying from 0 to 1.5 is 175% of the measurement uncertainty. The sensitivity on the outlet total pressure is also evaluated. Figure C.6b, shows the efficiency drop caused by pressure decrease steps of 10[Pa] in the range 0 [Pa] to 300 [Pa]. A 0.8% drop in efficiency is noticed for a decrease of 280[Pa].

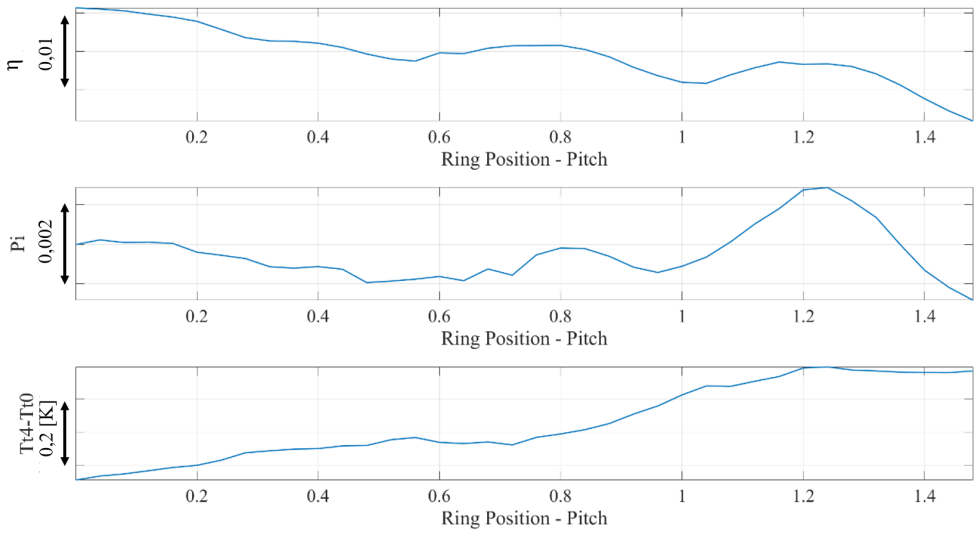

Figure C.5: H25 stage measured performance fluctuation as a function of instrumentation position in stage outlet plane - Ring position indicates the motor M1 value, expressed in pitch – Near stall operating conditions.

To identify the origin of averaged total pressure and total temperature variations, each rake values are

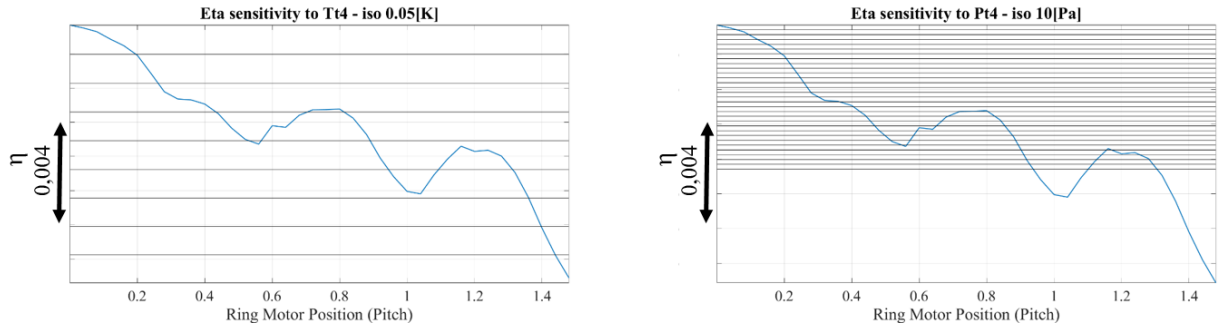

Figure C.6: H25 efficiency drop with ring motor position M1 - (a) Iso lines of efficiency if stage outlet temperature is increased by steps of 0.05[K] up to 0.45[K] (black lines) - (b) Iso lines of efficiency if stage outlet pressure is decreased by steps of 10[Pa] down to 300[Pa] (black lines).

independently investigated. Figure C.7a and Figure C.7b plot stage outlet to inlet total pressure ratio and total temperature differences for each rake, as a function of the motor ring position M1. The rake label is indicated by A, B, C, D, and E in accordance to Figure C.3. The presence of pressure and temperature non uniformities between rake sectors is visible. This phenomenon, already identified at stage inlet is also present at stage outlet. As an example, rakes C, D, E show on average hotter sectors than rakes A, B. Aside from thermal stratification induced by stage inlet conditions, non uniformities are also induced by the interaction between the test section and the laboratory environment by means of heat transfer.

To correct the efficiency at a stabilized point from which an azimuthal traversing has been performed (like in this example), individual pitch/span maps from the rakes are combined to obtain a 360° map of efficiency. Data for each rake are used for one fifth of the machine full annulus.

For each rake, a 1 pitch wide window (over the 1.5 pitch available) is sampled with rake A clocking as a reference. Figure C.8, gives an example of obtained cartography of efficiency. As mentioned previously, the zero value (starting value) for the pitch is taken in reference to the clocking of total pressure rake A.

The one pitch wide window selected for each rake has an impact on the final averaged efficiency value. In Figure C.9, an example of the average full annulus efficiency map obtained is plotted. In the example, depending on the window position in the 1.5 pitch sector available for each rake is giving a variation of measured efficiency of 0.25% (minimum to maximum difference). The final corrected value of efficiency for a stabilized point is the mean efficiency for all the window positions. The red squares for the design loading and the near stall loading points in Figure C.4 indicate the corrected efficiency value.

The minimum to maximum difference around the efficiency corrected value is computed for all the conditions investigated where an azimuthal traversing (MAP) is available in the stage outlet section. It fluctuates between 0.12% and 0.26% of efficiency.

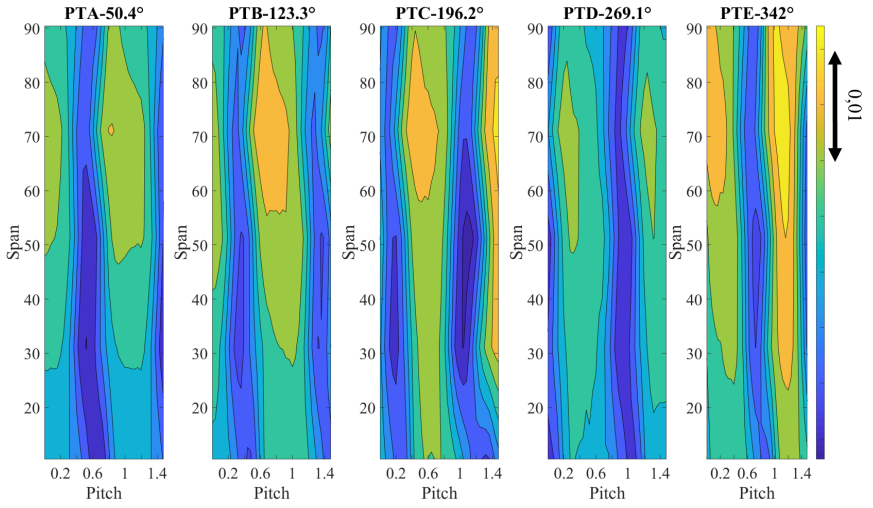

(a)

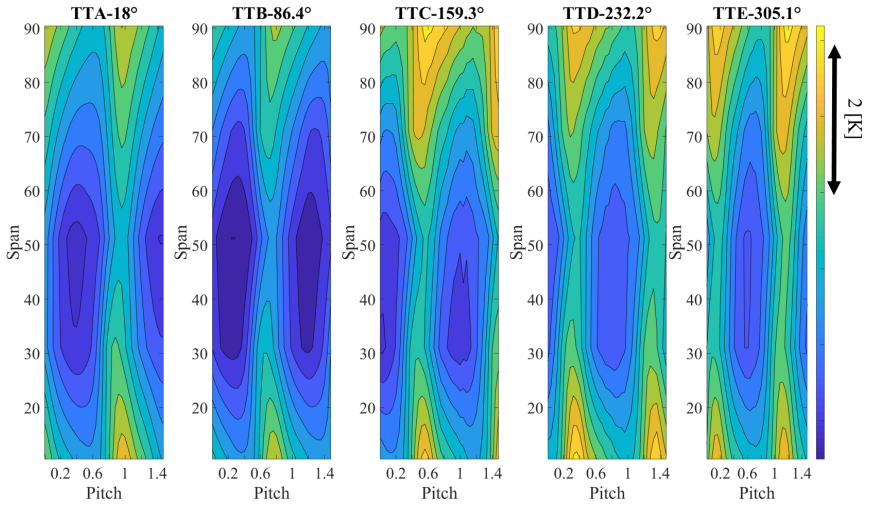

(b)

Figure C.7: Stage outlet flow map seen by each rake when M1 covers its full range - (a) Total to total pressure ratio Pt4/Pt0 - (b)Outlet to Inlet stage Temperature difference Tt4-Tt0 [K].

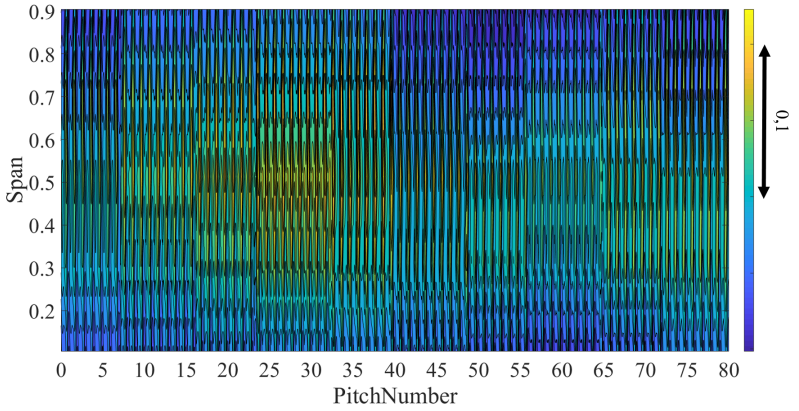

Figure C.8: Isentropic efficiency map at stage outlet. Combination of total pressure and total temperature rakes measurements for a given one pitch wide window per rake.

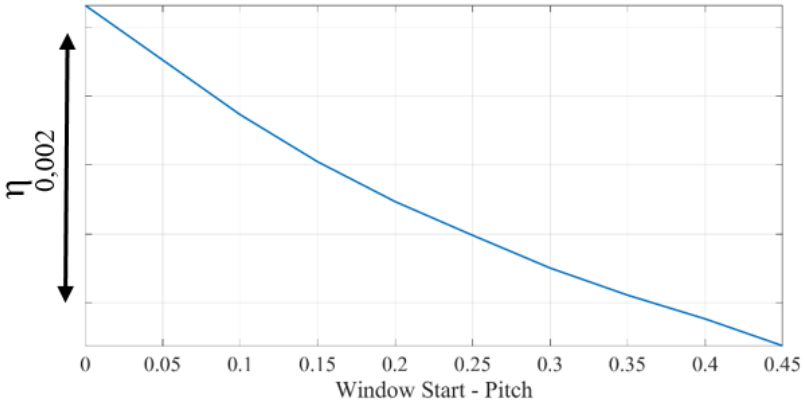

Figure C.9: Nominal speed near stall operating point isentropic efficiency as a function of the one pitch wide window starting point for the rakes sampling in the one and a half pitch available.

Bibliography

Ahmed, F. and Rajaratnam, N. (1997). Three-dimensional turbulent boundary layers: A review. *Journal of Hydraulic Research*, 35(1):81–98. 12

Andereck, C. D., Liu, S. S., and Swinney, H. L. (1986). Flow regimes in a circular Couette system with independently rotating cylinders. *Journal of Fluid Mechanics*, 164:155–183. xiv, 32

ASME (2005). Test Uncertainty. Technical Report ASME PTC 19.1-2005, The American Society of Mechanical Engineers. 51, 54

Auchoybur, K. and Miller, R. (2018). The sensitivity of 3D separations in multi-stage compressors. *Journal of the Global Power and Propulsion Society*. 45

Babin, C., Dumas, M., Ottavy, X., and Fontaneto, F. (2021). Numerical Characterisation of a HP Compressor Stage Equipped with a Closed Shrouded Stator Cavity. *Journal of Turbomachinery*, pages 1–27. 117

Bardina, J. E., Huang, P. G., and Coakley, T. J. (1997). Turbulence Modeling Validation, Testing, and Development. Technical Report NASA Technical Memorandum 110446, NASA Ames Research Center. 83

Batchelor, G. K. (1951). Note on a Class of Solutions of the Navier-Stokes Equations Representing Steady Rotationally-Symmetric Flow. *The Quarterly Journal of Mechanics and Applied Mathematics*, 4(1):29–41. 25, 26

Baumgartner, M., Kameier, F., and Hourmouziadis, J. (1995). Non-Engine Order Blade Vibration in a High Pressure Compressor. 159

Beard, P. F., Gao, F., Chana, K. S., and Chew, J. (2017). Unsteady Flow Phenomena in Turbine Rim Seals. *Journal of Engineering for Gas Turbines and Power*, 139(3):1–10. 45

Bentaleb, Y. and Leschziner, M. A. (2013). The structure of a three-dimensional boundary layer subjected to streamwise-varying spanwise-homogeneous pressure gradient. *International Journal of Heat and Fluid Flow*, 43:109–119. xiii, 18

Bergh, H., and Tijdeman, H (1965). Theoretical and experimental results for the dynamic response of pressure measuring systems. Technical Report F.238, NLR-TR. xxiii, 56, 57

Bode, C., Stark, U., and Afshar, N. F. (2015). Impact of a skewed inlet boundary layer on the aerodynamic performance of a stator-hub equivalent high-turning compressor cascade. In *FAN 2015 - International Conference on Fan Noise, Technology and Numerical Methods*, volume 2015-April, pages 1–11. 13

Bödewadt, U. T. (1940). Die Drehströmung über festem Grunde. *ZAMM - Journal of Applied Mathematics and Mechanics / Zeitschrift für Angewandte Mathematik und Mechanik*, 20(5):241–253. 25

Bordji, M. (2015). *Analyse physique et simulations numériques avancées des écoulements de jonction sur les avions*. PhD thesis, Université Pierre et Marie Curie - Paris VI, 2015. 9, 10, 14

Boufidi, E. (2017). Uncertainty Quantification of Turbulence Statistics Measured by Hot-Wire Anemometry. In *Von Karman Institute PhD Symposium*. 121

Boufidi, E., Alati, M., Fontaneto, F., and Lavagnoli, S. (2019). Design and Testing of a Miniaturized Five-Hole Fast Response Pressure Probe with a Large Frequency Bandwidth and High Angular Sensitivity. *ASME Turbo Expo GT2019-90470*. IV

Boufidi, E., Lavagnoli, S., and Fontaneto, F. (2020). A Probabilistic Uncertainty Estimation Method for Turbulence Parameters Measured by Hot-Wire Anemometry in Short-Duration Wind Tunnels. *Journal of Engineering for Gas Turbines and Power*, 142(3). 121

Brandstetter, C., Jüngst, M., and Schiffer, H.-P. (2018). Measurements of Radial Vortices, Spill Forward, and Vortex Breakdown in a Transonic Compressor. *Journal of Turbomachinery*, 140(6). 75

Bridel-Bertomeu, T. (2016). *Investigation of unsteady phenomena in rotor stator cavities using large eddy simulation*. PhD thesis. xiv, 31, 34, 35, 41

Brouckaert, J. F. (2004). Development of fast response pressure probes for time resolved measurements in turbomachines. *Diss. Ph. D. thesis Von Karman Institute of Fluid Dynamics*. III

Celik, I. B., Ghia, U., Roache, P. J., Freitas, C. J., Coleman, H., and Raad, P. E. (2008). Procedure for Estimation and Reporting of Uncertainty Due to Discretisation in CFD Applications. *Journal of Fluids Engineering*, 130(7):78001–78004. 84

Chew, J. W., Gao, F., and Palermo, D. M. (2019). Flow mechanisms in axial turbine rim sealing. *Proceedings of the Institution of Mechanical Engineers, Part C: Journal of Mechanical Engineering Science*, 233(23-24):7637–7657. 14, 45, 157

Childs, P. (2010). Rotor-Stator Disc Cavity Flow. In *Rotating Flow*, chapter 5. Butterworth-Heinemann, 1st edition. 118

Cochran, W. G. (1934). The flow due to a rotating disc. *Mathematical Proceedings of the Cambridge Philosophical Society*, 30(3):365–375. 24

Crespo del Arco, E., Serre, E., Bontoux, P., and Launder, B. (2005). Stability, transition and turbulence in rotating cavities. *Advances in Fluid Mechanics*, 41:141–196. xiii, 24, 25

Cukurel, B., Acarer, S., and Arts, T. (2012). A novel perspective to high-speed cross-hot-wire calibration methodology. *Experiments in Fluids (2012) 53:1073-1085*. 59

Daily, J. W. and Nece, R. E. (1960). Chamber Dimension Effects on Induced Flow and Frictional Resistance of Enclosed Rotating Disks. *Journal of Basic Engineering*, 82(1):217–230. 27

Dallmann, U. (1983). *Topological structures of three-dimensional vortex flow separation*. 11

De Ruyck, J. and Hirsch, C. (1981). Investigations of an axial compressor end-wall boundary layer prediction method. *Journal of Engineering for Power*, 103(1):20:33. 17

De Ruyck, J., Hirsch, C., and Kool, P. (1979). An axial compressor end-wall boundary layer calculation method. *Journal of Engineering for Power*, 101(2):233:245. 17

Dell'Era, G., Mersinligil, M., and Brouckaert, J. F. (2016). Assessment of Unsteady Pressure Measurement Uncertainty—Part II: Virtual Three-Hole Probe. *Journal of Engineering for Gas Turbines and Power 138.4*. 52, 54, 55

Demargne, A. A. and Longley, J. P. (2000). The aerodynamic interaction of stator shroud leakage and mainstream flows in compressors. *Proceedings of the ASME Turbo Expo*, 1(C):1–12. xiii, 15, 16, 19, 45, 107

Denton, J. D. (1993). Loss mechanisms in turbomachines. In *International Gas Turbine and Aeroengine Congress and Exposition*, number (Cambridge, U.K.: Sep. 1-3, 1987), Bury St. Edmunds, U.K., Mech. Engng. Publications Ltd., 1987, Pap, Concinnati. 8, 11, 161

Ekman, V. (1905). On the influence of the earth's rotation on ocean currents. *Arkiv fo¨r matematik, astronomi och fysik*, 2(11). 24

Farkas, B., Van De Wyer, N., and Brouckaert, J. F. (2013). Numerical study on the effect of seal leakage flow on low pressure axial compressor performance. *Proceedings of the ASME Turbo Expo*, 6 A:1–10. xiii, 19

Flores Galindo, D. R. (2018). *Influence of Labyrinth Seals in Cavities on the Flow of an Axial Compressor*. PhD thesis, Institut für Turbomaschinen und Fluid-Dynamik, Hannover. 16, 109

Fontaneto, F. and Lahalle, A. (2016). Highly Reliable Aerodynamic Calibration for Ground and Flight Testing Total Temperature Probes. *XXIII Biannual Symposium on Measuring Techniques in Turbomachinery Transonic and Supersonic Flow in Cascades and Turbomachines, Stuttgart, 09-2016*. 47, 51

Freeman, C. (1985). Tip clearance effects in axial turbomachines. In *Von Karman Institute Lecture Series*, volume 05. 13

Gaetani, P. and Persico, G. (2020). Technology Development of Fast-Response Aerodynamic Pressure Probes. *International Journal of Turbomachinery Propulsion and Power 2020, 5, 6*. 58, IV

Gao, F., Ma, W., Boudet, J., Ottavy, X., Lu, L., and Leboeuf, F. (2013). Numerical analysis of three-dimensional corner separation in a linear compressor cascade. *Proceedings of the ASME Turbo Expo*, 6 A(June 2013). 11

Gbadebo, S. A., Cumpsty, N. A., and Hynes, T. P. (2005). Three-dimensional separations in axial compressors. *Journal of Turbomachinery*, 127(2):331–339. 11

Greenspan, H. P. (1968). *The Theory of Rotating Fluids*, volume 49. John Wiley Sons, Ltd. 31

Grossmann, S., Lohse, D., and Sun, C. (2016). High-Reynolds Number Taylor-Couette Turbulence. *Annual Review of Fluid Mechanics*, 48(July):53–80. 32

Heidegger, N. J., Hall, E. J., and Delaney, R. A. (1996). Stator Seal Cavity Flow Investigation. Technical Report NASA CR 198504, NASA Lewis Research Center. 15

Hougen, J. O., Martin, O. R., and Walsh, R. A. (1963). Dynamics of Pneumatic Transmission Lines. *Control Engineering, 10, pp. 114-117*. xxiii, 56, 57

Huerre, P. and Monkewitz, P. A. (1990). Local and global instabilities in spatially developing flows. *Annual Review of Fluid Mechanics*, (22):473–537. xiv, 28, 30

Ishii, J. and Honami, S. (1986). A three-dimensional turbulent detached flow with a horseshoe vortex. *Journal of Engineering for Gas Turbines and Power*, 108(1):125–130. 10

Jia, X., He, L., and Zhang, H. (2020). Effect of turbine rotor disc vibration on hot gas ingestion and rotor-stator cavity flow. *Aerospace Science and Technology*, 98:105719. 156

Johnston, J. P. (1960). On the Three-Dimensional Turbulent Boundary Layer Generated by Secondary Flow. *Journal of Basic Engineering*, 82:233–248. 18

Johnston, J. P. and Fiack, K. A. (1996). Review — Advances in Three- Dimensional Turbulent Boundary Layers With Emphasis on the Wall-Layer Regions. *Journal of Fluids Engineering*, 118(June 1996). 12, 120

Kang, S. and Hirsch, C. (1991). Three dimensional flow in a linear compressor cascade at design conditions. *Proceedings of the ASME Turbo Expo*, 1(1984):6–13. xiii, 10, 11

Kármán, T. V. (1921). Über laminare und turbulente Reibung. *ZAMM - Journal of Applied Mathematics and Mechanics / Zeitschrift für Angewandte Mathematik und Mechanik*, 1(4):233–252. 24, 81

Kato, D., Yamagami, M., Tsuchiya, N., and Kodama, H. (2011). The Influence of Shrouded Stator Cavity Flows on the Aerodynamic Performace of a High Speed Multistage Axial Flow Compressor. *ASME Turbo Expo GT2011-46300*. xiii, 20

Lakshminarayana, B. and Ravindranath, A. (1982). Interaction of Compressor Rotor Blade Wake With Wall Boundary Layer/Vortex in the End-Wall Region. *Journal of Engineering for Power*, 104(2):467–478. 10

Lathrop, D. P., Fineberg, J., and Swinney, H. L. (1992). Transition to shear-driven turbulence in Couette-Taylor flow. *Physical Review A*, 46(10):6390–6405. 32

Lei, V.-m., Spakovszky, Z. S., and Greitzer, E. M. (2006). Compressor Hub-Corner Stall. *Proceedings of the ASME Turbo Expo*. xiii, 12, 18, 19, 89

Lewis, G. S. and Swinney, H. L. (1999). Velocity structure functions, scaling, and transitions in high-Reynolds-number Couette-Taylor flow. *Physical Review E - Statistical Physics, Plasmas, Fluids, and Related Interdisciplinary Topics*, 59(5):5457–5467. xiv, 32, 33

Lieblein, S. (1959). Loss and Stall Analysis of Compressor Cascades. *Journal of Basic Engineering*, 81(3):387–397. 12

Ligrani, P. M., Singer, B. A., and Baun, L. R. (1989). Spatial resolution and downwash velocity corrections for multiple-hole pressure probes in complex flows. *Experiments in Fluids*, 7(6):424–426. 51

Lingwood, R. J. and Alfredsson, P. . H. (2000). Experimental study of the stability of the Bödewadt layer. In *Laminar-Turbulent Transition*. 28, 31, 35

Lynch, S. P. (2016). Measurements and Predictions of the Three-Dimensional Boundary Layer in a Turbine Blade Passage. In *54th AIAA Aerospace Sciences Meeting*. 120

Mahmood, S. M. H. and Turner, M. G. (2017). Modeling Capability for Cavity Flows in an Axial Compressor. In *Proceedings of the ASME Turbo Expo*. 16

Manfredi, M., Babin, C., and Fontaneto, F. (2020). Transonic Axial Compressors Loss Correlations: Part II — Loss Models Validation. In *Proceedings of the ASME Turbo Expo*. 17

Mellor, G. L., Chapple, P. J., and Stokes, V. K. (1968). On the flow between a rotating and a stationary disk. *Journal of Fluid Mechanics*, 31(1):95–112. 27

Menter, F. R. (1994). Two-equation eddy-viscosity turbulence models for engineering applications. *AIAA Journal*, 32(8):1598–1605. 83

Moghaddam, E. R. (2015). Numerical investigation of fluid flow in protruded rotor-stator cavities. 157

Naylor, E., Montomoli, F., Hodson, H., and Lapworth, L. (2009). Numerical Modeling of Cavities in Multistage Compressors. In *ISABE-2009-1186*. 20

Ostilla-Mónico, R., van der Poel, E. P., Verzicco, R., Grossmann, S., and Lohse, D. (2014). Exploring the phase diagram of fully turbulent Taylor–Couette flow. *Journal of Fluid Mechanics*, 761:1–26. 32

Owen, J. and Rogers, R. (1989). *Flow and Heat Transfer in Rotating Disc Systems, Vol.1: Rotor-Stator Systems*. xiv, 28

Ozturk, J., Childs, P., Turner, A., Hannis, J., and Turner, J. (1998). A Three Dimensional Computational Study of Windage Heating Within an Axial Compressor Stator Well. In *International Gas Turbine and Aeroengine Congress and Exhibition*. 19

Peres, N., Poncet, S., and Serre, E. (2012). A 3D pseudospectral method for cylindrical coordinates. Application to the simulations of rotating cavity flows. *Journal of Computational Physics*, 231(19):6290–6305. xiv, 30

Persico, G., Gaetani, P., and Guardone, A. (2005). Design and Analysis of New Concept Fast-Response Pressure Probes. *Measurement Science and Technology. 16(2005) 1741-1750.* 56

Praisner, T. J. and Smith, C. R. (2006). The dynamics of the horseshoe vortex and associated endwall heat transfer - Part I: Temporal behavior. *Journal of Turbomachinery*, 128(4):747–754. 10, 13

Roache, P. J. (1994). Perspective : A Method for Uniform Reporting of Grid Refinement Studies. *Journal of Fluids Engineering*, 116(3):405–413. 84

Roache, P. J. (1997). Quantification of Uncertainty in Computational Fluid Dynamics. *Annual Review of Fluid Mechanics.* 84

Rossiter, J. E. (1964). Wind tunnel experiments on the flow over rectangular cavities at subsonic and transonic speeds. In *Aeronautical Research Council Reports and Memoranda.* 161

Savas, O. (1987). Stability of Bodewadt Flow. *Journal of Fluid Mechanics*, pages 77–94. 28, 34, 35

Savov, S. S., Atkins, N. R., and Uchida, S. (2016). Comparison of single and double lip rim seal geometry. In *Proceedings of the ASME Turbo Expo*, pages 1–15. 14, 45

Schouveiler, L., Le Gal, P., Chauve, M. P., and Takeda, Y. (1999). Spiral and circular waves in the flow between a rotating and a stationary disk. *Experiments in Fluids*, 26(3):179–187. xiv, 29

Schröder, T. R., Dohmen, H.-J., Brillert, D., and Benra, F.-K. (2020). Impact of Leakage Inlet Swirl Angle in a Rotor–Stator Cavity on Flow Pattern, Radial Pressure Distribution and Frictional Torque in a Wide Circumferential Reynolds Number Range. *International Journal of Turbomachinery, Propulsion and Power*, 5(2). 107

Serre, E., Crespo del Arco, E., and Bontoux, P. (2001). Annular and Spiral Patterns in Flows Between Rotating and Stationary Discs. *Journal of Fluid Mechanics, vol. 434, pp. 65-100.* 28, 29, 31, 33, 35, 53

Serre, E., Tuliszka-Sznitko, E., and Bontoux, P. (2004). Coupled numerical and theoretical study of the flow transition between a rotating and a stationary disk. *Physics of Fluids*, 16(3):688–706. 29, 31

Simpson, R. L. (2001). Junction flows. *Annual Review of Fluid Mechanics*, 33(C):415–443. 10

Sohn, D. W., Kim, T., and Song, S. J. (2006). Influence of the Leakage Flow Tangential Velocity on the Loss Generation and Leakage Flow Kinematics in Shrouded Axial Compressor Cascades. In *ASME Turbo Expo GT2006-90979*, pages 1–9. 15, 19, 45

Stewartson, K. (1953). On the flow between two rotating coaxial disks. *Mathematical Proceedings of the Cambridge Philosophical Society*, 49(2):333–341. 26

Sultanian, B. (2018). *Gas Turbines - Internal Flow Systems Modeling*, chapter 5, pages i–i. Cambridge Aerospace Series. Cambridge University Press. 80, 105, 161, 162

Taylor, J. V. and Miller, R. J. (2017). Competing Three-Dimensional Mechanisms in Compressor Flows. *Journal of Turbomachinery*, 139(2):21009–21010. xiii, 11, 12, 89

Taylor, D. J., Longley, J. P. (2019). Effects of Stator Platform Geometry Features on Blade Row Performance. *Journal of the Global Power and Propulsion Society, 3, 609-629.* 45, 157

Tuliska-Sznitko, E., Serre, E., and Bontoux, P. (2002). On the nature of the boundary layers instabilities in a flow between a rotating and a stationary disc. *Comptes Rendus de l'Academie de Sciences - Serie IIb: Mecanique*, 330(2):91–99. 28

Tyler, J. and Sofrin, T. (1962). Axial Flow Compressor Noise Studies. *SAE Transactions*, 70:309–332. 36

Welch, P. D. (1967). The use of fast Fourier transforms for the estimation of power spectra: A method based on time averaging over short modified periodograms. *IEEE Transactions on Audio and Electroacoustics*, 15:70–73. 67

Wellborn, S. R. and Okiishi, T. H. (1996). Effects of Shrouded Stator Cavity Flows on Multistge Axial Compressors Aerodynamic Performance. Technical Report NASA CR 135391, NASA Lewis Research Center. xiii, 15, 17, 18, 20, 45, 103, 104, 105

Wellborn, S. R. and Okiishi, T. H. (1998). The Influence of Shrouded Stator Cavity Flows on Multistage Compressor Performance. *ASME Turbo Expo 98-GT-012*. 20

Yoon, S., Selmeier, R., Cargill, P., and Wood, P. (2014). Effect of the Stator Hub Configuration and Stage Design. *Asme*, GT2014(26095):1–11. 18

Zambonini, G. (2016). *Unsteady dynamics of corner separation in a linear compressor cascade*. PhD thesis. 13

Publications

The work performed in this thesis allowed to publish or to contribute to the following publications:

Publications in international peer-reviewed journals:

1. **Babin, C.**, Dumas, M., Ottavy, X., Fontaneto, F.(2021). Numerical Characterisation of a HP Compressor Stage Equipped with a Closed Shrouded Stator Cavity. *Journal of Turbomachinery*, pages 1– 27. 115, TURBO-20-1256. https://doi.org/10.1115/1.4050333

2. De Laborderie, J., **Babin, C.**, Fontaneto, F. (2021). Aerodynamic simulation of a high-pressure compressor stage using the lattice Boltzmann method. *International Journal of Numerical Methods for Heat Fluid Flow*. Vol. ahead-of-print No. ahead-of-print. https://doi.org/10.1108/HFF-07-2021-0510

Proceedings papers

1. **Babin, C.**, Ottavy, X., Fontaneto, F. (2022). Leakage Flow Impact on Shrouded Stator Cavity Flow Topology and Associated high Speed Axial Compressor Stage Performance. *ASME TurboExpo 2021 - GT2022-82868*, (Accepted for journal publication in the *Journal of Turbomachinery*)

2. Cruz, G., **Babin, C.**, Ottavy, X., Fontaneto, F. (2021). Bayesian Inference of Experimental Data for Axial Compressor Performance Assessment. *ASME TurboExpo 2021 - GT2021-59200*. https://doi.org/10.1115/GT2021-59200

3. **Babin, C.**, Dumas, M., Ottavy, X, Fontaneto, F. (2020). Numerical Characterization of a HP Compressor Stage Equipped With a Closed Shrouded Stator Cavity. *Proceedings of the ASME Turbo Expo 2020: Turbomachinery Technical Conference and Exposition. Volume 2A: Turbomachinery. Virtual, Online. September 21–25, 2020*. https://doi.org/10.1115/GT2020-14908

4. Manfredi, M., **Babin, C.**, Fontaneto, F.(2020). Transonic axial compressors loss correlations – PART II: loss models validation. *ASME Turbo Expo 2020 Turbomachinery Technical Conference and Exposition - GT2020-16131*. https://doi.org/10.111/GT2020-16131

Conference papers

1. **Babin, C.** (2021). Measurement setup and strategy for shrouded stator cavity flow characterization in high speed axial compressor facility. *12th von Karman Institute for Fluid Dynamincs PhD Symposium*.

2. De Laborderie, J., Fali, K., **Babin, C.**, Fontaneto, F. (2020). On the applicability of the Lattice Boltzmann method for the aerodynamic characterization of a high-pressure axial compressor stage. *55th 3AF International Conference on Applied Aerodynamics*.

Respecting the precedent list order, the first page of each publication is given in the following pages.

TURBO-20-1256

NUMERICAL CHARACTERIZATION OF A HP COMPRESSOR STAGE EQUIPPED WITH A CLOSED SHROUDED STATOR CAVITY

Cedric Babin*
von Karman Institute for Fluid Dynamics
Rhode-St-Genèse, Belgium
cedric.babin@vki.ac.be

Michel Dumas
Safran Aircraft Engines
Moissy-Cramayel, France

Xavier Ottavy
Laboratoire de Mécanique des Fluides et d'Acoustique
Écully cedex, France

Fabrizio Fontaneto
von Karman Institute for Fluid Dynamics
Rhode-St-Genèse, Belgium

ABSTRACT

In axial compressors, shrouded stator cavity flows are responsible for performance degradation due to their interaction with the power stream. The present paper aims at exploring the possibility of employing a single stage high pressure axial compressor as a test vehicle for cavity flows investigations. In a first step, the robustness of the adopted RANS approach is tested against experimental data on the closed-cavity baseline configuration (i.e. no downstream-to-upstream recirculation). In a second phase, the effect of different hub cavities layouts of different levels of realism is numerically investigated. The focus is set on the representativeness of a closed cavity configuration with injection. The cavity flow topology and impact on the overall performance are considered in the analysis. At its final extent, this paper provides numerical and experimental guidelines for the robust assessment of cavity flows topology and performance effects.

Keywords: *leakage flows, cavity flow, axial compressors, technological effects, shrouded stator.*

INTRODUCTION

In classical turbomachinery components, performance degradation arises from the leakage flow generated at the interface between stationary and rotating parts. This effect is generally avoided by preserving a minimum operational clearance between them. In the case of stator rows, designers have the option of either cantilevered or shrouded blades [1], [2]. With shrouded stators, clearance is preserved under the hub platform, at the interface with the rotor shaft through labyrinth seals, as illustrated in the **Figure 1**. Since axial clearance

International Journal of Numerical Methods for Heat and Fluid Flow manuscript No.
(will be inserted by the editor)

Aerodynamic Simulation of a High-Pressure Compressor Stage using the Lattice Boltzmann Method

De Laborderie Jérôme* Babin Cedric**
Fontaneto Fabrizio**

Received: date / Accepted: date

Abstract Purpose - The present paper aims at evaluating the Lattice Boltzmann Method (LBM) on a high-subsonic high-pressure compressor stage at nominal regime.

Design/methodology/approach - The studied configuration corresponds to the H25 compressor operated in a closed-loop test rig at the von Karman Institute (VKI). Several operating points are simulated with LBM for two grids of successive refinements. A detailed analysis is performed on the time-averaged flow predicted by LBM, using a comparison with experimental and existing RANS data.

Findings - The finest grid is found to correctly predict the mean flow across the machine, as well as the influence of the rotor tip gap size. Going beyond time-averaged data, some flow analysis is performed to show the relevance of such a high-fidelity method applied to a compressor configuration. In particular, vortical structures and their evolution with the operating points are clearly highlighted. Spectral analyses finally hint at a proper prediction of tonal and broadband contents by LBM.

Originality - The application of LBM to high-speed turbomachinery flows is very recent. This paper validates one of the first LBM simulations of a high-subsonic high-pressure compressor stage.

Keywords Turbomachinery · Axial Compressor · LBM · Lattice Boltzmann Method

1 Introduction

High-fidelity methods in Computational Fluid Dynamics (CFD) are an active field of research for aerodynamic simulations of turbomachinery flows (e.g. [8, 18]). Indeed the resolution of a part of the turbulent spectrum allows removing the assumptions present in Reynolds-Averaged Navier-Stokes (RANS) turbulence models, widely used nowadays in industry. The latter are known to show limitations for specific flow topologies typically found in turbomachinery, such as secondary

*Safran Aircraft Engines, Moissy-Cramayel, France. **Turbomachinery and Propulsion Department, von Karman Institute for Fluid Dynamics, Rhode St Genese, Belgique

Proceedings of the ASME 2022 Turbomachinery Technical Conference & Exposition
ASME TurboExpo 2022
June 13-17, 2022, Rotterdam, The Netherlands

GT2022-82868

LEAKAGE FLOW IMPACT ON SHROUDED STATOR CAVITY FLOW TOPOLOGY AND ASSOCIATED HIGH SPEED AXIAL COMPRESSOR STAGE PERFORMANCE

Cedric BABIN*
Turbomachinery and Propulsion Department
Von Karman Institute for Fluid Dynamics
1640 Sint Genesius Rode, Belgium
Email: babin@vki.ac.be

Xavier Ottavy
Laboratoire de Mécanique
des Fluides et d'Acoustique
69130 Ecully, France

Fabrizio Fontaneto
Turbomachinery and Propulsion Department
Von Karman Institute for Fluid Dynamics
1640 Sint Genesius Rode, Belgium

ABSTRACT

This paper presents the investigation of realistic cavity leakage flow for the von Karman Institute for Fluid Dynamics H25 axial compressor stage, equipped with a shroud cavity of average Reynolds number $Re_r = 2.2 * 10^6$ and average aspect ratio $G = 0.06$. On top of overall performance measurements, time averaged data from unprecedented experimental dataset are used to characterize the stator hub shroud cavity flow field and its interaction with the power stream. The sensitivity of the stage performance and stability as well as the cavity flow topology is evaluated against injection conditions, compressor throttling and compressor speed. Parametric steady RANS simulations of the stage under injection are used to support the findings and state on the relevance of such approach in the preliminary design phase of axial compressors components.

As an example, a stage efficiency reduction of 0.97% for a leakage fraction of 0.56% at design point is retrieved. This performance drop is attributed to the effect of cavity flow on: the blockage ratio,the boundary layer skewness, and total temperature increase at stator row inlet. It is also presented that there is a mutual interaction between the cavity geometry and the cavity flow field organization. The injection homogenizes the cavity flow field and the associated pressure gradient. The various operating conditions presented also demonstrate that the cavity flow studied is, on average (i.e. time), sensitive to changes in compressor rotation speed and changes in stage loading.

NOMENCLATURE

Greek symbols

$\Delta\gamma$	Skewness induced additional turning [°].
η	Stage isentropic efficiency.
ι	Thermal expansion coefficient [1/K].
κ	Thermal diffusivity [m²/s].
λ	Throttle parameter.
ν	Kinematic viscosity [m²/s].
Ω	Rotor rotational speed [rad/s].
ϕ	Stage flow coefficient.
Φ	Meridional flow angle [°].
ψ	Stage loading coefficient.

Roman variables

a	Cavity radius ratio.
BF	Blockage factor.
G	Cavity local aspect ratio.
g	Acceleration of gravity [m/s²]
h	Cavity width [m].
L_f	Leakage fraction.
Nn	Compressor rotational speed in % of the nominal speed.
P	Pressure [mbar].
Q_e	Edge velocity component in 3D boundary layer.
r	Cavity local radius [m].
Re_i	Cylindrical Reynolds number (Taylor-Couette type flow).
Re_r	Local Reynolds number.
S_f	Swirl ratio.
T	Temperature [K].

*Address all correspondence to this author.

Proceedings of of ASME Turbo Expo 2021
Turbomachinery Technical Conference and Exposition
GT2021
June 7–11, 2021, Virtual, Online

#GT2021-59200

DRAFT: BAYESIAN INFERENCE OF EXPERIMENTAL DATA FOR AXIAL COMPRESSOR PERFORMANCE ASSESSMENT

Gonçalo G. Cruz*
von Karman Institute for Fluid Dynamics
Rhode-St-Genèse, Belgium

Cedric Babin
von Karman Institute for Fluid Dynamics
Rhode-St-Genèse, Belgium

Xavier Ottavy
Laboratoire de Mécanique des Fluides et d'Acoustique
Écully cedex, France

Fabrizio Fontaneto
von Karman Institute for Fluid Dynamics
Rhode-St-Genèse, Belgium

ABSTRACT

As the next generation of turbomachinery components becomes more sensitive to instrumentation intrusiveness, a reduction of the number of measurement devices required for the evaluation of performance is a possible and cost-effective way to mitigate the arising of non-mastered experimental errors. A first approach to a data assimilation methodology based on Bayesian inference is developed with the aim of reducing the instrumentation effort. A numerical model is employed to provide an initial belief of the flow, that is then updated based on experimental observations, using an ensemble Kalman filter algorithm for inverse problems. Validation of the algorithm is achieved with the usage of experimental measurements not used in the data assimilation process. The methodology is tested for a low aspect ratio axial compressor stage, showing a good prediction of the corrected compressor map, as well as a promising prediction of the inter-row radial pressure distribution and 2D flow field.

NOMENCLATURE

Acronyms

CFD	Computational Fluid Dynamics
DA	Data Assimilation
EnKF	Ensemble Kalman Filter
MAE	Mean Absolute Error
MCMC	Markov Chain Monte Carlo
PDF	Probability Density Function

Roman Symbols

a	Uniform distribution lower boundary
b	Uniform distribution upper boundary
C	Covariance Matrix
d	Flow field vector at experimental locations
$\mathscr{G}$	Forward Model
J	Ensemble size
$\mathscr{M}$	Measurement Matrix
$\mathscr{N}$	Normal Distribution with notation $\mathscr{N}(\mu,\sigma^2)$
n	Number of iterations
p	Pressure
q	Model error
u	Input Prior parameter
$\mathscr{U}$	Uniform Distribution with notation $\mathscr{U}(a,b)$
y	Experimental observation

Greek Symbols

ε	Experimental uncertainty
μ	Distribution mean
σ	Standard deviation
Φ	Flow field vector

Subscripts

0,1,2,4	Experimental plane location

*Address all correspondence to this author at goncalo.cruz@vki.ac.be

Proceedings of ASME Turbo Expo 2020
Turbomachinery Technical Conference and Exposition
GT2020
June 22-26, 2020, London, England

GT2020-14908

NUMERICAL CHARACTERIZATION OF A HP COMPRESSOR STAGE EQUIPPED WITH A CLOSED SHROUDED STATOR CAVITY

Cedric Babin
von Karman Institute for Fluid Dynamics
Rhode-St-Genèse, Belgium

Michel Dumas
Safran Aircraft Engines
Moissy-Cramayel, France

Xavier Ottavy
Laboratoire de Mécanique des Fluides et d'Acoustique
Écully cedex, France

Fabrizio Fontaneto
von Karman Institute for Fluid Dynamics
Rhode-St-Genèse, Belgium

ABSTRACT

In axial compressors, shrouded stator cavity flows are responsible for performance degradation due to their interaction with the power stream. The present paper aims at exploring the possibility of employing a single stage high pressure axial compressor as a test vehicle for cavity flows investigations. In a first step, the robustness of the adopted RANS approach is tested against experimental data on the closed-cavity baseline configuration (i.e. no downstream-to-upstream recirculation). In a second phase, the effect of different hub cavities layouts of different levels of realism is numerically investigated. The focus is set on the representativeness of a closed cavity configuration with injection. The cavity flow topology and impact on the overall performance are considered in the analysis. At its final extent, this paper provides numerical and experimental guidelines for the robust assessment of cavity flows topology and performance effects.

Keywords: *leakage flows, cavity flow, axial compressors, technological effects, shrouded stator.*

INTRODUCTION

In classical turbomachinery components, performance degradation arises from the leakage flow generated at the interface between stationary and rotating parts. This effect is generally avoided by preserving a minimum operational clearance between them. In the case of stator rows, designers have the option of either cantilevered or shrouded blades [1], [2]. With shrouded stators, clearance is preserved under the hub platform, at the interface with the rotor shaft through labyrinth seals, as illustrated in the **Figure 1**. Since axial clearance must also be ensured, the static pressure increase generated by the stator row drives a flow recirculation from the trailing edge region towards the leading edge. The so called leakage flow or cavity flow is proportional to the seal tooth clearance [3].

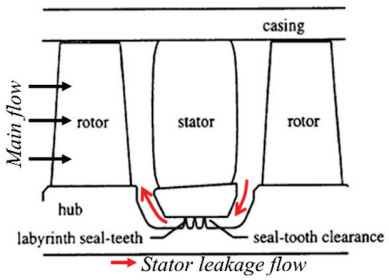

Figure 1: Shrouded stator configuration (adapted from [4]).

Cavity flow was the object of several investigations in the literature. It can be simplified through three quantities that are (1) the leakage fraction (Lf) that is the ratio of mass flow recirculating to the main channel one; (2) the swirl ratio that represents its tangential velocity component over the disc speed at same radius; (3) the increase of cavity flow total temperature due to viscous effects, so called windage heating. As far as topology is concerned Wellborn [5] highlighted that the upstream and downstream cavity trenches are characterized by similar flow structures. In these areas, a trench vortex is normally generated and drives the viscous interaction with the main stream flow.

The proximity of the blade row to the axial clearance trench is responsible for the generation in that region of ingress and egress regions in the pitch-wise direction [5], [6], [7]. In particular, Demargne and Longley [6] highlighted the pitch-wise modulation of the upstream trench flow structures as a consequence of the stator potential effect at multiple leakage fraction levels. It was found that for small recirculating mass flows, a localized ingestion of main stream takes place at mid-pitch.

Wellborn and Okiishi [4] and Mahmood and Turner [8] confirmed the linear dependency of the leakage fraction with respect to the rim seal gap value. Heidegger et al. [9] and

Proceedings of ASME Turbo Expo 2020
Turbomachinery Technical Conference and Exposition
ASME 2020
June 22 - 26, 2020, London, England UK

ASME 2020-16131

TRANSONIC AXIAL COMPRESSORS LOSS CORRELATIONS - PART II: LOSS MODELS VALIDATION

Marco Manfredi*, Cedric Babin, Fabrizio Fontaneto

von Karman Institute for Fluid Dynamics,
Rhode-Saint-Genèse, Belgium

ABSTRACT

The quest for greener, more efficient aircraft engines is the main driver for the development of innovative compression system designs. Reduced order design tools rely nevertheless on semi-empirical loss models, whose validity range is often not net or in general not verified. The present work aims at defining a set of loss correlations, which could readily be employed in the analysis and design process of modern transonic axial compressors. In Part I, various loss correlations were deeply described and, in some cases, updated to enhance both their generality and their prediction capability. In Part II, the effectiveness of both original and updated models will be tested for one specific low aspect ratio axial compressor stage. Experimental and numerical data will be used at such extent.

Keywords: loss correlations, axial compressors, profile loss, shock loss, end-wall loss, tip-leakage loss.

NOMENCLATURE

Subscripts

$1, 2$	Upstream, downstream stations
∞	Average condition between blade inlet and outlet
bl	Blade
e	Free-steam condition
ew	End-wall
h, t	Hub, tip
p	Profile
s	Shock
tl	Tip-leakage

Frame of Reference

r, ϑ, z	Radial, tangential, and axial directions
x	Streamline curvilinear abscissa

Greek Symbols

β	Relative flow angle from axial direction
δ	Boundary layer thickness
δ^*	Boundary layer displacement thickness
Π	Turbulent boundary layer wake parameter
ρ	Density
σ	Solidity, chord-to-pitch ratio
$\widetilde{\Omega}$	Span-wise mass-averaged total pressure loss coefficient
$\widetilde{\omega}$	Total pressure loss coefficient

Superscripts

$*$	Optimum incidence condition
r, s	Rotor, stator

Roman Symbols

a	Tip vortex radius
c	Blade chord
C_D, C_L	Drag, lift coefficients
d	Longitudinal distance covered by the vortex
i	Incidence angle $:= \beta - \beta_{bl}$
M	Mach number
p	Pressure
q	Inlet dynamic head $:= \frac{1}{2}\rho v_e^2$

*Currently PhD candidate at Politecnico di Milano, Italy, Laboratory of Fluid Machines (LFM)

Measurement setup and strategy for shrouded stator cavity flow characterization in high speed axial compressor facility

Cedric Babin

Turbomachinery and Propulsion Department, von Karman Institute for Fluid Dynamics, Belgium, cedric.babin@vki.ac.be

Supervisor: Fabrizio Fontaneto

Associate Professor, Turbomachinery and Propulsion Department , von Karman Institute for Fluid Dynamics, Belgium, fontaneto@vki.ac.be

University Supervisor: Xavier Ottavy

Head of Turbomachinery Department - LMFA , Ecole Centrale Lyon, France

Abstract

In axial compressors, shrouded stator cavity flows are responsible for performance degradation due to their interaction with the power stream. The present paper introduces the experimental setup update of the VKI R4 H25 test section to characterize cavity flow in a realistic turbomachinery environment under controlled leakage. The measurement key points and strategy is discussed to collect data on cavity flow effect on axial compressor performance and stability. Elements are introduced such as cavity wall measurements, cavity main volume measurements, and H25 stator inlet hub boundary layer measurements.

Keywords: leakage flows, cavity flow, axial compressors, technological effects, shrouded stator,experiments.

1. Introduction

In order to improve blade design for low aspect ratio configurations, a better understanding of leakage flow induced loss mechanism is crucial. The following study framework is centered on the hub leakage flow in the case of shrouded stator hub platforms. The choice of such technology rely on the stage design parameters [1]. With shrouded stators the rotating assembly clear the stationary parts below the hub level. Leakage flow generated in a downstream to upstream flow recirculation under the hub platform, triggered by the static pressure increase in the main channel. The end of the leakage path is associated with the injection of the recirculated flow in the main channel. The leakage flow is defined by three components [2]: (1) the leakage fraction in the cavity (ratio between the recirculated mass flow and the main channel mass flow); (2) the swirl ratio or swirl factor (ratio of cavity flow tangential velocity to the one of the rotor assembly); (3) the windage heating (total temperature increase from shear work induced by the rotating assembly). A literature review on cavity flow experimental investigation and their effect on axial compressor reveal the two type of configuration used: blade cascades or rotating machine assemblies. Studies in cascades ([3], [4], [5]) allow to have an independent control on flow leakage parameters. Usually performed without representative cavity geometries but rather with injection slots, they allow flexibility in generating multiple leakage conditions without any mechanical modification of the test section. Furthermore, cascade configuration provides with an ease of access for visualization techniques such as ink-dye, oil-dye, PIV, and concentration measurements of gas mixtures (ethylene, carbon dioxide). The results obtained in rotating assemblies ([2], [6]) are supported by the use of engine-like configurations. The analysis of cavity flow effect on axial compressor rely on the measurement of flow quantities in the main channel. In all the aforementioned studies, probe traversing is at least performed downstream of the blade row under investigation. Eventually, probe traversing is done in both radial and azimuthal direction. The type of instrumentation used is either steady (3-hole pneumatic probe, 5-hole pneumatic probe) or unsteady (such as

Association Aéronautique et Astronautique de France

55th 3AF International Conference on Applied Aerodynamics
23 — 25 March 2020, Poitiers – France

FP27-AERO2020-DELABORDERIE

ON THE APPLICABILITY OF THE LATTICE BOLTZMANN METHOD FOR THE AERODYNAMIC CHARACTERIZATION OF A HIGH-PRESSURE AXIAL COMPRESSOR STAGE

Jerome DE LABORDERIE[(1)*], Katia FALI[(1)], Cedric BABIN[(1,2)] and Fabrizio FONTANETO[(2)***]**

[(1)] *Safran Aircraft Engines, Rond-point R. Ravaud, 77550 Villaroche, FRANCE*

[(2)] *Von Karman Institute for Fluid Dynamics, Waterloosesteenweg 72, B-1640 Sint-Genesius-Rode, BELGIUM*

[*] *jerome.de-laborderie@safrangroup.com*

[**] *cedric.babin@safrangroup.com*

[***] *fontaneto@vki.ac.be*

ABSTRACT

The present paper aims at evaluating the Lattice Boltzmann Method (LBM) on a high-subsonic high-pressure compressor stage at nominal regime. The studied configuration corresponds to the H25 compressor operated in a closed-loop test rig at the von Karman Institute (VKI). Several operating points are simulated with LBM for two grids of successive refinements. A detailed analysis is performed on the time-averaged flow predicted by LBM, using a comparison with experimental and existing RANS data. The finest grid is found to correctly predict the mean flow across the machine. Going beyond time-averaged data, some flow analysis is performed to show the relevance of such a high-fidelity method applied to a compressor configuration. In particular, vortical structures and their evolution with the operating points are clearly highlighted. Spectral analyses finally hint at a proper prediction of tonal and broadband contents by LBM.

1. INTRODUCTION

High-fidelity methods in Computational Fluid Dynamics (CFD) are an active field of research for aerodynamic simulations of turbomachinery flows (e.g. [4, 10]). Indeed the resolution of a part of the turbulent spectrum allows removing the assumptions present in Reynolds-Averaged Navier-Stokes (RANS) turbulence models, widely used nowadays in industry. The latter are known to show limitations for specific flow topologies typically found in turbomachinery, such as secondary flows with high vorticity (tip leakage flows, corner stalls, interaction with cavity flows,...) and separated flows encountered at off-design conditions for instance. Providing that the software and its associated methodology are accurately validated, high-fidelity methods are thus expected to help engineers to improve aerodynamic designs of turbomachines, leading to fuel and emissions reductions of future aero-engines. Several high-fidelity methods have been developed, that can be sorted into two categories, according to the wall treatment: either the flow is resolved up to the wall, as performed in Direct Numerical Simulation (DNS) and in Wall Resolved Large Eddy Simulation (WRLES), or a model is used to predict the flow close to the wall, as in Wall Modeled Large Eddy Simulation (WMLES) and in the different approaches based on the Detached Eddy Simulation (DES), for which a RANS model is employed close to the wall. For industrial turbomachinery configurations containing several bladed rows, the first category cited above is still out-of-reach with the available computational resources available. In addition to this classification, all these methods are embedded within solvers with their own discretization. The finite volume approach is largely widespread in the CFD community. The Lattice Boltzmann Method (LBM) is much more recent for aerodynamics of turbomachinery. This method appears to be attractive for three main reasons [11]. First, the cost of one iteration per degree of freedom is recognized to be significantly smaller than in finite volume approaches, thanks to its naturally efficient parallelized algorithm. Second, the numerical scheme

dernière page de la thèse

AUTORISATION DE SOUTENANCE

Vu les dispositions de l'arrêté du 25 mai 2016,

Vu la demande du directeur de thèse

Monsieur X. OTTAVY

et les rapports de

M. L. GICQUEL
Senior Researcher HDR - CERFACS - 42 avenue Gaspard Coriolis - 31057 Toulouse cedex 1

et de

M. C. SANGAN
Reader - University of Bath - Department of Mechanical Engineering
Turbomachinery Research Centre - Claverton Down - Bath BA2 7AY - Royaume-Uni

Monsieur BABIN Cédric

est autorisé à soutenir une thèse pour l'obtention du grade de **DOCTEUR**

Ecole doctorale Mécanique, Energétique, Génie civil, Acoustique

Fait à Ecully, le 2 juin 2022

Pour le directeur de l'Ecole centrale de Lyon
Le directeur des Formations

Grégory VIAL